SKYRMIONIC BEAMS AND QUANTUM MATCHED FILTERING

Sijia Gao

A thesis submitted for the degree of Doctor of Philosophy

School of Physics and Astronomy
College of Science and Engineering
University of Glasgow

Dec, 2021

Abstract

This thesis is comprised of two parts. In the first part we introduce a new category of structured beams: the paraxial skyrmionic beams. In the second part of this thesis we introduce a quantum algorithm analogous to the classical matched filtering algorithm for gravitational wave data analysis.

Structured light refers to the generation and application of a customised light field, including intensity, phase and polarisation. In the first part of this thesis, we demonstrate that a specific class of structured beam possesses a topological property that derives both from the spatially varying amplitude of the field and also from its varying polarization. This type of beam is referred to as a skyrmionic beam. We are interested in skyrmionic beams mainly for three reasons: the mathematical appeal of this structure; the physical significance of this structure to link the spatial and polarisation component of structured beams; and the potential application of this property in modelling beam propagation.

There are three important aspects to the skyrmionic nature of paraxial beams: the skyrmion number, the skyrmion field, and the skyrmion vector potential field. In Chapter. 4 we introduce the construction of the skyrmion beams and their associate skyrmion number with two specific examples. In Chapter. 5 we introduce the skyrmion field along with proving that it is divergenceless. We will then proceed to illustrate this property with two examples. Lastly, in Chapter. 6 we introduce the skyrmion vector potential field. Our discussion throught this chapter will revolve around the analogy between this field and the superfluid velocity and accompanied by two examples.

In Chapter. 7 we explore the relation between the skyrmionic beams and the more familiar Poincaré beams to highlight their differences. During the discussion, we introduce another type of beam similar to the skyrmionic beam, namely the fractional skyrmionic beam, which lacks the topological robustness of its counterpart

It is also important to explore the experimental realisation of skyrmionic beams. In particular, collaborating with the Optics group we wish to develop a method to extract the skyrmion number of arbitrary beams through experimental measurements. In Chapter. 8 we propose three candidate methods and discuss their current results and roadblocks, respectively.

The second part of thesis will focus on quantum algorithms. We propose a quantum algorithm analogous to the classical matched filter algorithm in Chapter. 11. Comparing with its classical counterpart, our algorithm provides a square-root speed-up, which would make possible otherwise intractable searches. We will also demonstrate both a proof-of-principle quantum circuit implementation, and a simulation of the algorithm's application to the detection of the first gravitational wave signal GW150914 as well as a discussion on the time complexity and space requirements.

Acknowledgements

I would like to start with my main supervisor Prof. Stephen Barnett. Steve has always been patient, encouraging and helpful throughout my PhD. It meant a great deal to me when he took my naive question seriously and started our journey in skyrmions. Similarly, I would like to thank Dr. Sarah Croke. Without her, the quantum matched filtering project would still remain as a kitchen chat. Sarah has not only offered great insight to me academically, but also have been a role model as a female researcher who cared for me when I was down. Then I would also like to thank Dr. Jörg B Götte for tolerating my nonsense questions and enduring my unstructured Mathematica code.

Before going on to other individuals I would like to express my gratitude to the Quantum Theory (QT) Group collectively. Joining this group in my fourth year undergraduate was the start of my physics research journey and I have not left since. QT as a whole has allowed me to explore physics in both breadth and depth. This journey cultivated and preserved my child-like curiosity. As a second home, it has shaped me to who I am today.

As for the individuals in QT, I would like to mention Dr. Messinger for all the office chat, the time we spent in winter/summer school and conferences as well as teaching me to boulder. You have always been a motivation and great friend throughout my PhD. Next, Dr. Flatt for the random chats, pub tours and great help in both life as well as work. I would also like to thank Dr. Speirits for all the afternoon tea talks and Dr. Crimin for all the wonderful cakes. Dr. Brougham, Dr. Ritboon and Dr. Weir, thanks for the fun times when we were in the office; Dr. Ferenczi, Zhujun, Madeline, Hector and Ben, thank you all for the zoom game nights and online socials during the pandemic; Dr. Cresser, Dr. Butera, Dr. Bennett and Dr. Westerberg, thanks for all the insightful conversations both in person and during zoom calls.

I would also like to thank my collaborators in IGR and Optics group for the fun discussions and great effort to bring our theory to life.

Finally, a massive thank you to all my family and friends. Without the financial and emotional support of my parents I would not be able to start, let alone finish my PhD. Thanks for being there for me despite the time and geographical distances and enduring my stubbornness. A big shout out to my loving boyfriend and collaborator Fergus. Without you, there would not be the quantum matched filtering part. Thanks for being there with me through thick and thin and offering nothing but unwavering support regardless of my choices. This also extends to the loving Hayes family who took me in during the pandemic time so I was not stuck in my flat in Glasgow. I would also like to thank Dan for listening to all my rants in the gym and for his support when I was down; Arthur for all the badminton time during thesis writing; and Will for all the emotional and edit support through my PhD... In the end, I would like to thank all the cat videos on Instagram and Spotify recommendation algorithm for providing me with laughter and comfort.

Author's declaration

I certify that the thesis presented here for examination for a PhD degree of the University of Glasgow is solely my own work other than where I have clearly indicated that it is the work of others (in which case the extent of any work carried out jointly by me and any other person is clearly identified in it) and that the thesis has not been edited by a third party beyond what is permitted by the University's PGR Code of Practice.

The copyright of this thesis rests with the author. No quotation from it is permitted without full acknowledgement.

I declare that the thesis does not include work forming part of a thesis presented successfully for another degree.

I declare that this thesis has been produced in accordance with the University of Glasgow's Code of Good Practice in Research.

I acknowledge that if any issues are raised regarding good research practice based on review of the thesis, the examination may be postponed pending the outcome of any investigation of the issues.

Parts of this work either have been, or will be, published in:

- Sijia Gao, Fiona C Speirits, Francesco Castellucci, Sonja Franke-Arnold, Stephen M Barnett, and Jörg B Götte. Paraxial skyrmionic beams. *Physical Review A*, 102(5):053513, 2020

- Sijia Gao, Fergus Hayes, Sarah Croke, Chris Messenger, and John Veitch. A quantum algorithm for gravitational wave matched filtering. *arXiv preprint arXiv:2109.01535*, 2021

Sijia Gao
Dec, 2021

I'll think about that tomorrow. Tomorrow is another day.

Scarlett O'Hara, *Gone with the wind* by Margaret Mitchell

Contents

Chapter 1

Introduction

During recent decades, the manipulation of light beams has become more efficient and meticulous owing to the development of technology [3]. In particular structured light has produced many applications across various disciplines, including optical traps and tweezers [4, 5, 6, 7, 8] and more effective commumications [9]. In order to further understand the topology structure of structured beams, we look into how to incorporate the theory of magnetic skyrmions into the categorisation of structured beams.

Magnetic skyrmions are topologically protected quasiparticles mainly studied in condensed matter theory. It was first demonstrated that optical skyrmions exist in the evanescent field of a plasmonic surface [10] and subsequently in the local spin field of focused vector beams [11]. However, skyrmionic paraxial beams still remained an untouched area which prompted our investigation. In previous studies, it has been shown that because of their topological nature, optical skyrmions could be applied in ultrafast nanometric metrology [12], deeply subwavelength microscopy [11], and topological Hall devices [13].

Through the first half of this thesis, we will focus on developing the theory of paraxial skyrmionic beams. This theory includes the associated skyrmion number, skyrmion field and skyrmion vector potential field. These features will be discussed in Chapter. 4, 5 and 6, respectively. The relationship between our proposed skyrmionic beams and the more familiar Poincaré beams will be discussed in Chapter. 7, from which we then derive the fractional skyrmion beams. At the end of Part. I, we will propose three methods to experimentally extract the skyrmion number of arbitrary structured beams as well as a discussion on their advantages and disadvantages, respectively.

Part. II is related to one of the potential applications of optical skyrmions, quantum computing. In Part. II, we propose a quantum algorithm analogous to the classical matched filter algorithm. Various quantum algorithms demonstrated that they are more efficient than classical algorithms in certain problems, including square-root speed-up in unstructured search [14] and exponential speed-up in factoring large numbers [15]. Recently, from Google's superconducting quantum computer 'Sycamore' in 2019 [16], to the Chinese photonic quantum computer 'Jiuzhang' in 2020 [17], quantum computers are developing faster than ever. Therefore, with this in mind we look to explore the advancements and changes quantum computers will potentially introduce. After the first detection of the binary black hole merger, known as GW150914 [18], the detection of gravitational waves from the merger of compact binary systems is now a regular occurrence. However, with the increased sensitivity of detectors in order to detect weaker signals, the compu-

tational power required for gravitational wave data analysis is beyond the limit of current classical computers. Therefore, we are motivated to propose a quantum algorithm based on the Grover's algorithm (which we will introduce in Chapter. 11) that offers a square-root speed-up compared to its classical counterpart. Although it is by no means an algorithm applicable to noisy intermediate-scale quantum (NISQ) devices, it does represent the first step in constructing possible applications of quantum computation to gravitational wave data analysis.

Part I

Skyrmionic Beams

Chapter 2

Structured beams

The darkest night gave me dark-colored eyes
Yet with them I'm seeking light
—Cheng Gu, "A Generation", 1979, (translated by Juan Yuchi)

Light has been used as the representation of ideal, freedom and the transcendent across different cultures throughout history. Humanity has therefore trying to study, understand [19] and manipulate light in the same way as we wish our own existence. Nowadays, light has been used to advance people's lives in various ways, one important example of which is transferring information. From fiber broadband to radio waves bringing live sports broadcasting in our homes, light has become an indispensable element in our modern life styles. As an emerging tool, structured light has the potential to further shape our life in the near future.

Structured light refers to the generation and application of a customised light field, including intensity, phase and polarisation. Although the idea of controlling light has existed for long time, precise manipulation of light was not achieved until the advent of laser in 1960s. The emergence of SLMs (spatial light modulators) and DMDs (Digital micromirror devices) has also led to advances in more efficient and meticulous manipulation of light beams [3]. During recent decades, structured light has produced many applications across various disciplines. For example, the varying intensity provides the gradient force to create optical traps and tweezers, which are now an essential toolkit to manipulate matter at nano scale [4, 5, 6, 7, 8]. Because structured light possesses more degrees of freedom, which feeds the exponentially growing demand of data capacity, it has also gained traction in the optical communication community in recent years. Both classical optical systems [20, 21, 22, 23] and quantum optical systems [24, 25, 26] have demonstrated that it is possible to utilise structured light for effective communication. This makes it possible to realise high-dimensional QKD (quantum key distribution) [9] and therefore further increase data security.

One of the important elements in structured light is vortex beams. There have been numerous studies of vortices since the early 1950 [27] [28]. The first systematic study, however, was not carried out until 1974 by two groups of people: Nye and Berry, and Hirschfelder [29][30]. Although vortices have been known to people from then, people did not connect this wave mode with orbital angular momentum until 1992 by Allen [31]. This leads to a new intense era of studying vortex beams both theoretically and experimentally, which laid the foundations for the versatile applications of structured beams as we noted previously.

In this chapter, we will start with Maxwell's equations in free space to obtain the Gaussian beams as solutions in the paraxial limit in Section. 2.1. In Section. 2.2 we will review the concept of definition of polarisation, before introducing vector beams in Section. 2.3.

2.1 Paraxial Optics

2.1.1 Wave Equations

We are mainly interested in light travelling in free space. In free space, the electric displacement **D** and the magnetic field strength **H** are related to the electric field **E** and the magnetic field **B** by [32]:

$$\mathbf{D} = \epsilon_0 \mathbf{E}; \tag{2.1}$$

$$\mathbf{H} = \frac{\mathbf{B}}{\mu_0}, \tag{2.2}$$

where ϵ_0 and μ_0 are fundamental physical constants, namely, the permittivity and permeability of free space. As an electromagnetic wave, light is best described by Maxwell equations. The derivative form of the full Maxwell equations is [32]:

$$\nabla \cdot \mathbf{D} = \rho; \tag{2.3}$$

$$\nabla \cdot \mathbf{B} = 0; \tag{2.4}$$

$$\nabla \times \mathbf{E} = -\frac{\partial \mathbf{B}}{\partial t}; \tag{2.5}$$

$$\nabla \times \mathbf{H} = \mathbf{J} + \frac{\partial \mathbf{D}}{\partial t}, \tag{2.6}$$

where ρ and **J** are the electric charge and current density respectively. In free space where there are no charges or currents, we can replace the full Maxwell equations by the following form [32]:

$$\nabla \cdot \mathbf{E} = 0; \tag{2.7}$$

$$\nabla \cdot \mathbf{B} = 0; \tag{2.8}$$

$$\nabla \times \mathbf{E} = -\frac{\partial \mathbf{B}}{\partial t}; \tag{2.9}$$

$$\nabla \times \mathbf{B} = \epsilon_0 \mu_0 \frac{\partial \mathbf{E}}{\partial t}. \tag{2.10}$$

From Eq. 2.5 and Eq. 2.6 we can obtain the full vector wave equation:

$$\nabla \times (\nabla \times \mathbf{E}) = -\mu_0 \epsilon_0 \frac{\partial^2 \mathbf{E}}{\partial t^2}. \tag{2.11}$$

According to Lagrange's formula of vector cross-product identity [33], this is explicitly:

$$\nabla (\nabla \cdot \mathbf{E}) - \nabla^2 \mathbf{E} = -\mu_0 \epsilon_0 \frac{\partial^2 \mathbf{E}}{\partial t^2}, \tag{2.12}$$

Because we are mainly focusing on cases that light travelling in a source-free space, in which the

above wave equation simplifies to:

$$\nabla^2 \mathbf{E} - \mu_0 \epsilon_0 \frac{\partial^2 \mathbf{E}}{\partial t^2} = 0, \tag{2.13}$$

where $1/(\mu_0 \epsilon_0) = c^2$, indicating the velocity of light in vacuum. The simplest solutions to the above equation are the complex monochromatic wave solutions:

$$\mathbf{E}(\mathbf{r}, t) = \mathbf{E}_0 e^{i(\mathbf{k}\cdot\mathbf{r} \pm \omega t)}, \tag{2.14}$$

where $\mathbf{E}_0$ is the initial electric field at the origin and $\omega = 2\pi f$ is the frequency of the wave. From Eq. 2.7 and 2.8 we obtain the relationship that:

$$\mathbf{k} \cdot \mathbf{E}_0 = \mathbf{k} \cdot \mathbf{B}_0 = 0. \tag{2.15}$$

This means that both the electric field and the magnetic field are oscillating in the cross-sections perpendicular to the wave propagating direction. The wave vector $\mathbf{k}$ indicates the direction of the propagation of the wave with a magnitude of $|\mathbf{k}| = 2\pi/\lambda$. The relationship between $\mathbf{k}$ and ω is:

$$\frac{\omega}{k} = c. \tag{2.16}$$

The solution with $\mathbf{k} \cdot \mathbf{r} - \omega t$, the wave travels in the same direction as $\mathbf{k}$ [32]. Substituting this solution into the wave equation Eq. 2.13, it becomes the so-called Helmholtz equation [32]:

$$\nabla^2 \mathbf{E} + k^2 \mathbf{E} = 0. \tag{2.17}$$

We will first concentrate on the scalar form of the Helmholtz equation. This can be obtained by choosing a constant direction $\mathbf{g}$ for the electric field [34]:

$$\mathbf{E}(\mathbf{r}) = \mathbf{g}\Psi(\mathbf{r})e^{-i\omega t}. \tag{2.18}$$

In this way, the scalar Helmholtz equation can be expressed as:

$$\nabla^2 \Psi + k^2 \Psi = 0. \tag{2.19}$$

2.1.2 Paraxial approximation

The paraxial approximation is essential to Gaussian optics: an elementary theory in which only rays and points in the immediate neighbourhood of the axis are considered [35]. It provides an adequate description of laser optics in real life [36]. Mathematically, this means the inclination angle between the wave fronts and the axis is sufficiently small and consequently eligible for small angle approximation. For a beam propagating in the z direction, this indicates that the x and y components of the wavevector are very small compared with k:

$$\frac{\sqrt{k_x^2 + k_y^2}}{k} \ll 1, \tag{2.20}$$

or alternatively:

$$k_z \approx k - \frac{k_x^2 + k_y^2}{2k}, \tag{2.21}$$

Without losing generality, a monochromatic optical wave beam propagating in the z direction is considered here:

$$\Psi(\mathbf{r}) = u(x, y, z)e^{ikz}, \tag{2.22}$$

where $u(x, y, z)$ is referred to as the complex envelope as it describes the shape of the beam [37]. Because the beam is restricted to a certain distance around the z-axis based on the definition of paraxial beams, the z-dependence of u is essentially due to diffraction effects. Therefore, u is generally slow varying in z direction compared with the transverse variation in the width of the beam [36]. The slowing varying envelope approximations corresponds to working in the regime with

$$\frac{\partial^2 u}{\partial z^2} \ll k^2 u, k\frac{\partial u}{\partial z}, \tag{2.23}$$

If we employ the relation in eq. 2.16 and neglecting the term $\partial^2 u/\partial z^2$, the scalar Helmholtz equation Eq. 2.17 reduces to the paraxial equation:

$$\nabla_\perp^2 u + 2ik\frac{\partial u}{\partial z} = 0, \tag{2.24}$$

where $\nabla_\perp^2$ denotes the derivatives with respect to the transverse plane [38].

The derivative of a paraxial beam in the transverse direction is nonzero, which indicates that the wavefront of a paraxial wave is not a plane wave. This means that the local wave vectors which are normal to the local wavefront are not exactly parallel to the propagation direction. However, this does not contradict Maxwell's equations as the corresponding electric and magnetic fields are still divergenceless [36, 39].

Solutions to the paraxial equations including Laguerre-Gaussian and Hermite-Gaussian beams [38] and can be obtained by separating variables. One particular example used in this thesis is the Laguerre-Gaussian beams.

2.1.3 Gaussian beam

Solutions to paraxial wave equation have been widely used in laser optics. Hermite-Gaussian beams and Laguerre-Gaussian beams are two of the most established examples [40]. While both of these form a set of complete solutions, they correspond to physical systems with rectangular and cylindrical symmetries respectively. In this thesis, the main examples are constructed by Laguerre-Gaussian beams.

Laguerre-Gaussian beams are solutions to paraxial wave equations in cylindrical coordinates:

$$\left(\frac{1}{\rho}\frac{\partial}{\partial\rho} + \frac{\partial^2}{\partial\rho^2} + \frac{1}{\rho^2}\frac{\partial^2}{\partial\phi^2} + 2ik\frac{\partial}{\partial z}\right)u_p^\ell = 0, \tag{2.25}$$

where ρ is the radial coordinate and ϕ is the azimuthal or polar angle. The normalised form of

Laguerre-Gaussian modes are given by:

$$u_p^\ell = \frac{C_{\ell p}^{LG}}{w(z)}\left(\frac{\rho\sqrt{2}}{w(z)}\right)^{|\ell|} L_p^{|\ell|}\left(\frac{2\rho^2}{w(z)^2}\right)\exp\left(-\frac{\rho^2}{w(z)^2}\right)\exp\left(-ik\frac{\rho^2}{2R(z)}\right)\exp\left(i\ell\phi\right)\exp\Big(i(2p+|\ell|+1)\xi(z)\Big). \tag{2.26}$$

In this form, ℓ is the winding number, characterising the number of phase dislocations in the wave

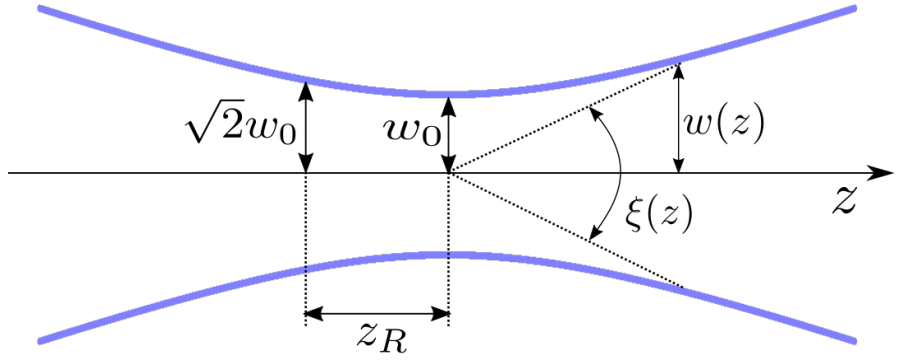

Figure 2.1 Gaussian beam width $w(z)$ as a function of the distance z along the propagation direction of the beam and beam waist of w_0. The 'edge' of the beam, which is outlined in blue, is considered to be where its radius $r = w(z)$. At $w(z)$, the intensity has dropped to $1/e$ of its on-axis intensity. The beam waist w_0 is considered to be the narrowest plane, dependent on the wavelength and the curvature of the beam. Typically for paraxial beams, w_0 is larger than $2\lambda/\pi \approx 10^{-6}$m. Z_R is the Rayleigh range (the distance along the beam propagation direction from the waist to where the area of the cross section is doubled) and is typically of wavelength size.

front of the beam, $C_{lp}^{LG} = \sqrt{\frac{2p!}{\pi(p+|\ell|)!}}$ is the required normalization constant; $L_p^{|\ell|}(x)$ is the generalised Laguerre polynomial; $p = 0, 1, 2, ...$ is the radial quantum number; w_0 is the beam waist where the beam is at its narrowest; $w(z) = w_0\sqrt{1+\frac{z^2}{z_R^2}}$ is the beam width; $R(z) = z(1+z_R^2/z^2)$ is the radius of curvature of wavefronts, Z_R is the Rayleigh range (the distance along the beam propagation direction from the waist to where the area of the cross section is doubled), and $\xi(z) = \arctan(z/z_R)$ is the Gouy phase, as shown in Figure. 2.1.

The Laguerre-Gaussian beams are orthonormal in both the mode index p and the azimuthal index ℓ over the radial coordinate ρ and the azimuthal angle ϕ respectively:

$$\int_{\theta_0}^{\theta_0+2\pi} d\phi \int_0^\infty \rho d\rho u_p^\ell \left(u_q^m\right)^* = \delta_{pq}\delta_{\ell m}; \tag{2.27}$$

where θ_0 is an arbitrary starting angle and δ denotes the Kronecker-delta function. The orthogonality of the p mode is based on the orthogonality relation of generalised Laguerre polynomials [41] whereas that of the ℓ mode owes to the 2π periodic property of e^{ix}. One particular physical implication of the mode index p and ℓ is on the intensity profile of the beams as shown in Fig. 2.2. Beams with a non-zero value of ℓ have an undefined phase on the z axis with also zero intensity there. The indices p and ℓ determine the number of concentric rings and intertwined helical wavefronts respectively.

The phase term $e^{i\ell\phi}$ in Laguerre-Gaussian beams is associated with the idea that each photon carries $\hbar\ell$ of orbital angular momentum [31]. Therefore, ℓ is also called the topological charge

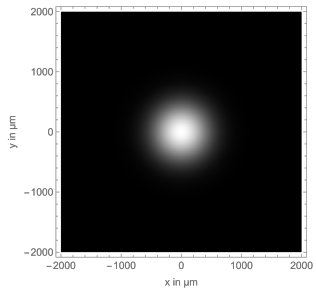

(a) $\ell = 0$, $p = 0$.

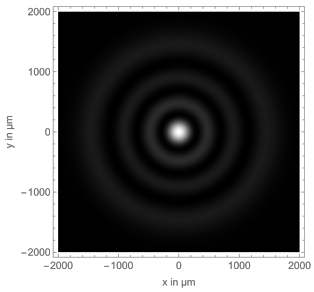

(b) $\ell = 0$, $p = 3$.

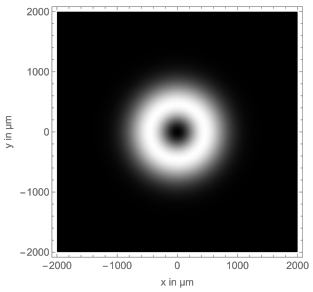

(c) $\ell = 1$, $p = 0$.

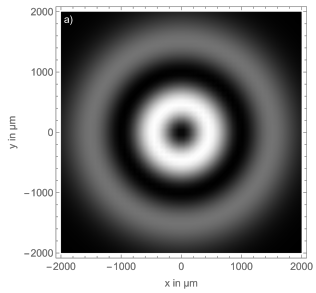

(d) $\ell = 1$, $p = 1$.

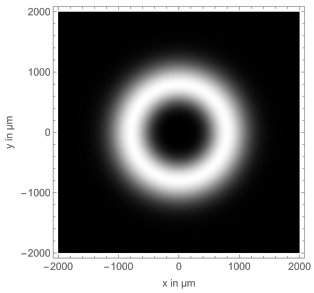

(e) $\ell = 3$, $p = 0$.

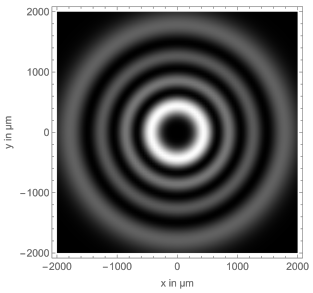

(f) $\ell = 3$, $p = 3$.

Figure 2.2 Intensity profiles of different modes of Laguerre-Gaussian beams generated using Mathematica.

of a beam. Vortex beams are beams containing vortices, i.e. phase singularities or dislocations of phase fronts. This orbital angular momentum is an intrinsic value [42, 43], in contrast with the mechanical orbital angular momentum of point particles.

It is also common to link the phase factor in Laguerre-Gaussian beams to optical vortices [44]. Optical vortices are phase singularities and have zero intensity at its centre. Typically, as shown in Fg. 2.2b to 2.2f, optical vortices exist in the centre of the beam profile. The topological charge ℓ can also be recovered from a closed path integral around the phase singularity [45]:

$$\ell = \frac{1}{2\pi} \oint d\mathbf{s} \cdot \nabla \arg(\Psi), \tag{2.28}$$

where $\arg(\Psi)$ is the phase factor and the non-vanishing part in $\arg(\Psi)$ after the integration is $\ell\phi$ in Laguerre-Gaussian beams.

Recent developments have demonstrated that propagating electrons can also possess vortices as well. This is clear from the similarity of form between the Schrödinger equation and the paraxial wave equation in Eq. 2.24:

$$i\hbar \frac{\partial \psi}{\partial t} + \frac{\hbar^2}{2m} \nabla^2 \psi = 0. \tag{2.29}$$

In a similar form to optical beams, it can be described by a phase singularity in the wave function of the form $e^{i\ell\phi}$ [46, 47, 48, 49]. Although the existence of vortex beams is obvious in low energy regime when electrons can be described by the Schrödinger equation, it is not unanimously agreed that they exist in higher energy regime [50, 51, 52]. The fact that the vortex structure is a

topological feature leads to the assumption that it should not change or vanish just by moving the electron beams to a higher energy regime. Although high energy electron beams are not of much practical use yet, let alone high energy vortex beams, the study itself at least will provide us with motivation for experimental works in this area.

2.2 Polarisation

The spatial variation of the paraxial mode in the transverse plane requires the extreme of a small electric field component in the z direction. Without this, the transversality condition, $\nabla \cdot \mathbf{E} = 0$, would be violated. Hence, the full electric filed for our paraxial beam has the form of:

$$\mathbf{E}(\mathbf{r}, t) = e^{i(kz-\omega t)} \left(u(\mathbf{r}) \left(E_x^0 \hat{x} + E_y^0 \hat{y} \right) + E_z(\mathbf{r}) \hat{z} \right), \tag{2.30}$$

where $\hat{x}$, $\hat{y}$ and $\hat{z}$ are unit vectors in the corresponding directions and E_x^0, E_y^0 are constants. The transversality condition in Eq. 2.7 has the form:

$$\frac{\partial u}{\partial x} E_x^0 e^{ikz} + \frac{\partial u}{\partial y} E_y^0 e^{ikz} + \frac{\partial (E_z e^{ikz})}{\partial z} = 0, \tag{2.31}$$

which implies that E_z must satisfy the equation:

$$ikE_z + \frac{\partial E_z}{\partial z} = -E_x^0 \frac{\partial u}{\partial x} - E_y^0 \frac{\partial u}{\partial y}. \tag{2.32}$$

The variation of E_z in the z direction in the paraxial regime, $\frac{\partial E_z}{\partial z}$, is very slow compared with the wavelength scale variation associated with the term ikE_z. Therefore, we can neglect the z-derivative of $E - z$ to obtain an approximated expression of E_z as:

$$E_z \approx \frac{i}{k} \left(E_x^0 \frac{\partial u}{\partial x} + E_y^0 \frac{\partial u}{\partial y} \right) \tag{2.33}$$

The typical length scale on which u varies with respect to x or y is the beam waist, $w(z)$, and hence:

$$|E_z| \approx \frac{\lambda}{2\pi w(z)} \sqrt{|E_x|^2 + |E_y|^2} \tag{2.34}$$

It follows that the z-component of the electric field is less in magnitude than the transverse component by the ratio of the wavelength to the beam waist [39]. This is necessarily a very small quantity in the paraxial regime. Therefore, we can discuss the polarisation (the electric field direction) solely in terms of the electric field component in the transverse plane.

Polarization describes the oscillations of the electric and magnetic fields of a transverse wave [32]. As stated above, without losing generality, we choose the direction of the propagation in the z direction. Because we can approximate the electric and magnetic fields to be perpendicular to the propagation direction, only the x and y components of $\mathbf{E}$ and $\mathbf{H}$ field are non-zero. In order to consider the polarisation ellipse, namely, the end curve formed by the end points of the electric

field vector at a given point, the electric field can be described by:

$$\begin{aligned} E_x &= a_1 \cos(\tau + \delta_1); \\ E_y &= a_2 \cos(\tau + \delta_2); \\ E_z &= 0, \end{aligned} \tag{2.35}$$

where $\tau = \omega t - kz$. Using multiple angle addition functions it can be shown that the following relation exists between E_x and E_y [35]:

$$\left(\frac{E_x}{a_1}\right)^2 + \left(\frac{E_y}{a_2}\right)^2 - 2\frac{E_x}{a_1}\frac{E_y}{a_2}\cos\delta = \sin^2\delta, \tag{2.36}$$

where $\delta = \delta_2 - \delta_1$. This relation demonstrates that the locus of the points whose coordinates are $\left(E_x, E_y\right)$ from an ellipse as shown in Fig. 2.3, where η and ζ represents the set of axes along that of the ellipse. We can define the components along the new set of axes as [35]:

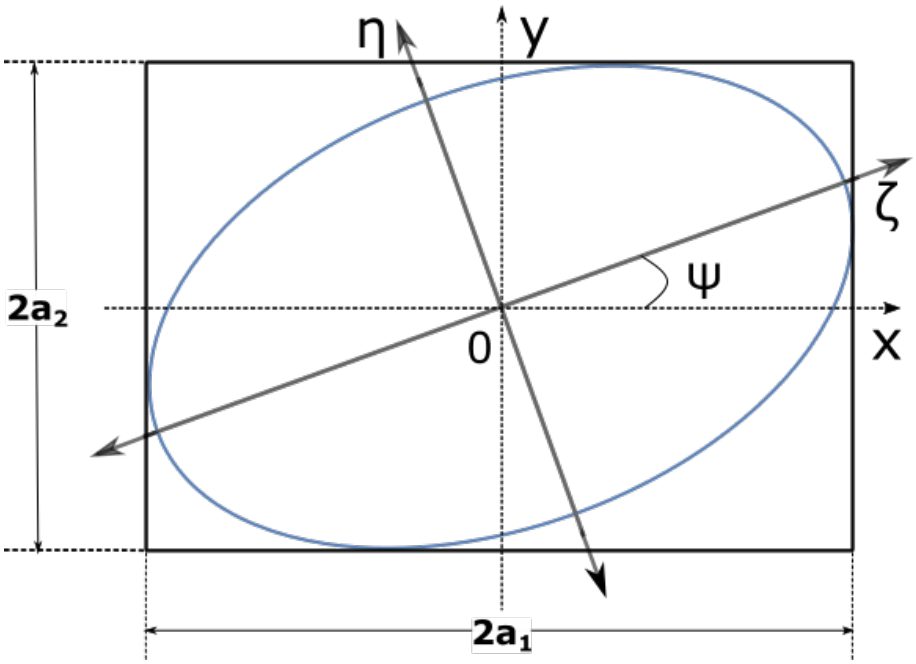

Figure 2.3 The polarisation ellipse.

$$\begin{aligned} E_\zeta &= E_x \cos\psi + E_y \sin\psi = a\cos(\tau + \delta_0); \\ E_\eta &= -E_x \sin\psi + E_y \cos\psi = b\sin(\tau + \delta_0), \end{aligned} \tag{2.37}$$

where, without losing generality, $a \geq b$. Here, we introduce two auxiliary angles [35]:

$$\tan\alpha = \frac{a_2}{a_1}; \quad \tan\chi = \frac{b}{a}, \tag{2.38}$$

where $\alpha \in [0, \pi/2]$ denotes the ratio between the x and y components of the electric field and $\chi \in [0, \pi/4]$ specifies the shape and orientation of the polarisation ellipse. To summarise, the relationship between the principle semi-axes of the polarisation ellipse and its orientation with

respect to the x axes is as following:

$$\begin{aligned} a^2 + b^2 &= a_1^2 + a_2^2; \\ \tan(2\psi) &= \tan(2\alpha)\cos\delta; \\ \tan(2\chi) &= \sin(2\alpha)\sin\delta. \end{aligned} \tag{2.39}$$

It is necessary to use three independent parameters to describe a polarisation state out of these variables [35].

2.2.1 Linear and circular polarisation

There are two kinds of polarisation states that are of particular interest here: the linear polarisation and the circular polarisation, namely when the polarisation ellipse reduces to a line or a circle.

The linear polarisation typically happens when the ratio between the x and y components of the electric field remains a constant throughout propagation. If either E_x or E_y is zero, then the polarisation state is referred to as the horizontal polarisation and the vertical polarisation respectively, demonstrated in Fig. 2.4a and 2.4b. When both of these two components are non-zero, according to Eq. 2.35, a linear polarisation indicates:

$$\delta = m\pi; \quad \frac{E_y}{E_x} = (-1)^m \frac{a_2}{a_1}, \tag{2.40}$$

where m is an integer [35]. Typically, when m is an even number, the polarisation state is referred to as the diagonal polarisation as shown in Fig. 2.4c; if m is an odd number, it is an anti-diagonal polarisation shown in Fig. 2.4d.

We can deduce two essential criteria for polarisation ellipses to reduce to a circle:

$$a_1 = a_2 = a; \quad \delta = \pm\frac{\pi}{2} + 2n\pi, \tag{2.41}$$

where n is an integer. Conventionally, the handedness of the polarisation is defined when an observer is looking towards the direction from which the light is coming. Specifically, this indicated the end points of a right-handed polarisation is rotating clockwise, as demonstrated in Fig. 2.4e, indicating $\delta = \frac{\pi}{2} + 2n\pi$. For left-handed polarisation all the characteristics would be the opposite, namely, rotating anti-clockwise and $\delta = -\frac{\pi}{2} + 2n\pi$ [35].

Another way to represent polarisation is using the Jones vectors. If we rewrite E_x and E_y in the complex representation:

$$\begin{aligned} E_x &= \Re(\mathcal{E}_x) = \Re\left(a_1 e^{-i(\tau+\delta_1)}\right); \\ E_x &= \Re\left(\mathcal{E}_y\right) = \Re\left(a_2 e^{-i(\tau+\delta_2)}\right), \end{aligned} \tag{2.42}$$

we can define its polarisation state using the Jones vector:

$$\begin{bmatrix} a_1 e^{-i(\tau+\delta_1)} \\ a_2 e^{-i(\tau+\delta_2)}. \end{bmatrix} \tag{2.43}$$

Based on the previous discussion, we can define the right-handed polarisation by the vector $|R\rangle$; the left-handed polarisation by $|L\rangle$; the horizontal polarisation by $|H\rangle$; the vertical polarisation by

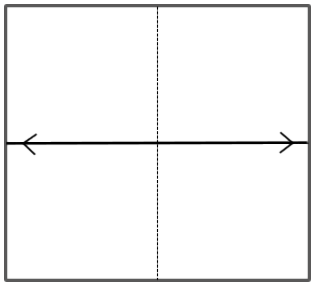

(a) $a_2 = 0$: horizontal polarisation.

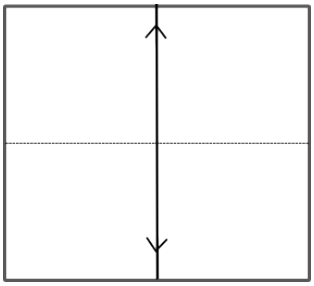

(b) $a_1 = 0$: vertical polarisation.

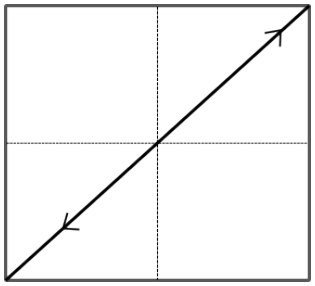

(c) $\delta = 2m\pi$: diagonal polarisation.

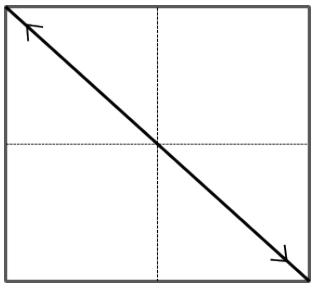

(d) $\delta = \pi + 2m\pi$: anti-diagonal polarisation.

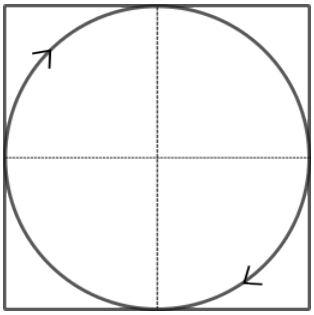

(e) $\delta = \frac{\pi}{2} + 2m\pi$: right-handed polarisation.

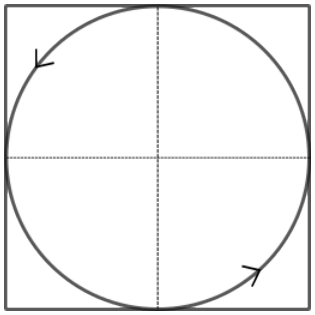

(f) $\delta = -\frac{\pi}{2} + 2m\pi$: left-handed polarisation.

Figure 2.4 Three sets of orthogonal polarization directions

$|V\rangle$; the diagonal polarisation by $|D\rangle$; the anti-diagonal polarisation by $|A\rangle$ as following [53, 54]:

$$|R\rangle = \begin{bmatrix}1\\0\end{bmatrix}; |L\rangle = \begin{bmatrix}0\\1\end{bmatrix}; |H\rangle = \frac{1}{\sqrt{2}}\begin{bmatrix}1\\1\end{bmatrix}; |V\rangle = \frac{-i}{\sqrt{2}}\begin{bmatrix}1\\-1\end{bmatrix}; |D\rangle = \frac{1}{\sqrt{2}}\begin{bmatrix}1\\i\end{bmatrix}; |A\rangle = \frac{-i}{\sqrt{2}}\begin{bmatrix}1\\-i\end{bmatrix}, \tag{2.44}$$

where we have chosen the phase so that:

$$\begin{aligned} |R\rangle &= \frac{1}{\sqrt{2}}\left(|H\rangle + i|V\rangle\right) = \frac{1}{\sqrt{2}}\left(|D\rangle + i|A\rangle\right) \\ |L\rangle &= \frac{1}{\sqrt{2}}\left(|H\rangle - i|V\rangle\right) = \frac{1}{\sqrt{2}}\left(|D\rangle - i|A\rangle\right). \end{aligned} \tag{2.45}$$

2.2.2 Stokes parameters and the Poincaré sphere

G.G Stokes introduced the set of parameters commonly used to unambiguously describe polarisation states nowadays, i.e. the Stokes parameters. There are four of these [35]:

$$\begin{aligned} s_0 &= a_1^2 + a_2^2; \\ s_1 &= a_1^2 - a_2^2; \\ s_2 &= 2a_1a_2\cos\delta; \\ s_3 &= 2a_1a_2\sin\delta, \end{aligned} \tag{2.46}$$

from which we can obtain the relation:

$$s_0^2 = s_1^2 + s_2^2 + s_3^2. \tag{2.47}$$

Therefore, only three out of the four Stokes parameters are independent. Among them, s_0 is related to the intensity of the wave while s_1, s_2 and s_3 are related to the polarisation ellipse [35]:

$$\begin{aligned} s_1 &= s_0 \cos(2\chi)\cos(2\psi); \\ s_2 &= s_0 \cos(2\chi)\sin(2\psi); \\ s_3 &= s_0 \sin(2\chi). \end{aligned} \tag{2.48}$$

This suggests a geometric representation of polarisation involving a unit sphere. By mapping s_1, s_2 and s_3 on to the Cartesian coordinates, and associate angles χ and ψ to the spherical angular coordinates, we can establish a bijective relation between every possible polarisation in paraxial beams of a given intensity and all the points on the unit sphere as shown in Fig. 2.5.

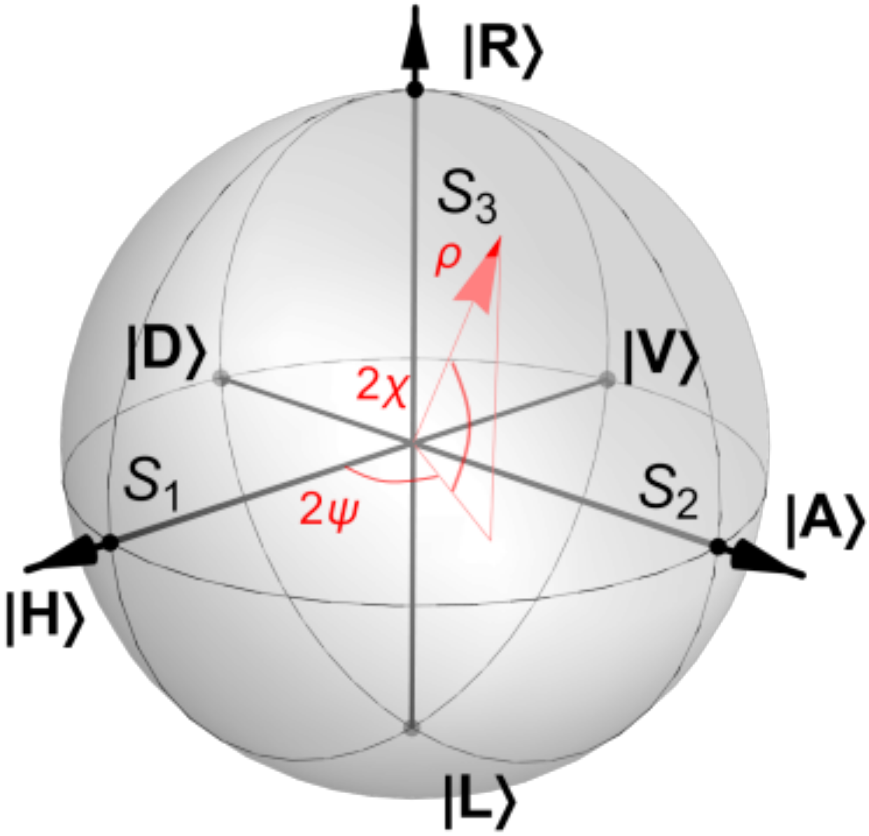

Figure 2.5 The Poincaré sphere.

As stated in Eq. 2.39, angle χ is related to δ. Therefore, on the Poincaré sphere, the north pole represents the right-handed polarisation while the south pole corresponds to the left-handed polarisation. In the same way, based on Eq. 2.38 and 2.39, the horizontal, vertical, diagonal and anti-diagonal polarisation states are placed on the equator, corresponding to the crossover points of s_1 and s_2 axes on the sphere respectively. Other points on the equator correspond to all the

possible linear polarisations and the rest of the points on the sphere represent all the possible elliptic polarisations.

Stokes parameters can also be calculated from Pauli matrices using Jones's vectors [40]. Pauli matrices were a set of 2×2 unitary matrices defined by Wolfgang Pauli:

$$\sigma_1 = \begin{bmatrix} 0 & 1 \\ 1 & 0 \end{bmatrix}; \sigma_2 = \begin{bmatrix} 0 & -i \\ i & 0 \end{bmatrix}; \sigma_3 = \begin{bmatrix} 1 & 0 \\ 0 & -1 \end{bmatrix}. \tag{2.49}$$

It is clear that $|H\rangle$ and $|V\rangle$ are eigenvectors of σ_1 with eigenvalue of 1 and -1 respectively; $|A\rangle$ and $|D\rangle$ are eigenvectors of σ_2; $|R\rangle$ and $|L\rangle$ are eigenvectors of σ_3. Namely:

$$\begin{aligned} \sigma_1|H\rangle &= |H\rangle; \qquad \sigma_1|V\rangle = -|V\rangle; \\ \sigma_2|A\rangle &= |A\rangle; \qquad \sigma_2|D\rangle = -|D\rangle; \\ \sigma_3|R\rangle &= |R\rangle; \qquad \sigma_3|L\rangle = -|L\rangle. \end{aligned} \tag{2.50}$$

Therefore, if we use $|P\rangle$ to represent an arbitrary polarisation state, Stokes parameters can be calculated from Pauli matrices by:

$$s_i = \langle P|\sigma_i|P\rangle, \tag{2.51}$$

where $i = 1, 2, 3$.

2.2.3 Non-paraxial beams

For non-paraxial beams, the z component of the electric field is no longer small comparing with E_x and E_y anymore. However, in general the end point of the electric field still describes an ellipse. The difference between the polarisation in paraxial beams and non-paraxial beams is that the planes where the ellipse lies in now varies from point to point [35, 45].

We use a general vector $\mathbf{V}(\rho, t)$ to represent the electric field:

$$\begin{aligned} V_x(\rho, t) &= a_1(\rho)\cos(\omega t - g_1(\rho)); \\ V_y(\rho, t) &= a_2(\rho)\cos(\omega t - g_2(\rho)); \\ V_z(\rho, t) &= a_3(\rho)\cos(\omega t - g_3(\rho)), \end{aligned} \tag{2.52}$$

where a_i and g_i are all real functions. Using trigonometric addition formulas this expression can be rewritten into:

$$V_i(\rho, t) = \mathbf{p}_i(\rho)\cos(\omega t) + \mathbf{q}_i(\rho)\sin(\omega t), \tag{2.53}$$

where using i in place of x, y and z and

$$\begin{aligned} \mathbf{p}_i(\rho) &= a_i(\rho)\cos(g_i(\rho)); \\ \mathbf{q}_i(\rho) &= a_i(\rho)\sin(g_i(\rho)). \end{aligned} \tag{2.54}$$

By constructing two new vectors: $\mathbf{p} = (p_x, p_y, p_z)$ and $\mathbf{q} = (q_x, q_y, q_z)$, we can express $\mathbf{V}(\rho)$ in the following complex representation:

$$\mathbf{V}(\rho, t) = \Re(\mathbf{U}(\rho)e^{i\omega t}), \tag{2.55}$$

where $\mathbf{U}(\rho) = \mathbf{p}(\rho) + i\mathbf{q}(\rho)$.

We can choose a parameter ϵ such that a new set of vectors: $\mathbf{a}_{non}$ and $\mathbf{b}_{non}$ are perpendicular to each other,

$$\mathbf{p}(\rho) + i\mathbf{q}(\rho) = (\mathbf{a}_{non}(\rho) + i\mathbf{b}_{non}(\rho))e^{i\epsilon}. \tag{2.56}$$

In other words:

$$(\mathbf{p}\cos\epsilon + \mathbf{q}\sin\epsilon)\cdot(-\mathbf{p}\sin\epsilon + \mathbf{q}\cos\epsilon) = 0, \tag{2.57}$$

which indicates:

$$\tan(2\epsilon) = \frac{2\mathbf{p}\cdot\mathbf{q}}{|\mathbf{p}|^2 - |\mathbf{q}|^2}. \tag{2.58}$$

In this way, we can rewrite the electric field $\mathbf{V}$ as:

$$\mathbf{V}(\rho, t) = \Re\Big(\mathbf{a}_{non}(\rho) + i\mathbf{b}_{non}(\rho))e^{-i(\omega t - \epsilon)}\Big). \tag{2.59}$$

At a given point r_0, we can choose a set of coordinate such that its x and y axes align with $\mathbf{a}_{non}$ and $\mathbf{b}_{non}$.

Therefore, the end points of the electric field describe an ellipse in a plane defined by $\mathbf{p}(\mathbf{r_0})$ and $\mathbf{q}(\mathbf{r_0})$ the same way as in the paraxial beams. The difference is this plane varies at different points in space for non-paraxial beams. Because this thesis mainly focuses on the paraxial skyrmionic beams, we will not be discussing generalised Stokes parameters for non-paraxial beams here.

2.3 Vector beam

The solutions we derived in Sec.2.1.1 are to the scalar Helmholtz equation, which corresponds to paraxial beams with spatially homogeneous polarisation. However, in structured light, we are interested in spatially varying polarisations [55, 56]. Therefore, instead of choosing a constant polarisation $\mathbf{t}$ with respect to ρ for the electric field as we did in Eq. 2.18, the polarisation should be dependent on the position as well. Typically, this can be done by expressing a vector beam by superposing multiple modes with different spatially homogeneous polarisations:

$$\mathbf{E}(\mathbf{r}, t) = \sum \mathbf{g}_i \Psi_i(\mathbf{r}) e^{-i\omega_i t}. \tag{2.60}$$

This is because any linear combinations of solutions to scalar Helmholtz equation should satisfy the vector Helmholtz equation Eq. 2.17.

We here provide two examples to produce vector beams by superposing scalar Laguerre-Gaussian beams. The first example is to construct a radially polarized beam which is shown in Fig 2.6a:

$$\mathbf{u}_r = u_{r0}(\rho, z)e^{ikz}\,\hat{\rho}, \tag{2.61}$$

where $\hat{\rho}$ can be expressed as:

$$\hat{\rho} = \cos(\phi)\hat{x} + \sin(\phi)\hat{y}. \tag{2.62}$$

We start with a Laguerre-Gaussian beam with mode $p = 0$ and $\ell = 1$ that has a uniform left-handed polarisation. Then it is superposed with another Laguerre-Gaussian beam with mode

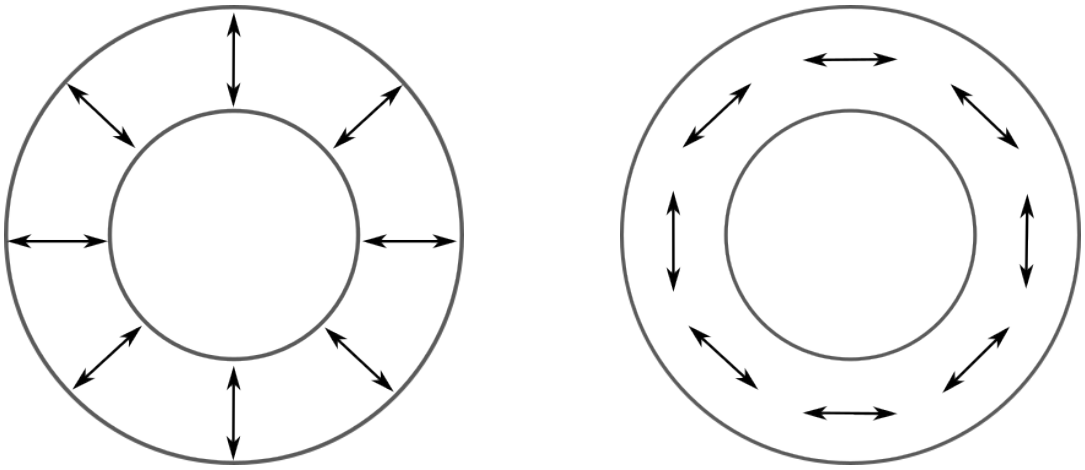

(a) Example beam with radial polarisation.

(b) Example beam with azimuthal polarisation.

Figure 2.6 Examples of beams with spatially varying polarisations: vector beams.

$p = 0$ and $\ell = -1$ that has a uniform right-handed polarisation:

$$\mathbf{u}_{spp1} = u_0^1|L\rangle + u_0^{-1}|R\rangle. \tag{2.63}$$

According to the realtionship we introduced in Jones vector notation in Eq. 2.45, if we represent the horizontal polarisation as in the x direction and the vertical polarisation in the y direction this can be further simplified into:

$$\mathbf{u}_{spp1} = \frac{U_0^1}{\sqrt{2}}\left(e^{i\phi}\,(\hat{x} - i\hat{y}) + e^{-i\phi}\,(\hat{x} + i\hat{y})\right), \tag{2.64}$$

where U_0^1 represent the non ϕ related part of the beam. Expanding the terms in the bracket we obtain:

$$\begin{aligned}\mathbf{u}_{spp1} &= \frac{U_0^1}{\sqrt{2}}\Big(\big(\cos(\phi) + i\sin(\phi)\big)(\hat{x} - i\hat{y}) + \big(\cos(\phi) - i\sin(\phi)\big)(\hat{x} + i\hat{y})\Big) \\ &= \sqrt{2}U_0^1\big(\cos(\phi)\hat{x} + \sin(\phi)\hat{y}\big) \\ &= \sqrt{2}U_0^1\,\hat{\rho}.\end{aligned} \tag{2.65}$$

Comparing with Eq. 2.61, we showed that by superposing two scalar beam it is possible to produce a vector beam with radial polarisation.

Another example is to construct an azimuthally polarised beam with scalar beams as shown in Fig 2.6b. The general form of this type of beam is:

$$\mathbf{u}_a = u_{a0}(\rho, z)e^{ikz}\,\hat{\phi} \tag{2.66}$$

where $\hat{\phi}$ can be rewritten as:

$$\hat{\phi} = -\sin(\phi)\hat{x} + \cos(\phi)\hat{y}. \tag{2.67}$$

Consider the same two Laguerre-Gaussian modes as we did for radially polarized beam but with

an addition global phase of $-\pi/2$:

$$\mathbf{u}_{spp2} = e^{-\frac{i\pi}{2}}\left(-u_0^1|L\rangle + u_0^{-1}|R\rangle\right). \tag{2.68}$$

Similarly to the previous superposed beam, this can be simplified into:

$$\begin{aligned}
\mathbf{u}_{spp2} &= \frac{U_0^1}{\sqrt{2}}e^{-\frac{i\pi}{2}}\left(-e^{i\phi}\,(\hat{x}-i\hat{y}) + e^{-i\phi}\,(\hat{x}+i\hat{y})\right)\\
&= -i\frac{U_0^1}{\sqrt{2}}\Big(-\Big(\cos(\phi)+i\sin(\phi)\Big)(\hat{x}-i\hat{y}) + \Big(\cos(\phi)-i\sin(\phi)\Big)(\hat{x}+i\hat{y})\Big)\\
&= -i\sqrt{2}U_0^1\Big(-i\sin(\phi)\hat{x} + i\cos(\phi)\hat{y}\Big)\\
&= \sqrt{2}U_0^1\Big(-\sin(\phi)\hat{x} + \cos(\phi)\hat{y}\Big)\\
&= \sqrt{2}U_0^1\,\hat{\phi}.
\end{aligned} \tag{2.69}$$

Therefore, this shows that by superposing two orthogonally polarised beams we can obtain a vector beam with azimuthal polarisation. By demonstrating those two examples, we showed that spatially varying polarised beams can be constructed by superposing spatially homogeneous polarized beams with different spatial mode.

In this chapter we have reviewed the Maxwell equations and showed how paraxial wave solutions are obtained from them. We also introduced polarisation and showed how to construct cylindrical vector beams using scalar beams. This is the foundation of construction of skyrmionic beams. In the next chapter, we are going to introduce skyrmions and the related topological concepts.

Chapter 3

Skyrmions

Point set topology is a disease from which the human race will soon recover.
—Henri Poincaré, Quoted in D MacHale, Comic Sections (Dublin 1993)

3.1 Introduction

Skyrmions were originally proposed by Tony Skyrme in the 1960s as topological solitons in a nonlinear field theory [57, 58]. Although not being accepted in the mainstream particle theory, it was adopted by the condensed matter community for spin structures in magnetic materials. This idea was later named magnetic skyrmions, which are topologically protected quasiparticles. Not only have magnetic skyrmions been experimentally realised [59, 60, 61], their creation and annihilation has also been demonstrated [62]. Therefore, one of the various applications proposed for magnetic skyrmions is the next generation of information storage devices [63]. Features that are analogous to skyrmions appear, also, in the theory of superfluids, especially in the A phase of liquid ^{3}He [64, 65, 66].

We propose, here, a brief introduction to skyrmions as they appear in other branches of physics. This shall act as a prelude to our own work on skyrmions in paraxial optics. Some of the ideas introduced here, notably in the theory of superfluids, find ready application of paraxial optical skyrmions.

In this chapter, we will start with solitons in Section. 3.2. Before we introduce the original Skyrme's theory in Section. 3.4, we will first review the idea of topological solitons in Section. 3.3. Then, closely related to skyrmions, the concepts of magnetic skyrmions and superfluids are introduced in Section. 3.5 and Section. 3.6, respectively. Lastly, in Section. 3.7, we will briefly review the emerging field of optical skyrmions before detailing the plan for the remainder of the thesis.

3.2 Solitons

As stated above, skyrmions were introduced as topological solitons and therefore we start with a brief introduction to solitons and topological solitons. In 1834, John Scott Russell noticed something unexpected in the Union Canal in Scotland, for what he named as the "Wave of Translation". In his own words, he described the event as:

> I was observing the motion of a boat which was rapidly drawn along a narrow channel by a pair of horses, when the boat suddenly stopped – not so the mass of water in the channel which it had put in motion; it accumulated round the prow of the vessel in a state of violent agitation, then suddenly leaving it behind, rolled forward with great velocity, assuming the form of a large solitary elevation, a rounded, smooth and well-defined heap of water, which continued its course along the channel apparently without change of form or diminution of speed. I followed it on horseback, and overtook it still rolling on at a rate of some eight or nine miles an hour, preserving its original figure some thirty feet long and a foot to a foot and a half in height. Its height gradually diminished, and after a chase of one or two miles I lost it in the windings of the channel. Such, in the month of August 1834, was my first chance interview with that singular and beautiful phenomenon which I have called the Wave of Translation. [67]

This is the first written observation of a soliton, a single wave packet that maintains its shape and form while propagates. Solitons include the undular tidal bores where the wavefront is followed by a train of well-defined free-surface undulations known as whelps, that formed a standing wave pattern relative to the wavefront [68]. Another example is the undersea internal waves due to seabed topography that propagate on the oceanic pycnocline, i.e. the layer with the largest density gradient. Aother more mundane example would be the wave at the interface of oil and vinegar when a bottle of salad dressing is shaken. It has also been suggested but not widely accepted that neural signals conduction can be explained as pressure solitons [69].

In optics, solitons are referred to any optical field that remains unchanged during propagation. This is a result of the balance between the linear and non-linear effect [70]. For example, optical solitons can be created by dispersion and the non-linear Kerr effect. When a light pulse with non-zero bandwidth travels through a medium whose refractive index is dependent on the frequency, the pulse widens during propagation. However, the non-linear Kerr effect, a change in the refractive index of a material in response to an applied electric field, will squeeze the wave packet. Therefore, they counteract each other in the change of frequencies, resulting in a temporal optical soliton. This has been known since the 1970s and have been thus suggested and applied in telecommunication [71].

3.3 Topological solitons

Topological solitons are a more recent concept that has only been examined by theoretical physicists and mathematicians in the recent half a century. In this context, a topological soliton is a solution of a system of partial differential equations that are homotopically different from the vacuum solutions [72]. A topological space is the most general type of a mathematical space that allows for the definition of limits, continuity, and connectedness [73] and ”homotopy” refers to the relation between two functions from one topological space that can be ‘continuously deformed’. i.e. manipulation without tearing, into the other [74].

In the 1960s and 1970s topological solitons were introduced as a novel approach to interpret some of the solutions of fully non-linear classical field equations. They are different from the

elementary particle that arises from quantization of the wave-like excitation of the fields. These quantum excitations are smooth deformations of the field and do not change its topology. Therefore, typically elementary particles do not possess any topological feature. On the other hand, the stability of topological solitons emerges from their topological features: when two adjoining structures are ”out of phase” with each other making it impossible to transition seamlessly between each other [72]. In other words, this lack of homotopical mapping of the topological soliton onto vacuum solutions makes them not only stable against perturbation, but also stable against spontaneously decaying into topologically trivial states.

To get an intuition about topological solitions let us look at the twisted coiled telephone cords. They are usually coiled clockwise yet some parts of it would end up coiling counterclockwise after years of usage. The transition loop joining the two directions of coiling would be a larger loop which is neither clockwise nor counterclockwise. This is an example of a topological soliton demonstrating the same separation between two spaces as exhibited in more complex examples.

An integer N is normally used to characterise the topological feature of a field. This value is referred to as the topological charge or the general winding number of the field. One can also identify an anti-soliton with a topological charge of $(-N)$ as a result of a reflection transformation acting on the soliton of charge N. Solitons with $N > 1$ are called multi-soliton states which are sometimes energetically favourable to decay into N ground soliton states of topological charge 1 or a classical bound state of N solitons [72].

3.4 Skyrmions

The Skyrmion is the first example of a topological soliton particle model [72]. The Skyrmion model was first introduced by Tony Skyrme in 1962 within a field theoretical framework, to understand spin $1/2$ nucleons and the three pions (consisting of a quark and an antiquark). Skyrme believed that the nucleus is moving in a nonlinear, classical pion medium, resulting in a special form of Lagrangian with a soliton solution which could be used to explain the stability of hadrons. He proposed that if hadrons are described as topological defects of a quantum vector field, they could be characterized by a topological integer (later known as the skyrmion number, n) which would not change through any deformation of the field [75]. In his theory, each singularity in the field contributes one unit to the baryon number [57].

Although this idea is not part of the mainstream particle theory, it has been expanded as topologically-protected excitation where the field takes values corresponding to a sphere [76] and has since found wide application in many areas of physics including magnetic materials [77, 78, 79], 2D photonic materials [80] and in the study of fractional statistics [81]. Skyrmions also have been applied in superfluid research [82, 83], a liquid-like state in which matter flows with zero viscosity [64, 84, 65]. Optical skyrmions have been observed in optics by the controlled interference of plasmon polaritons [10, 11]. Recently, it has been experimentally demonstrated that optical skyrmions also exists in free propagating beams [85, 86].

The most important distinction of Skyrme’s theory from others is that, angular variables are used to represent the fundamental field quantities instead of linear variables. The quantum vector field in Skyrme’s theory is a vector in a four-dimensional iso-space (a form of spacetime that

rotates around some certain axis). The components of this vector ϕ_i are real fields and constrained by

$$\sum_{i=1}^{4} \phi_i^2 = 1. \tag{3.1}$$

These four fields can also be described as a spinor K, from which the angular variables Θ_i can be defined by specifying a rotation $\hat{U}$ to obtain K from a standard spinor $(0, 1)$ [72]:

$$K = \hat{U}(0, 1) = e^{\frac{i}{2}\sigma_i \Theta_i}(0, 1), \tag{3.2}$$

where σ_i are Pauli matrices and note that we are using Einstein repeated index summation throughout this thesis.

The rotation operators in the four-dimensional space form two independent three-dimensional rotation groups: one is identified with isospin; the other is associated with hypercharge or the quantum number known as 'strangeness' [87].

In his earlier work, Skyrme introduced a simpler model with one dimension and one angular variable [87]. In this model, the number of sources, in other words the particle number, is proportional to the total change in the angle variable θ across the one dimension x as:

$$\theta(\infty) - \theta(-\infty) = \int_{-\infty}^{\infty} \partial_x \theta \, dx \tag{3.3}$$

By extending this model to four dimensional space, Skyrme introduced the concept of the skyrmion current which is independent of the particular angular representation. Using the Levi-Civita symbol and the Einstein summation convention, the skyrmion current is defined as:

$$N_\lambda = \frac{i}{12\pi^2} \epsilon_{\alpha\beta\gamma\delta} \epsilon_{\lambda\mu\nu\rho} \phi_\alpha \left(\partial_\mu \phi_\beta\right)\left(\partial_\nu \phi_\gamma\right)\left(\partial_\rho \phi_\delta\right), \tag{3.4}$$

from which we can extract the conservation law:

$$\partial_\lambda N_\lambda = 0. \tag{3.5}$$

The above conservation law is a consequence of Eq. 3.1 which imposes the amplitude summation constraint on ϕ_i.

3.5 Magnetic skyrmions

Based on the original 3 spatial +1 temporal dimensional skyrmion model, the (2 + 1) dimensional solution, i.e. the Baby Skyrmion model, is of more interest to the condensed matter community. This is present in quantum Hall ferrogmagnets, [60] namely magnetic skyrmions. This is because the energy expression of the Baby Skyrmion model is very similar to that of the quantum Hall ferromagnets. Magnetic skyrmions can also be understood as quasi particles. They are topologically non-trivial, point-like regions of magnetisation, localised in a two-dimensional space, which have been predicted [88][89][90] and experimentally observed [91][92][93]. They typically exist as planar analogues of skymrions. Magnetic skyrmions can also be extended into three-dimensional

space as skyrmion strings [94, 95].

Within an isolated skyrmion, the spin $\mathbf{m}$ rotates smoothly in a three-dimensional space with a fixed norm: $|\mathbf{m}| = 1$. Therefore, its order parameter space can be envisioned as a unit sphere, S^2. This unit sphere can be stereographically projected onto the physical space $\mathcal{R}^2$ with a missing point, i.e. $\rho \to \infty$. This is shown in Fig. 3.1a and 3.1b using an example of the Neel skyrmion, which we will introduce in detail in the following paragraph. The skyrmion number for magnetic skyrmions is defined as the number of spin configurations wrapping the unit sphere and can be obtained by the total flux of magnetisation $\mathbf{m}$ on a surface [96]:

$$n = \frac{1}{4\pi} \int_S \mathbf{m} \cdot \left(\frac{\partial \mathbf{m}}{\partial x} \times \frac{\partial \mathbf{m}}{\partial y} \right) dxdy, \tag{3.6}$$

where S is the area of the magnetic skyrmion.

One main mechanism contributing to the stability of magnetic skyrmion structure is the competition between the Dzyaloshinskii-Mpriya and ferromagnetic exchange interactions [97, 98, 99]. The former interaction induces an alignment perpendicular to the spin alignment and the latter favours a colinear alignment. Therefore, the magnetisation vectors which are oriented in the opposite of the external field cannot 'flip around' to align themselves with the rest of the atoms in the film, without overcoming an energy barrier. As we have previously discussed, the integer topological charge of a soliton implies that the soliton is robust against small deformations and cannot be continuously deformed into a topologically trivial state. Therefore, for magnetic skyrmions with non-zero skyrmion number, i.e. $n \neq 0$, they cannot spontaneously deform into $n = 0$ states.

For magnetic skyrmions, we can use the polar coordinates $(\rho\cos(\varphi), \rho\sin(\varphi))$ to describe the physical position of a spin with ρ as the distance from the centre of the magnetic skyrmion. Because of the stereographic mapping between the unit sphere and the magnetic spin discussed before, the orientation of the spin $\mathbf{m}$ can be expressed using two angular variables θ and ϕ. As the azimuthal angle, θ is only dependent on ρ whereas ϕ is a function of φ:

$$\phi = n\varphi + \varphi_0, \tag{3.7}$$

in which n is the vorticity in some literature, corresponding the number of wrapping on the unit sphere and φ_0 is referred to as the helicity. Magnetic skyrmions are the configurations with $n > 0$ as shown in Fig. 3.1a 3.1c, whereas the solutions with $n < 0$ are referred to as anti-skrymions as depicted in Fig. 3.1d [100]. One way to understand this is that, at a fixed distance from the centre, the spin would wind n times along the travelling direction. In an anti-skyrmion, it means that the spin direction rotates exactly the opposite of the travelling direction along a physical circular contour. For skyrmions with $n = 1$, there are two distinctive types of skyrmions: the hedgehog or Neel skyrmion (see Fig. 3.1a) with helicity $\varphi_0 = 0$ or π; and the chiral or Bloch skyrmion in Fig. 3.1c with helicity $\varphi_0 = \pi/2$ or $\pi/3$. The magnetisation $\mathbf{m}$ in Neel skyrmions points along the radial direction, ρ whereas that in Bloch skyrmions exhibits a phase difference between it and the radial direction [101].

Magnetic skyrmions have attracted increasing research interest due to their potential applications in various fields, especially in data storage. The fact that magnetic skyrmions can be moved with spin torques associated with spin polarized currents, makes them a compelling candidate

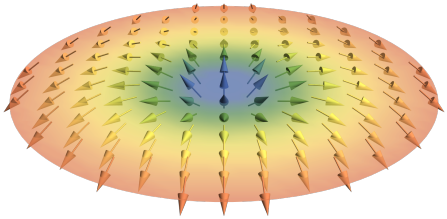

(a) A 'Neel' or hedgehog magnetic skyrmion with skyrmion number $n = 1$. Its magnetisation is along the radial direction.

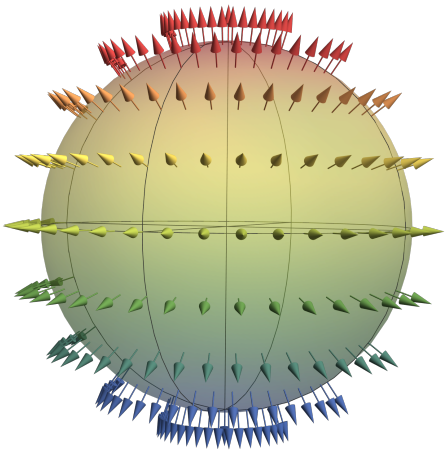

(b) A 'Neel' or hedgehog skyrmion with skyrmion number $n = 1$. Its magnetisation is along the radial direction.

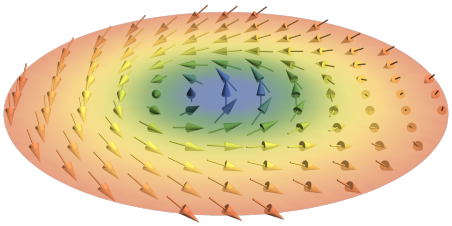

(c) A Bloch or chiral skyrmion with skyrmion number $n = 1$.Its magnetisation differes from the radial direction by a phase.

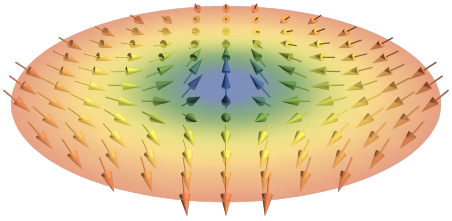

(d) An anti-skyrmion with skyrmion number $n = -1$. Its magnetisation has a saddle structure.

Figure 3.1 This is an illustration of different kinds of magnetic skyrmions. The colour coding here corresponding to the z componenet of the magnetisation with red indicates that $m_z = 1$ and blue refers to $m_z = -1$. a) c) and d) are magnetic skyrmions, corresponding to Neel type, Bloch type and antiskyrmin respectivly. b) is a 3-dimensional skyrmion and a) is its stereographic projection.

for potential spintronics applications in data storage and logic devices[102, 103, 93]. It has been proposed that magnetic skyrmion can be localised down to nanometer scale [90, 104]. Furthermore, they exhibit a particle-like behaviour including the possibility of annihilating skyrmion-antiskyrmion pairs which can be explored as memory erasing mechanism. All of these properties lead to the new concept of logical devices [105, 106] with magnetic skyrmions as movable information bits in future spintronics devices.

3.6 Superfluid vorticity

A many-particle system is categorized as a quantum liquid if it experiences both quantum mechanical effects and quantum statistical effects. The former criteria requires the de Broglie wavelength of particles in the system to be of the order of interparticle distance and the latter requires that the particles able to change positions easily. Therefore, there are mainly two types of quantum liquids: 1) Electrons in any solid or liquid metal and; 2) Any collection of atoms or molecules that experiences quantum mechanical effects and is in both liquid and gaseous states simultaneously. This thesis mainly involves the second kind, which consists of the liquid isotopes of Helium [65].

Two of the simplest form of quantum liquids are ^{3}He and ^{4}He, two stable isotopes of helium. They have the lowest boiling points of all known substances, 3.19K for ^{3}He and 4.21K for ^{4}He. The mechanism for those two isotopes remaining liquid comprises of two factors: a) the low mass of the atoms; and b) the extremely weak forces between atoms due to its closed shell of two electrons and absence of dipole moments [66]. Under normal low-temperature conditions and in the absence of irradiation, the helium atom is assumed to be in its ground state. Therefore, the internal degree of freedom of ^{3}He and ^{4}He solely depend on their nuclear spin. Nuclear spin depends on the total number of fermions (nucleons plus electrons) in an atom. Therefore, ^{4}He and ^{3}He follow Boson-Einstein statistics and Fermi-Dirac statistics respectively [65].

Both ^{3}He and ^{4}He would exhibit superfluid properties below a certain temperature. A superfluid is a state of matter that behaves like a fluid with zero viscosity. This property allows superfluids to continue circulating over obstructions and through pores in their containers [64]. Superfluidity and superconductivity are essentially the same property - with the former occurring in an electrically neutral system and the latter in a charged system. This phenomenon is the result of BEC (Bose-Einstein condensate) in a Bose system and of Cooper pairing in a Fermi system. The former applies to ^{4}He while the latter applies to ^{3}He and electrons. [65].

^{3}He can undergo a phase transition (BCS theory) to a state analogous to Boson-Einstein condensate through atom pairing (Cooper pairing). There are two theoretical models proposed with respect to the spin function. In the AM model put forward by Anderson and Morel [107] in 1961, the spin wave function is $|00\rangle + |11\rangle$, which corresponds to the first order transition B phase observed experimentally. The other theoretical model is known as the BW model which is proposed by Balian and Werthamer [108] in 1962 which has the spin function of $|01\rangle + |10\rangle$, and corresponds to the second order transition A phase. Balian and Werthamer also managed to prove that BW state would have a lower energy than the AM model [66].

A quantised value named circulation $\kappa = n\kappa_0$ is an important quantity in superfluid. This quantity is measured through the line integral of the superfluid velocity along any contour wholly within the liquid:

$$\kappa = \oint v_s \cdot dl. \tag{3.8}$$

If we use a wavefunction $|\psi|e^{i\phi}$ to describe a superfluid, the superfluid velocity is directly related to the gradient of the phase ϕ. Namely, in ^{4}He it is:

$$\mathbf{v}_s = \frac{\hbar}{m_4}\nabla\phi, \tag{3.9}$$

where m_4 is the mass of a ^{4}He atom. This leads to the Landau irrotational condition:

$$\nabla \times \mathbf{v}_s = 0. \tag{3.10}$$

However, in order for the circulation κ to be non-zero as in:

$$\kappa = \int_A \nabla\phi \cdot d\mathbf{A} = n\kappa_0 \tag{3.11}$$

there must exist either a solid obstacle or a vortex core within the contour.

The topology of quantised vortex lines in ^{3}He is fundamentally different from those in ^{4}He due to the breaking of symmetry that occurs in ^{3}He while in the superfluid state at low temperatures. One main difference is in the superfluid velocity v_s for the A phase [109]. As a Fermi system ^{3}He is described by a set of order parameters, including an orthogonal triad $\hat{\mathbf{l}}$, $\hat{\mathbf{m}}_s$ and $\hat{\mathbf{n}}_\mathbf{s}$ following the constraint of $\hat{\mathbf{m}}_s \times \hat{\mathbf{n}}_\mathbf{s} = \hat{\mathbf{l}}$ for the orbital degrees of freedom [64]. In the A phase, there exists a combined gauge-orbital symmetry which means that a rotation in the orbital space by any angle about the axis $\hat{\mathbf{l}}$ does not change the order parameter. This directly results in breaking the curl-lessness of ϕ in Eq. 3.10. Rather, the superfluid velocity becomes:

$$\mathbf{v}_s = \frac{h}{2m_3}\left(\nabla\phi + m_{si}\nabla n_{si}\right), \tag{3.12}$$

where Einstein summation notation is used and $2m_3$ is the mass of a pair of ^{3}He in Cooper pairing. The vorticity of the superfluid would follow the Mermin-Ho relation [110]. The vortices in ^{3}He can be either singular or continuous. The latter is particularly interesting in the context of this thesis. It indicates the ^{3}He retains A phase everywhere and is categorised by a winding number ν_n [111]:

$$\nu_n = \frac{1}{4\pi}\int_S \mathbf{l}\cdot\left(\frac{\partial\mathbf{l}}{\partial x}\times\frac{\partial\mathbf{l}}{\partial y}\right)dxdy, \tag{3.13}$$

which is identical to the skyrmion number introduced in Eq. 3.6. It is interesting that although this relation seems obvious and there have been studies about skyrmions in superfluids [112, 82], there has been a lack of literature pointing to the skyrmionic structure of the inherent vorticity of ^{3}He.

Another interesting property of the continuous vortex line in ^{3}He is that it can terminate at a singular vortex, which forms a monopole-like object. Because they all exist in the same bulk of superfluid, this means that it is impossible to separate the singular vortex from its tail. This vortex line is therefore the string that couples the two monopoles [111]. The superfluid velocity field around this object is therefore analogous to the gauge-field distribution around the Dirac magnetic monopole and the continuous vortex line is analogous to the Dirac string linking the monopoles [113].

3.7 Optical skyrmion

Optical skyrmionic fields were first demonstrated in the evanescent field of a plasmonic surface [10] and subsequently in the local spin field of focused vector beams [11]. However, skyrmionic paraxial beams still remained an untouched area until we started to investigate them. In previous studies, it has been shown that because of their topological nature, optical skyrmions could be

applied in ultrafast nanometric metrology [12], deep-subwavelength microscopy [11], and topological Hall devices [13].

However, the study of an optical skyrmionic structure in free propagating beams remains an unexplored area and we wish to understand more about the intrinsic topological structure of vector beams in this thesis. Recently, after the publication of our first paper on optical skyrmions in paraxial beams there has been experimentally demonstrated that optical skyrmions also exists in free propagating beams [85, 86].

In this thesis, we will introduce the concept of optical skyrmions in structured beams, their associated properties and potential application within experiment. The thesis is organised as follows: In chapter 4, we will introduce the general form of skyrmion beams, their spin structure and associated skyrmion numbers. We will also present two example beams, one with a constant integer skyrmion number and the other with a varying skyrmion number during propagation. In chapter 5, we will introduce the concept of the skyrmion field and prove that it is a conserved field. In this chapter, the same two examples as in chapter 4 are presented with their skyrmion field. We will prove that, for these specific examples, the skyrmion field is conserved from a both analytic and visual point of view. In chapter 6, motivated by three drivers: a pure mathematical interest; an analogy from superfluid and an alternative way to measure skyrmion number experimently, we will introduce another vector field in skyrmionic beams - the skyrmion vector potential field. We will define its mathematical structure and demonstrate its property through the same two examples as in the previous chapters. In chapter 7, we will introduce a new concept of fractional skyrmions. This special type of skyrmionic beas shares certain similarities with skyrmionic beams but lack topological stability. In this chapter, we will also discuss the relationship between skyrmionic beams and Poincaré beams. In chapter 8, we will discuss how skyrmionic beams can be measured in experiments and their potential practical application in the future. A graphical way to follow the structure of chapter 4-7 is shown in Fig. 3.2.

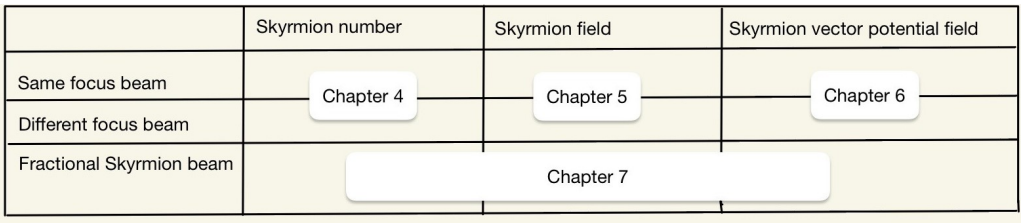

Figure 3.2 A table illustrating the structure of this thesis' chapters 4-7.

Chapter 4

Skyrmionic beams

4.1 Skyrmion number in general

In this chapter, we will introduce structured beams with skyrmionic structures, which are referred to as skyrmioc beam. As introduced in the previous chapter in Section. 3.5, the magnetic skyrmion can be considered as a planner analogue of a three-dimensional skyrmion. Therefore, for optical and electron beams it is natural to return to the 3D skyrmion model and link it with the two spheres familiar to us: the Poincaré sphere and the Bloch sphere. This becomes less obvious concerning non paraxial beams. According to [45, 114], a polarisation ellipse can be defined at any point in non-paraxial beams. However, because the direction of the plane in which the polarisation eclipse lies in varies from point to point, no consensus has yet reached concerning their corresponding generalised Stokes parameters or corresponding geometric representations [115]. The material in this chapter are included in [1] by the author.

In general, the equivalent magnetisation $\mathbf{M}$ in optical skyrmions analogous to the spin $\mathbf{m}$ in magnetic skyrmions should be chosen as a vector field comprising of three orthonormal vectors. In this way, we can define the effective magnetisation as local direction in the Poincaré sphere associated with it for paraxial optical beams or spin in for electron beams. For non-paraxial beams it should still be possible to define a equivalent magnetisation $\mathbf{M}$. For example, [116] has utilised the electric spin angular momentum density as $\mathbf{M}$ despite that it is not a unit vector and [10] used the electric field $\mathbf{E}$. This, however, is not be the focus of this paper.

$\mathbf{M}$ is not dependent on the intensity of the beam of interest, which is a feature different from other well-studied properties such as the electromagnetic field, spin angular momentum, orbital angular momentum, linear momentum and energy.

4.2 Constructing paraxial skyrmionic beams

Although this idea can be applied to both classical and quantum beams, it is convenient if we introduce the definition here using a convenient representation of the Jones vector as a wave vector $|\Psi(\mathbf{r})\rangle$. This then represents the polarisation of the light or direction of the electron spin at the point $\mathbf{r}$. Taking $\mathbf{S}$ as the crossection across the beam in the direction of the propagation, we introduce

the exact form of **M**:

$$\mathbf{M} = \frac{\langle \Psi(\mathbf{r}) | \boldsymbol{\sigma} | \Psi(\mathbf{r}) \rangle}{\langle \Psi(\mathbf{r}) | \Psi(\mathbf{r}) \rangle}, \tag{4.1}$$

where $\boldsymbol{\sigma}$ is the vector form of the Pauli matrices. In this definition, for electron beams, **M** would be the Bloch vector. As for paraxial optical beams, **M** would be the normalised Stokes parameter:

$$\mathbf{M} = \left[S_1, S_2, S_3 \right]^T. \tag{4.2}$$

In order to realise the skyrmion structure as introduced above, we first propose a family of beams constructed by a coaxial superposition of two varying spatial components with orthogonal polarisations. The electron skyrmionic beams would possess similar structure except carrying orthogonal spin instead of polarisations. For optical beams, polarisation is represented by the Stokes parameters and we shall start with with the circular polarisation. We adopt the convention that $|0\rangle$ and $|1\rangle$ represent the left-handed polarisation and the right-handed polarisation with eigenvalues of -1 and 1 for the S_3 component in the Stokes parameter respectively. Similarly, for electron beams, we choose the z component of the spin, i.e. S_z, to start with, for which the states $|0\rangle$ and $|1\rangle$ correspond to the spin up and spin down states respectively. We will later prove that this choice of direction will not affect the result. In this way, the spatially varying polarisation of our beam of interest can be written in the following form:

$$|\psi(\mathbf{r})\rangle = \frac{u_0(\mathbf{r})|0\rangle + u_1(\mathbf{r})|1\rangle}{\sqrt{|u_0(\mathbf{r})|^2 + |u_1(\mathbf{r})|^2}}, \tag{4.3}$$

which the $u_0(\mathbf{r})$ and $u_1(\mathbf{r})$ are spatial amplitudes.

In order to simplify the wave vector described above, we choose $u_0(\mathbf{r})$ and $u_1(\mathbf{r})$ to be orthogonal modes. For an arbitrary wave vector Ψ_A, using the Schmidt decomposition, it can be re-expressed as a combination of a set of orthonormal basis $\{\hat{\beta}_i\}$:

$$\Psi_A = \sum \alpha_{ij} \hat{\beta}_i \otimes |j\rangle, \tag{4.4}$$

where α_{ij} are real, non-negative scalars and $j = 0, 1$. Therefore, for the superposed beams with arbitrary wave vectors as the spatial component u_0 and u_1, they can always be transformed into the simplest scenarios that are introduced here along with the combination and interaction of those basic scenarios.

In this thesis, we assume the beams are paraxial and propagating mainly in the z direction and thus they can be expressed in cylindrical coordinates. In order to satisfy the requirement of a varying spatial component, one particular example would be the Laguerre Gaussian beams introduced in Section. 2.1.3. In this way, the general form of a vector beam in Eq. 4.3 can be further simplified into:

$$|\Psi\rangle = \frac{|0\rangle + \mu|1\rangle}{\sqrt{1 + |\mu|^2}}, \tag{4.5}$$

where μ is the ratio between the two spatial components $u_0(\mathbf{r})$ and $u_1(\mathbf{r})$, in the form of:

$$\mu = f(\rho, z) e^{i\Phi(\rho,z)} = f(\rho, z) e^{i\ell_d \phi} e^{i\theta(\rho,z)}. \tag{4.6}$$

Here, $f(\rho, z)$ is the modulus of μ and Φ is is the phase difference between $u_0(\mathbf{r})$ and $u_1(\mathbf{r})$. The phase difference can be seperated into two parts: $e^{i\ell_d\phi}$ that is associated with Laguerre Gaussian winding number; and $e^{i\theta(\rho,z)}$ including the Gouy phase which is the phase change during propagation. For paraxial beams described above, their effective magnetisation can be explicitly written as:

$$M_x = \frac{2|f|}{1+|f|^2}\cos\Phi; \quad M_y = \frac{2|f|}{1+|f|^2}\sin\Phi; \quad M_z = \frac{1-|f|^2}{1+|f|^2}. \tag{4.7}$$

Utilising the cylindrical symmetry of the system, we can modify the definition for the skyrmion number Eq. 3.6 as:

$$n = \frac{1}{4\pi}\int_S \mathbf{M}\cdot\left(\frac{\partial\mathbf{M}}{\partial\rho}\times\left(\frac{1}{\rho}\frac{\partial\mathbf{M}}{\partial\phi}\right)\right)\rho d\rho d\phi, \tag{4.8}$$

where the integral is taken over a plane perpendicular to the z-direction. Here from Eq. 4.7, the derivatives of $\mathbf{M}$ are:

$$\begin{cases} \frac{\partial M_x}{\partial\rho} &= \frac{M_z M_x}{f}\frac{\partial f}{\partial\rho} - M_y\frac{\partial\Phi}{\partial\rho} \\ \frac{\partial M_y}{\partial\rho} &= \frac{M_z M_y}{f}\frac{\partial f}{\partial\rho} + M_x\frac{\partial\Phi}{\partial\rho} \\ \frac{\partial M_z}{\partial\rho} &= -\frac{M_x^2+M_y^2}{f}\frac{\partial f}{\partial\rho} \end{cases}, \quad \begin{cases} \frac{\partial M_x}{\partial\phi} &= -M_y\frac{\partial\Phi}{\partial\phi} \\ \frac{\partial M_y}{\partial\phi} &= M_x\frac{\partial\Phi}{\partial\phi} \\ \frac{\partial M_z}{\partial\phi} &= 0 \end{cases}. \tag{4.9}$$

In this way, the cross-product can be calculated as:

$$\begin{aligned} \frac{\partial\mathbf{M}}{\partial\rho}\times\frac{\partial\mathbf{M}}{\partial\phi} &= \begin{bmatrix} \hat{x} & \hat{y} & \hat{z} \\ \frac{M_z M_x}{f}\frac{\partial f}{\partial\rho} - M_y\frac{\partial\Phi}{\partial\rho} & \frac{M_z M_y}{f}\frac{\partial f}{\partial\rho} + M_x\frac{\partial\Phi}{\partial\rho} & -\frac{M_x^2+M_y^2}{f}\frac{\partial f}{\partial\rho} \\ -M_y\frac{\partial\Phi}{\partial\phi} & M_x\frac{\partial\Phi}{\partial\phi} & 0 \end{bmatrix} \\ &= \hat{x}\left(\frac{M_x^2+M_y^2}{f}\frac{\partial f}{\partial\rho}M_x\frac{\partial\Phi}{\partial\phi}\right) \\ &+ \hat{y}\left(\frac{M_x^2+M_y^2}{f}\frac{\partial f}{\partial\rho}M_y\frac{\partial\Phi}{\partial\phi}\right) \\ &+ \hat{z}\left(\left(\frac{M_z M_x}{f}\frac{\partial f}{\partial\rho} - M_y\frac{\partial\Phi}{\partial\rho}\right)M_x\frac{\partial\Phi}{\partial\phi} + \left(\frac{M_z M_y}{f}\frac{\partial f}{\partial\rho} + M_x\frac{\partial\Phi}{\partial\rho}\right)M_y\frac{\partial\Phi}{\partial\phi}\right), \end{aligned} \tag{4.10}$$

from which the dot product can be obtained as:

$$\begin{aligned} \mathbf{M}\cdot\left(\frac{\partial\mathbf{M}}{\partial\rho}\times\frac{\partial\mathbf{M}}{\partial\phi}\right) &= \frac{M_x^2+M_y^2}{f}\frac{\partial f}{\partial\rho}M_x^2\frac{\partial\Phi}{\partial\phi} \\ &+ \frac{M_x^2+M_y^2}{f}\frac{\partial f}{\partial\rho}M_y^2\frac{\partial\Phi}{\partial\phi} \\ &+ M_z\left(\left(\frac{M_z M_x}{f}\frac{\partial f}{\partial\rho} - M_y\frac{\partial\Phi}{\partial\rho}\right)M_x\frac{\partial\Phi}{\partial\phi} + \left(\frac{M_z M_y}{f}\frac{\partial f}{\partial\rho} + M_x\frac{\partial\Phi}{\partial\rho}\right)M_y\frac{\partial\Phi}{\partial\phi}\right) \\ &= \frac{\partial f}{\partial\rho}\frac{\partial\Phi}{\partial\phi}\frac{1}{f}\left(\left(M_x^2+M_y^2\right)^2 + M_z^2M_x^2 + M_z^2M_y^2\right) \\ &= \frac{\partial f}{\partial\rho}\frac{\partial\Phi}{\partial\phi}\frac{1}{f}\left(M_x^2+M_y^2+M_z^2\right)\left(M_x^2+M_y^2\right). \end{aligned} \tag{4.11}$$

Because $\mathbf{M}$ is a unit vector, $M_x^2+M_y^2+M_z^2=1$, and substitute M_x and M_y in Eq. 4.7 as functions

of f and Φ, the dot product can be expressed as:

$$\begin{aligned}\mathbf{M}\cdot\left(\frac{\partial\mathbf{M}}{\partial\rho}\times\frac{\partial\mathbf{M}}{\partial\phi}\right) &= \frac{\partial f}{\partial\rho}\frac{\partial\Phi}{\partial\phi}\frac{4f}{(1+f^2)^2}\\ &= \frac{\partial f^2}{\partial\rho}\frac{\partial\Phi}{\partial\phi}\frac{2}{(1+f^2)^2}.\end{aligned} \tag{4.12}$$

In this way, the skyrmion number can be calculated as:

$$\begin{aligned}n &= \frac{1}{4\pi}\int_S \frac{\partial f^2}{\partial\rho}\frac{\partial\Phi}{\partial\phi}\frac{2}{(1+f^2)^2}d\rho d\phi\\ &= \frac{1}{4\pi}\int_0^\infty d\rho\frac{\partial f^2}{\partial\rho}\frac{2}{(1+f^2)^2}\int_0^{2\pi}d\phi\frac{\partial\Phi}{\partial\phi}\\ &= \frac{1}{4\pi}4\pi\ell_d\int_0^\infty d\rho\frac{\partial f^2}{\partial\rho}\frac{1}{(1+f^2)^2}\\ &= \ell_d\frac{-1}{1+f^2}\Big|_{\rho=0}^{\rho=\infty}.\end{aligned} \tag{4.13}$$

Now, we have obtained the general form of the Skyrmion number of paraxial beams in the form specified in Eq. 4.3

$$n = \ell_d\left(\frac{1}{1+f^2(0,z)}-\frac{1}{1+f^2(\infty,z)}\right). \tag{4.14}$$

Because $f(\rho,z)^2$ is defined as the ratio between the intensity of the two spatial components, Eq. 4.14 indicates that the skyrmion number is determined only by the ratio between the intensity of the two spatial components at the centre of the beam ($\rho = 0$) and that at infinity. In the case of the two spatial components propagating differently, either far from the beam axis or at the centre of the field there would be one component dominant over the other one. If it is the same component dominants at both places, then the value in the bracket would be 0, which means the skyrmion number for this vector beam would be 0. On the other hand, we would obtain either ℓ_d or $-\ell_d$ for the skyrmion number.

This also verifies our previous conclusion that the skyrmion structure is independent of the polarisation choices. For example, if we switch the polarisation of the two spatial components, although the deference between the winding number ℓ_d would become $(-\ell_d)$, the ratio between the two components f will also change to $1/f$. The latter change ensures the the intensity ratio between at the centre of the beam and the region far from the beam axis also flipped. Therefore, both of the two components in Eq. 4.14 gained a negative sign, leaving the skyrmion number unchanged. Therefore, the skyrmion number is limited to an integer. According to Skyrme's theory introduced in Section 3.4, this shows that this structure cannot change continuously to vacuum and thus it is a manifestation of topological robustness.

Another way to understand this result is by expressing the effective magnetisation $\mathbf{M} = \left[S_1, S_2, S_3\right]^T$ of this beam as:

$$S_1 = \sin\chi\cos\Phi; S_2 = \sin\chi\sin\Phi; S_3 = \cos\chi. \tag{4.15}$$

This is due to $(\frac{1-|f|^2}{1+|f|^2})^2 + (\frac{2|f|}{1+|f|^2})^2 = 1$, which allows for introducing an auxiliary angle ξ:

$$\frac{1-|f(\rho,z)|^2}{1+|f(\rho,z)|^2} = \cos\chi(\rho,z), \tag{4.16}$$

The expression in Eq. 4.15 indicates that an effective magnetisation vector corresponds to a point on a sphere, as shown in Fig. 4.1. This also proves that the optical and electrical skyrmions of a paraxial beam is in fact, a stereo-graphic projection of the Poincaré and Bloch sphere respectively. Particularly, each circle on the planner optical/electrical skyrmion correspond to a latitude on the the Poincaré/Bloch sphere, as depicted in Fig. 4.1, with the innermost circle mapping to the North pole.

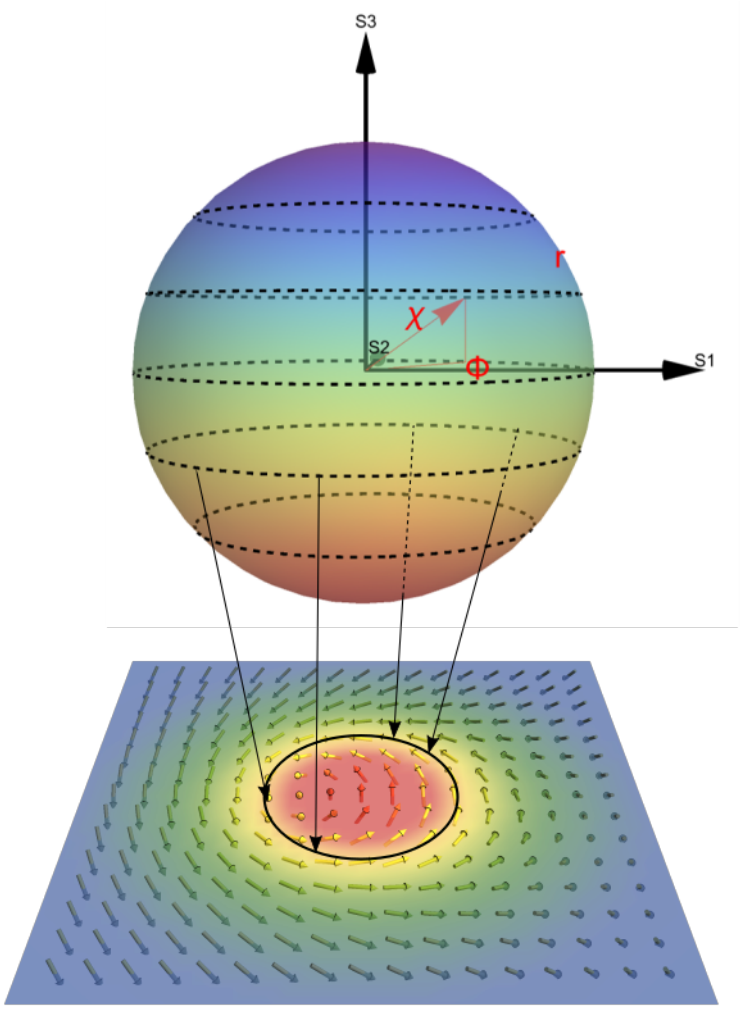

Figure 4.1 Visualisation of the effective magnetisation of the optical beam. The vectors represent the related Poincaré vector and the colour mapping represents the magnitude of its S_3 component. This is identical to the magnetisation of magnetic skyrmions shown in Fig. 3.1.

4.3 Comparing optical and electron beams

As we previously introduced in Section. 3.5 of Chapter. 3, there are two kinds of skyrmions: chiral skyrmions and hedgehog skyrmions. Hedgehog skyrmions take their name from the fact that their magnetisation vectors point radially outward from the origin at all points [72]. In other words, they exist, and only exist when the physical space and the magnetisation vector space are rotating at the same pace [117]. Chiral skyrmions have helical progression of their magnetisation vectors when traced along the diameter, and are also known as the vortex skyrmions.

As we stated in Section. 4.1, the physical meaning of the skyrmion number n is the number of vectors wrapped around the sphere that the baby skyrmion is projected from. For magnetic skyrmions, this means hedgehog skyrmions would only exist in the $n = 1$ case. This also applies to optical skyrmions.

The spin states of electron beams are visualised on the Bloch sphere. Therefore, the similarity between optical skyrmions in electron beams and magnetic skyrmions is self evident, as we can observe in Fig. 4.2 a) and c). In Fig. 4.2 a1) and a2), where the skyrmion number is 1, the unit vector $\mathbf{M}$ has rotated exactly once. In comparison, in Fig. 4.2 c2), where the skyrmion number is 2, the unit vector $\mathbf{M}$ has rotated twice before it returns to its original position. Among all four skyrmions, only Fig. 4.2 a1) resembles a hedgehog skyrmion. However, this similarity between magnetic skyrmions and optical skyrmions is more subtle for optical beams due to the structure of the Poincaré sphere. For optical beams, all possible polarisations can be visualised on the Poincaré sphere as double end vectors, on which the orthogonal polarisations are represented by two opposite points. This means a polarisation ellipse that has travelled π angles on the Poincaré itself has only rotated $\pi/2$. Therefore, for a full rotation of the space, i.e. 2π, the polarisation ellipse is required to only rotate π. This is reflected in Fig. 4.2 b1) b2) and d2). Although physically Fig. 4.2 d2) appear more similar to Fig. 4.2 a1) as a hedgehog skyrmion, it actually corresponds to Fig. 4.2 c2) which is a spiral skrymion with $n = 2$. This difference is due to the different representation of the effective magnetisation vector using the Poincaré sphere and the Bloch sphere.

4.4 Skyrmion number in specific examples

We will start with the simplest case with the radial number $p = 0$, where both $u_0(\mathbf{r})$ and $u_1(\mathbf{r})$ are single modes of LG beams and can be expressed in the form of:

$$\varphi_0^l \propto \sqrt{\frac{1}{\pi|\ell|!}}\frac{1}{w(z)}\left(\frac{\rho\sqrt{2}}{w(z)}\right)^{|l|} e^{il\phi}\exp\left(i(|\ell|+1)\xi(z) - ik\frac{\rho^2}{2R(z)} - \frac{\rho^2}{w(z)^2}\right), \tag{4.17}$$

with $\ell = \ell_{u_0}$ and $\ell = \ell_{u_1}$ respectively. We here provide two more specific examples.

4.4.1 Same focus

We start with the case in which the two spatial components are focused at the same point, as shown in Fig. 4.3. In the figure, the arrows represent the unit Bloch vector and the colour mapping corresponds to the magnitude M_z vector. The red beam represents a LG beam with $\ell = 0$ and left-handed polarisation while the blue beams represents a LG beam with $\ell = 1$ (hence the helical

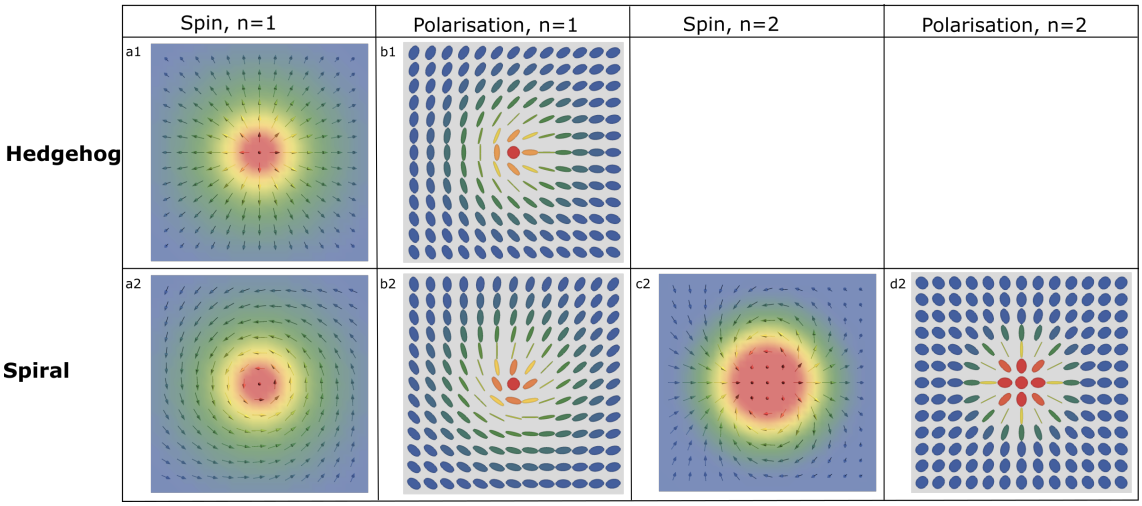

Figure 4.2 This is a table showing skyrmion structures in optical beams and electron beams. For electron beams, the skyrmion structure is seen in the visualisation of spin, whereas for optical beams the skyrmion structure is depicted by polarisation eclipses. Sets a) and c) ($n = 2$) and ($n = 1$) skyrmion structures in electron beams whilst b) and d) compare the optical beams. Sets a) and b) compare electron beams and optical beams both with an $n = 1$ skyrmion structure whilst c) and d) compare the $n = 2$ skyrmion structure. The table also shows the differences between hedgehog and spiral skyrmions in each case by sets 1) and 2) - that hedgehog skyrmions only exist when $n = 1$.

phase front) and right-handed polarisation. The corresponding Poincaré vectors are presented in Fig. 4.2 and their comparisons are discussed in Section. 4.3. If the two spatial components possess the same beam waist and wavelength, the ratio μ between the two spatial components can be written as:

$$\mu = f(\rho, z)e^{i\Phi(\rho,z,\phi)} = \sqrt{\frac{|\ell_{u_0}|!}{|\ell_{u_1}|!}}\left(\frac{\rho\sqrt{2}}{w(z)}\right)^{\ell_\Delta} e^{i\ell_d\phi}e^{-i\ell_\Delta\xi(z)}, \tag{4.18}$$

where $\ell_\Delta = |\ell_{u_1}| - |\ell_{u_0}|$. According to Eq. 4.7, the effective magnetisation $\mathbf{M}$ is:

$$\begin{aligned} M_x &= \frac{2\sqrt{\frac{|\ell_{u_0}|!}{|\ell_{u_1}|!}}\left(\frac{\rho\sqrt{2}}{w(z)}\right)^{\ell_\Delta}}{1+\frac{|\ell_{u_0}|!}{|\ell_{u_1}|!}\left(\frac{2\rho^2}{w(z)^2}\right)^{\ell_\Delta}}\cos\left(\ell_d\phi + \ell_\Delta\xi(z)\right); \\ M_y &= \frac{2\sqrt{\frac{|\ell_{u_0}|!}{|\ell_{u_1}|!}}\left(\frac{\rho\sqrt{2}}{w(z)}\right)^{\ell_\Delta}}{1+\frac{|\ell_{u_0}|!}{|\ell_{u_1}|!}\left(\frac{2\rho^2}{w(z)^2}\right)^{\ell_\Delta}}\sin\left(\ell_d\phi + \ell_\Delta\xi(z)\right); \\ M_z &= -1 + \frac{2}{1+\frac{|\ell_{u_0}|!}{|\ell_{u_1}|!}\left(\frac{2\rho^2}{w(z)^2}\right)^{\ell_\Delta}}. \end{aligned} \tag{4.19}$$

According to the general form of the skyrmion number introduced in Eq.4.6 and Eq.4.14, the skyrmion number is:

$$n = \ell_d. \tag{4.20}$$

The orientation of effective magnetisation $\mathbf{M}$ on a cross-section depends on the ratio between

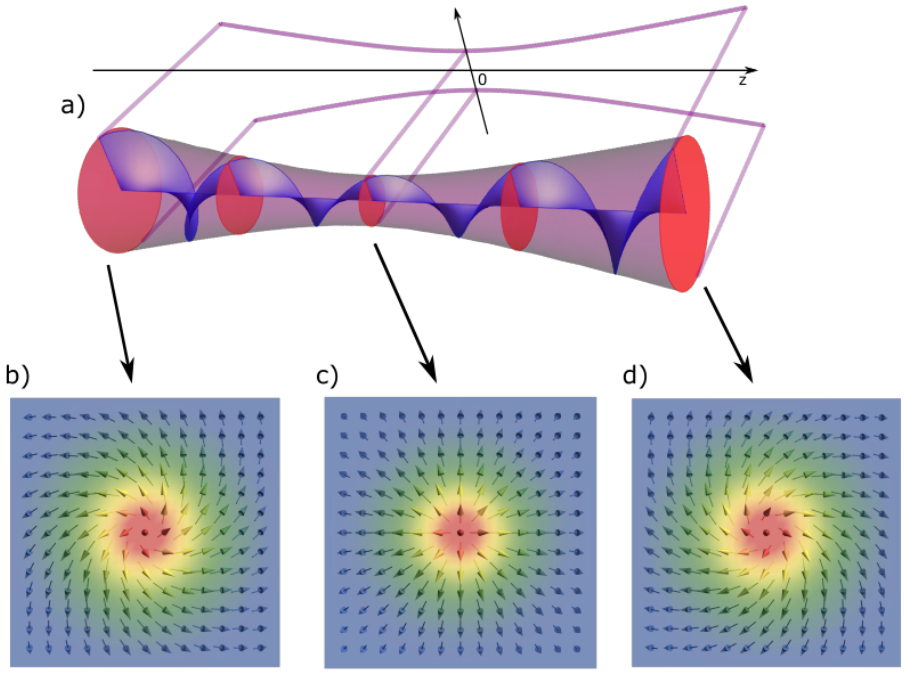

Figure 4.3 This is an illustration of the skyrmionic beam given in Eq. 4.3. Here, the two spatial modes are Laguerre-Gaussian modes with $\ell_{u_0} = 0$ and $\ell_{u_1} = 1$ focusing at the same point, $z = 0$: a) A schematic diagram of the beam; b) The $\mathbf{M}$ vector field at negative z coordinate, when the relative phase difference is negative resulting in a chiral skyrmion; c) The $\mathbf{M}$ vector field at $z = 0$,where the relative phase difference is 0, resulting in a hedghog skyrmion; d) The $\mathbf{M}$ vector field for positive z coordinate, when the relative phase difference is positive, resulting in a chiral skyrmion again.

M_y and M_x. As demonstrated in Eq. 4.19, this ratio is $\tan(\ell_d\phi + \ell_\Delta\xi(z))$. Because Gouy phase $\xi(z) = \arctan(z/z_R)$ depends on z, this ratio is also dependent on z. Therefore, the orientation of $\mathbf{M}$ on a cross-section changes during beam propagation. As shown Fig. 4.3, the cross-section would change from a chiral skyrmion (Fig. 4.3 b)), to a hedgehog skyrmion at the focus point (Fig. 4.3 c)) and then progress to a chiral skyrmion winding in the opposite direction (Fig. 4.3 d)). As demonstrated in Fig. 4.2, hedgehog skyrmions only exist when $\ell_d = 1$ and the space rotates at the same pace. According to the explicit form of $\mathbf{M}$ for when $\ell_d = 1$, this only happens when $\ell_\Delta\xi(z) = 0$. In other words, when $z = 0$.

4.4.2 Different focus

The second example is when the same spatial components as Section. 4.4.1 focus at different positions, z_0 and z_1 for u_0 and u_1 respectively as depicted in Fig. 4.4. Without losing generality, we choose the LG_0^0 component to focus first. The ratio $\mu = f(\rho, z)e^{i\Phi(\rho,z)}$ between the two spatial components can be written as:

$$f = \sqrt{\frac{|\ell_{u_0}|!}{|\ell_{u_1}|!}} \frac{(w_{u_0}(z))^{|\ell_{u_0}|+1}}{(w_{u_1}(z))^{|\ell_{u_1}|+1}} \left(\sqrt{2}\rho\right)^{|\ell_{u_1}|-|\ell_{u_0}|} \exp\left(-\rho^2\left(\frac{1}{w_{u_1}^2(z)} - \frac{1}{w_{u_0}^2(z)}\right)\right); \tag{4.21}$$

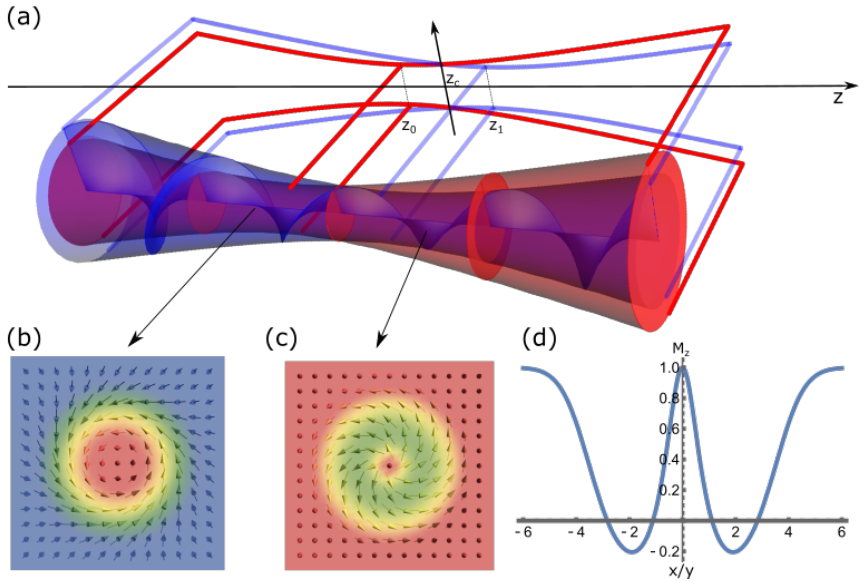

Figure 4.4 This is an illustration of the paraxial beam given in Eq. 4.3, when the two spatial modes are Laguerre-Gaussian modes with $\ell_{u_0} = 0$ and $\ell_{u_1} = 1$ focusing at z_0 and z_1, respectively. It shows a clear change of skyrmion number as it propagates, where $z_c = \frac{z_0+z_1}{2}$ denotes the crossover plane. (a) A schematic diagram of the beam; (b) The effective magnetisation $\mathbf{M}$ at cross-section at $z < z_0$ with skyrmion number 1; (c) The effective magnetisation $\mathbf{M}$ at cross-section at $z > z_1$ with skyrmion number 0; (d) S_3 (M_z) vector ranges across the x axis and the y axis respectively on the cross-section in (c).

$$\Phi(\rho, z, \phi) = \ell_d \phi - \frac{\kappa\rho^2}{2}\left(\frac{1}{R_{u_1}(z)} - \frac{1}{R_{u_0}(z)}\right) + \Big(\big(|\ell_{u_1}| + 1\big)\xi_{u_1}(z)\Big) - \Big(\big(|\ell_{u_0}| + 1\big)\xi_{u_0}(z)\Big), \tag{4.22}$$

where the under script u_0 and u_1 represent the corresponding component of u_0 and u_1 respectively. In this particular example, because of the doughnut shaped intensity profile of higher orders LG beams, the LG_0^0 component will always dominate the centre of the beam. Therefore, the ratio between the intensity of two spatial components at the centre $f(0, z)$ would always be 0. As shown in Eq. 4.21, this result is generally applicable to u_0 other than LG_0^0. Far from the beam axis, the ratio $f(\infty, z)$ is either ∞ or 0 depending on whether the term $(\frac{1}{w_{u_1}^2(z)} - \frac{1}{w_{u_0}^2(z)})$ is positive or negative. Because $w(z)$ is proportional to the distance from the cross-section to its focus point, the critical plane z_c of $f(\infty, z)$ changing from ∞ to 0 occurs at the midpoint between two focus points, and its skyrmion number will change from ℓ_d to 0 according to Eq. 4.14. At the critical plane, $f(\infty, z_c) = \infty$ and the skyrmion number at this plane would be ℓ_d. In Fig. 4.4(d) we show how the value of the S_3 (M_z) vector changes with respect to position from the centre of the beam at a cross-section beyond z_1. It shows that M_z cannot exactly reach 1 to expand fully along the longitude. With $\ell_d = 1$, according to previous discussions in Section. 4.3, it therefore demonstrates a non-skyrmion.

4.5 Conclusion

In this chapter, we introduced the general form of skyrmionic beams and its associated skyrmion numbers. We propose that skyrmionic beams can be constructed by superposing two coaxially varying spatial components with orthogonal polarisations or spin. We have demonstrated that the skyrmion numbers of these beams only depend on the ratio between the intensity of the two spatial components at the centre of the beam and at infinity. Given how the intensity of the two spatial components varies differently throughout propagation, the skyrmion number would always be an integer. When it is non-zero, we refer to this type of beam as skyrmionic beams. We also have demonstrated the physical meaning of the skyrmion number by associating the effective magnetisation **M** with the Stokes parameters.

We have also presented two specific examples of skyrmionic beams to further illustrate this concept. In the first example, the beam is comprised of two *LG* beams with different winding number, ℓ, but sharing the same beam width, wavelength and focal plane as the spatial components. This type of beam possesses an integer skyrmion number. In the second example the two spatial components are focused differently, while still sharing the same beam width and wavelength. This type of beam starts with a non-zero integer skyrmion number before suddenly changing to 0 after the cross-over plane, and therefore becoming a non-skyrmion beam.

The second example poses an important question: *what does the change of skyrmion number mean for the topological stability of this type of beam?* In the next chapter, we will introduce the skyrmion field to explain these changes in skyrmion numbers and why despite the changes, this type of beams is still topologically stable. We will also demonstrate that the skyrmion field is a conserved field, and therefore can be utilised to categorise structured beams.

Chapter 5

Skyrmion field in Skyrmionic beams

In the previous chapter, we have introduced the concept of skyrmionic beams, their associated effective magnetisation **M** and the general form of skrymion numbers. We have left one question at the end of last chapter: *what does the change of skyrmion number during propagation mean for the topological stability of this type of beam?* In this chapter, we will introduce the skyrmion field **Σ** and prove that it is a conserved field. We will use this new field to further explain the topological stability of skyrmionic beams and how we can use it to categorize structured beams. The material in this chapter is produced by the author and partly published in [1] while the rest will be included in future publications that are currently under preparation.

5.1 Skyrmion field in general

The idea of the skyrmion field can be derived from the definition of the skyrmion number (Eq.3.6). Because $dxdy$ can be regard as the cross-section in the z direction, the definition of the skyrmion number in Eq. 3.6 can be modified to:

$$n = \frac{1}{4\pi}\int_S (\Sigma_z \hat{z}) \cdot (\hat{z} ds), \tag{5.1}$$

where $\Sigma_z = \mathbf{M} \cdot (\frac{\partial \mathbf{M}}{\partial x} \times \frac{\partial \mathbf{M}}{\partial y})$ is the z-component of a vector field. We can write down the form of this field as:

$$\Sigma_i = \frac{1}{2}\varepsilon_{ijk}\varepsilon_{pqr} M_p (\partial_j M_q \partial_k M_r), \tag{5.2}$$

where ε_{ijk} and ε_{pqr} are the Levi-Civitta symbols and we also adopted the Einstein summation convention. This is in the similar form to the 'skyrmion current' in the original paper of Skryme [58]. Under this new definition, we can reinterpret the skyrmion number as the flux of the skyrmion field lines in the z direction.

The skyrmion field is independent of the choice of the physical coordinate system. We can rewrite Eq. 5.2 as:

$$\Sigma_i = \frac{1}{2}\varepsilon_{ijk} \det \begin{bmatrix} M_x & M_y & M_z \\ \partial_j M_x & \partial_j M_y & \partial_j M_z \\ \partial_k M_x & \partial_k M_y & \partial_k M_z \end{bmatrix}. \tag{5.3}$$

Any change of the global orientation of **M** is equivalent to a multiplication of a global rotational

matrix. As the determinant of a rotational matrix is 1, this operation would not effect the skyrmion field. This means that the choice of the physical coordinate system would not affect the skyrmion field.
It is not difficult to verify that this field is divergence-less, i.e.

$$\nabla \cdot \mathbf{\Sigma} = 0. \tag{5.4}$$

The proof is as below, based on the nature of $\mathbf{M}$ as a normalised field. The divergence of $\mathbf{\Sigma}$ has the form:

$$\nabla \cdot \mathbf{\Sigma} = \frac{1}{2}\varepsilon_{ijk}\varepsilon_{pqr}(\partial_i M_p)(\partial_j M_q)(\partial_k M_r). \tag{5.5}$$

In the vicinity of any given point $\mathbf{r_0}$, the $\mathbf{M}$ can be expanded using Taylor expansion. The unit vector magnetisation is:

$$\mathbf{M}|_r = \mathbf{M}|_{r_0} + \Big((\mathbf{r} - \mathbf{r_0}) \cdot \nabla\Big)\mathbf{M}|_{r_0} \tag{5.6}$$

As $\mathbf{M}$ is a unit vector everywhere, $|\mathbf{M}|^2|_r$, and this provides a constraint on the derivative of $\mathbf{M}$ at $\mathbf{r_0}$. As $\mathbf{r} - \mathbf{r_0}$ is small, Eq. 5.6 leads to:

$$\begin{aligned} |\mathbf{M}|_r|^2 &= |\mathbf{M}|_{r_0}|^2 + 2M_i|_r\Big((\mathbf{r} - \mathbf{r_0}) \cdot \nabla\Big)M_i|_{r_0} + O(\mathbf{r} - \mathbf{r_0})^2 \\ &= 1. \end{aligned} \tag{5.7}$$

This means that

$$0 = M_i|_r(\mathbf{r} - \mathbf{r_0}) \cdot \nabla M_i|_{r_0}. \tag{5.8}$$

Because $\mathbf{M}$ is a unit vector, the components M_i cannot all be zero. This leads to the conclusion that for one of the components, its gradients ∇M_i is required to be 0. Therefore, because the expression of the divergence of the skyrmion field in Eq. 5.5 includes the product of derivatives of all the three components of $\mathbf{M}$, the skyrmion field at $\mathbf{r}_0$ is divergenceless. Furthermore, because $\mathbf{r_0}$ is an arbitrary point, we can easily extend this argument to the whole space. In this way we proved that:

$$\nabla \cdot \mathbf{\Sigma} = 0. \tag{5.9}$$

Hence, the skyrmion field is divergence-less because the effective magnetisation $\mathbf{M}$ is a unit vector.

A divergenceless field is often also referred to as a source-less, sink-less field. According to the divergence theorem:

$$\iiint_V (\nabla \cdot \mathbf{F})dV = \oint_S (\mathbf{F} \cdot \hat{\mathbf{n}})dS, \tag{5.10}$$

it is obvious that for a divergence-less field, the flux flowing through an enclosed area would be zero as well. That is to say, the skyrmion field is conserved.

5.2 Skyrmion field in paraxial skyrmionic beams

The skyrmion field in paraxial beams we introduced in Sec.4.2 can be simplified as following based on Eq.5.2:

$$\Sigma_i = \frac{4\varepsilon_{ijk}}{(1+|\mu|^2)^2}\left(\partial_j \Re(\mu)\partial_k \Im(\mu)\right), \tag{5.11}$$

where $\Re(\mu)$ represents the real part of μ and $\Im(\mu)$ is the imaginary part of it. This can be proved as following.

According to the definition of skyrmion number, skyrmion field can be written as:

$$\Sigma_i = \frac{1}{2}\varepsilon_{ijk}\mathbf{M}\cdot(\partial_j\mathbf{M}\times\partial_k\mathbf{M}). \tag{5.12}$$

and therefore skyrmion field can be further expanded as:

$$\Sigma_i = \varepsilon_{ijk}\left(M_x\partial_j M_y\partial_k M_z + M_y\partial_j M_z\partial_k M_x + M_z\partial_j M_x\partial_k M_y\right). \tag{5.13}$$

According the explicit forms of $\mathbf{M}$ in Eq. 4.7 and the form of μ in Eq. 4.6, we can rewrite $\mathbf{M}$ and their corresponding derivatives as:

$$M_x = \frac{2\Re(\mu)}{1+|\mu|^2}; \quad M_y = \frac{2\Im(\mu)}{1+|\mu|^2}; \quad M_z = \frac{1-|\mu|^2}{1+|\mu|^2}. \tag{5.14}$$

$$\partial_j M_x = 2\left(\frac{\partial_j\Re(\mu)}{1+|\mu|^2} - \frac{\Re(\mu)\partial_j|\mu|^2}{(1+|\mu|^2)^2}\right); \quad \partial_j M_y = 2\left(\frac{\partial_j\Im(\mu)}{1+|\mu|^2} - \frac{\Im(\mu)\partial_j|\mu|^2}{(1+|\mu|^2)^2}\right); \quad \partial_j M_z = \frac{-2\partial_j|\mu|^2}{(1+|\mu|^2)^2}. \tag{5.15}$$

Adopting these expressions, Eq. 5.13 can be re-expressed as:

$$\begin{aligned}
\Sigma_i = 4\varepsilon_{ijk}\Bigg(&\left(\frac{\Re(\mu)}{1+|\mu|^2}\right)\partial_j\left(\frac{\Im(\mu)}{1+|\mu|^2}\right)\partial_k\left(\frac{1-|\mu|^2}{1+|\mu|^2}\right)\\
&+\left(\frac{\Im(\mu)}{1+|\mu|^2}\right)\partial_j\left(\frac{1-|\mu|^2}{1+|\mu|^2}\right)\partial_k\left(\frac{\Re(\mu)}{1+|\mu|^2}\right)+\left(\frac{1-|\mu|^2}{1+|\mu|^2}\right)\partial_j\left(\frac{\Re(\mu)}{1+|\mu|^2}\right)\partial_k\left(\frac{\Im(\mu)}{1+|\mu|^2}\right)\Bigg)\\
=4\varepsilon_{ijk}\Bigg(&\left(\frac{\Re(\mu)}{1+|\mu|^2}\right)\left(\frac{\partial_j\Im(\mu)}{1+|\mu|^2}-\frac{\Im(\mu)\partial_j|\mu|^2}{(1+|\mu|^2)^2}\right)\left(\frac{-\partial_k|\mu|^2}{(1+|\mu|^2)^2}\right)\\
&+\left(\frac{\Im(\mu)}{1+|\mu|^2}\right)\left(\frac{-\partial_j|\mu|^2}{(1+|\mu|^2)^2}\right)\left(\frac{\partial_k\Re(\mu)}{1+|\mu|^2}-\frac{\Re(\mu)\partial_k|\mu|^2}{(1+|\mu|^2)^2}\right)\\
&+\left(\frac{1-|\mu|^2}{1+|\mu|^2}\right)\left(\frac{\partial_j\Re(\mu)}{1+|\mu|^2}-\frac{\Re(\mu)\partial_j|\mu|^2}{(1+|\mu|^2)^2}\right)\left(\frac{\partial_k\Im(\mu)}{1+|\mu|^2}-\frac{\Im(\mu)\partial_k|\mu|^2}{(1+|\mu|^2)^2}\right)\Bigg).
\end{aligned} \tag{5.16}$$

Using the relation $\varepsilon_{ijk}\partial_j A\partial_k A = 0$, the above expression can be simplified into:

$$\Sigma_i = 4\varepsilon_{ijk}\frac{(1-|\mu|^2)\left(\partial_j\Re(\mu)\partial_k\Im(\mu)\right)+\left(\frac{2-(1-|\mu|^2)}{1+|\mu|^2}\right)\left(\Re(\mu)\partial_k\Im(\mu)\partial_j|\mu|^2+\Im(\mu)\partial_j\Re(\mu)\partial_k|\mu|^2\right)}{(1+|\mu|^2)^3}. \tag{5.17}$$

Because $|\mu|^2 = \Re(\mu)^2 + \Im(\mu)^2$, this can be further reduced to:

$$\begin{aligned}
\Sigma_i =& 4\varepsilon_{ijk}(1+|\mu|^2)^{-3}\Big((1-|\mu|^2)\partial_j\Re(\mu)\partial_k\Im(\mu) \\
&+ 2\left(\Re(\mu)\partial_k\Im(\mu)\left(\Re(\mu)\partial_j\Re(\mu)+\Im(\mu)\partial_j\Im(\mu)\right)+\Im(\mu)\partial_j\Re(\mu)\left(\Re(\mu)\partial_k\Re(\mu)+\Im(\mu)\partial_k\Im(\mu)\right)\right)\Big) \\
=& 4\varepsilon_{ijk}(1+|\mu|^2)^{-3}\Big((1-|\mu|^2)\partial_j\Re(\mu)\partial_k\Im(\mu)+2\left(\Re(\mu)^2\partial_k\Im(\mu)\partial_j\Re(\mu)+\Im(\mu)^2\partial_j\Re(\mu)\partial_k\Im(\mu)\right)\Big) \\
=& 4\varepsilon_{ijk}\frac{(1-|\mu|^2+2|\mu|^2)\partial_j\Re(\mu)\partial_k\Im(\mu)}{(1+|\mu|^2)^3} \\
=& \frac{4\varepsilon_{ijk}\partial_j\Re(\mu)\partial_k\Im(\mu)}{(1+|\mu|^2)^2}.
\end{aligned} \tag{5.18}$$

Explicitly, using the cylindrical symmetry, the skyrmion field components for the beam described by Eq. 4.5 can be explicitly written as:

$$\begin{aligned}
\Sigma_\rho &= \frac{-2}{\rho(1+f^2)^2}\frac{\partial f^2}{\partial z}\frac{\partial\Phi}{\partial\phi}; \\
\Sigma_\varphi &= \frac{2}{(1+f^2)^2}\left(-\frac{\partial f^2}{\partial\rho}\frac{\partial\Phi}{\partial z}+\frac{\partial f^2}{\partial z}\frac{\partial\Phi}{\partial\rho}\right); \\
\Sigma_z &= \frac{2}{\rho(1+f^2)^2}\frac{\partial f^2}{\partial\rho}\frac{\partial\Phi}{\partial\phi}.
\end{aligned} \tag{5.19}$$

This expression also allows us to retrieve the skyrmion number result in Eq. 4.14 through the flux of skyrmion field in the z direction introduced in Eq. 5.1.

We are interested in the effect of different polarisation/spin of the beams on our results. We name the basis for the new arbitrary axis as $|P\rangle$ and $|V\rangle$, which are defined by:

$$|P\rangle = \cos\gamma|0\rangle + e^{i\theta}\sin\gamma|1\rangle; \qquad |V\rangle = -\sin\gamma|0\rangle + e^{i\theta}\cos\gamma|1\rangle, \tag{5.20}$$

where γ and θ are both arbitrary. Therefore, a skyrmionic beam with arbitrary polarisation/spin can be written as:

$$|\Psi\rangle = \frac{|P\rangle + \mu|V\rangle}{\sqrt{1+|\mu|^2}}, \tag{5.21}$$

where μ is defined as Eq. 4.6. Input this into the definition for the skyrmion field in Eq. 5.2, it is obvious that the skyrmion field is exactly the same as Eq. 5.11. On this account, we have proved that the skyrmion field of a skyrmionic beam does not depend on the direction of its polarisation/spin. We are free to assign the different Pauli matrices to any components of the magnetisation as long as we retain the order of the Pauli matrices. In this work, $\mathbf{M} = \left[M_x, M_y, M_z\right]^T = \left[S_1, S_2, S_3\right]^T$ are chosen in the way that M_z/S_3 corresponds to the polarisation/magnetisation of the spatial components.

This result of independence of the choice of the direction of the polarisation/spin does not only apply to the skyrmion field but also the skyrmion number as well. Because the skyrmion number is the flux in the direction of the beam propagation, it is also independent of the basis of the polarisation/spin.

5.3 Skyrmion Field in specific examples

In this section, we will present and discuss the corresponding Skyrmion field of the examples introduced in Sec. 4.4.

5.3.1 Same focus

In this example structure, the skyrmion field is explicitly as following according to Eq. 5.19:

$$\begin{aligned}\Sigma_\rho &= \frac{-4\ell_d\ell_\Delta f^2}{\rho(1+f^2)^2}\frac{1}{R(z)};\\ \Sigma_\varphi &= \frac{-4\ell_\Delta f^2}{\rho(1+f^2)^2}\frac{1}{R(z)}\frac{z_R}{z};\\ \Sigma_z &= \frac{4f^2\ell_d}{\rho^2(1+f^2)^2}.\end{aligned} \tag{5.22}$$

This is plotted accordingly in Fig. 5.1, with $\ell_{u_0} = 0$, $\ell_{u_1} = 1$ and $\lambda = 0.5$, $w_0 = 1$.

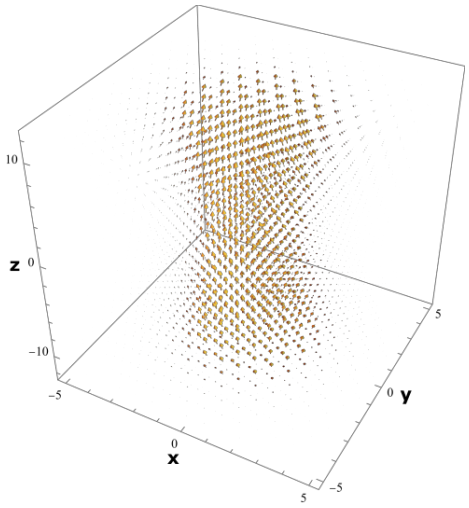

(a) The 3-D plot of the skyrmion field.

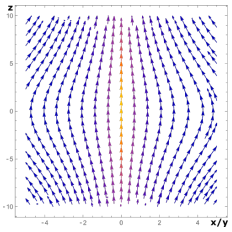

(b) The streamline plot of the skyrmion field in the $x-z$ or $y-z$ cross-section.

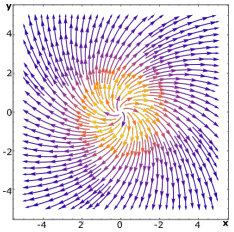

(c) The streamline plot of the skyrmion field in the xy cross-section at $z = -10$.

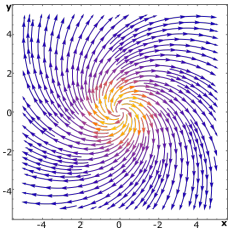

(d) The streamline plot of the skyrmion field in the xy cross-section at $z = -5$.

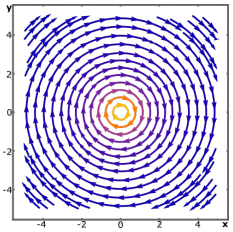

(e) The streamline plot of the skyrmion field in the xy cross-section at $z = 0$.

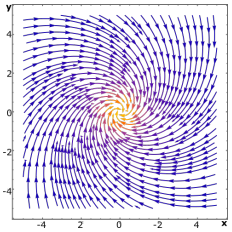

(f) The streamline plot of the skyrmion field in the xy cross-section at $z = 5$.

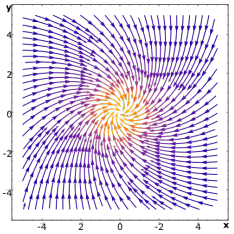

(g) The streamline plot of the skyrmion field in the xy cross-section at $z = 10$.

Figure 5.1 This is an illustration of the skyrmion field of the beam in Fig. 4.3. Here, the two spatial modes are Laguerre-Gaussian modes with $\ell_{u_0} = 0$ and $\ell_{u_1} = 1$ focusing at the same point, $z = 0$. For scale reference, $\lambda = 0.5, w_0 = 1$. The colour in the streamline plots denotes the strength of the magnitude of the relevant components in the plot, where the higher value corresponds to more orange colour.

Fig. 5.1a shows a 3D view of the skyrmion field, while the field stretches from ∞ and extends to $-\infty$, the plot depicts the area around the focal plane, namely $z = -10$ to $z = 10$. At every point in space the skyrmion field spirals in the same direction and tightens near the focal plane. This is further illustrated in the rest of the cross-section plots in Fig. 5.1b to Fig. 5.1g. The colour coding in these plots is according to the strength of the skyrmion field, where orange represents higher intensity whereas blue represents lower intensity, demonstrating that the field is concentrated in the centre of the beam and expands as it propagates away from the focal plane. Although in Fig. 5.1b the field lines seem to be expanding rather than tightening near the focal plane, this does not contradict the trend shown in Fig. 5.1a. Although the vectors are pointing away from the beam axis near the focal plane, the further away from the axis, the magnitude of vectors are considerably smaller. Fig. 5.1c to Fig. 5.1g tells an interesting story about how the field line propagates in space. If we trace one field line from $-\infty$, it is spiralling clockwise and outwards while propagating along the direction of the beam as shown in Fig. 5.1c and Fig. 5.1d. When it comes to the focal plane, the field line is still spiralling clockwise but forms a closed loop itself while still propagating along the direction of the beam as shown Fig. 5.1e. As soon as it passes the focal plane, it starts to spirally inwards to expand while keeping the clockwise rotation as shown in Fig. 5.1f and Fig. 5.1g. Therefore, Fig. 5.1 confirms that the skyrmion field has no sources nor sinks and spirals through space.

5.3.2 Different focus

In the example where the two spatial components are focused at different points introduced in Sec. 4.4.2, although there is a change in the skyrmion number in the propagation, this does not violate the conservation of the skyrmion field as we established in Eq. 5.4. Because according to the definition of the skyrmion number in Eq. 5.1, it is only the flux of the skyrmion field in the z direction rather than in a closed surface. The skyrmion field in this example can be expressed as:

$$
\begin{aligned}
\Sigma_\rho &= \frac{4\ell_d f^2}{\rho(1+f^2)^2}\Big(\frac{1}{R_{u_1}(z)}\Big(|\ell_{u_1}|+1-\frac{2\rho^2}{w_{u_1}^2(z)}\Big)-\frac{1}{R_{u_0}(z)}\Big(|\ell_{u_0}|+1-\frac{2\rho^2}{w_{u_0}^2(z)}\Big)\Big);\\
\Sigma_\varphi &= \frac{-4f^2}{\rho(1+f^2)^2}\Big(\frac{-1}{\rho}\Big(\ell_\Delta-2\rho^2\Big(\frac{1}{w_{u_1}^2(z)}-\frac{1}{w_{u_0}^2(z)}\Big)\Big)\\
&\quad\Big(\frac{\kappa\rho^2}{2}\Big(\frac{1}{R_{u_1}^2(z)}(1-(\frac{z_R}{z_{u_1}})^2)-\frac{1}{R_{u_0}^2(z)}(1-(\frac{z_R}{z_{u_0}})^2)\Big)+z_R\Big(\frac{|\ell_{u_1}|+1}{R_{u_1}z_{u_1}}-\frac{|\ell_{u_0}|+1}{R_{u_0}z_{u_0}}\Big)\Big)\\
&\quad+\Big(\frac{-1}{R_{u_1}(z)}\Big(|\ell_{u_1}|+1-\frac{2\rho^2}{w_{u_1}^2(z)}\Big)+\frac{1}{R_{u_0}(z)}\Big(|\ell_{u_0}|+1-\frac{2\rho^2}{w_{u_0}^2(z)}\Big)\Big)\kappa\rho\Big(\frac{1}{R_{u_1}(z)}-\frac{1}{R_{u_0}(z)}\Big)\Big);\\
\Sigma_z &= \frac{4f^2\ell_d}{\rho^2(1+f^2)^2}\left(\ell_\Delta-2\rho^2\left(\frac{1}{w_{u_1}^2(z)}-\frac{1}{w_{u_0}^2(z)}\right)\right),
\end{aligned}
\tag{5.23}
$$

and illustrated in Fig. 5.2, Fig. 5.3 and Fig. 5.5.

Fig. 5.2 shows 3D views of this skyrmion field where the first focal plane is at $z_0 = -10$; the crossover plane at $z_c = 0$; and the second focal plane at $z_1 = 10$. Because the width of the field varies much more than the same-focus example in Sec. 5.3.1, the field is plotted in four sections. Fig. 5.2a depicts the skyrmion field beyond the first focal plane to the region between the first focal plane and the crossover plane, namely, the region from $z < z_0$ to $z_0 < z < z_c$. In this

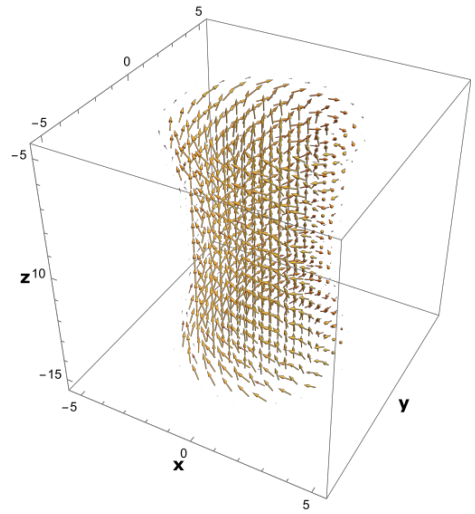

(a) Between $z < z_0$ and $z_0 < z < z_c$: The field is spiralling and propagting in the same direction as the beam travelling.

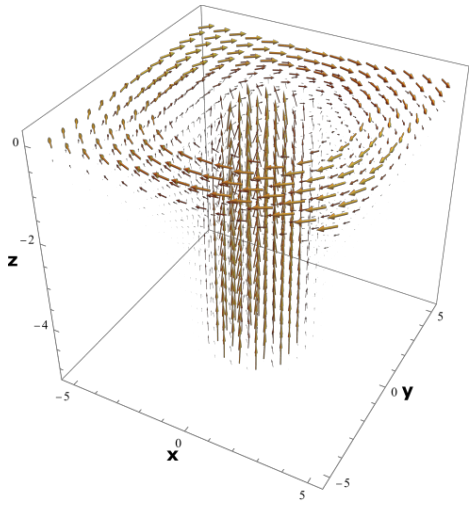

(b) Between $z_0 < z < z_c$ and $z = z_c$: The field lines are winding more in the xy plane except in the centre, until they are parallel to the xy plane at $z = z_c$ where the field lines escape to infinity. This is responsible for the change of the skyrmion number while keeping the skyrmion field conserved.

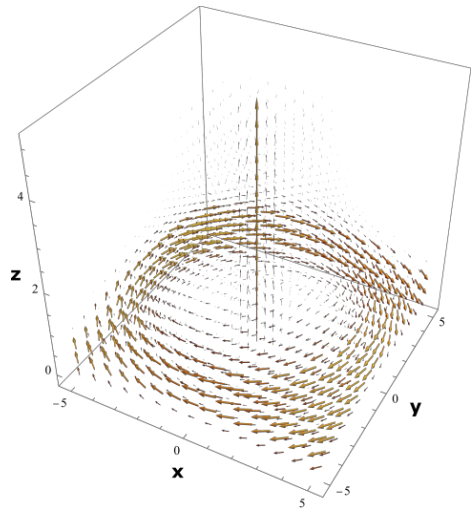

(c) Between $z = z_c$ and $z_c < z < z_1$: The skyrmion field lines are spiraling down from $z > z_c$ until they are parallel to the xy plane at $z = z_c$, except in the centre, where it is propagating in the same direction as the beam travelling. This explains the fact of $n = 0$ when $z > z_c$.

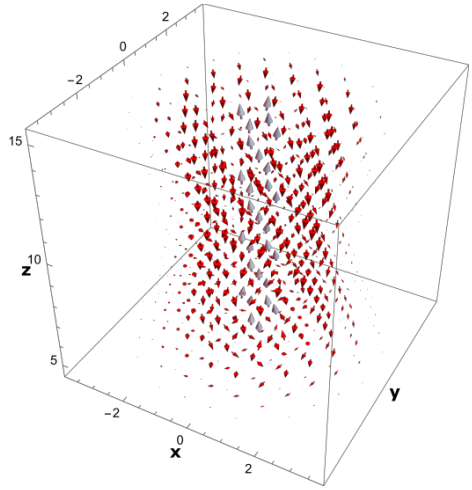

(d) Between $z_c < z < z_1$ and $z > z_1$: By colouring the field vectors with $\Sigma_z > 0$ blue and otherwise red, it is obvious the flux difference between the centre and the rest of the beam. This further demonstrates the fact of $n = 0$ when $z > z_c$.

Figure 5.2 This is an illustration of the skyrmion field line, in accordance to Fig. 4.4. This shows that the z-component of the skyrmion field line escapes to infinity at the cross-over point, which results in the change of the skyrmion number. Before the cross-over plane, as shown in (a) and (b), Σ_z is the same direction everywhere in the beam. However, as shown in (c), after the cross-over plane at the centre of the beam Σ_z is travelling in the opposite direction to everywhere else. This explains the change in the skyrmion number - the skyrmion field flux in the z direction.

region, the skyrmion field behaves very much like the one in the same focus example, where the field is spiraling along the beam propagation direction at every point in space and tightens at the

first focal plane $z = z_0$. The skyrmion field between the the first focal plane and the crossover plane is illustrated in Fig. 5.2b. From this region onward, the skyrmion field in this example start to demonstrate different features from the one in the same-focus example. The skyrmion field line still spirals along the beam propagation direction but escapes to infinity while retaining the rotation. This explains the sudden change of the skyrmion number despite the conservation of the skyrmion field: the skyrmion field line does not end, rather it forms a closed loop while expanding to ∞ in the transverse plane.

The next two subplots, Fig. 5.2c and Fig. 5.2d, demonstrate how the skyrmion number remains 0 while keeping the field lines intact. Fig. 5.2c illustrates the region between the crossover plane and the second focal plane where the skyrmion field line starts spiralling while travelling *against* the beam propagation direction except in the centre of the field. In the centre of the beam, the skyrmion field line is still travelling *along* the beam propagation direction. Therefore, the flux through a transverse plane in this region would be 0. However, due to the fact that the field is more concentrated in the centre and the crossover plane, when the sizes of the arrows are related to the field strength this contrast is not very obvious. This will be further illustrated in Fig. 5.2d. From this region to beyond the second focal plane, namely between $z_c < z < z_1$ and $z > z_1$, is depicted in Fig. 5.2d. If the field line has a positive z component, in other words, travelling along the beam propagating direction, it is coloured in blue, otherwise in red. This colour scheme is chosen to emphasize the feature we observed in the previous region, that the centre of the skyrmion field is travelling in a different direction from the rest of the field. To summarise, Fig. 5.2 explains how the skyrmion field remains conserved while the skyrmion number changes during propagation and therefore demonstrates that the skyrmion field has no sources nor sinks.

Fig. 5.3 is provided to further illustrate how the skyrmion field at the centre of beam behaves differently from the rest of the space. In Fig. 5.3a, the normalised density plot of Σ_z covers the same range as the 3D plot in Fig. 5.2a, namely, $z < z_c$. As shown in the plot, the z component of the field is positive everywhere. This is different in regions towards the second focal plane, i.e. $z_c < z$. This is demonstrated by the normalised density plot Fig. 5.3b, where the field at the centre of the beam is positive while being negative everywhere else (Note the change of the range of values of intensity which is now from -1 to 1). A non-normalised density plot of this region is also provided in Fig. 5.3c. Further to the feature shown previously, this subplot illustrates that the z component of the skyrmion field is concentrated at the centre of the beam, which is also demonstrated in Fig. 5.3d. Fig. 5.3d shows Σ_z value at $z = 0.5$, $y = 0$ across the x axis, where not only Σ_z is positive at the centre of the beam but it is considerable larger than anywhere else as well. The fact that the flux at this transverse plane (and any other transverse plane at $z > z_c$) is because the tail of Σ_z extends to $-\infty$ and ∞ due to the $e^{-2\rho^2}$ term (which is constrained within the ratio f) on the numerator in Eq. 5.23.

In addition to the graphical demonstration of the conservation of the skyrmion field despite a change in the skyrmion number, we also provide an analytical proof. If we draw a closed surface enclosing the crossover plane at $z = 0$ as shown in Fig. 5.4, the flux change can be calculated by combining the changes in the radial direction and the z direction due to the cylindrical symmetry of the beam. The flux change in the radial direction can be calculated from the radial component

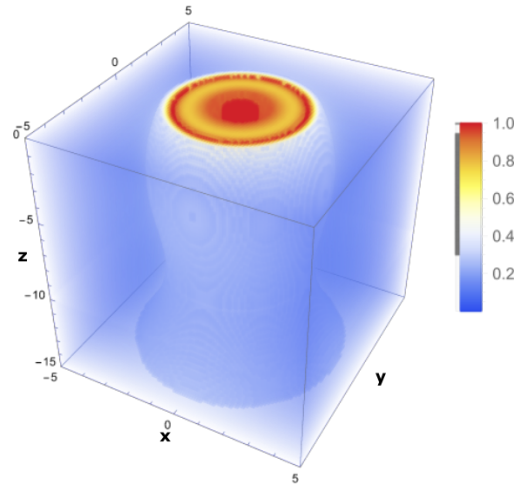

(a) Density plot of $\Sigma_z/|\boldsymbol{\Sigma}|$ from $z < z_0$ to $z = z_c$.

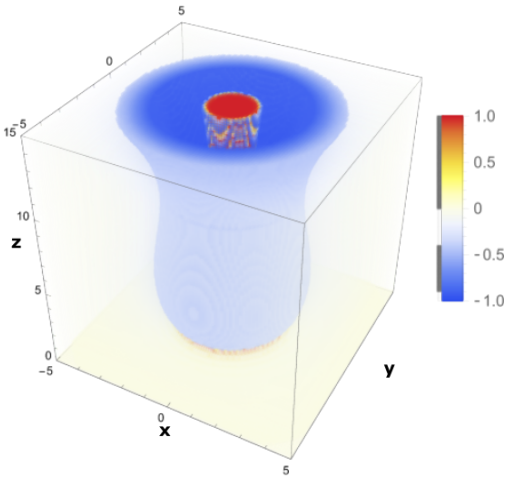

(b) Density plot of $\Sigma_z/|\boldsymbol{\Sigma}|$ from $z = z_c$ to $z > z_1$.

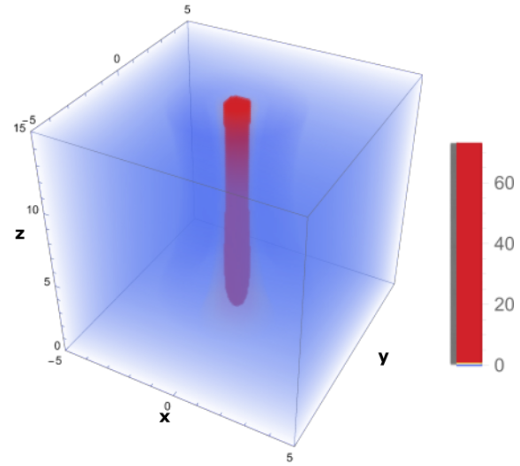

(c) Density plot of Σ_z from $z = z_c$ to $z > z_1$.

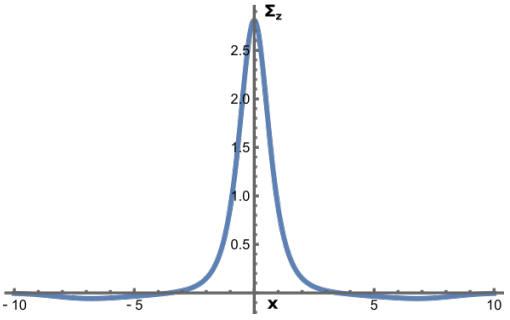

(d) Σ_z at $z = 0.5$, $y = 0$ between $-10 \leq x \leq 10$.

Figure 5.3 Density plots of Σ_z, in accordance to Fig.4.4. Before the cross-over plane, as shown in (a), $\Sigma_z/|\boldsymbol{\Sigma}|$ is positive, meaning that Σ_z is travelling in the same direction everywhere in the beam. However, as shown in (c), after the cross-over plane, at the centre of the beam $\Sigma_z/|\boldsymbol{\Sigma}|$ is positive while being negative everywhere else. This demonstrates that while skyrmion number changes when the skyrmion field changes its direction, the field itself remains conserved.

of the skyrmion field in Eq.5.11:

$$\frac{1}{4\pi}\int_0^\infty \Sigma_\rho dS_\rho = \ell_d\left(\frac{1}{1+|f(\infty,z)|^2} - \frac{1}{1+|f(\infty,-z)|^2}\right). \tag{5.24}$$

Because the ratio f at the centre ($\rho = 0$) is unchanged, $\frac{1}{1+|f(0,-z)|^2} = \frac{1}{1+|f(0,z)|^2}$. Therefore the change of flux (skyrmion number) in the z direction, according to Eq.4.14 is:

$$n(z) - n(-z) = -\ell_d\left(\frac{1}{1+|f(\infty,z)|^2} - \frac{1}{1+|f(\infty,-z)|^2}\right). \tag{5.25}$$

As specified by Eq.5.24 and Eq.5.25, we can see the total flux change:

$$\frac{1}{4\pi}\left(-\oint_{-z}\Sigma_z dS_z + \oint_z \Sigma_z dS_z + \int_{-z}^{z}\Sigma_\rho dS_\rho\right) = 0. \tag{5.26}$$

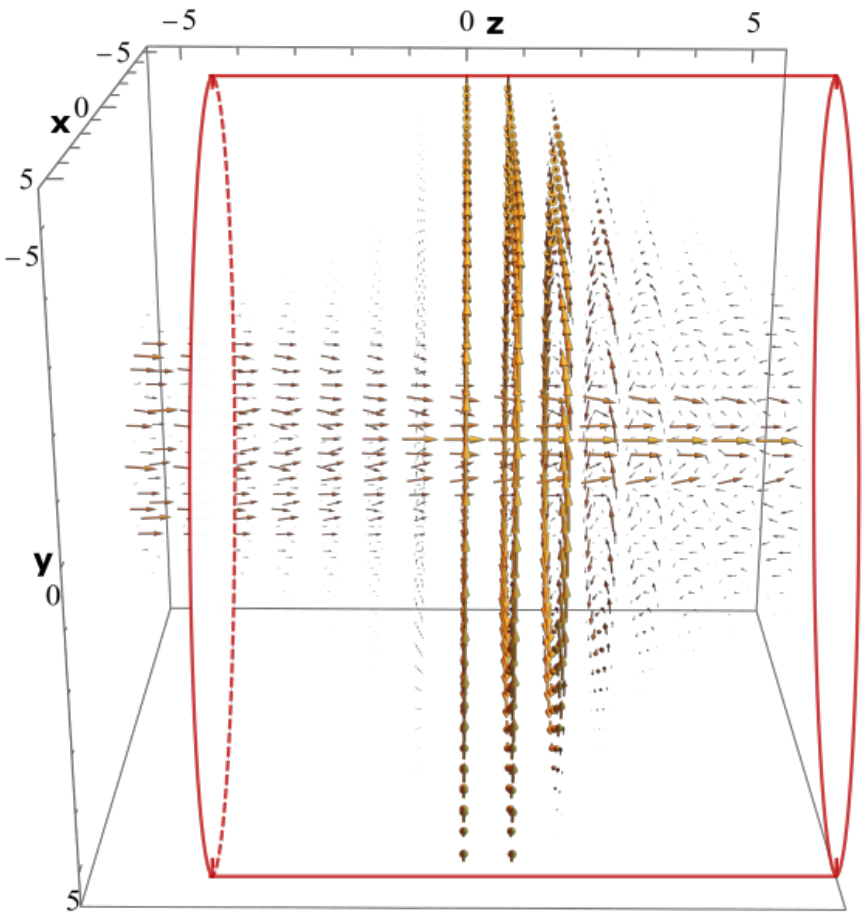

Figure 5.4 Schematic illustration of a cylindrical closed surface enclosing the cross-over plane to calculate the total skyrmion field flux change. In the actual calculation, the radius of the cylinder should be ∞. This shows the flux changes in both **z** and **rho** direction, explaining the net 0 flux change.

Therefore we proved the skyrmion field is conserved when the two spatial components have different focus and the skyrmion number has changed in propagation.

Another way to interpret a conserved field is that there is no breaks or joints of field lines. This feature is illustrated in Fig. 5.5, where we provide stream plots of the skyrmion field in six cross sections.

The colour scheme in Fig. 5.5a corresponds to the skyrmion field strength in the xz or the yz direction, namely, either $|\Sigma_x\hat{x} + \Sigma_z\hat{z}|$ or $\Sigma_y\hat{y}| + \Sigma_z\hat{z}|$. In Fig. 5.5b to Fig. 5.5f, the colour scheme denotes the strength of the transverse component of the skyrmion field, i.e. $|\Sigma_\rho\hat{\rho} + \Sigma_\varphi\hat{\phi}|$. The colour orange corresponds to higher strength of the skyrmion field, whereas the colour blue corresponds to lower strength.

In Fig. 5.5a, which demonstrates the cross-section of the skyrmion field in xz or yz plane, we can observe that the field lines are propagating in the same direction until the crossover plane, z_c, where a portion of the field lines escape to the infinity in the $\hat{\rho}$ direction. After z_c, except for the field line in the centre, field lines elsewhere is travelling opposite to the beam propagating direction. Another important observation is that the field strength in the centre of the beam at $z > z_c$ is considerable larger than other places, making it possible to maintain a net flux of 0.

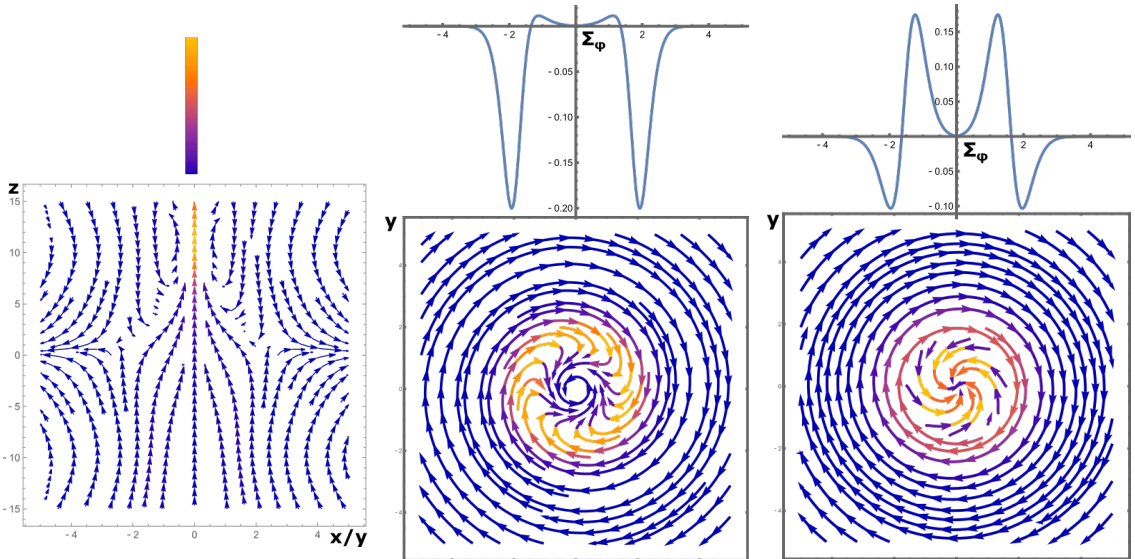

(a) The xz and yz Cross-section from $z < z_0$ to $z > z_1$.

(b) The xy Cross-section at $z < z_0$.

(c) The xy Cross-section at $z_0 < z < z_c$.

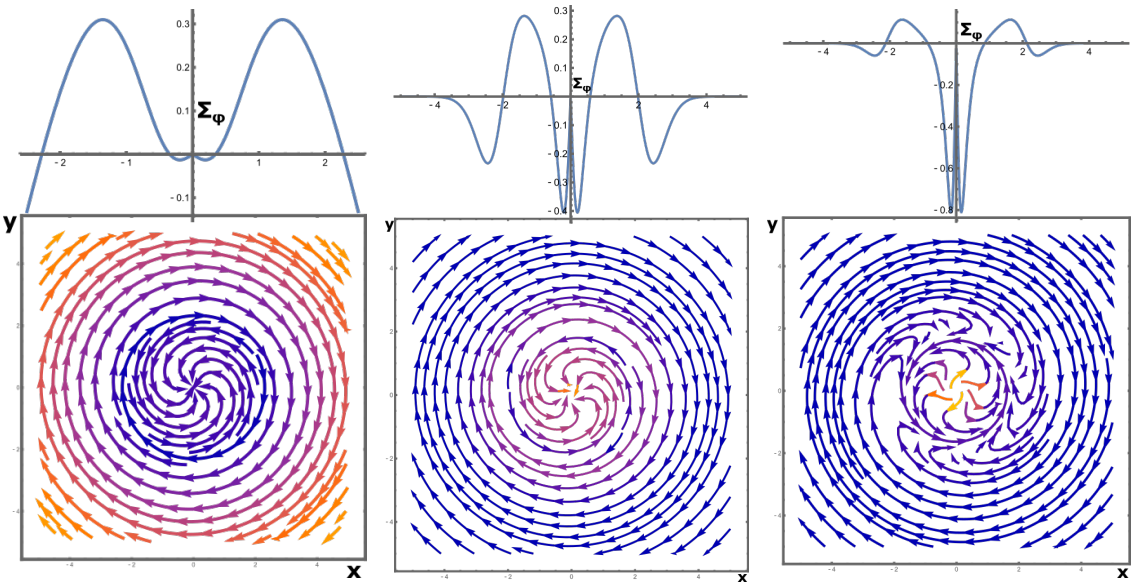

(d) The xy Cross-section at $z = z_c$.

(e) The xy Cross-section at $z_c < z < z_1$.

(f) The xy Cross-section at $z_1 < z$.

Figure 5.5 Cross-sections of skyrmion field lines, and their corresponding Σ_φ value across $x = 0$, in accordance to Fig. 4.4, demonstrating that skyrmion field lines have no sources nor sinks.

In Fig. 5.5b to Fig. 5.5f, we illustrated the cross section of the skyrmion field in the xy direction with the Σ_φ across $x = 0$ at $z < z_0$, $z_0 < z < z_c$, $z = z_c$, $z_c < z < z_1$ and $z > z_1$ respectively. At $z < z_c$, shown in Fig. 5.5b and Fig. 5.5c, the field line is rotating anti-clockwise at the centre of the beam, corresponding to the positive Σ_φ. As it expands the field lines start to rotate clockwise, corresponding to the negative Σ_φ. At $z = z_c$ (Fig. 5.5d), the field line rotates in the clockwise direction at the centre of the beam and as it expands, the field lines start to rotate in the anti-clockwise direction before changing back to clockwise rotation. At $z > z_c$, shown in Fig. 5.5e and Fig. 5.5f, the field line is rotating clockwise at the centre of the beam, corresponding to the

negative Σ_φ. Further from the centre, the field lines start to rotate anti-clockwise before changing back to clockwise again. Except for the cross-section plane, at any other transverse planes, as the field expands further to infinity, the rotation tends to zero.

A field line therefore can be visualised as a line spiraling up, then while it is still propagating upwards, it spirals in the opposite direction and circulates tending to the centre of the beam. Therefore, it does not break nor join itself during the whole process.

One thing to note is that at the centre of the beam $\Sigma_\varphi = 0$, regardless where the transverse plane is. Except the crossover plane, all the other transverse planes show that the centre of the beam is much stronger than elsewhere in the beam. At the crossover plane, however, the centre of the beam is the weakest. This verifies our previous observation that the field lines escape to infinity in the $\hat{\rho}$ direction at the crossover plane, explaining the change in skyrmion number.

5.4 Conclusion

In this chapter, we introduced the skyrmion field for skyrmionic beams. We demonstrated that the skyrmion field is a conserved field which means that there are no sources nor sinks in skyrmionic beams. We have also proved that the skyrmion field is independent of the global orientation of the effective magnetisation $\mathbf{M}$. We have also obtained a simple form of the skyrmion field that only depends on the complex ratio μ between the two spatial components. From this, we are able to demonstrate that the skyrmion field does not depend on the direction of the polarisation coupled with the spatial components.

We have also included two specific examples in this chapter. In the first example, the beam is comprised of two *LG* beams with different winding number ℓ sharing the same beam width, wavelength and focal plane as the spatial components. And in the second example the two spatial components have different foci, while still sharing the same beam width and wavelength. For each example we have demonstrated the skyrmion field lines in a 3D model, and on different cross-sections. Using these graphic illustrations and the analytical expression of the skyrmion field in each example, we are able to explain how the changes in skyrmion numbers do not contradict the conservation of the skyrmion field.

It is important to note that this skyrmionic property of structured beams is different from other properties we are more familiar with, such as the spin and angular momentum [34, 31, 118]. Although skyrmionic beams also require that both the vortex structure and the polarisation exist in a beam, the skyrmionic structure is a topological rather than mechanical structure. For example, because the skyrmion field is independent of the polarisation direction, the skyrmion number would remain the same if we apply reflection or phase retardation to the constituent beams. On the other hand, in the second example where the skyrmion number has changed, the total spin and angular momentum passing through each transverse plane remains unchanged.

However, despite all the interesting properties, many of the characteristic features of the skyrmion field introduced in this chapter happen in the region with low light intensity. This poses further challenge to experimental observation. Therefore, in the next chapter, we will introduce another vector field, the skyrmion vector potential field, in the hope to shine more light onto the nature of skyrmionic beams and providing another tool in experiments to examine skyrmionic

beams.

Chapter 6

Vector potential field in Skyrmionic beams

We will introduce another vector field: the skyrmion vector potential field in this chapter. This has three motivations. The first being that it could serve as an alternative tool to the skyrmion field to experimentally examine the skyrmion structure. As mentioned in Chapter. 5, the skyrmion field includes the cross product of two derivatives of the effective magnetisation **M** which requires accurate measurement at regions with low light. This will pose great challenges in experimental measurement. Therefore, we are motivated to find an alternative method to examine the skyrmion structure in experiments. The second reason is the analogous properties between the skyrmion structure and the superfluid. As introduced in Section. 3.6, the winding number of superfluid is similar to the skyrmion number. By introducing the skyrmion vector potential field, we will be able to explore the analogy between skyrmionic beams and superfluid even further. Last but not least, it is mathematically interesting to explore the fact that the skyrmion field is a divergenceless field. This is analogous to the magnetic vector potential field **A** of the magnetic field **B** in classical electromagnetic theory. The material in this chapter are produced by the author and partly published in [1] while the rest will be included in future publications that are currently under preparation.

6.1 Skyrmion vector potential field in general

As a divergenceless field, the Skyrmion field can be written as a curl of another vector field $\mathbf{v}_0$:

$$\nabla \times \mathbf{v}_0 = \mathbf{\Sigma}. \tag{6.1}$$

By inputting the general form of the skyrmion field defined as in Eq. 5.2 into this expression, we have:

$$(\nabla \times \mathbf{v})_i = \mathbf{\Sigma}_i = \frac{1}{2}\varepsilon_{ijk}\varepsilon_{pqr}M_p(\partial_j M_q \partial_k M_r). \tag{6.2}$$

Surprisingly, we find that this is in a similar form to the so-called 'Mermin-Ho' relation in the theory of superfluid ^{3}He [110]:

$$(\nabla \times \mathbf{v}_{sf})_i = \frac{\hbar}{4m}\varepsilon_{ijk}\hat{\mathbf{l}} \cdot (\partial_j \hat{\mathbf{l}} \times \partial_k \hat{\mathbf{l}}), \tag{6.3}$$

where $\hat{\mathbf{l}}$ is a unit vector in orbital space representing the orientation of the order parameter, with $\mathbf{v_{sf}}$ and $\nabla \times \mathbf{v_{sf}}$ representing the velocity and the vorticity of the superfluid respectively. In the 'Mermin-Ho' relation, it also provides the definition of $\mathbf{v_{sf}}$:

$$(v_{sf})_i = \frac{\hbar}{2m}\hat{\mathbf{m}}_s \cdot \partial_i \hat{\mathbf{n}}_s, \tag{6.4}$$

where $\hat{\mathbf{m}}_s$ and $\hat{\mathbf{n}}_s$ are also unit vectors and there exists the restriction:

$$\hat{\mathbf{m}}_s \times \hat{\mathbf{n}}_s = \hat{\mathbf{l}}. \tag{6.5}$$

This does not determine $\mathbf{m}$ and $\mathbf{n}$ and hence there is some freedom in the way we choose $\mathbf{v}_{sf}$. This is analogous to the gauge freedom in choosing the magnetic vector potential $\mathbf{A}$ in electromagnetism. In order to understand the meaning of gauge transformation on the skyrmion vector potential, we can perform the following analysis. Based on the orthogonality of $\hat{\mathbf{m}}_s$ and $\hat{\mathbf{n}}_s$ ($\hat{\mathbf{m}}_s \cdot \hat{\mathbf{n}}_s = 0$), Eq. 6.4 can be written as:

$$\begin{aligned}(v_{sf})_i &= \frac{\hbar}{2m}\hat{\mathbf{m}}_s \cdot \partial_i \hat{\mathbf{n}}_s \\ &= -\frac{\hbar}{2m}\hat{\mathbf{n}}_s \cdot \partial_i \hat{\mathbf{m}}_s \\ &= \frac{\hbar}{2m}\Im\left(\frac{1}{2}\left(\hat{\mathbf{m}}_s - i\hat{\mathbf{n}}_s\right)\cdot\partial_i\left(\hat{\mathbf{m}}_s + i\hat{\mathbf{n}}_s\right)\right).\end{aligned} \tag{6.6}$$

As we introduced earlier in Section. 3.6 of Chapter. 3 that $\hat{\mathbf{m}}_s$, $\hat{\mathbf{n}}_s$ and $\hat{\mathbf{l}}$ from a set of orthogonal triad, we can define a 2-D rotation $e^{i\chi(\mathbf{r})}$ on this set of axes around $\hat{\mathbf{l}}$:

$$\begin{aligned}\left(\hat{\mathbf{m}}_s + i\hat{\mathbf{n}}_s\right) &\rightarrow e^{i\chi}\left(\hat{\mathbf{m}}_s + i\hat{\mathbf{n}}_s\right) \\ \left(\hat{\mathbf{m}}_s - i\hat{\mathbf{n}}_s\right) &\rightarrow e^{-i\chi}\left(\hat{\mathbf{m}}_s - i\hat{\mathbf{n}}_s\right).\end{aligned} \tag{6.7}$$

After the rotation, the $\mathbf{v_{sf}}$ field becomes:

$$\begin{aligned}(v'_{sf})_i &= \frac{\hbar}{2m}\Im\left(\frac{1}{2}\left(\hat{\mathbf{m}}_s - i\hat{\mathbf{n}}_s\right)e^{-i\chi(\mathbf{r})}\cdot\partial_i\left(e^{i\chi(\mathbf{r})}\left(\hat{\mathbf{m}}_s + i\hat{\mathbf{n}}_s\right)\right)\right) \\ &= \frac{\hbar}{2m}\Im\left(\frac{1}{2}\left(\hat{\mathbf{m}}_s - i\hat{\mathbf{n}}_s\right)\cdot\partial_i\left(\hat{\mathbf{m}}_s + i\hat{\mathbf{n}}_s\right)\right) + \Im\left(\frac{1}{2}\left(\hat{\mathbf{m}}_s - i\hat{\mathbf{n}}_s\right)\cdot\partial_i\left(\hat{\mathbf{m}}_s + i\hat{\mathbf{n}}_s\right)i\chi(\mathbf{r})\right) \\ &= \frac{\hbar}{2m}\hat{\mathbf{m}}_s \cdot \partial_i \hat{\mathbf{n}}_s + \partial_i\chi(\mathbf{r})_i.\end{aligned} \tag{6.8}$$

Because $\nabla \times (\nabla\chi(\mathbf{r})) = 0$, we have proved that applying a rotation to $\hat{\mathbf{m}}_s$ and $\hat{\mathbf{m}}_s$ is a gauge transformation on the skyrmion vector potential field.

If we compare our $\mathbf{M}$ (Eq. 4.1) to vector $\hat{\mathbf{l}}$, we can obtain the corresponding vector $\hat{\mathbf{m}}_s$ and vector $\hat{\mathbf{n}}_s$. One obvious approach is defining those three vectors as:

$$\hat{\mathbf{l}} = \begin{bmatrix}M_x \\ M_y \\ M_z\end{bmatrix}; \hat{\mathbf{m}}_s = \frac{1}{\sqrt{M_x^2 + M_y^2}}\begin{bmatrix}M_y \\ -M_x \\ 0\end{bmatrix}; \hat{\mathbf{n}}_s = \frac{1}{\sqrt{M_x^2 + M_y^2}}\begin{bmatrix}-M_z M_x \\ -M_z M_y \\ M_x^2 + M_y^2\end{bmatrix} \tag{6.9}$$

Inserting this result into the definition for the superfluid velocity $\mathbf{v_{sf}}$ in Eq. 6.4, we arrive at the

equivalent of the $\mathbf{v_{sf}}$ for our skyrmion field, which we use $\mathbf{v}$ to represent:

$$(\mathbf{v})_i = \frac{M_z}{(M_x^2 + M_y^2)}(M_y \partial_i M_x - M_x \partial_i M_y). \tag{6.10}$$

Because $\mathbf{M}$ is a unit vector, the normalisation factor $1/(M_x^2+M_y^2)$ can also be written as $1/(1-M_z^2)$. Combining this result, the 'Mermin-Ho' relation Eq. 6.3, Eq. 6.4 and our requirement to write the skyrmion field Eq. 6.2 as a curl, we finally achieve the answer:

$$(\mathbf{v})_i = \frac{M_z}{1 - M_z^2}(M_y \partial_i M_x - M_x \partial_i M_y). \tag{6.11}$$

Because the curl of the newly found vector field $\mathbf{v}$ is the skyrmion field $\mathbf{\Sigma}$, and based on the Stokes' theorem, we can draw the following conclusion:

$$\oint_{\mathcal{L}} \mathbf{v} \cdot d\mathbf{l} = \int_S \mathbf{\Sigma} \cdot d\mathbf{S}, \tag{6.12}$$

where $\mathcal{L}$ is the simple closed curve around a surface $\mathbf{S}$. If we choose $\mathbf{S}$ to be in the $\mathbf{z}$ direction, then according to Eq. 6.12, we find an alternative way to calculate the skyrmion number using the line integral of the $\mathbf{v}$ field. There is one caveat however, that vector field $\mathbf{v}$ is defined and continuous on surface $\mathbf{S}$. As shown in Eq. 6.10, there are two scenarios in which such singularities might exist. The first being the denominator $(M_x^2 + M_y^2)$ is 0, and that the derivatives are not approaching 0 in the same rate. This indicates that M_x and M_y components are rapidly changing as they approaches 0. The second which is the more important scenario being that the derivatives are not well-defined at certain points on the surface. To demonstrate this is a general concern, we provide the explicit form of the ϕ component of the $\mathbf{v}$ field in cylindrical coordinates:

$$\mathbf{v}_\varphi = \frac{M_z}{(M_x^2 + M_y^2)\,\rho}\frac{1}{\rho}(M_y \frac{\partial}{\partial \varphi} M_x - M_x \frac{\partial}{\partial \varphi} M_y). \tag{6.13}$$

If the terms in the bracket do not possess an explicit ρ term, there would exist a singularity at the centre of the surface where $\rho = 0$. It is worth noting that if such singularity exists, this is not a coordinate singularity, but rather, a physical one. In other words, the singularity would always exist, regardless of how the coordinates are shifted.

This issue of singularities can be solved by defining the boundary $\mathcal{L}$ as a connected sum of countable-many Jordan curves that loop around such singularities [119] as shown in Fig. 6.1. If we choose those loops carefully as boundaries of all the singularities in the cross-section in $\mathbf{\Sigma}_z$ direction, skyrmion numbers can be evaluated by line integrals of the $\mathbf{v}$ field through:

$$n = \frac{1}{4\pi}\left(\oint_{\mathcal{L}_S} \mathbf{v} \cdot d\mathbf{l} - \sum \oint_{\mathcal{L}_i} \mathbf{v} \cdot d\mathbf{l}\right), \tag{6.14}$$

where $\mathcal{L}_S$ and $\mathcal{L}_i$ denote the boundary around the cross-section in the direction of $\mathbf{\Sigma}_z$ and the singularities respectively. Despite the theoretical interest in constructing this vector field, it is also practically useful for obtaining skyrmion number in two situations: a) when there are any singularities in the skyrmion field $\mathbf{\Sigma}$ on surface S, b) in skyrmion related experiments. As we have discussed above, according to Eq. 5.1, skyrmion number is calculated through the surface integral

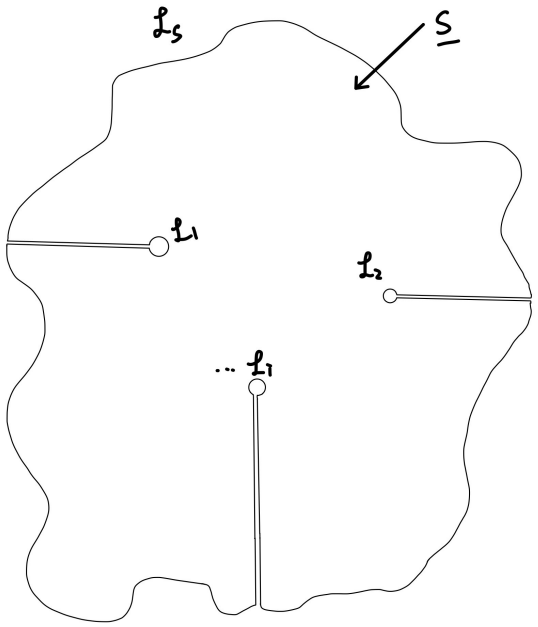

Figure 6.1 Visualisation of applying Stoke's theorem of $\mathbf{v}$ on $\mathbf{S}$ which is a smooth oriented surface with boundary $\mathcal{L}_S$. $\mathcal{L}_i$ represent a series of countable number of singularities.

of the cross-section of the beam, inevitably relying on the low intensity area, such as the centre and the edge of a beam. Experimentally obtaining local spin/polarisation direction in low intensity areas requires high precision measurements, and even higher precision is required for obtaining first-order derivatives with certainty. Using the Skyrmion field as shown in Eq. 5.1 requires cross products of two first-order derivatives, whereas using the vector potential for skyrmion field as demonstrated by Eq. 6.14 only requires one first-order derivatives. Switching to a line integral of vector potential for skyrmion fields can therefore potentially reduce uncertainty from experiments.

Another way in that skyrmionic beams are analogous to superfluid lies in the similarity between the circulation and the skyrmion number. In the superfluid theory 'circulation' κ is defined as the line integral of its velocity along every closed path '$\mathcal{L}$' in the liquid [64]:

$$\kappa = \oint_{\mathcal{L}} \mathbf{v_{sf}} \cdot d\mathbf{l}. \tag{6.15}$$

For isotropic superfluid such as ^{4}He and ^{3}He B phase (^{3}He-B), circulation is quantized and can be written as:

$$\kappa = N\kappa_0, \tag{6.16}$$

where N is a non-zero integer for multiply connected containers and $\kappa_0 = h/2m$ is the quantum of circulation [64]. As for the anisotropic superfluid such as ^{3}He A phase (^{3}He-A), in general the circulation is no longer quantized except at the wall of the container. From Eq. 6.14, the skyrmion number is very similar to the circulation of anistropic superfluid, if we consider the boundary of the beam and its associated singularities as the 'walls' of the container. The parallels in this analogy between superfluids and skyrmion beams will be summaries in Table 6.1 in Section. 4.2.

6.2 Skyrmion vector potential field in paraxial skyrmionic beams

For paraxial beams, their corresponding vector potential for skyrmion field can be expressed as using Eq. 4.5

$$\mathbf{v} = -M_z \nabla \Phi, \tag{6.17}$$

where Φ is defined in Eq. 4.5 as the phase of the ratio between the two spatial components. Adopting the cylindrical coordinate due to the symmetry of paraxial beams, in calculating skyrmion number Eq. 6.12, v_φ is the only component not perpendicular to either the cross-section of the beam or its boundary. Eq. 6.17 shows that for skyrmion beams with a well-defined phase number ℓ_d, there exists only one singularity which is at $\rho = 0$. Therefore, skyrmion number for paraxial skyrmionic beams can be generalised as:

$$n = \frac{1}{4\pi}\left(\lim_{\rho\to\infty}\oint_{\mathcal{L}} \mathbf{v}\cdot d\mathbf{l} - \lim_{\rho\to 0}\oint_{\mathcal{L}} \mathbf{v}\cdot d\mathbf{l}\right), \tag{6.18}$$

from which we can recover Eq. 4.14.

In general, for a circular contour in the xy plane centred on the z axis, the analogous circulation would be:

$$\oint_{\mathcal{L}} \mathbf{v}\cdot d\mathbf{l} = -2\pi\ell_d M_z(\rho_{\mathcal{L}}, z_{\mathcal{L}}), \tag{6.19}$$

which is not necessarily an integer. This is similar to the circulation in anisotropic superfluid, which is [120, 121]:

$$\kappa = \oint_{\mathcal{L}} \mathbf{v}_{sf}\cdot d\mathbf{l} = \frac{\hbar}{2m}\left(S(\hat{\mathbf{l}}) + 4\pi n\right), \tag{6.20}$$

where $S(\hat{\mathbf{l}})$ is an area on the unit sphere ranging between $[0, 4\pi]$ and n is an integer. n depends on the mapping relation between $\hat{\mathbf{l}}(\mathbf{r})$ and its corresponding points on $\mathcal{L}(\hat{\mathbf{l}})$: if it is a one-one mapping, $n = 0$; otherwise, n corresponds to the extra times of wrapping around $\mathcal{L}(\hat{\mathbf{l}})$ [120].

$S(\hat{\mathbf{l}})$ can be visualised in Fig. 6.2. as we traverse the closed contour $\mathcal{L}(\hat{\mathbf{l}})$, it can be mapped as a closed curve $\mathbf{L}(\hat{\mathbf{l}})$ on a unit sphere by recording the orientation of vector $\hat{\mathbf{l}}$. Since $L(\hat{\mathbf{l}})$ has a direction, $S(\hat{\mathbf{l}})$ refers to the surface area of the unit sphere to its left. Therefore, for an anisotropic superfluid, quantized circulation only exists when $\hat{\mathbf{l}}$ has a fixed direction, i.e. at the surface of its container. This means $\hat{\mathbf{l}}$ maps to a polar point on the unit sphere and $L(\hat{\mathbf{l}})$ shrinks to that point as well. From our previous discussion, similar to $\hat{\mathbf{l}}$, $\mathbf{M}$ can also represent a point on a unit sphere. As shown in Fig. 6.2, for each M_z, we can associate a spherical cap with it. The surface area of a spherical cap is $2\pi(1-\cos\chi)$, which according to Eq. 4.15 can be rewritten into $2\pi(1-M_z)$. This allows us to adapt Eq. 6.19 as:

$$\oint_{\mathcal{L}} \mathbf{v}\cdot d\mathbf{l} = \ell_d\left(S(\mathbf{M}) - 2\pi\right) = n\left(S(\mathbf{M}) - 2\pi\right), \tag{6.21}$$

where $S(\mathbf{M})$ denotes the area of the spherical cap created by $\mathbf{M}$. The similarities and differences between superfluid velocity $\mathbf{v}$ and vector potential for skyrmionic beams are summarized in Table. 6.1.

In Table. 6.1, $-\phi$, β and α are Euler angles used to describe the orientation of the orbital triad $(\hat{\mathbf{m}}_s, \hat{\mathbf{n}}_s, \hat{\mathbf{l}})$ of the order parameter of anisotropic superfluid relative to some fixed coordinate

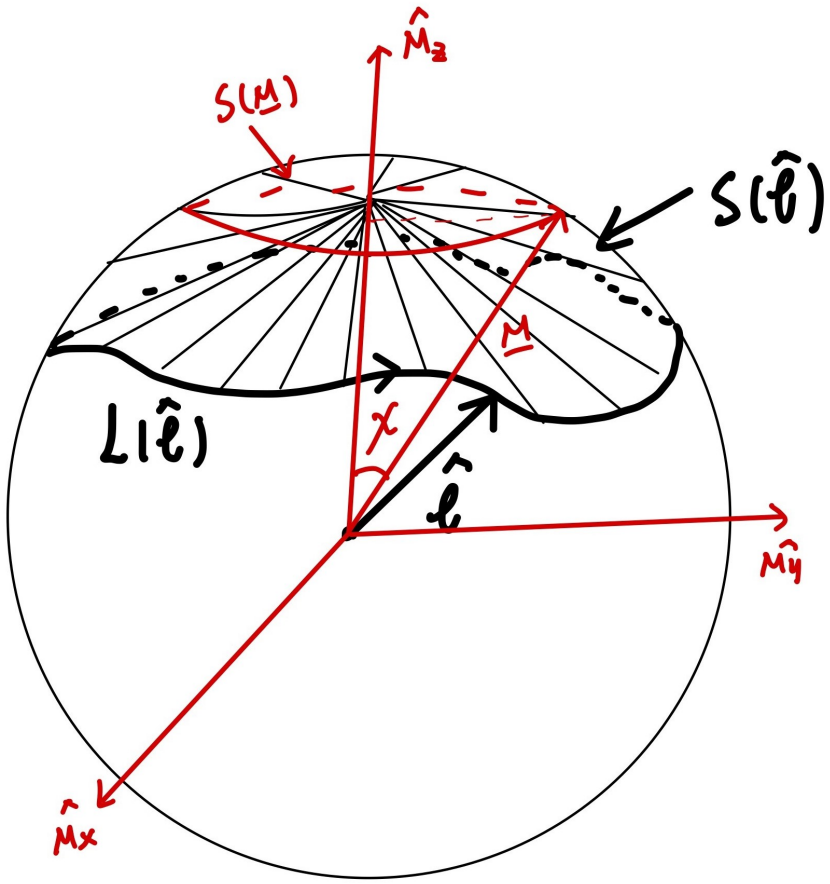

Figure 6.2 This graph is a visualisation of $S(\hat{\mathbf{l}})$ on a unit sphere, recording the mapping of the orientation $\hat{\mathbf{l}}$ of the order parameter on a closed contour in an anisotropic superfluid.

system $(\hat{\mathbf{x}}, \hat{\mathbf{y}}, \hat{\mathbf{z}})$. ϕ is also referred to as the phase of the order parameter. $0 \leq S(\hat{\mathbf{l}}) \leq 4\pi$ is an area on the unit sphere, which would take the boundary value at the 'walls' of the container, leading anisotropic superfluid possessing an integer circulation. κ is the circulation of the superfluid and κ_0 denotes the 'quantum of circulation' [64]. Although we have provided 4π as the equivalent of κ_0 in skyrmionic beams, it is merely an analogy. $\mathbf{M}$ is the local magnetisation/polarisation of the skyrmionic beams and $\mathbf{\Sigma}$ denotes the corresponding skyrmion field. Φ represents the phase of the ratio between the two spatial components in the paraxial beams of interest. $\mathcal{L}_S$ and $\mathcal{L}_i$ are the boundaries of the beam and any singularities exist within the beam respectively. $S(\mathbf{M})$ denotes the area of the spherical cap created by $\mathbf{M}$ on a unit sphere. Both n and N are integers, representing the skyrmion number and the number of circulation in superfluid respectively.

We have demonstrated that there is a line along which $\mathbf{v}$ is ill-defined or singular as shown in Eq. 6.11. This is a reminiscent of Dirac strings. We recall that in his seminal paper on magnetic monopoles [113], Dirac showed that the existence of a monopole was necessarily accompanied by a line connected to the monopole along which the vector potential, $\mathbf{A}$, was singular. Such string extend out to infinity unless connected to a second monopole. As introduced in Section. 3.6 of Chapter. 3, there also exists a vortex line with an inseparable single vortex in ^{3}He. This vortex line is also analogous to a Dirac string. In the theory of paraxial skyrmionic beams introduced in this thesis, however, there is no analogous to the monopole and it follows, necessarily, that the line or

Table 6.1 Comparison between superfluid velocity and the vector potential of the skyrmion field. $-\phi$, β and α are Euler angles used to describe the orientation of the orbital triad $(\hat{\mathbf{m}}_s, \hat{\mathbf{n}}_s, \hat{\mathbf{l}})$ of the order parameter of anisotropic superfluid relative to some fixed coordinate system $(\hat{\mathbf{x}}, \hat{\mathbf{y}}, \hat{\mathbf{z}})$. ϕ is also referred to as the phase of the order parameter. $0 \leq S(\hat{\mathbf{l}}) \leq 4\pi$ is an area on the unit sphere, which would take the boundary value at the 'walls' of the container, leading anisotropic superfluid possessing an integer circulation. κ is the circulation of the superfluid and κ_0 denotes the 'quantum of circulation' [64]. $\mathbf{M}$ is the effective magnetisation field, or Stokes parameters for paraxial skyrmionic beams. Φ is the phase component of the ration between the two spatial components in skyrmionic beams.

	Superfluid		Skyrmionic beams	
	Anisotropic	Isotropic	General	Paraxial Beams
$\mathbf{v}$	$\frac{\hbar}{2m}(\nabla\phi - \cos\beta\nabla\alpha)$	$\frac{\hbar}{2m}\nabla\phi$	$\frac{M_z}{1-M_z^2}(M_y\nabla M_x - M_x\nabla M_y)$	$-M_z\nabla\Phi$
$(\nabla\times\mathbf{v})_i$	$\frac{\hbar}{4m}\varepsilon_{ijk}\hat{\mathbf{l}}\cdot(\partial_j\hat{\mathbf{l}}\times\partial_k\hat{\mathbf{l}})$	0	$(\mathbf{\Sigma})_i = \frac{1}{2}\varepsilon_{ijk}\mathbf{M}\cdot(\partial_j\mathbf{M}\times\partial_k\mathbf{M})$	
$\oint_{\mathcal{L}}\mathbf{v}\cdot d\mathbf{l}$	κ		$\oint_{\mathcal{L}_S}\mathbf{v}\cdot d\mathbf{l} - \sum\oint_{\mathcal{L}_i}\mathbf{v}\cdot d\mathbf{l} = 4\pi n$	$2\pi\ell_d\mathbf{M}_z = n(S(\mathbf{M}) - 2\pi)$
	$\frac{\hbar}{2m}\left(S(\hat{\mathbf{l}}) + 4\pi n\right)$	$N\kappa_0$		
κ_0	$\frac{h}{2m}$		4π	

string along which $\mathbf{v}$ is singular extends to infinity in both directions.

6.3 Skyrmion vector potential field in specific examples

In this section, we will present and discuss the corresponding skyrmion vector potential field of the examples presented in Section. 4.4.

6.3.1 Same focus

We now consider the vector potential $\mathbf{v}$ field of the skyrmion field for the example where the two spatial components are focused at the same point introduced in Section. 4.4.1. According to Eq. 6.17, the $\mathbf{v}$ field is explicitly:

$$\begin{aligned} v_\rho &= 0; \\ v_\varphi &= \left(1 - \frac{2}{1+f^2}\right)\frac{\ell_d}{\rho}; \\ v_z &= \left(1 - \frac{2}{1+f^2}\right)\frac{\ell_{\Delta z_R}}{z_R^2 + z^2}. \end{aligned} \tag{6.22}$$

This is plotted accordingly in Fig. 6.3, with $\ell_{u_0} = 0$, $\ell_{u_1} = 1$. Fig. 6.3a shows a 3D view of the the vector potential field, the $\mathbf{v}$ field. While the field stretches from ∞ and extends to $-\infty$, the plot depicts the area around the focal point, namely -10 to 10. At every point in space it spirals in the same direction and expands near the focal point. This is further illustrated in the rest of the cross-section plots in Fig. 6.3b to Fig. 6.3c. The colour scheme in Fig. 6.3a and Fig. 6.3b are according to the intensity of the field, where orange represents higher intensity whereas blue

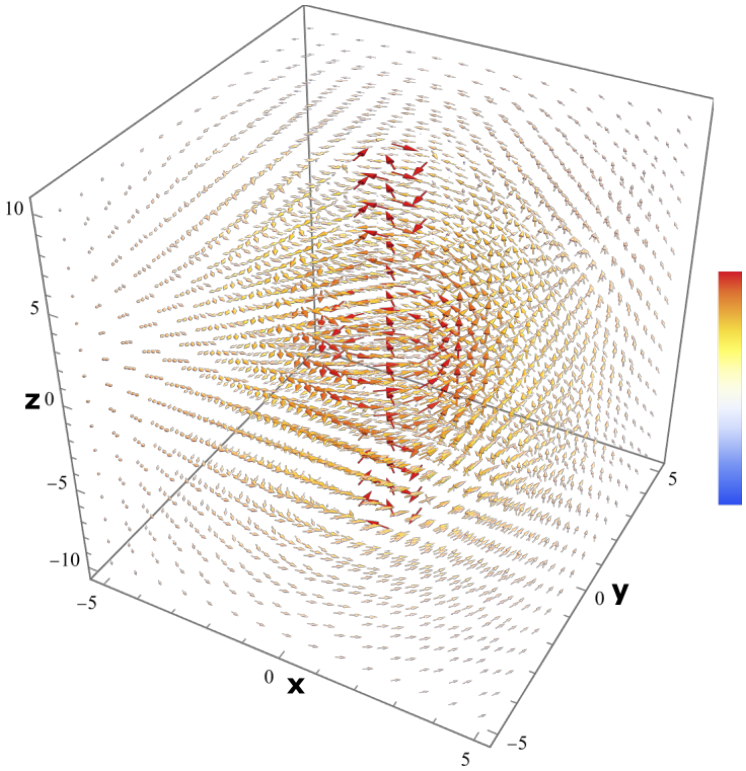

(a) 3-D plot of the **v** field.

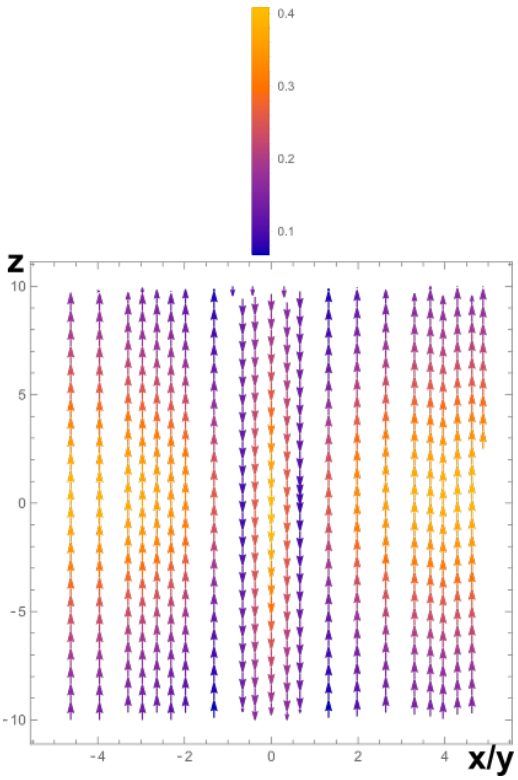

(b) Streamline plot of the **v** field in the *xz* and *yz* cross-sections.

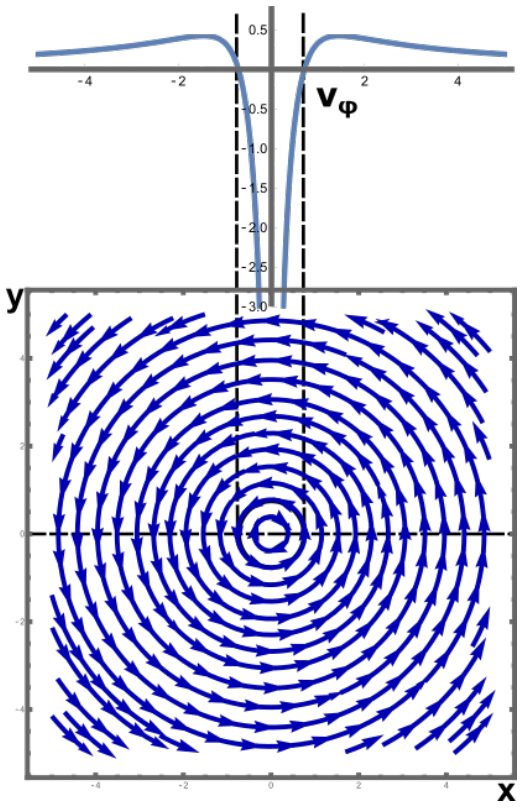

(c) Streamline plot of the **v** field in the *xy* cross-section, which is the same at every *z*.

Figure 6.3 Illustration of the **v** field of the beam in Fig. 4.3, showing no change during propagation.

represents lower intensity, demonstrating that the field is concentrated near the focus of the beam and diminishes as it propagates away from the focal point. The low intensity in the middle of the field corresponds to the change over point of v_φ where it is 0. It also demonstrated that it has no ρ element. The bottom half of Fig. 6.3c demonstrates that the $\mathbf{v}$ field spirals perpendicular to the beam propagation direction and rotates clockwise everywhere in the space, except in the centre. This corresponds to the plot at the top of Fig. 6.3c of v_φ across x being negative at the centre of the beam and positive everywhere else. Examining closer to the expression of v_φ in Eq. 6.22 and the plot of v_φ across x axis, it is clear that there exists a singularity at $\rho = 0$ along the z axis, forming a string of singularities.

We can also use using Eq. 6.18 to reproduce the skyrmion number ℓ_d based on the explicit expression of the v field in Eq. 6.22:

$$\begin{aligned} n &= \frac{1}{4\pi}\left(\lim_{\rho\to\infty}\oint_{\mathcal{L}}\mathbf{v}\cdot d\mathbf{l} - \lim_{\rho\to 0}\oint_{\mathcal{L}}\mathbf{v}\cdot d\mathbf{l}\right) \\ &= \frac{1}{4\pi}2\pi\rho\left(v_\varphi(\rho\to\infty) - v_\varphi(\rho\to 0)\right) \\ &= \ell_d\left(\frac{1}{1+f(\rho\to\infty)^2} - \frac{1}{1+f(\rho\to 0)^2)}\right). \end{aligned} \tag{6.23}$$

According to Eq. 4.18, $f = \sqrt{\frac{|\ell_{u_0}|!}{|\ell_{u_1}|!}}\left(\frac{\rho\sqrt{2}}{w(z)}\right)^{\ell_\Delta}$. Therefore, we are able to reproduce the same result of skyrmion number $n = \ell_d$ when the two spatial components are focused on the same point as in Section. 4.4.1 by using the vector potential field.

6.3.2 Different focus

In the example where the two spatial components are focused at different points introduced in Section. 4.4.2, the change in the skyrmion number can also be demonstrated through the corresponding vector potential field. The $\mathbf{v}$ field in this example is explicitly as following according to Eq.6.17:

$$\begin{aligned} v_\rho &= \left(-1+\frac{2}{1+f^2}\right)\kappa\rho\left(\frac{1}{R_{u_1}(z)} - \frac{1}{R_{u_0}(z)}\right); \\ v_\varphi &= \left(1-\frac{2}{1+f^2}\right)\frac{\ell_d}{\rho}; \\ v_z &= \left(1-\frac{2}{1+f^2}\right)\left\{\frac{\kappa\rho^2}{2}\left[\frac{1}{R_{u_1}^2(z)}\left(1-\left(\frac{z_R}{z_{u_1}}\right)^2\right) - \frac{1}{R_{u_0}^2(z)}\left(1-\left(\frac{z_R}{z_{u_0}}\right)^2\right)\right] + z_R\left(\frac{|\ell_{u_1}|+1}{R_{u_1}z_{u_1}} - \frac{|\ell_{u_0}|+1}{R_{u_0}z_{u_0}}\right)\right\}. \end{aligned} \tag{6.24}$$

This is plotted accordingly in Fig. 6.4, with $\ell_{u_0} = 0$, $\ell_{u_1} = 1$. Fig. 6.4 and Fig. 5.5 provide a one-to-one correspondence between the v field and the skyrmion field at different cross-sections.

Fig. 6.4a demonstrates the cross-section of the vector potential field in xz and yz plane and the colour scheme corresponds to the field intensity. Fig. 6.4a shows some interesting insights on the vector potential field: a) Contrary to the skyrmion field in Fig. 5.5a, the vector potential field is stronger on the outside of the beam rather than the centre of the beam. The vector potential field also expands at the cross over plane rather than focuses in as with the skyrmion field; b) Before the cross-over plane at $z_c = 0$ in this case, the field lines are travelling towards the z axis at the centre

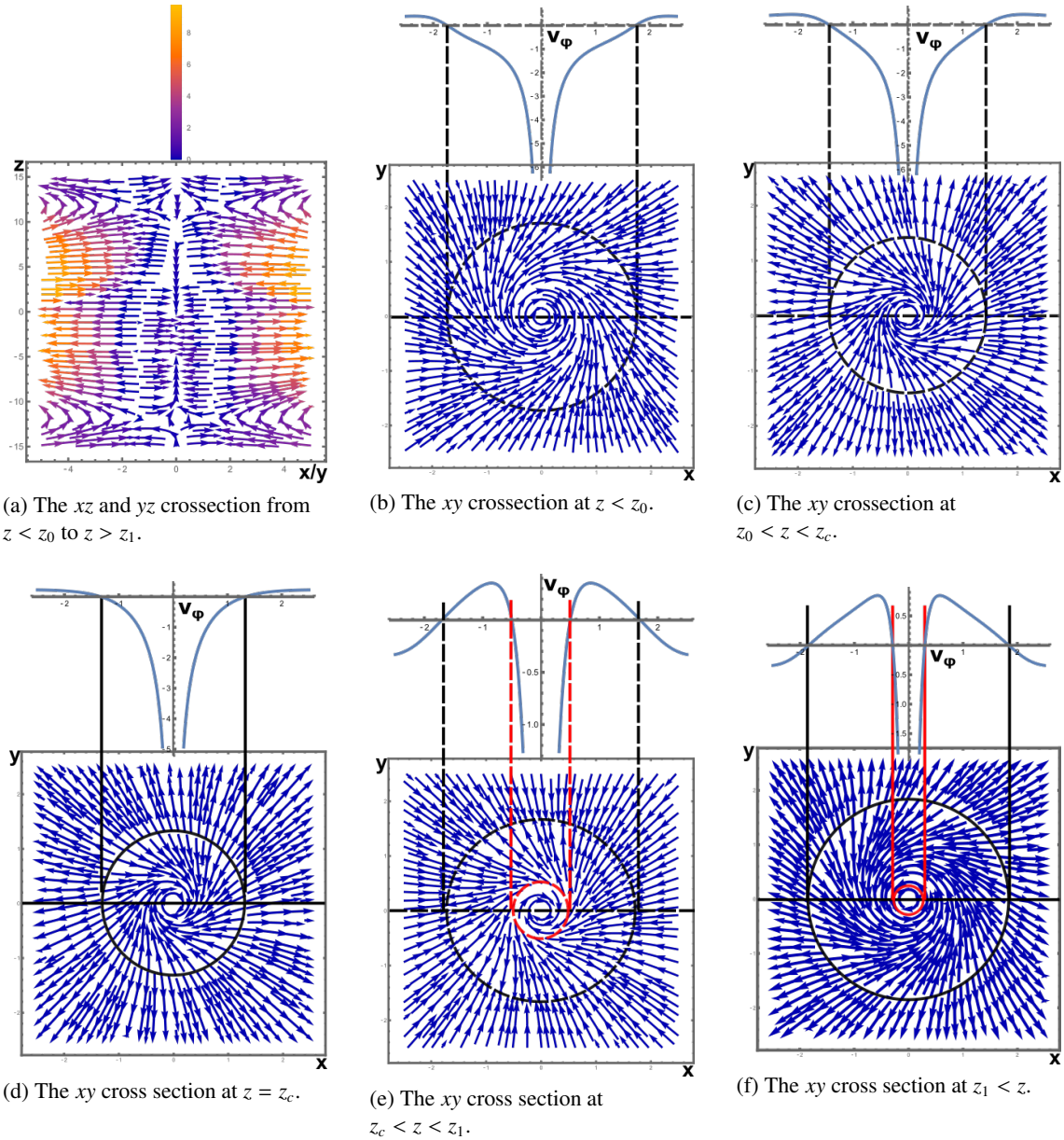

(a) The xz and yz crossection from $z < z_0$ to $z > z_1$.

(b) The xy crossection at $z < z_0$.

(c) The xy crossection at $z_0 < z < z_c$.

(d) The xy cross section at $z = z_c$.

(e) The xy cross section at $z_c < z < z_1$.

(f) The xy cross section at $z_1 < z$.

Figure 6.4 The vector potential **v** field, and their corresponding v_φ value across $x = 0$, in accordance to Fig.4.4. The red and black dotted lines illustrates the paths where v_φ changes sign. This highlighted the different behaviour before and after the crossover plane and further explains the change in the skyrmion number.

of the beam while the rest are travelling away from the z axis. However, after the cross-over plane, it is exactly the opposite. The field lines in the centre are travelling away from the z axis and those on the outside are travelling towards the z axis; c) At the centre of the beam, the vector potential field originally travels along the beam propagation direction but changes to opposite direction after the cross-over plane.

In Fig. 6.4b to Fig. 6.4f, we illustrated different cross sections of the vector potential field in the xy direction with their corresponding v_φ across $x = 0$ at $z < z_0$, $z_0 < z < z_c$, $z = z_c$, $z_c < z < z_1$ and $z > z_1$ respectively. At $z \leq z_c$, shown in Fig. 6.4b, Fig. 6.4c and Fig. 6.4d, the field lines are rotating clockwise at the centre of the beam, corresponding to a negative v_φ. As it expands

the field lines start to rotate anti-clockwise, corresponding to a positive v_φ. The changing point of the rotation is denoted by a black circle. At $z > z_c$, shown in Fig. 5.5e and Fig. 5.5f, the field lines rotate in a clockwise direction fashion at the centre of the beam and as it expands, the field lines start to rotate in the anti-clockwise direction, corresponding to the change of a negative v_φ to a positive v_φ. This first change is denoted by a red circle. Then the field line changed back to a clockwise rotation as it expands across the second changing point which is marked by a black circle. This change corresponds to the change of a positive v_φ back to a negative v_φ when ρ tends to ∞.

Similarly to Section. 6.3, from both Eq. 6.24 and Fig. 6.4, it is clear that there exists a singularity at $\rho = 0$. Therefore, The skyrmion number should be be obtained using Eq. 6.18. Without explicit calculating the skyrmion number, its change at $z = z_c$ can also be inferred from Fig. 6.4. At $z \leq z_c$, from $\rho = 0$ to $\rho = \infty$, there is only one change in direction of v_φ, from negative to positive, whereas at $z > z_c$, v_φ changes twice, from negative to positive and back to negative. Hence, from Eq. 6.18, the difference between the line integral of v_φ changes from ℓ_d to 0 at z_c.

6.4 Conclusion

In this chapter, we introduced the skyrmion vector potential field derived from the divergenceless nature of the skyrmion field. We then reproduced the associated skyrmion number of paraxial skyrmionic beams from this new field, using Stoke's theorem, which fulfilled our pursuit of mathematical interest mentioned at the beginning of this chapter.

We also explored the analogy between the skyrmion vector potential field, and the superfluid velocity. Adopting the 'Mermin-Ho' relationship in superfluid, we are able to produce a form of the skyrmion vector potential field purely from the experimentally measurable effective magnetisation **M**.

Two specific examples are included in this chapter as in the previous chapters. In the first example, the beam is comprised of two *LG* beams with different winding number ℓ sharing the same beam width, wavelength and focal point as the spatial components. In the second example, the two spatial components have different foci, while still sharing the same beam width and wavelength. For each example we have demonstrated the skyrmion vector potential field in a 3D model, and on different cross-sections. Using these graphic illustrations and the analytical expression of the skyrmion vector potential field in each example, we are able to present an alternative explanation to the changes in skyrmion numbers from the analysis in Chapter. 5.

Contrary to the skyrmion field, where many of its characteristic features manifest in the region with low light intensity, there is less spatial constraint in the vector potential field on where we should collect data. This is because we can adjust the two line integrals that are used to produce the skyrmion number. Therefore, it provides a more feasible method to extract the skyrmion number in a pure experimental manner.

In the previous Chapters. 4, 5 and this chapter, we have introduced the three basic features of paraxial skyrmion beams. Before we start to discuss the potential experimental realisation of skyrmionic beams, it is important to explore the relationship of the skyrmionic beams with other categories of structured beams to understand it further.

Chapter 7

Fractional Skyrmionic beams

7.1 Introduction

In order to understand more about skyrmionic beams we wish to explore its relation with the other categories of structured beams. One of the main ones we will discuss in this thesis is the full Poincaré beam. This is because of its close relationship with the Poincaré sphere and that it can also be constructed from superposing two LG beams.

The concept of full Poincaré beams is first formally introduced by A. Beckley, T. Brown and M. Alonso in 2010 [122]. It has since become one of the most popular categories of vector beams [123, 3, 124]. Full Poincaré beams require every possible polarisation being found at some location in the plane perpendicular to the propagation direction. Usng the same notation introduced in Section. 4.2 to describe the Poincaré sphere, this means that the polar angles χ and azimuthal angel Φ need to span across the whole sphere, ranging from 0 to π and 0 to 2π respectively. The most simple construction of a full Poincaré beam is also from superposing two different modes of LG beams with orthogonal polarisations [122].

The material in this chapter is produced by the author and partly published in [1] while the rest will be included in future publications that are currently under preparation.

7.2 The relationship between skyrmionic beams and Poincaré beam

Skyrmion structure has been observed in Poincaré beams and has been considered as a property of them [125]. We find, however, that skyrmion beams are not equivalent to Poincaré beams, but rather, in a relationship illustrated in Figure. 7.1.

In order to identify the types of paraxial beams possessing an integer skyrmion number, and its relationship with the full Poincaré beams, the skyrmion number expression in Eq. 4.14 is rewritten as following by incorporating $\cos\chi$ in Eq. 4.16 as $\frac{2}{1+|f|^2} - 1$:

$$n = \frac{\ell_d}{2}\left(\cos\chi(0,z) - \cos\chi(\infty,z)\right). \tag{7.1}$$

This suggests that there are two situations with integer skyrmion number:

- Both ℓ_d and $\frac{1}{2}\left(\cos\chi(0,z) - \cos\chi(\infty,z)\right)$ are integers:

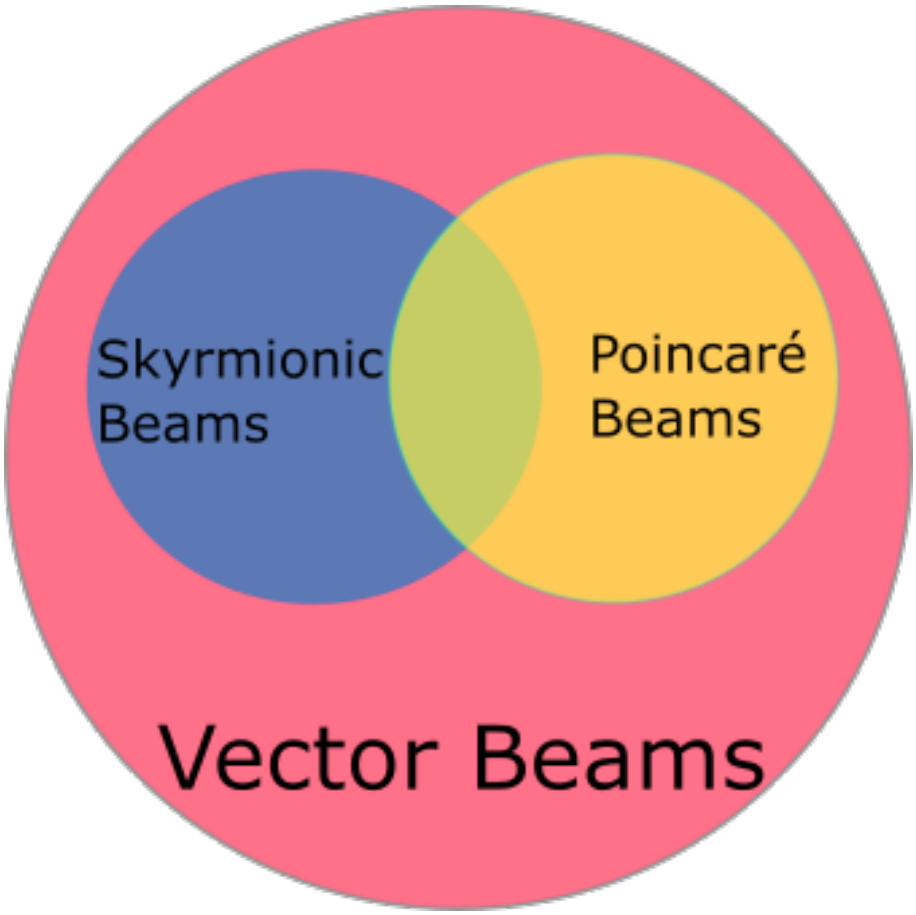

Figure 7.1 This shows the inclusive relationship among vector beams, Poincaré beams and skyrmionic beams.

$\frac{1}{2}(\cos\chi(0,z) - \cos\chi(\infty,z))$ would be an integer if and only if the angle χ ranges from the North pole to the South pole of the Poincaré sphere. ℓ_d indicates the rotation around the S_3 axis. In this case, the skyrmionic beams in this case covers the whole surface of the Poincaré sphere, and therefore are also full Poincaré beams. More specific example beams are illustrated in Section. 4.4

- Only ℓ_d is an integer:

  In these cases, for example, when $l_d = 2$ and χ only ranges from the North pole to equator, the extra rotation around the S_3 axis is able to make up for the lack of range of angle χ. These beams are skyrmionic beams but, they do not cover the full Poincaré sphere. Therefore, they are not full Poincaré beams.

  One example would be the type of beams we named as fractional skyrmions which shall be explored more thoroughly in the following sections of this chapter. In this example, the two spatial components u_0 and u_1 would be Laguerre Gaussian beams whose ℓ modes possess the equal magnitude but opposite signs, namely $-\ell_0 = \ell_1 = \ell$ focusing at different positions. In this way, $\ell_d = 2\ell$. According to the discussion in Section. 7.3, when the fractional beam propagates away from the crossover plane, i.e. $z > z_c$, $\frac{1}{2}(\cos\chi(0,z) - \cos\chi(\infty,z)) = \left(1 + (\frac{w_{u_0}(z)}{w_{u_1}(z)})^{2(\ell+1)}\right)^{-1}$. For example, when $\ell_f = 2$, if $\frac{w_{u_0}(z)}{w_{u_1}(z)} = \sqrt[6]{3}$, the skyrmion number n

remains as 1. This is visually demonstrated in Fig. 7.2.

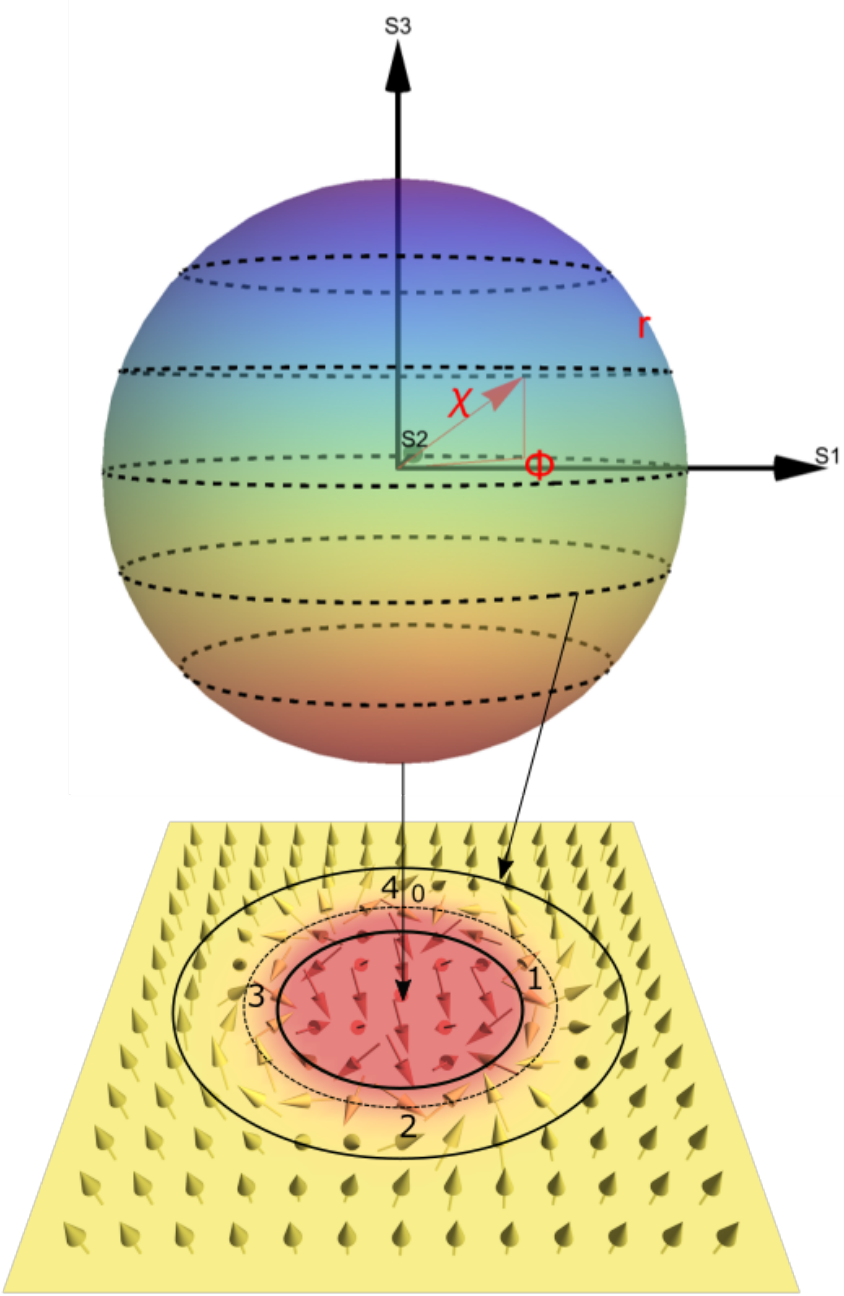

Figure 7.2 Visualisation of an optical beam with integer number -1 without spanning the whole Poincaré sphere. The numbers on the circle without dotted line demonstrates that $\ell_d = 4$. $\cos\chi(0,z) = -1$ whereas $\cos\chi(\infty,z) = -0.5$.

Then are all full Poincaré beams skyrmionic beams? We here provide an example to prove this is not always the case. Consider a structured beam with the beam profile:

$$|\psi(\mathbf{r})\rangle = \frac{LG_1^0(\mathbf{r})|0\rangle + LG_0^1(\mathbf{r})|1\rangle}{\sqrt{|LG_1^0(\mathbf{r}))|^2 + |LG_0^1(\mathbf{r})|^2}}, \tag{7.2}$$

with LG_1^0 and LG_0^1 represent Laguerre Gaussian beams with the winding number ℓ equals to 1

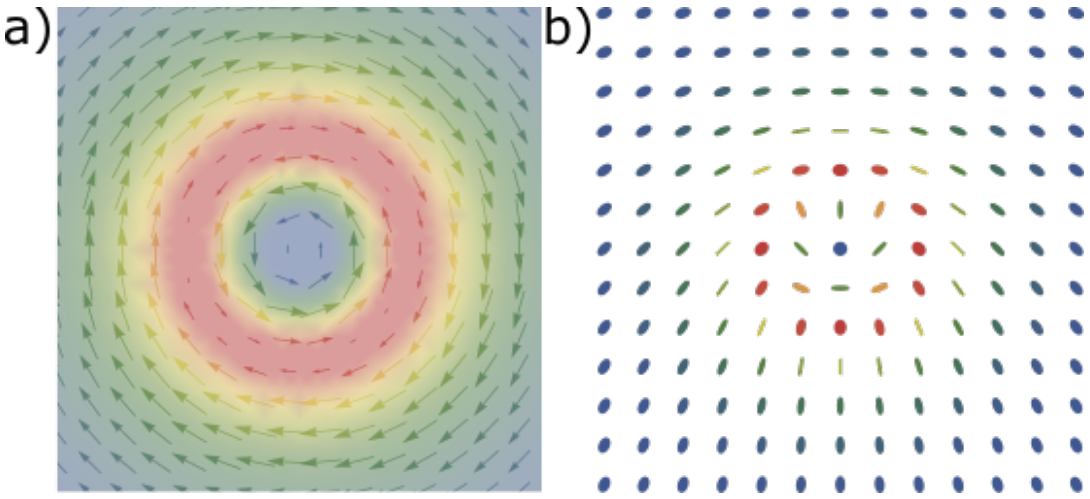

Figure 7.3 a) Magnetisation and b) polarisation visualisation of a Poincaré beam with Skyrmion number 0. Although it looks like a $n = 1$ and a $n = -1$ skyrmions being molded together, it is not comprised of an anti-skyrmion imprinted on a skyrmion. Because it is not possible to separate this structure into two isolated skyrmions. This is also proved mathematically that the skyrmion number of this structure is 0.

and 0 and the radial number p equals to 0 and 1 respectively. The effective magnetisation and corresponding optical polarisation for this beam are depicted in Fig. 7.3. f would take value of 0 at the 0 intensity rings of LG_0^1; and ∞ at the centre of beam due to the doughnut beam profile of LG_1^0. This ensures the range of 0 to π of the angle χ. $\ell_d = 1$ also ensures the angle Φ ranging from 0 to 2π. It follows that this beam is a full Poincaré beam.

This beam profile has a skyrmion number of 0, however, according to Eq. 4.14. We can understand this in the way that, the LG_1^0 mode will be dominant both in the centre and at infinity while LG_0^1 will only be dominant in the dark rings of LG_1^0. This is also vividly shown in Fig. 7.3: with red and blue represent the two orthogonal polarisation states, instead of having the typical skyrmion structure, where the colour mapping changes from one to the other continuously from the centre to the edge, these plots changed back blue on the edge. This suggests that this specific beam, although it is a Poincaré beam, it does not have a skyrmion structure. Although it looks like two skyrmion molded together, it is not comprised of an anti-skyrmion imprinted on a skyrmion. Therefore, this beams is not a skyrmionic beam both in the sense that $n = 0$ and that it is not possible to separate this structure into two isolated skyrmions.

To summarize, comparing with the requirement for full Poincaré beams - coverage of the full Poincaré sphere, a skyrmionic beam requires strict stereographic projection of a sphere-like object. When this sphere-like object is the Poincaré sphere, Skyrmionic beams are Poincaré beams; when it is a sphere constructed from two of the same hemisphere of the Poincaré sphere, Skyrmionic beams are not Poincaré beams; and lastly, when the coverage of Poincaré sphere is repeated multiple times with respect to the polar angle χ, then these beams are full Poincaré beams but not Skyrmionic beams.

7.3 Skyrmion number of fractional skyrmions

In the previous section,we discussed the relation between full Poincaré beams and Skyrmionic beams. During the discussion, we introduced a type of beams named fractional skyrmion beams. In fractional skyrmion beams, the two spatial components u_0 and u_1 would be Laguerre Gaussian beams with ℓ having the equal magnitude but opposite signs.

In the general expression for the skyrmion number in Eq. 4.14, the skyrmion number is only related to $f(\rho, z)$, the modulus of the ratio between the two spatial components $u_0(\mathbf{r})$ and $u_1(\mathbf{r})$. For *LG* beams with the same focal points and beam waists, f takes the following form:

$$\mu = f = \sqrt{\frac{|\ell_{u_0}|!}{|\ell_{u_1}|!}} \left(\frac{\rho\sqrt{2}}{w(z)}\right)^{|\ell_{u_1}|-|\ell_{u_0}|}. \tag{7.3}$$

When $|\ell_{u_0}| = |\ell_{u_1}| = \ell$, f is a constant, not a function of ρ or z anymore. In this way, the skyrmion number would inevitably becomes 0 based on Eq. 4.14, as shown in Fig. 7.4.

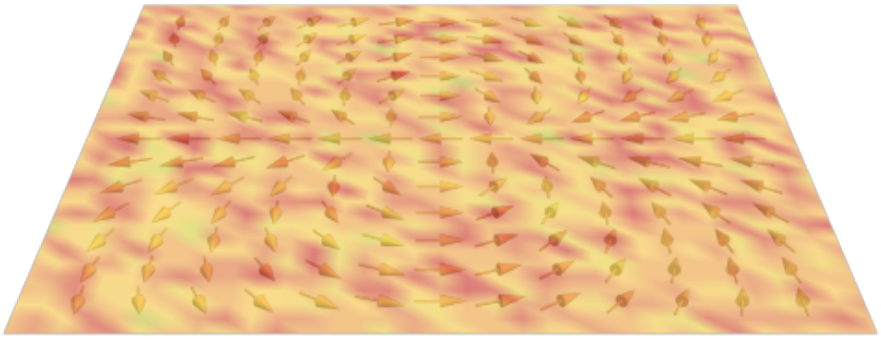

Figure 7.4 The **M** field of the beam when the winding number of two spatial components have the same magnitude, focus point and beam waist. It is 0 everywhere in the beam and therefore appears to be a 'mush' due to Mathematica calculating using LG functions.

When the two spatial components do not share the same focal point, μ would be more complicated as shown in the following equation:

$$f = \left(\frac{w_{u_0}(z)}{w_{u_1}(z)}\right)^{\ell+1} \exp\left(-\rho^2\left(\frac{1}{w_{u_1}^2(z)} - \frac{1}{w_{u_0}^2(z)}\right)\right). \tag{7.4}$$

$$\Phi(\rho, z, \phi) = -\frac{\kappa\rho^2}{2}\left(\frac{1}{R_{u_1}(z)} - \frac{1}{R_{u_0}(z)}\right) + (\ell+1)\left(\xi_{u_1}(z) - \xi_{u_0}(z)\right) + 2\ell\phi. \tag{7.5}$$

Without losing generality, here we choose $-\ell_{u_0} = \ell_{u_1} = \ell$ to be positive. At the centre of the beam, i.e. $\rho = 0$, $f = \left(\frac{w_{u_0}(z)}{w_{u_1}(z)}\right)^{\ell+1}$, at every z in the beam except z_c. In regions far from the beam axis, i.e. $\rho = \infty$, we have to consider three scenarios:

- $z < z_c$:

  Because u_0 focuses first, this means that $w_{u_0}(z) = w_0\sqrt{1 + \frac{(z_0-z)^2}{z_R^2}}$ is smaller than $w_{u_1}(z) = w_0\sqrt{1 + \frac{(z_1-z)^2}{z_R^2}}$. Therefore, the exponential component in f: $e^{-\rho^2(\frac{1}{w_{u_1}^2(z)} - \frac{1}{w_{u_0}^2(z)})}$,tends to ∞

when $\rho = \infty$. In this way, the skyrmion number at $z < z_c$ according to Eq. 4.14 is:

$$n = 2\ell \Big/ \left[1 + \left(\frac{w_{u_0}(z)}{w_{u_1}(z)}\right)^{2(\ell+1)}\right]; \tag{7.6}$$

- $z = z_c$:

  This means that $w_{u_0}(z_c) = w_{u_1}(z_c)$ leading to that $f = 1$ at both the centre of the field and far from the beam axis. Therefore, the skyrmion number is:

$$n = 0; \tag{7.7}$$

- $z > z_c$:

  Similar to the discussion but contrary to the result when $z < z_c$, the relation between the beam waists is that $w_{u_0}(z_c) > w_{u_1}(z_c)$ here. This leads to the exponential term tends to 0 when $\rho = \infty$. Thus, the skyrmion number becomes:

$$n = -2\ell \left(\frac{w_{u_0}(z)}{w_{u_1}(z)}\right)^{2(\ell+1)} \Big/ \left[1 + \left(\frac{w_{u_0}(z)}{w_{u_1}(z)}\right)^{2(\ell+1)}\right] \tag{7.8}$$

As shown in Fig. 7.5, the M_z value does not extend from -1 to 1 as a regular skyrmion structure typically would. Therefore, the skyrmion number would not be an integer anywhere along the beam. This result implies there is no full skyrmion structure in this system. In other words, although they share similar appearance of skyrmion structure, they do not possess the topological stability that integer skyrmion beams have.

To understand this result, we should revisit Eq. 4.17, where the dependence of ρ, in other words, how the beam propagates radially, only depends on the absolute value of ℓ. This means, when $|\ell_{u_0}| = |\ell_{u_1}|$, both spatial components propagate at the same rate radially, regardless of the focusing point. This indicates neither part would be dominant over the other one far from the beam axis or at the center of the beam. Therefore, there is no change in the dominant polarisation or spin pattern. Hence, there is no skyrmion structure.

7.4 Skyrmion field of fractional skyrmion

In this section we will explore the skyrmion field introduced in Chapter. 5 for fractional skyrmions introduced in the previous section Section. 7.3, and discuss its relation with the skyrmion field of integer skyrmionic beams.

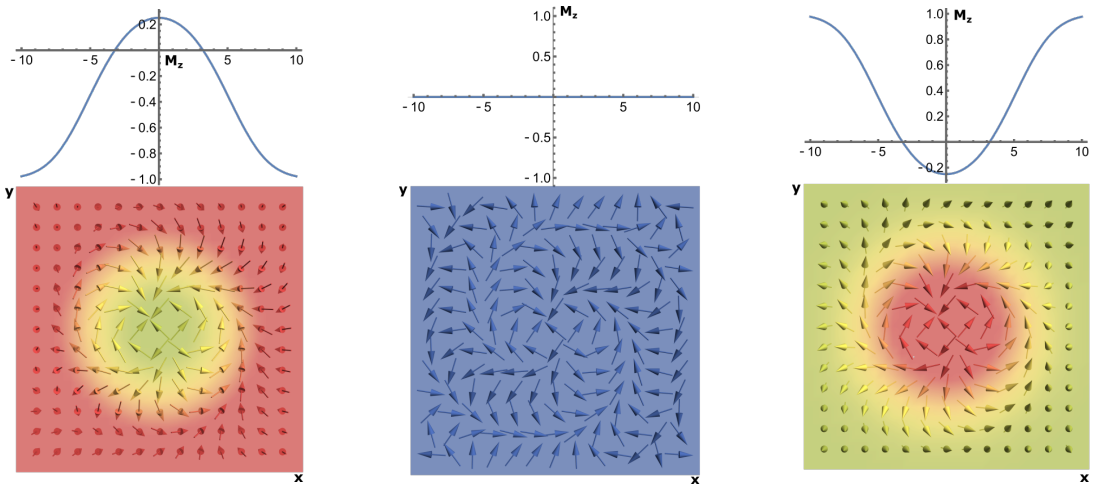

(a) $z < z_c$. (b) $z = z_c$. (c) $z > z_c$.

Figure 7.5 The **M** field of the beam and its corresponding M_z value across $x = 0$ at different z when the winding number of two spatial components have the same magnitude, focal point and beam waist.

The skyrmion field of this kind of fractional skyrmionic beams has the following form:

$$
\begin{aligned}
\Sigma_\rho &= \frac{-8f^2\ell}{\rho(1+f^2)^2}\left((\ell+1)\left(\frac{-1}{R_{u_1}(z)}+\frac{1}{R_{u_0}(z)}\right)+2\rho^2\left(\frac{1}{w_{u_1}^2(z)R_{u_1}(z)}-\frac{1}{w_{u_0}^2(z)R_{u_0}(z)}\right)\right);\\
\Sigma_\varphi &= \frac{-4f^2}{(1+f^2)^2}\left\{2\left[\frac{1}{w_{u_1}^2(z)}-\frac{1}{w_{u_0}^2(z)}\right]\left[\frac{\kappa\rho^2}{2}\left(\frac{1}{R_{u_1}^2(z)}\left(1-\left(\frac{z_R}{z_{u_1}}\right)^2\right)-\frac{1}{R_{u_0}^2(z)}\left(1-\left(\frac{z_R}{z_{u_0}}\right)^2\right)\right)\right.\right.\\
&\quad \left.+z_R(\ell+1)\left(\frac{1}{R_{u_1}z_{u_1}}-\frac{1}{R_{u_0}z_{u_0}}\right)\right]+\\
&\quad \left.\left[(\ell+1)\left(\frac{-1}{R_{u_1}(z)}+\frac{1}{R_{u_0}(z)}\right)+2\rho^2\left(\frac{1}{w_{u_1}^2(z)R_{u_1}(z)}-\frac{1}{w_{u_0}^2(z)R_{u_0}(z)}\right)\right]\left[\kappa\left(\frac{1}{R_{u_1}(z)}-\frac{1}{R_{u_0}(z)}\right)\right]\right\};\\
\Sigma_z &= \frac{16f^2\ell}{(1+f^2)^2}\left(\frac{1}{w_{u_1}^2(z)}-\frac{1}{w_{u_0}^2(z)}\right),
\end{aligned}
\tag{7.9}
$$

which is illustrated in Fig. 7.6 with the corresponding cross-sections in Fig. 7.7. Both Eq. 7.9 and Fig. 7.7 indicates that this type of fractional skyrmion is completely symmetric in the transverse plane with respect to the crossestion plane z_c. Namely, $\Sigma_\rho(z - z_c) = \Sigma_\rho(-z + z_c)$ and $\Sigma_\varphi(z - z_c) = \Sigma_\varphi(-z + z_c)$.

Fig. 7.6 shows a series of 3D views of the skyrmion field of this fractional skyrmion. Similarly to the reasoning for Fig. 5.2, the skyrmion field is plotted in four sections. The region from $z < z_0$ to $z_0 < z < z_c$, in other words, the skyrmion field beyond the first focal point to the region between the first focal point and the crossover plane is depicted in Fig. 7.6a. The skyrmion field between the the first focal point and the crossover plane, i.e. from $z_0 < z < z_c$ to z_c, is illustrated in Fig. 7.6b. Fig. 7.6c illustrates the region between the crossover plane and the second focal point, i.e. from z_c to $z_c < z < z_1$. From this region to beyond the second focal point, namely from $z_c < z < z_1$ to $z > z_1$, is depicted in Fig. 7.6d. In all four regions, the skyrmion field behaves similarly to the skyrmion field in the different focus example illustrated in Fig. 5.2. There is one main differences between the two beams, manifesting itself at the centre of the field. At the centre

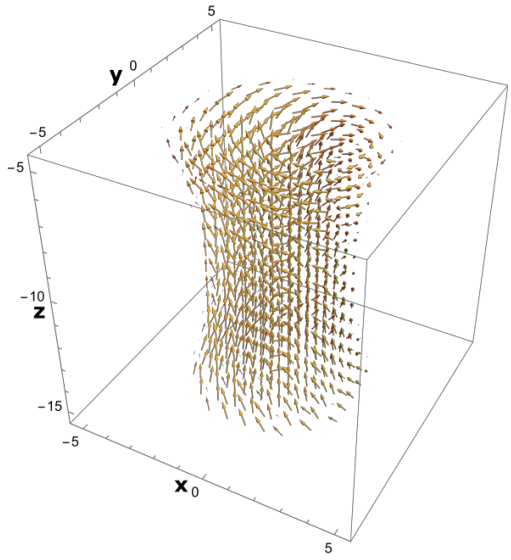

(a) Between $z < z_0$ and $z_0 < z < z_c$.

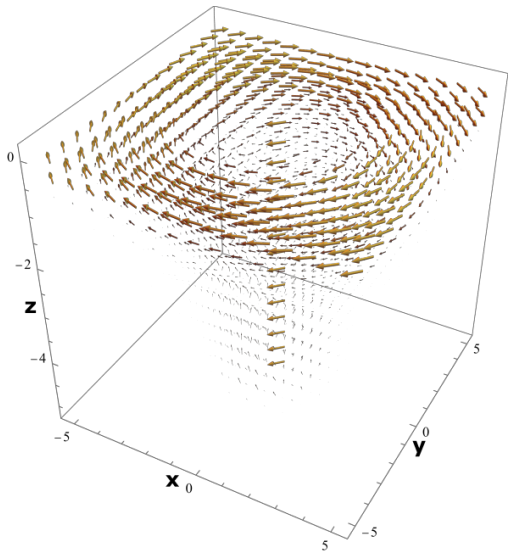

(b) Between $z_0 < z < z_c$ and $z = z_c$.

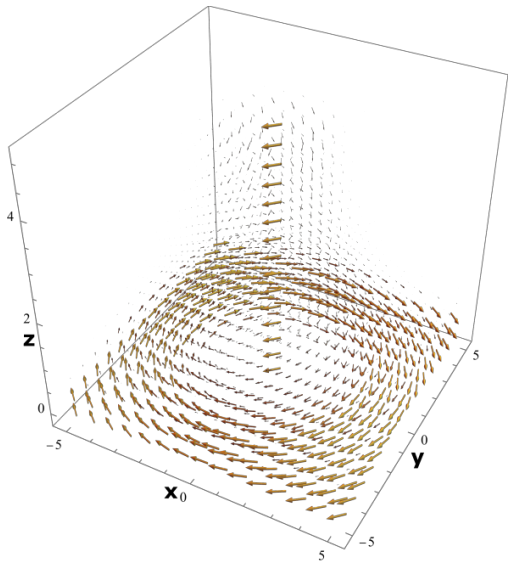

(c) Between $z = z_c$ and $z_c < z < z_1$.

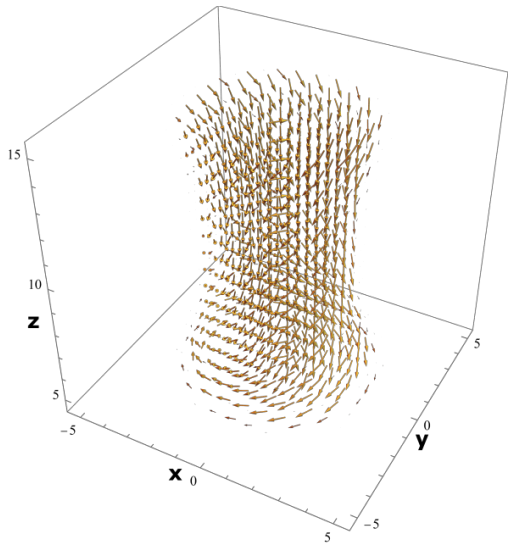

(d) Between $z_c < z < z_1$ and $z > z_1$.

Figure 7.6 This is a illustration of the skyrmion field line of a fractional skyrmion with its spatial component focusing at different points. This shows that the z-component of the skyrmion field line escapes to infinity at the cross-over point, which results in the change of the skyrmion number.

of fractional skyrmions the skyrmion field is undefined unlike in the integer skyrmion beam. This can be observed in Fig. 7.6 that the vectors in the centre of the field is orienting differently from those in Fig. 5.2 pointing in the beam propagation direction.

This can be explained by examining the three components of the skyrmion field in Eq. 7.9 and the ratio f in Eq. 7.4. Different from the integer skyrmion beams, the ratio f of the fractional skyrmion beams has no ρ dependency except for in the exponential term. This results in a non-zero ratio f on the axis where $\rho \to 0$. Therefore, the skyrmion field terms, especially Σ_ρ are badly-behaved on the axis.

The result of the skyrmion field being ill-defined on the axis can be shown analytically using

net flux change. If we draw an enclosed surface from $z < z_c$ to z_c, the flux change in the radial direction is

$$8\pi\ell\left(\frac{1}{1+|f(\infty,z)|^2}-\frac{1}{1+|f(\infty,0)|^2}\right). \tag{7.10}$$

according to Eq. 5.24. The explicit expression of f from Eq. 7.4 suggests that at $\rho \to \infty$ the ratio would be 0 at every z. Therefore the flux change in the radial direction would be 0.

The skyrmion number change on the other hand, according to the discussion in Eq. 7.6 and Eq. 7.7 is:

$$n(0)-n(-z) = -2\ell\frac{1}{1+(\frac{w_{u_0}(z)}{w_{u_1}(z)})^{2(\ell+1)}}. \tag{7.11}$$

In the different focus case discussed in Section. 5.3.2 , the ratio f at the centre ($\rho = 0$) is unchanged, i.e. $\frac{1}{1+|f(0,-z)|^2} = \frac{1}{1+|f(0,z)|^2}$. Therefore, the net flux is 0 for integer beams. However, here it is not the case. $1/(1+|f(0,z)|^2)$ changes at different z. In this way, the net flux change does not equal 0.

This does not mean that the conservation law introduced in Chapter. 5 is flawed. According to previous discussion, because the ratio would tends to 0 when $\rho \to \infty$, the total flux flow through a cylinder extends from z to $z + \Delta z$ is:

$$\oint_{cylinder} \mathbf{\Sigma}\cdot d\mathbf{S} = 8\pi\ell(\frac{1}{1+|f(0,z+\Delta z)|^2}-\frac{1}{1+|f(0,z)|^2}). \tag{7.12}$$

This implies that the total flux change only depends on the polarisation on the axis. Using Gaussian theorem, we can rewrite this as:

$$\begin{aligned}\int_{cylinder} \nabla\cdot\mathbf{\Sigma}dV &= \oint_{cylinder}\mathbf{\Sigma}\cdot d\mathbf{S}\\ &= 8\pi\ell(\frac{1}{1+|f(0,z+\Delta z)|^2}-\frac{1}{1+|f(0,z)|^2}).\end{aligned} \tag{7.13}$$

From this, we can deduce the form of the divergence of the skyrmion field being:

$$\nabla\cdot\mathbf{\Sigma} = 4\ell\frac{\delta(\rho)}{\rho}\frac{\partial}{\partial z}\frac{1}{1+|f(\rho,z)|^2}, \tag{7.14}$$

where $\delta(\rho)$ is the Dirac-delta function, ensuring only the on-axis term contributing to the total flux change.

This result is different from the theorem we established in Eq. 5.4 in Chapter. 5. This is because that on the z axis, the skyrmion field in a fractional skyrmionic beam is not defined and therefore does not possess a properly defined derivative there. In our earlier discussion in Section. 5.1, we used Taylor expansion to prove that the skyrmion field is divergenceless. The caveat in using Taylor expansion is that the effective magnetisation $\mathbf{M}$ field is slowly varying everywhere in the beam. The result suggests that this caveat is not true on the z axis of fractional skymionic beams. The fact that $\nabla\cdot\mathbf{\Sigma} = 0$ everywhere except on the axis suggests that the axis acts like a source or a sink in the fractional skyrmion beam. Therefore, skyrmion field lines can end or start on the axis. If we draw another infinitesimally small tube around the z axis and calculate the flux between this tube and the cylinder, the skyrmion filed would still follow the result in in Chapter. 5, i.e.

divergenceless and have a total flux of 0. This also explains why the skyrmion number can change continuously in fractional skyrmion beams.

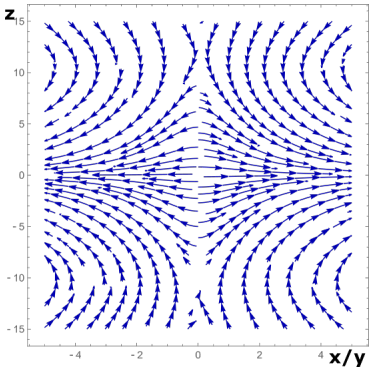

(a) The xz and yz crossection from $z < z_0$ to $z > z_1$.

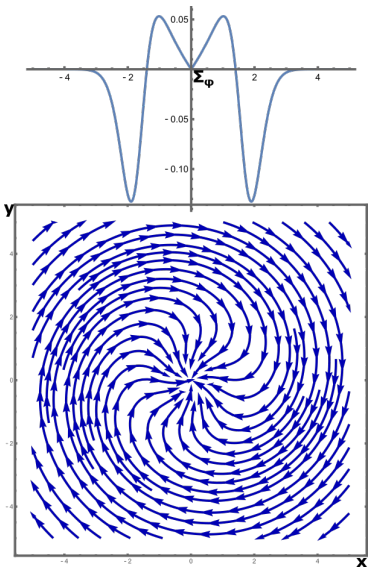

(b) The xy crossection at $z < z_0$.

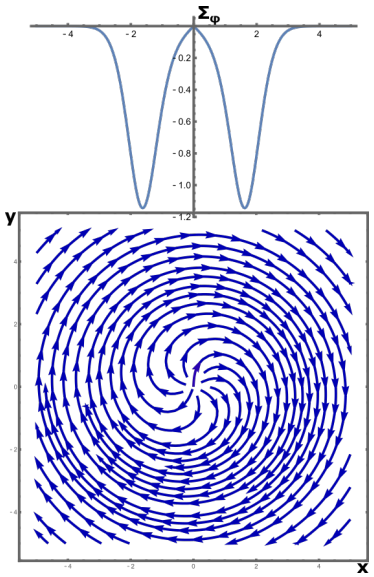

(c) The xy crossection at $z_0 < z < z_c$.

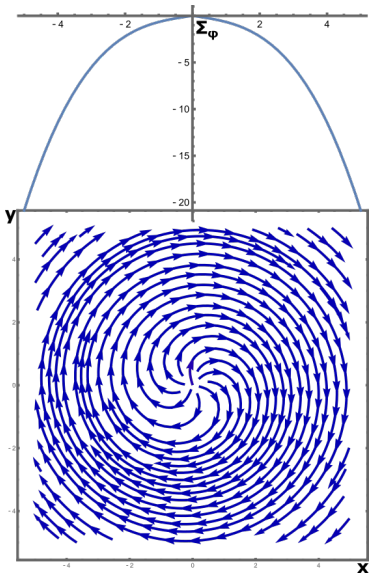

(d) The xy crossection at $z = z_c$.

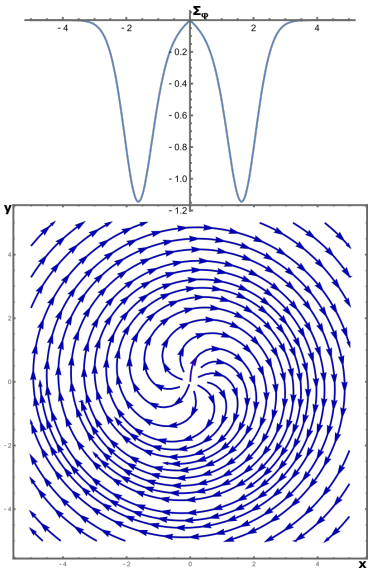

(e) The xy crossection at $z_c < z < z_1$.

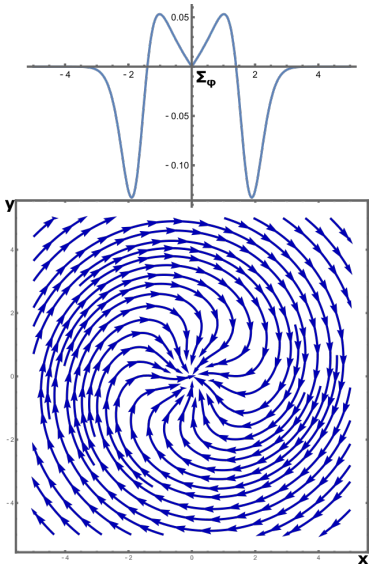

(f) The xy crossection at $z_1 < z$.

Figure 7.7 Cross-sections of skyrmion field lines, and their corresponding Σ_φ value across $x = 0$ of a fractional skyrmion with its spatial component focusing at different points, demonstrating that skyrmion field lines have no sources nor sinks.

Similarly to Fig. 5.5, we provide stream plots of the skyrmion field for fractional skyrmions in six cross sections in Fig. 7.7.

In Fig. 7.7a, which demonstrates the cross-section of the skyrmion field in xz and yz plane, we can observe that the field lines are propagating in the same direction until the crossover plane, z_c, where all the field lines escape to the infinity in the $\hat{\rho}$ direction. After z_c, field lines are all travelling opposite to the beam propagating direction. Another important observation is that the field strength in the centre of the beam is 0, in contrast to the previous situations where the field is

the strongest in the centre of the beam.

In Fig. 7.7b to Fig. 7.7f, we illustrated the cross section of the skyrmion field in the xy direction with the Σ_φ across $x = 0$ at $z < z_0$, $z_0 < z < z_c$, $z = z_c$, $z_c < z < z_1$ and $z > z_1$ respectively. At $z < z_0$, shown in Fig. 7.7b the rotation of the field line anti-clockwise at the centre of the beam and becomes clockwise further from the centre, as shown in the change of Σ_φ. At $z_0 < z < z_c$ as shown in Fig. 7.7c, $z = z_c$ (Fig. 7.7d), and $z > z_c$ (Fig. 7.7e), the field line rotates in the clockwise direction everywhere in the beam. At $z > z_1$, as shown in Fig. 7.7f, the field line behaves in the same way as in $z < z_0$ where the field line rotates anti-clockwise at the centre and clockwise elsewhere. The cross-section plane behaves uniquely at region far from the beam axis, where at any other transverse planes the rotation tends to zero and at z_c, the rotation tends to $-\infty$.

7.5 Vector potential field of fractional skyrmion

In this section, we will discuss the corresponding vector potential field for fractional skyrmions introduced in Section. 7.3. The explicit form of the $\mathbf{v}$ field for fractional skyrmions can be derived from Eq. 6.17:

$$
\begin{aligned}
v_\rho &= \left(-1 + \frac{2}{1+f^2}\right)\kappa\rho\left(\frac{1}{R_{u_1}(z)} - \frac{1}{R_{u_0}(z)}\right);\\
v_\varphi &= \left(1 - \frac{2}{1+f^2}\right)\frac{2\ell}{\rho};\\
v_z &= \left(1 - \frac{2}{1+f^2}\right)\left\{\frac{\kappa\rho^2}{2}\left[\frac{1}{R_{u_1}^2(z)}\left(1 - \left(\frac{z_R}{z_{u_1}}\right)^2\right) - \frac{1}{R_{u_0}^2(z)}\left(1 - \left(\frac{z_R}{z_{u_0}}\right)^2\right)\right] + z_R(\ell+1)\left(\frac{1}{R_{u_1}z_{u_1}} - \frac{1}{R_{u_0}z_{u_0}}\right)\right\}.
\end{aligned}
\tag{7.15}
$$

This is plotted accordingly in Fig. 7.8, with $\ell = 1$. Similarly to Fig. 6.4, we provide stream plots of the vector potential field for fractional skyrmions in six cross sections in Fig. 7.8 with a one-to-one correspondence between the v field and the skyrmion field shown in Fig. 7.7.

Fig. 7.8a demonstrates the cross-section of the vector potential field in xz and yz plane and the colour scheme corresponds to the field intensity. Fig. 7.8a shows that the vector field in fractional skyrmion in the xz and yz plane is similar to that in the previous example, depicted in Fig. 6.4a with all three two features listed in Section. 6.3.2. Although it seems like that the v field is propagating in the same direction as the beam propagating direction at the centre of the beam without changing its direction at the cross over plane, this is actually not true. From Eq. 7.15, we obtain that:

$$
v_z(\rho = 0) = \frac{z_{u1}^2 - z_{u0}^2}{\left(z_{u1}^2 + z_R^2\right)\left(z_{u0}^2 + z_R^2\right)},
\tag{7.16}
$$

which proves that the v field is propagating in the same direction as that of the beam at the centre of the beam and changes to propagating in the opposite direction after the crossover plane. The reason for the inconstant in calculation and the plot only appears to deviate from its true value due to the limited resolution in the plotting.

In Fig. 7.8b to Fig. 7.8f, we illustrated different cross sections of the vector potential field in the xy direction with their corresponding v_φ across $x = 0$ at $z < z_0$, $z_0 < z < z_c$, $z = z_c$, $z_c < z < z_1$ and $z > z_1$ respectively. At $z < z_c$, shown in Fig. 7.8b and Fig. 7.8c the field lines are rotating

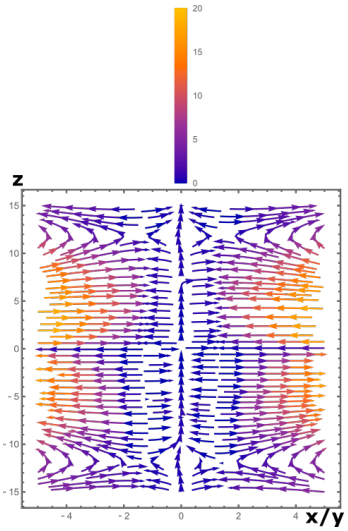

(a) The xz and yz crossection from $z < z_0$ to $z > z_1$.

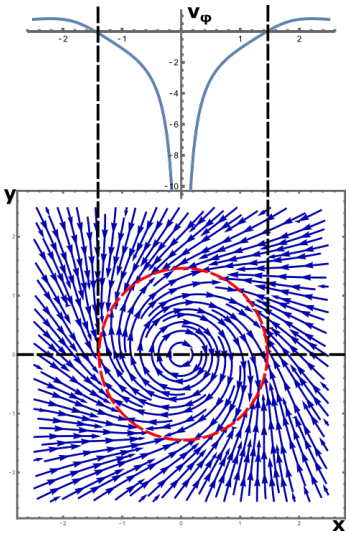

(b) The xy crossection at $z < z_0$.

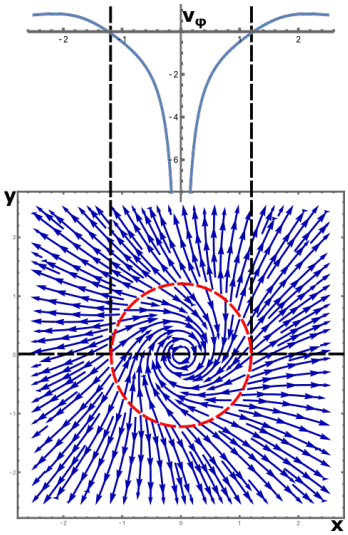

(c) The xy crossection at $z_0 < z < z_c$.

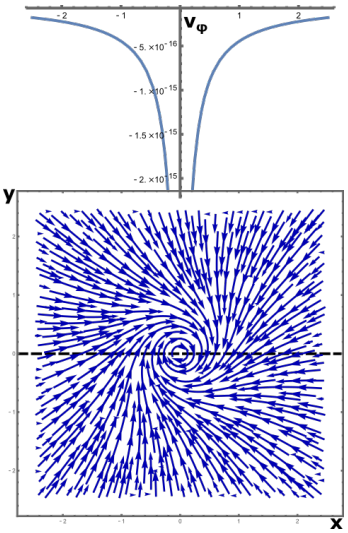

(d) The xy crossection at $z = z_c$. Although the skyrmion number is 0 on this plane, contrary to the double changes of v_φ in Fig. 6.4e and Fig. 6.4f, it has a constant $v_\varphi = 0$

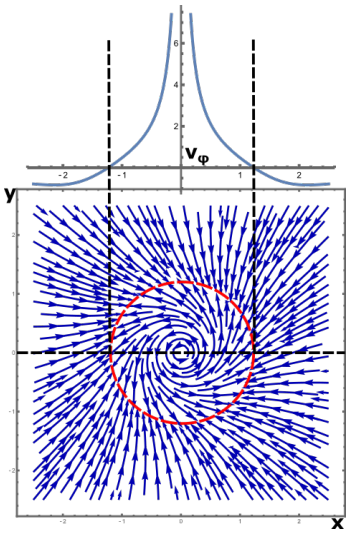

(e) The xy crossection at $z_c < z < z_1$.

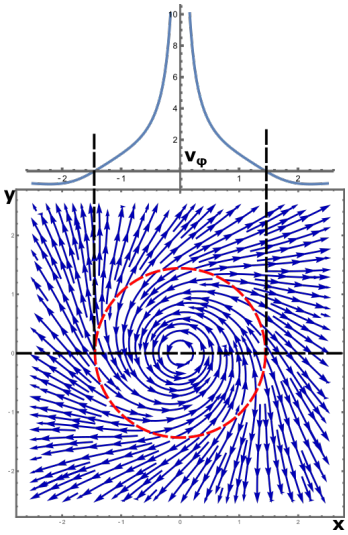

(f) The xy cross-section at $z_1 < z$.

Figure 7.8 The vector potential $\mathbf{v}$ field, and their corresponding v_φ value across $x = 0$ of a fractional skyrmion with its spatial component focusing at different points. This is similar to the integer skyrmion cases in Fig. 6.4b except at the cross-section plan $z = z_c$.

clockwise at the centre of the beam, corresponding to a negative v_φ. As it expands the field lines start to rotate anti-clockwise, corresponding to a positive v_φ. The changing point of the rotation is denoted by a red circle. At $z = z_c$ (Fig. 7.8d), the field line rotates in the clockwise direction everywhere in space. At $z > z_c$, shown in Fig. 5.5e and Fig. 5.5f, the field lines are rotating anti-clockwise at the centre of the beam and as it expands, they changed to a clockwise rotation, corresponding to the change of a positive v_φ to a negative v_φ. This change is denoted by a black circle.

As shown in Fig. 7.8 and Eq. 7.15, there still exists a singularity at $\rho = 0$. the same as the

integer skyrmion cases. The skyrmion number is not self-evident from Fig. 7.8 because v_φ only has changed once at $z \neq z_c$. This is similiar to integer skyrmion cases in Fig. 6.4b, Fig. 6.4c and Fig. 6.4d. At $z = z_c$, however, although it has a skyrmion number of 0, contrary to the double changes of v_φ in Fig. 6.4e and Fig. 6.4f, it has a constant $v_\varphi = 0$.

7.6 Conclusion

In this chapter, we firstly discussed the relation between skyrmioinc beams and full Poincaré beams, a more widely known category of structured beams. We proved that contrary to earlier belief in experimental publications, skyrmionic beams are not a sub-category of full Poincaré beams. Rather, they share some overlap but more generally are two different kinds of beams.

During the discussion, we introduced the concept of fractional skyrmion beams. Typically, they are comprised of two spatial components u_0 and u_1. They are Laguerre Gaussian beams whose ℓ modes possess the equal magnitude but opposite signs, each carrying orthogonal polarisation. Unlike integer skyrmionic beams, not only are their skyrmion numbers fractional, their skyrmion numbers also change continuously throughout propagation. Therefore, they are lack of the topological stability of integer skyrmionic beams.

Furthermore, we examined the skyrmion field of fractional skyrmionic beams. Interestingly, the skyrmion field appears not to be conserved nor is it divergenceless anymore. This is because unlike the integer skyrmionic beams, the z axis of a fractional skyrmionic beam acts like a sink of the skyrmion field. Therefore, the skyrmion field lines can start from the z axis and the skyrmion number can change continuously during propagation.

We also present the skyrmion vector potential field of fractional skyrmion beams. Contrary to integer skyrmion beams, the v field of a fractional skyrmion beam changes winding direction during propagation and is symmetric with respect to the crossover plane.

After all the analytically interesting properties of skyrmion beams, we will start to discuss the experimental measure of paraxial skyrmionic beams. We will present both our ambitions with the applications of paraxial skyrmionic beams and the challenges we are facing.

Chapter 8

Towards Experimental measurement of paraxial Skyrmionic beams

8.1 Introduction

In the previous chapters we have introduced the concept and theory of paraxial skyrmionic beams. There is now interest within the community to see this concept to move from theory into practical realisation. Ever since our paper introduced this idea into the optics community [1], there have been a few publications on the experimental realisations on paraxial skyrmionic beams including [85, 86, 116]. In these papers, their authors construct paraxial skyrmion beams according to our illustration in the previous chapters by superposing two *LG* mode with orthogonal polarisations. By measuring the Stokes parameters in a crosssection, it is proven that paraxial skyrmionic beams can be constructed according to our theory. Our own work on this area goes further than this. Currently collaborating with the Optics group in University of Glasgow, we are developing a mechanism to experimentally extract the skyrmion number from an arbitrary optical beam.

In the following sections, we will introduce the current state, the roadblocks and the outlook of this ambition. This work is currently at the last stage of writing up and will add to the toolkit of structured beams soon.

8.2 Experiment set up

In order to develop a mechanism to experimentally extract the skyrmion number from an arbitrary optical beam, we first need to construct a paraxial skyrmionic beam with a known skyrmion number. In this way, we can verify that our mechanism indeed is able to obtain the skyrmion number accurately.

The experimental setup to construct a paraxial skyrmionic beam as shown in Fig. 8.1 has been created by the Optics group in University of Glasgow. In this set up, a helium-neon laser is used to generate the laser beams; a Wollaston prism to separate light into two separate horizontal and vertically polarized beams; and a digital micromirror device (DMD) to shape the amplitude and phase of the horizontal and vertically polarised beams into our desired spatial components independently using a multiplexed hologram. Brown and Lohmann has shown in the 1960s that binary amplitude masks can be used to shape both the intensity and phase of light [126]. Nowadays, the

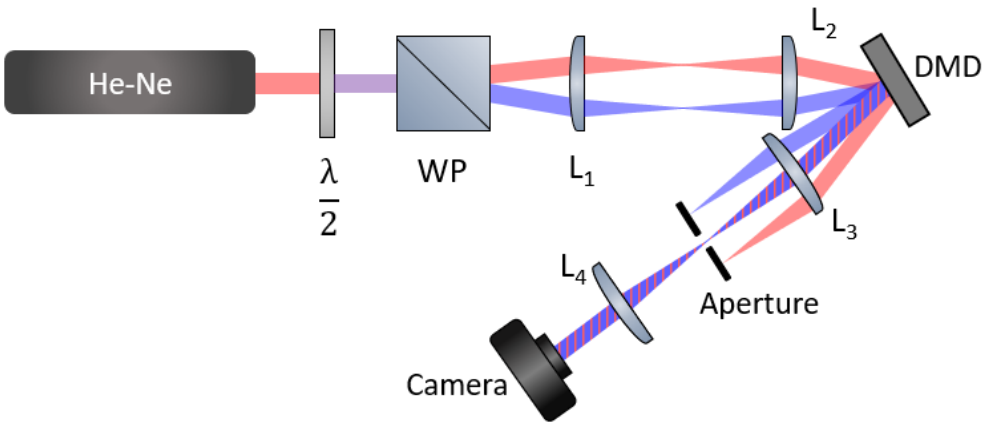

Figure 8.1 The experimental realisation of paraxial skyrmionic beams based on [1] using a digital micromirror device (DMD). He-Ne: helium-neon laser with wavelength 633 nm. $\lambda/2$: half-wave plate, WP: Wollaston prism, $L_{1,2,4}$ denote lenses with a focal length of 150 mm. L_3 has a focal length of 125 mm.

computer-generated hologram method is able to design and apply binary amplitude gratings on DMDs to diffract light into two independent orders, each travelling at different angles. The first diffraction order will possess the desired spatial intensity and phase profile [127]. Because the two orders are travelling in different directions, it is possible to separate the two orders using an aperture. Therefore, by locally varying the width of the grating to control the diffraction intensity, and locally varying the lateral position of the apertures to control the optical phase of the diffracted light, we can achieve spatially varying intensity and phase modulation [128]. The hologram used to generate a skyrmion number 1 beam comprised of LG_1^0 and LG_0^0 beams is shown in Figure. 8.2

8.3 Stokes parameters from experimental data

In the experiment, LG_1^0 and LG_0^0 are used as the spatial components of the skyrmion beam. The Stokes parameters are collected by measuring the intensity of each polarisation. By normalising and using Eq. 2.50 the Stokes parameters are calculated through:

$$S_1 = \frac{I_H - I_V}{I_H + I_V}; S_2 = \frac{I_A - I_D}{I_A + I_D}; S_3 = \frac{I_R - I_L}{I_R + I_L}, \tag{8.1}$$

where I represents intensity and the subscripts denote the corresponding polarisation. The measured polarisation pattern is shown in Fig. 8.3.

As discussed in Chapter. 4 the skyrmion number corresponds to the number of wrappings of the polarisation pattern around the Poincaré sphere on any cross-section perpendicular to the direction of propagation. In the case of $n = 1$, we can use inverse stereographic projection construction to obtain the skyrmion number from a direct mapping of the polarisation pattern onto the Poincaré sphere. Assuming the centre of the beam is precisely horizontally polarised, then by using Ω_S as the area enclosed by the points on the Poincaré sphere from the outermost contour of the beam

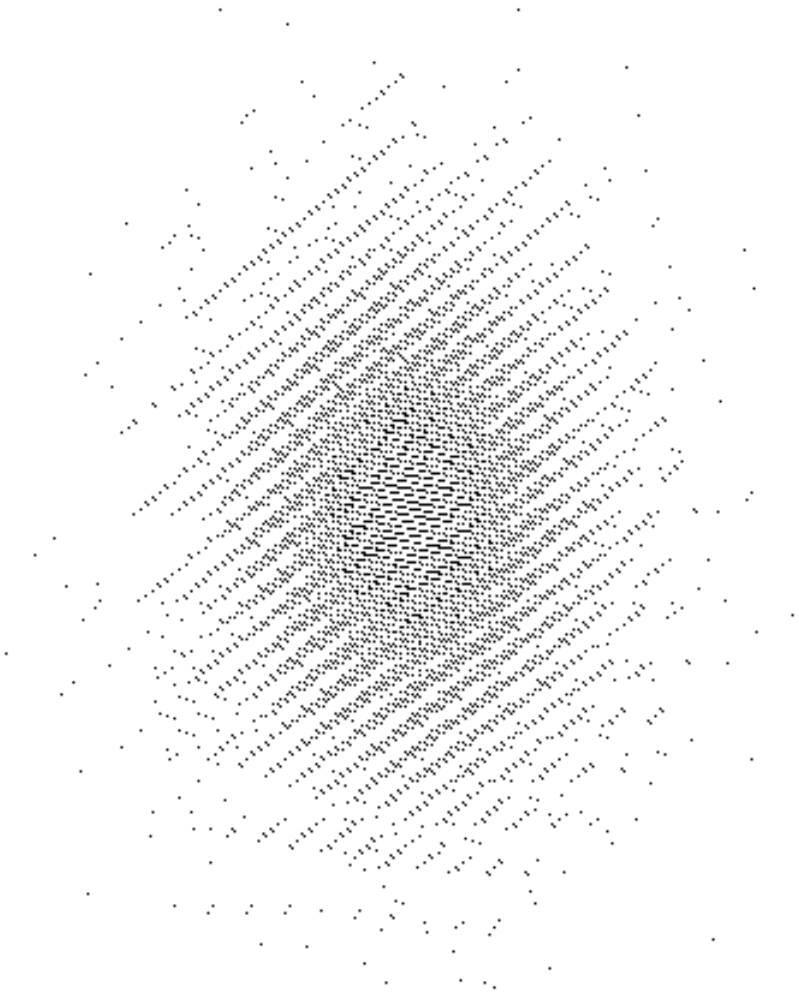

Figure 8.2 The hologram used to generate a skyrmion number 1 beam comprised of LG_1^0 and LG_0^0 beams. The reason that the holograms are not round is because of the way the mirrors are arranged on the DMD.

allows us to obtain the skyrmion number through:

$$n = 1 - \frac{\Omega_S}{4\pi}. \tag{8.2}$$

This is demonstrated by our colleagues in the Optics group in Fig. 8.4, from which a skyrmion number of $n = 0.82$ is obtained. There are two potential drawback of this method: 1) it is difficult to determine the polarisation pattern on the outermost ring where the intensity is very low to measure; 2) for skyrmionic beams with $n > 1$, this method might require some alternation to add the number of wrappings on the Poincaré sphere as extra degree of freedom.

8.4 Using skyrmion field to extract the skyrmion number

The second method to extract the skyrmion number from paraxial skyrmion beams is through the skyrmion field, i.e. using Eq. 5.1: $n = \frac{1}{4\pi}\int_S (\Sigma_z \hat{z}) \cdot (\hat{z} ds)$. The z component of the skyrmion field

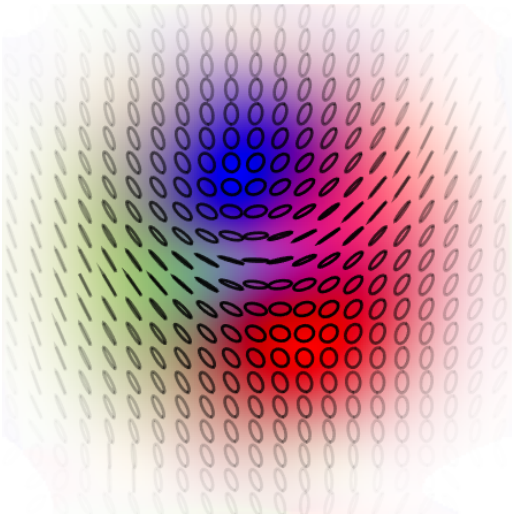

(a) Polarisation pattern reconstructed from measured intensity of different polarisations.

(b) Colour coding used in Fig. 8.3a to denote different polarisations.

Figure 8.3 The experimentally measured polarisation pattern of a paraxial skyrmionic beam with LG_0^0 and LG_0^1 as the spatial components with horizontal and vertical polarisation respectively.

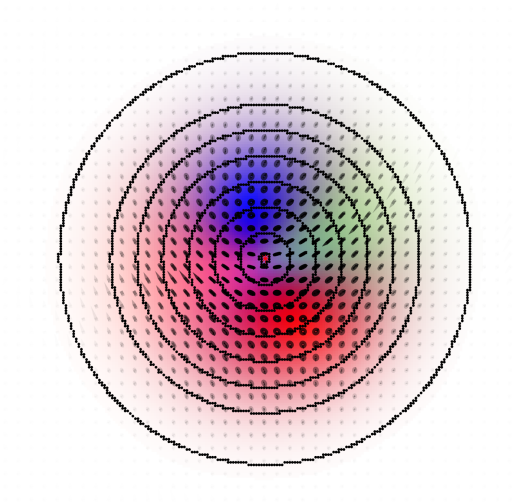

(a) The concentric circles on the polarisation pattern of a paraxial skyrmionic beam with LG_0^0 and LG_0^1 as the spatial components with horizontal and vertical polarisation respectively.

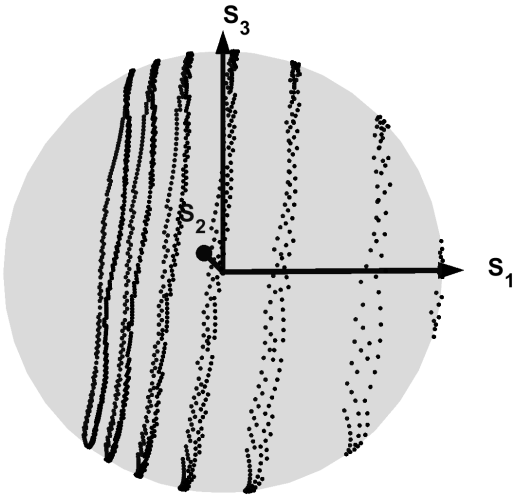

(b) Illustration of wrapping the concentric cirlces shown in Fig. 8.4a on the Poincaré sphere.

Figure 8.4 Demonstration of using inverse stereographic projection to obtain the skyrmion number $n = 0.82$ from experimentally measured polarisation pattern of a paraxial beam with $n = 1$.

can be obtained directly from the Stokes parameters by using Eq. 5.2:

$$\Sigma_z = \mathbf{M} \cdot \left(\frac{\partial \mathbf{M}}{\partial x} \times \frac{\partial \mathbf{M}}{\partial y} \right). \tag{8.3}$$

The experimental data of polarisation are measured by the Optics group from University of Glasgow. The analysis in this section is done by the author.

In this section we will discuss two scenarios: the first one is the same as in the previous

sections where the spatial components of the beam are LG_0^0 and LG_0^1 with horizontal and vertical polarisation, respectively; in the second beam the spatial components are HG_1^0 and HG_0^1 instead. The z component of the skyrmion field for those two scenarios are plotted in Fig. 8.5a and Fig. 8.5b, respectively. In the first beam comprised of LG beams, the skyrmion number according to Eq. 3.6 and the previous section is 0. However, using this method, by integrating Σ_z across the cross-section, the result is approximately 0.64. In the second beams comprised of HG beams, the skyrmion number is analytically 0, but according to this method, it is 1.38. In both situations, the skyrmion number obtained from experimental results deviates from the analytical result by an unacceptable amount. This is because the skyrmion field requires the cross product

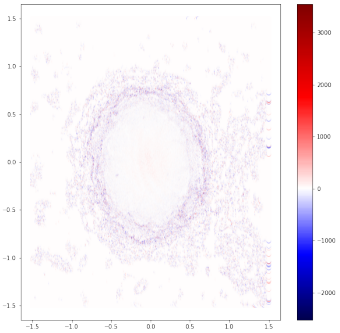

(a) Σ_z of a paraxial skyrmion beam with LG_0^0 and LG_0^1 as the spatial components with horizontal and vertical polarisation respectively.

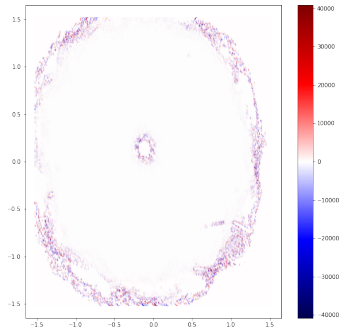

(b) Σ_z of a paraxial skyrmion beam with HG_1^0 and HG_0^1 as the spatial components with horizontal and vertical polarisation respectively.

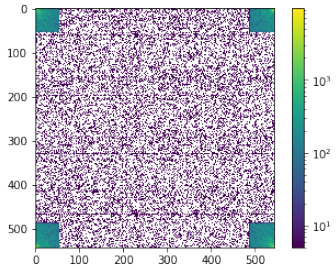

(c) The Fourier low pass filter that will be applied to Fig. 8.5a and Fig. 8.5b.

Figure 8.5 The z component of the skyrmion field for paraxial skyrmion beams with LG_0^0 and LG_0^1 and HG_1^0 and HG_0^1 as the spatial components respectively and the Fourier low pass filter that will be applied to these fields.

of two derivatives across the whole cross-section which would amplify any uncertainty in the process of measurement. This results in high sensitivity of noise in the skyrmion field leading to an inaccurate evaluation of the integral. Furthermore, it also requires a full surface integral including areas with low light, such as in the centre and at the edges of the cross-section. For experimental measurement, these areas are dominated with noises. Therefore, we decide to apply a low pass filter as shown in Fig. 8.5c to the Stokes parameter before calculating the Skyrmion field. The green areas denote the 'passing area' in the frequency domain. The reason for them to be located in the four corners rather than in the centre is because how image is represented in Python. Python uses an array to represent an image, resulting in the pixel with indices $(0, 0)$ is the one on the top right. This is the effective centre of the image from a mathematical viewpoint. We adjust the ratio between the size of the green areas and the total frequency domain to control the upper limit of the frequency of elements preserved in the image post filter application. In this case, the ratio is set to be $1.6 * 10^{-3}$.

In order to compare the result of the filter, we also constructed another set of data from simulation. Adopting the key metrics including wavelength, the beamwaists, the size of the polarisation plot and the number of pixels, we reproduced another set of Stokes parameters based on analytical result from the beam construction.

In Fig. 8.6, the z component of the skyrmion field of the simulation result of the skyrmion beam

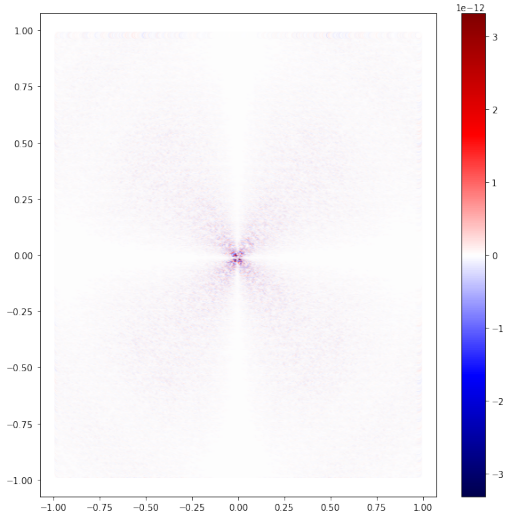

(a) Σ_z of a paraxial skyrmion beam with HG_1^0 and HG_0^1 based on simulation result.

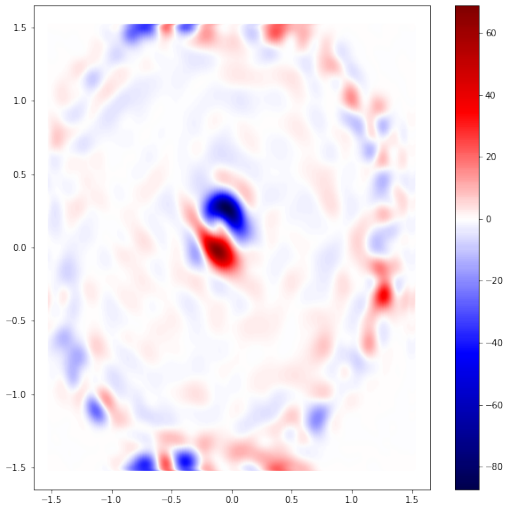

(b) Σ_z of a paraxial skyrmion beam with HG_1^0 and HG_0^1 based on experimental result post low pass filter.
.

Figure 8.6 Comparison of Σ_z of a paraxial skyrmion beam with HG_1^0 and HG_0^1 based on simulated result and experimental result, respectively, both with low pass filter applied.

comprised of *HG* beams (Fig. 8.6a) is compared with that of the experimental result (Fig. 8.6b). Although the two plots are quite different, the skyrmion number extracted from the post filter skyrmion field is 0.18. This number is still not ideal but, has shown great improvement from the pre-filter result.

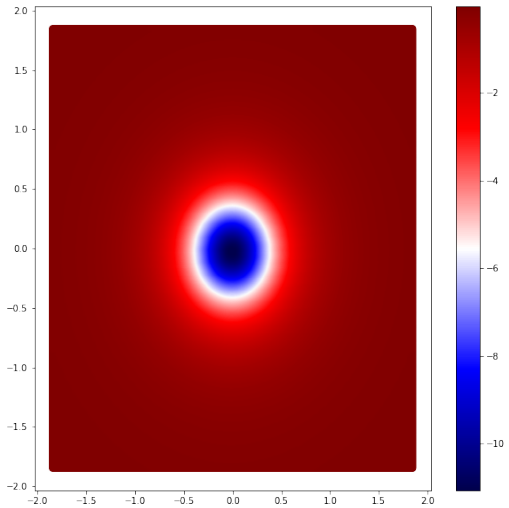

(a) Σ_z of a paraxial skyrmion beam with LG_0^0 and LG_0^1 based on simulation result.

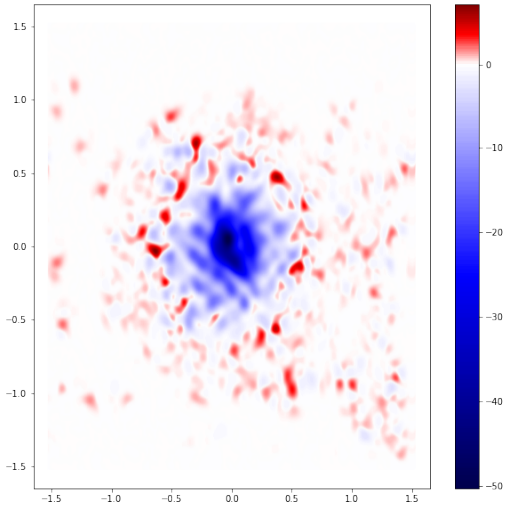

(b) Σ_z of a paraxial skyrmion beam with LG_0^0 and LG_0^1 based on experimental result post low pass filter.

Figure 8.7 Comparison of Σ_z of a paraxial skyrmion beam with LG_0^0 and LG_0^1 based on simulated result and experimental result, respectively, both with low pass filter applied.

Likewise, in Fig. 8.7, the z component of the skyrmion field of the simulation result of the skyrmion beam (Fig. 8.7a) comprised of *LG* beams is compared with that of the experimental result (Fig. 8.7b). Similar to the results in Fig. 8.6, the two plots are far from identical. De-

spite the difference in plots, the skyrmion number extracted from the post filter skyrmion field is 0.70, an improvement from the pre-filter result. The differences in Σ_z value is possibly due to the background noise in the low light areas including the centre and towards the edge of the beam.

8.5 Using skyrmion vector potential field to extract the skyrmion number

Using the skyrmion field to directly obtain skyrmion number proves to be difficult mainly due to two reasons: 1) it requires the cross-product of two derivatives which will amplify the noise in experimental data; 2) it requires full surface integral, including low light areas such as the centre and the area at large distances from the centre of the beam, posing great difficulty to experimental measurement. One of the main motivations for introducing the skyrmion vector potential field is that it may circumvent those issues by switching from surface integrals to line integrals. In this section the experimental data collection and process are conducted by the Optics group, while the simulation is processed by the author.

According to the previous discussion on skyrmion vector field in Chapter. 6, in order to obtain the skyrmion number according to Eq. 6.14 we need to define two contour lines and take the difference between those two line integrals. Because the pixels are aligned in squares we first chose the contour paths as rectangles, as shown in Fig. 8.8a. The result based on simulated data is shown in Fig. 8.8c. The x and y axes represent the ratio between the inner and outer contour line with respect to the beam measured cross section, respectively. In the simulation result, with the inner loop chosen to be smaller than 0.1 of the whole data size, and bigger loop larger than 0.8, we can obtain a skyrmion number no less than 0.77. This analysis has not been carried out on experimental data yet.

However, according to the discussions in Sec. 6.1, the shape of the contour lines does matter. The most ideal contour lines should be circles, as shown in Fig. 8.8b. Because interpolation is needed to circumvent the griding of the pixels, this requires even further process of the experimental data.

Although using the vector potential field to obtain the skyrmion number should theoretically perform better than directly using the skyrmion field, it will still encounters similiar issue: 1) the vector potential field still requires first-order derivatives, leading to increased sensitivity towards noises in measurement; 2) it still depends on measurement of low light field areas including areas closing to the centre of the field and towards the edge of the field. Our collaborators are currently working on perfecting the integrating methods and data processing to overcome these issues.

8.6 Conclusion

In this section, we have introduced the motivation, current status and the obstructions of our current path towards experimental measurement of skyrmionic beams. Our aim is to obtain the skyrmion number of an arbitrary beam rather than simply construct a skymionic beam based on known structure.

We have proposed three different methods in this chapter. The first one is to use inverse

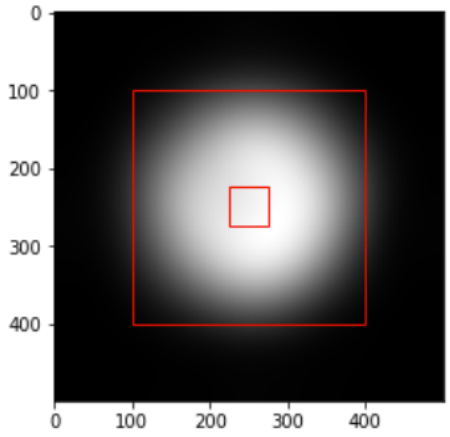

(a) Illustration of the two contour paths in rectangles on the measured plane of a skyrmion beam.

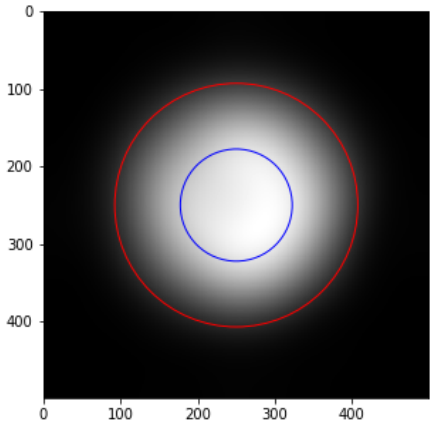

(b) Illustration of the paths of the two contour integrals in circles.

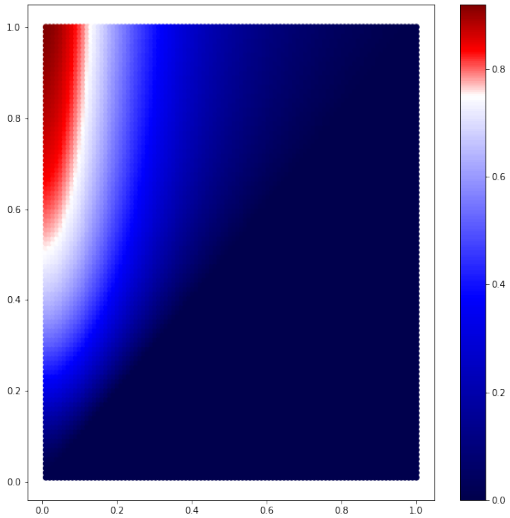

(c) Skyrmion number result based on the ratio of the sizes of the two contour integrals in the simulated data. This demonstrates that for a skyrmion number 1 beam, when the inner loop is smaller than 10% and the bigger loop is larger than 80% of the whole beam size, the obtained skyrmion number is no less than 0.77.

Figure 8.8 Demonstration of using skyrmion vector potential to obtain the skyrmion number of the skyrmionic beams comprised of LG_0^0 and LG_0^1.

steroegraphic projection. By mapping the polarisation pattern onto the Poincaré sphere, skymion number is obtained by calculating the area enclosed by points corresponding to the outermost contour line in the beam. This method is the most robust to uncertainties in measurement among all three because it does not require any form of derivatives of the measured values - Stokes parameters. However, this method mainly has two concerns: 1) it does require fairly accurate measurement of polarisation at the edge of the beam. Low light intensity areas like this pose great difficult in practical measurement; 2) the current method does not apply to cases with skyrmion number higher than 1 and thus requires further adaptations.

The second method is using the skyrmion field to obtain the skyrmion number. This method proves to be the least favourite currently mainly due to two reasons. It requires the cross-product of two derivatives of the measured values. This process greatly increases the sensitivity of the result to any noise in the measured values. The second reason is that this method also requires accurate measurement of polarisation at the centre and the edge of the beam. Similarly to the previous methods, these low light intensity areas are dominated by noises and thus almost impossible to provide an accurate measurement.

The last method involves the skyrmion vector potential field. By changing the surface integral to two line integrals and only requiring one derivative, this method should be more resilient to noise compared with the second method. However, this method still shares the same issues encountered in the second method. Although the skyrmion vector potential field only requires one derivative, this condition still amplifies the noises in the measured values. Despite the fact we can choose the contour lines in this method to circumvent the low light areas, in order to provide a more exact skyrmion number, it still requires accurate measurement of polarisations in close to low light areas. However, we do think this issue will be solved by considering more advanced data processing and integral methods.

Once we have nailed the method to extract accurate skyrmion numbers of arbitrary optical beams, we will be able to categorise structured beams that are analytically challenging to obtain skyrmion numbers. Our immediate next step is to use skyrmion numbers to model beam propagation that are otherwise difficult to predict or explain. In the next chapter, we will go into more details about the future application and outlook of skyrmionic beams.

Chapter 9

Summary and outlook of Part 1

In Part. I, we have introduced a novel theory on paraxial skyrmionic beams to fulfil a gap in the research of optical skyrmions. This thoery includes three features: the skyrmion number, the skyrmion field and the skyrmion vector field.

In Chapter. 3, we proposed the construction of paraxial skyrmionic beams and have demonstrated their associated skyrmion number is only dependent on the ratio between the two spatial components at the centre and far from the axis of the beam. By associating the effective magnetisation **M** with the Stoke's parameters, we have revealed the physical meaning of the skyrmion number: the number of times the polarisation pattern wraps around the Poincaré sphere.

After introducing the concept of the skyrmion field in Chapter. 5, we have proved this field is divergenceless. This is an important result as this shows the skyrmion field is a conserved field. Therefore, this feature can be used to categorise structured beams. Despite this, we have also proved that the skyrmion field is independent of the global orientation of the effective magnetisation **M** and the direction of the polarisation coupled with the spatial components.

The fact that the skyrmion field is a divergenceless field enables us to further construct a skyrmion vector potential field which is analogous to the magnetic vector potential **A** in Chapter. 6. In this chapter, we explored the analogy between this field and the superfluid velocity using the 'Mermin-Ho' relationship in ^{3}He theory.

For all three features, we have presented two examples to illustrate. In the first example, the beam is comprised of two *LG* beams with different winding number, ℓ, but share the same beam width, wavelength and focal point as the spatial components. This type of beam possesses an integer skyrmion number. In the second example the two spatial components are focused differently, while still sharing the same beam width and wavelength. This type of beam starts with an non-zero integer skyrmion number before suddenly changing to 0 after the cross-over plane, and therefore becomes a non-skyrmion beam. We are able to explain how this change in the skyrmion number does not contradict the topological robustness using both the skyrmion field and the skyrmion vector potential field.

In Chapter. 7, after concluding that the skyrmionic beam is not a subset of the Poincaré beams and vice versa, we introduced the concept of the fractional skyrmion beam. This type of beam has a similar structure to skyrmionic beams but lack its topological robustness. This is due to the axis in the fractional skyrmion beam acts as a source/sink of the skyrmion field lines.

The theory of optical skyrmions is still a young and emerging field and there are numerous

blank pages that awaits other researchers to fill in. For example, the analogy between optical skyrmions and superfluid still requires a more rigorous investigation into its theoretical significance and potential practical application. Another natural extension of our paraxial skyrmionic beams in structured beams in the strongly focused regime. It is interesting to explore if they still possess the same skyrmionic nature and if so, how will it be presented in this regime.

We wish to devise a method to experimentally extract the skyrmion number from an arbitrary optical beam, which is a step further from the current experimental realisations of paraxial skyrmionic beams. In Chapter. 8 we proposed three methods and discussed their advantages and disadvantages. The first method is using inverse stereographic projection to map measured polarisaion pattern onto the Poincaré sphere. This method is the most robust to uncertainties among the three methods but not readily available for applications in $n > 1$ beams. The second method is using the skyrmion field to derive the skyrmion number. This method is straightforward and compatible with the grid pixels used in experiments. However, due to the cross-product of two derivatives required for the skyrmion field, this method will be very sensitive to noise and will require more precise experimentation than current level. The last method involves calculating the line integral of the skyrmion vector potential. Although this method is less sensitive to noises comparing with the second method, it will still amplify the noises in the measured value. This is due to the derivative of the Stokes parameters in the expression of the skyrmion vector potential field.

The most ideal way to experimentally extract the skyrmion number from an arbitrary optical beam is still a matter of ongoing research. Once we have reached a satisfactory result, we will be able to utilise it to model beam propagation due to the conservation nature of the skyrmion field. Another potential application of paraxial optical skyrmion theory is in light-atom interaction. In another ongoing work from the author, we have proved that it is possible to imprint the skyrmionic structure into the excited states of an atom. Namely, the spatial information of the left-handed polarized light and the right-handed polarized light are imprinted separately on the two degenerate excited states. It can also be shown that in regions close to the quantum core (an idea introduced in [129]), the two states are highly entangled. As imprinting vortex structure onto atoms has been demonstrated experimentally [130], it is natural to explore using skyrmion beams to imprint the skyrmion structure on atoms. Just like their magnetic skyrmion counterparts, atoms with internal skyrmion structures have the potential to be applied as quantum memory.

Part II

Quantum Matched Filtering Algorithm

Chapter 10

Quantum Matched filtering background

10.1 Introduction

I think there is a world market for maybe five computers.
—Thomas Watson, chairman of IBM, 1943

Quantum computers have acquired extensive attention not only in academia but also with the public over the recent few years. From Google's superconducting quantum computer 'Sycamore' in 2019 [16], to the Chinese photonic quantum computer 'Jiuzhang' in 2020 [17], various news have been announced they have achieved quantum supremacy. Controversial as these announcements might be, quantum computers have demonstrated their ability to outperform classical computers in certain tasks. In the mean time, IBM along with other technology giants have announced their road map from small quantum processors to NISQ (Noisy Intermediate-Scale Quantum) devices available for commercial uses in the next ten years, as well as launching the new cloud quantum computing technology available to companies, researches and general public to experiment and contribute to this new technology. Therefore, with quantum computers no longer being just an academic exercise with distant implications, this is a more important than ever time to explore the advancements and changes quantum computers will potentially introduce.

Quantum computers are first proposed by Richard Feynman in 1980s to understand quantum systems, which would be exponentially costly to simulate on classical computers [131]. In addition to its original purpose, quantum computers have also demonstrated that they are more efficient than classical computers in certain problems, including square-root speed-up in unstructured search [14] and exponential speed-up in factoring large numbers [15]. There are three substantial differences between classical computers and quantum computers: 1) While classical computers store information using bits as 0s and 1s, quantum computers use qubits, which can exist in superpositions of $|0\rangle$ and $|1\rangle$; 2) Qubits can be extracted through entanglement, allowing a quantum register to have stronger correlations than are allowed classically; 3) We can increase the probability of favourable states by interference, due to the wave-like nature of quantum states. However, there is a limit to the efficiency of quantum computers, which is yet unknown to us. In fact, the relationship between classical and quantum complexity classes still remains an open question [132].

Over the past fifty years, significant progression has happened in both classical computers and algorithms. Especially in the recent decade, deep learning based on neural networks has changed

how data influences our lives. Classical machine learning methods like this can not only recognise statistical patterns but also reproduce them. Quantum algorithms have proven useful to speedup classical machine learning algorithms [133, 134, 135]. Researchers could not help but wonder what if we can produce quantum processors that can recognise and reproduce patterns that are computationally difficult for classical computers? This is later referred to as quantum machine learning.

Quantum machine learning can refer to the learning process involving either quantum machine or quantum data. In the scope of this project, we are mainly discussing classical data processed by quantum algorithms. Although algorithms like HHL algorithm (the quantum algorithm for linear systems of equations) [136], quantum PCA (principle Component Analyisis) [137] and qBLAS (quantum basic linear algebra subroutines) [138] offer potential exponential speedups, there are three major problems prohibiting the applicability of these methods [139]: 1) The input problem of loading the classical data into a quantum system can require exponential time. Although this can be solved by using qRAM (quantum random access memory), it is still highly costly energy-wise because loading data into qRAM would take exponential time [140]. So far, qRAM is considered difficult to construct experimentally and would require further error correction [141]; 2) The output problem of obtaining the full solution. This is an inherent limitation of the probabilistic nature of quantum computers. This is similar to the problem of sampling with substitution; 3) Minimal number of elementary gates needed for implementing practical quantum algorithms is still an open question.

One area in physics that has greatly benefited from machine learning algorithms, or big data analysis in general is gravitational wave detection. Gravitational waves are emitted by the cumulative mass and momentum of systems. In contrast to electromagnetic waves, they generally have longer wavelength and carry information about bigger scale objects. They are also more difficult to interact with matter, which makes them difficult to detect but able to travel through space and time undisturbed. Gravitational waves are important to physics research not only because they can test Einstein's theory of general relativity, but also to observe exotic objects in the universe like black holes. Furthermore, as 96% of the mass-energy of the universe carries no charges, gravitational waves detection is likely to open a new window to observe the universe [142].

The first direct detection of gravitational waves was made in 2015 from a binary black hole coalescence. Ever since then, there have been 39 candidate events observed by the Advanced LIGO and Advanced Virgo gravitational wave detectors [143]. These events are results of merger of compact binary systems, which allow us to understand more about neutron stars [144] and gamma-ray bursts [145], as well as set new restraints on the accuracy of general relativity [146]. However, researchers are not satisfied with this unprecedented achievement. They wish to expand this new tool to the realm of continuously emitted gravitational waves. With more advanced detectors increased in sensitivity [147, 148, 149] and additional detectors built around the world [150, 151], it is possible to detect weaker classes of gravitational wave signals like continuous waves. Currently, a matched filtering approach is adopted in detection of the gravitational waves[152, 153, 154, 155, 156], using theoretically modelled templates generated from an associated parameter space. However, because continuous wave sources require such a big number of templates [157, 158, 159] for a fully coherent analysis, the search becomes unfeasible. There-

fore, searches for gravitational wave signals is limited in sensitivity by our current computational power, making quantum machine learning a natural contender to solve this problem.

We will review match-filtering in Section 10.2, complexity theory in Section 10.3, basics about quantum circuits in Section 10.4, Grover's algorithm in Section 10.5 and quantum counting in Section 10.6. We will present our algorithm and its relevant analysis in Section 11.1. In the following sections, we will present the implementation of algorithm on Qiskit in Sections 11.2 along with its application on GW150914, the first gravitational wave signal detected, in Section 11.3.

10.2 Matched filtering

Matched filtering is a signal processing technique widely used in data analysis including gravitational wave signal detection. It is the optimal method for detecting a known signal buried in Gaussian noise [160] by maximising the signal-to-noise ratio (SNR) ρ by correlating signal templates to the detector data.

To calculate the SNR, we first consider the data $x(t)$ collected from the detector in the form of:

$$x(t) = s(t) + n(t), \tag{10.1}$$

where s is the signal embedded in some zero-mean noise n. If the signal is of finite duration, we can apply a linear filter $q(t)$ to it. This can be written as an inner product in the frequency domain:

$$\begin{aligned} q \cdot x &= \int_{-\infty}^{\infty} \tilde{q}^*(f)\tilde{x}(f)\,df \\ &= \int_{-\infty}^{\infty} \tilde{q}^*(f)\tilde{s}(f)\,df + \int_{-\infty}^{\infty} \tilde{q}^*(f)\tilde{n}(f)\,df, \end{aligned} \tag{10.2}$$

where $\tilde{}$ represents the Fourier transform of a function. Using the example of the linear filter $q(t)$, Fourier transform is defined as:

$$\tilde{q}(f) = \mathscr{F}(q(t)) = \frac{1}{\sqrt{2\pi}} \int_{-\infty}^{\infty} q(t) e^{i2\pi f t} dt \tag{10.3}$$

In order to optimise the detection of the signal, we should choose a filter such that it maximises its inner product with the signal and minimises its inner product with the noise. In the case of zero-mean noise, the SNR is defined as:

$$\begin{aligned} \mathrm{SNR}^2 =& \frac{\left|\int_{-\infty}^{\infty} \tilde{q}^*(f)\tilde{s}(f)\,df\right|^2}{\mathrm{E}\left[\left|\int_{-\infty}^{\infty} \tilde{q}^*(f)\tilde{n}(f)\,df\right|^2\right]} \\ =& 2\frac{\left|\int_{-\infty}^{\infty} \left(S_n^{1/2}(|f|)\tilde{q}(f)\right)^* \left(S_n^{-1/2}(|f|)\tilde{s}(f)\right) df\right|^2}{\int_{-\infty}^{\infty} S_n(|f|)|\tilde{q}(f)|^2 df}, \end{aligned} \tag{10.4}$$

where $E[\ldots]$ denotes an expection value over noise realisations, and S_n is the single-sided noise power spectral density (**PSD**), defined here as:

$$\frac{1}{2} S_n(|f|)\delta(f - f') = \mathrm{E}\left[\tilde{n}(f)\tilde{n}^*(f')\right], \tag{10.5}$$

where δ is the delta function. Using the Cauchy-Schwarz inequality, we can place an upper limit on ρ as:

$$\mathrm{SNR}^2 \leq 2 \int_{-\infty}^{\infty} S_n^{-1}(f)|\tilde{s}(f)|^2 df, \tag{10.6}$$

which is achieved when the linear filter is proportional to the noise-weighted copy of the signal:

$$\tilde{q}(f) \propto \frac{\tilde{s}(f)}{S_n(f)}. \tag{10.7}$$

Because the noise has zero mean value, we can choose the following relationship to ease calculation:

$$\mathrm{E}\left[\left|\int_{-\infty}^{\infty} \tilde{q}^*(f)\tilde{n}(f)df\right|^2\right] = 1, \tag{10.8}$$

from which we can deduct the optimal form of the filter should be:

$$\tilde{q}(f) = \frac{\tilde{s}(f)}{S_n(f)}\left|\int_{-\infty}^{\infty} \frac{\tilde{s}^*(f)\tilde{s}(f)}{S_n(f)}df\right|^{-1/2} = \frac{\tilde{h}(f)}{S_n(f)}. \tag{10.9}$$

We refer to these linear filters as templates, which are therefore normalised waveforms h of the signal that are weighted in the frequency domain by the detector noise PSD. The inner product in Eq. 10.2 can be applied across signal start times by instead considering a convolution, resulting with an additional phase component:

$$\rho(t) = \int_{-\infty}^{\infty} \frac{\tilde{x}(f)h(f)}{S_n(f)} e^{2\pi i t f} df, \tag{10.10}$$

where ρ represents the matched filter **SNR**. For discretised time-series data of N_t time steps separated by $\Delta t = t_j - t_{j-1}$, the discrete ρ at each time step becomes:

$$\begin{aligned} \rho(t_j) &= \frac{1}{N_t \Delta t} \sum_{k=1}^{N_t} \frac{\tilde{x}(f_k)\tilde{h}^*(f_k)}{S_n(f_k)} e^{2\pi i j k/N_t} \\ &= \frac{1}{N_t \Delta t} \sum_{k=1}^{N_t} \tilde{\rho}(f_k) e^{2\pi i j k/N_t}. \end{aligned} \tag{10.11}$$

The calculation of ρ across all N_t time steps effectively involves Fourier transforming the product of the signal with the template, and therefore can benefit from the use of the fast Fourier transform (FFT) algorithm. For a function of N discrete steps, the time required for FFT is $N \log N$ whereas for discrete Fourier transform it is N^2. This is achieved by FFT breaking the size of N into a number of smaller transforms [161]. As it is possible to produce the templates in the frequency domain, FFT is used to speed up the production of $\tilde{x}(f_k)$ and $\rho(t_j)$.

For signal detection, the parameter space of interest is discretised and determined by the variable associated with the signal we wish to detect. For example, in the case of binary black hole merger, the parameter space is typically comprised of the component masses $m_{1,2}$ and the aligned spin magnitudes $s_{1,2}$ of the binary system. This list of potential templated generated from the parameter space is called the *template bank*. A template is considered a *matched* template if it produces a ρ greater than some set threshold ρ_{thr} at any point in the given data time series.

10.3 Complexity theory

Any computation problems require certain amount of resources, such as time, space and energy. The minimum requirement of the resources is of particular interest to researchers. This will help us to determine if the problem is solvable and when there are more than one solution, which one requires least resources. In order to use resource quantification in later sections, we will here introduce some key ideas of computational complexity.

The computational resources for a certain problem are normally model dependent. In order to measure the cost irrespective of trivial changes in computation devices, one of the tools commonly used is the asymptotic notation. This is developed to summarize the essential behaviour of a function, taking the limit of large problem size and disregarding constant factors. The asymptotic notation consists of three notations [132, 162]:

The O notation denotes the upper bound of a given function. For example, the claim '$f(n)$ is $O(g(n))$' means that there exist constants n_0 and c such that for any $n > n_0$, $f(n) \leq cg(n)$. This notation is especially useful for studying the worst-case scenario of a specific algorithm.

Another useful notation is the Ω notation, which sets the lower bound of a given function. If a function $f(n)$ is said to be $\Omega(g(n))$, then there exists constants c and n_0 such that for any $n > n_0$, $f(n) \geq cg(n)$. This notation is more used to understand the behaviour of a class of algorithms.

The last notation is Θ to indicate an asymptotic behaviour of a given function $f(n)$ when $f(n)$ is both $O(f(n))$ and $\Omega(f(n))$.

Now we have the tool to describe and compare the complexity of different algorithms, we need a theory to categorise algorithms into different classes. This theory is called computational complexity, which is utilized to study the lower bounds on the resources required to solve a problem. The different classes are used to distinct between n-bit problems requiring resources that are bound by a polynomial in n, and those requiring resources grow faster than any polynomial in n. Although the latter is often referred to as exponential in n, this expression is not accurate. The reason for adopting the polynomial performance as a criteria is because a) a polynomial algorithm is in general faster than exponential algorithms; b) the Strong Church-Turing theorem indicates that if a polynomial resource solution does not exist on a probabilistic Turing machine, then an efficient solution does not exist on any computation device [132].

Most computational problems can be formulated as language recognition problems. If we use the alphabet $\Sigma = \{0, 1\}$, the set Σ^* includes all finite-length strings formulated from Σ. A language L is a subset of Σ^*. If an algorithm solves the language recognition problem, then it would accept any string $x \in L$ and reject otherwise.

If for any string x in question of length n, and there exists a Turing machine which can decide if x is in language L in time $O(n^k)$, then this class of language L is denoted **P**. Unfortunately, not all problems are **P** problems. Another important category is the **NP** problems. For **NP** problems, there exists a witness string w, that would allow us to determine if $x \in L$. It is clear that **P** is a subset of **NP**, but if **P** = **NP** still remains one of the greatest open problems in mathematics. Within **NP** problems there exists a subcategory called the **NP**-complete problems. They represent the 'most difficult' types of problems in **NP**. If they can be reduced to **P** problems, then we can prove **P** = **NP** [162].

The last two complexity classes of interest here are **BPP** and **BQP**. In **BPP** class, there exist a

probabilistic Turing machine that accepts x if $x \in L$ with a probability larger than $1/2$ and rejects x with the same probability if $x \notin L$. **BQP** is the quantum analogue of **BPP** and it has been proved that **P** $\subseteq$ **BPP** $\subseteq$ **BQP**. Understanding the relationship between **BQP** and the other three complexity classes are crucial to the study of quantum algorithms [163].

Most of the common quantum algorithms including the ones used in this project are black-box models. For these algorithms, the input is submitted to a black box, which will return if this input is accepted. When comparing the quantum and classical algorithms explicitly, the quantum speedup is categorised by query complexity and gate complexity. Query complexity measures the number of queries to the blackbox and gate complexity is made up of the number of elementary gates needed for the algorithm.

10.4 Quantum circuit

Like classical computers run algorithms by electronic circuits, a quantum computer uses quantum circuits. Quantum circuit is roughly composed of three parts: 1) Quantum registers to store qubits; 2) A series of quantum gates to perform unitary transformations on the input states; and 3) the measurement procedure to readout the final result [162].

The qubits have only two orthogonal states, similar to classical computation. Qubits are represented as points on the surface of the Bloch sphere, as shown in Fig. 10.1. The computational basis states are labeled by the associated binary string. They are often represented by column vectors as [161]:

$$|0\rangle = \begin{bmatrix} 1 \\ 0 \end{bmatrix}, \quad |1\rangle = \begin{bmatrix} 0 \\ 1 \end{bmatrix}. \tag{10.12}$$

The other pair of orthogonal states frequently used are $|+\rangle$ and $|-\rangle$, defined as:

$$\begin{aligned} |+\rangle &= \frac{1}{\sqrt{2}}(|0\rangle + |1\rangle) = \frac{1}{\sqrt{2}} \begin{bmatrix} 1 \\ 1 \end{bmatrix}, \\ |-\rangle &= \frac{1}{\sqrt{2}}(|0\rangle - |1\rangle) = \frac{1}{\sqrt{2}} \begin{bmatrix} 1 \\ -1 \end{bmatrix}. \end{aligned} \tag{10.13}$$

Quantum circuits refers to the model where quantum gates acting on the logical qubits from left to right along the 'wire'. An example of a quantum circuit is shown in Figure 10.2. in which quantum gates are shown as rectangle blocks and 'wires' as horizontal lines [162]. In this example, a quantum state $|\psi_i\rangle = |0\rangle \otimes |0\rangle \otimes |0\rangle$ enters the circuit from the left-hand side of the circuit. $\otimes$ represents the tensor product. These qubits are then being operated on by the quantum gates U_1 U_2 and U_3 before they form the output state $|\psi_f\rangle$, which is consequently measured in the computational basis. Single qubit measurement in the computational basis is symbolized by a meter dial rectangle in this thesis.

For convenience, all the quantum gates discussed here are all unitary, which can be represented by unitary matrices. The quantum gates only applied to one qubit are called single-qubit gates and the ones involve multiple qubits are called multiple-qubit gates.

One set of the most frequently used single-qubit gates are the Pauli gates, whose matrix forms

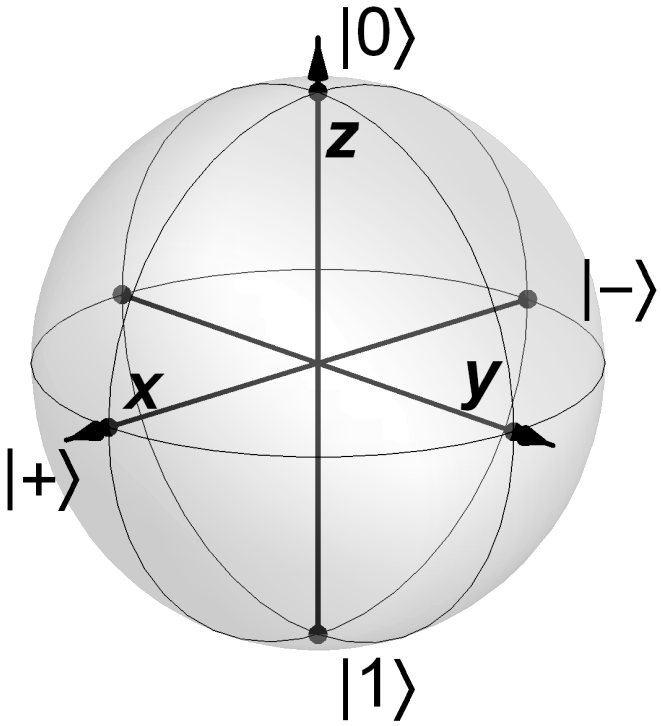

Figure 10.1 A schematic plot of the Bloch sphere. A qubit can be represented by a point on its surface. The two points on either side of the z-axis are state $|0\rangle$ and $|1\rangle$ (defined in Eq. 10.12).The two points on either side of the x-axis are state $|+\rangle$ and $|-\rangle$ (defined in Eq. 10.13.

are the associated Pauli matrices as shown in Eq. 10.14.

$$\hat{X} \equiv \begin{bmatrix} 0 & 1 \\ 1 & 0 \end{bmatrix}, \quad \hat{Y} = \begin{bmatrix} 0 & -i \\ i & 0 \end{bmatrix}, \quad \hat{Z} = \begin{bmatrix} 1 & 0 \\ 0 & -1 \end{bmatrix} \tag{10.14}$$

They rotate the qubit by π radians around the corresponding axis on the Bloch sphere. The Pauli-X operator is particular of interest, because it functions as the classical NOT gate, that exchanges state $|0\rangle$ and $|1\rangle$. They are represented in a quantum circuit diagram shown in Fig. 10.3.

Another important single qubit gate is the Hadamard gate, which interchanges the states between the computational basis and the $|+\rangle$ and $|-\rangle$ basis:

$$\hat{H} = \frac{1}{\sqrt{2}} \begin{bmatrix} 1 & 1 \\ 1 & -1 \end{bmatrix}. \tag{10.15}$$

It is represented in a quantum circuit as shown in Fig. 10.4.

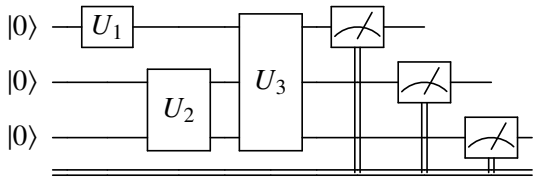

Figure 10.2 A quantum circuit start with three qubits initialised in state $|0\rangle$. The rectangles labeled as U_1 U_2 U_3 are quantum gates applied to the qubits, in the order of from left to right. The meter dial rectangles on the right-hand side indicates that each of the three qubits is measured in the computational basis in their final state. This result would be presented as the output of the circuit.

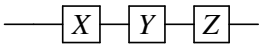

Figure 10.3 The Pauli gates expressed in a quantum circuit.

The multiple-qubit gates act on multiple qubits at the same time. The ones of particular interest here are multiple-controlled-U gates which is often written as C^n-U. A controlled gate acts on the state of two types of qubits: the control qubits and the target qubits. The operation will be applied to the target qubit if and only if all the n control qubits are in state $|1\rangle$. A general expression of a C^n-U gate in quantum circuit diagrams is shown in Fig. 10.5.

One particular example would be the CNOT gate:

$$\hat{U}_{CNOT} = \begin{bmatrix} 1 & 0 & 0 & 0 \\ 0 & 1 & 0 & 0 \\ 0 & 0 & 0 & 1 \\ 0 & 0 & 1 & 0 \end{bmatrix}, \tag{10.16}$$

and its corresponding quantum circuit expression is shown in Fig. 10.6. This is applied to the 4-dimension vectors representing two-qubit states, namely:

$$|0_C 0_T\rangle = \begin{bmatrix} 1 \\ 0 \\ 0 \\ 0 \end{bmatrix}; \quad |0_C 1_T\rangle = \begin{bmatrix} 0 \\ 1 \\ 0 \\ 0 \end{bmatrix}; \quad |1_C 0_T\rangle = \begin{bmatrix} 0 \\ 0 \\ 1 \\ 0 \end{bmatrix}; \quad |0_C 0_T\rangle = \begin{bmatrix} 0 \\ 0 \\ 0 \\ 1 \end{bmatrix}. \tag{10.17}$$

10.5 Grover's Algorithm

The search for the closest matching template or templates in gravitational wave detection may be thought of as belonging to the class of generic search problems. For such problems, we wish to identify a "marked" solution, i.e., one satisfying a certain set of criteria, from within an unstructured database of possible solutions. In fact, any problem for which it is easy to verify a solution, but difficult to find one, may be thought of as a search problem. This is exactly the set of problems which makes up the computational complexity class NP [162]. Indeed for certain NP-hard problems the best known classical algorithms offer limited improvement over brute-force search [163]. In the case of matched-filtering, we can consider the database as a template bank comprising of

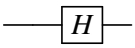

Figure 10.4 The Hadamard gate expressed in a quantum circuit.

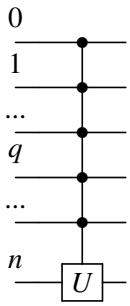

Figure 10.5 The C^n-U gate expressed in a quantum circuit. Operation $\hat{U}$ will and only will be applied to the n-th qubit if all the previous ones are in the state $|1\rangle$.

numerous predetermined templates, and we are searching for one or more for which the match with the data is above a specified threshold. Typically the number of templates is much larger than the size of the data, which determines the complexity of checking whether a given template is a match. Therefore the number of templates is the limiting factor in determining the time needed for matched-filtering in gravitational wave data analysis. Depending on the specific data analysis problem, the number of templates can range up to a $O(10^{12})$ [164] resulting in a total computational time of $\sim 10^6$ CPU hours. For a database with N entries and exactly one good solution, we need to check $\frac{N}{2}$ entries on average before finding the marked entry; thus the required search time for a classical algorithm is $O(N)$ [161].

Grover's algorithm, proposed by Lov Grover in 1996, provides a polynomial speed-up for these problems, finding a solution in $O(\sqrt{N})$ search time [14]. It was later proved that this is asymptotically optimal; $\Omega(\sqrt{N})$ queries are required for a quantum algorithm to succeed with high probability[163]. Although it is exciting we have a tight bound for quantum search algorithms, it is also disappointing because we cannot solve this **NP**-complete problem using a search method efficiently in polynomial time on a quantum computer. This is not a nail in the coffin because there could exist some unknown hidden structure in **NP**-complete problems that would allow us to further explore the relationship between **BQP** and **NP**-complete problems.

Grover's algorithm establishes a gap in query complexity between classical and quantum computers, in an oracle model. That is, it assumes that we have access to an oracle, a "black box" which computes a desired function, but not necessarily a description of the function itself. The query complexity is then given by the number of calls required to the oracle, as each execution of the oracle only costs unit time [161].

To cast the search problem as an oracle problem, we can define a function $f(x)$, according to which $f(x) = 1$ if and only if x is our marked entry in the database, otherwise $f(x) = 0$. In the quantum case, we imagine we have a quantum black box or oracle U_f that can perform the following procedure:

$$U_f : |x\rangle \otimes |b\rangle \longmapsto |x\rangle|b \oplus f(x)\rangle, \tag{10.18}$$

where $\oplus$ is bitwise addition modulo 2. $|x\rangle$ is the input register containing the input x, stored as a

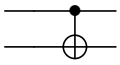

Figure 10.6 The CNOT gate expressed in a quantum circuit.

classical bit-string in one of a set of orthogonal register states, known as the computational basis, and $|b\rangle$ is an output register. We see that for $b = 0$ the evaluation of the function would be contained in the output register. The key difference in the quantum case is that we can query the oracle in superposition, that is, we can prepare the input register in a superposition over all input states. We begin by noting that if we prepare our output register in the state $|-\rangle$ (see Eq. 10.13), the operation given in Eq. 10.18 is equivalent to the following procedure, known as phase kickback, on the input register alone [161]:

$$U_f : |x\rangle \longmapsto (-1)^{f(x)}|x\rangle. \tag{10.19}$$

Although in the actual algorithm we need the output register for the oracle, in the following discussion, we prefer to use Eq. 10.19 for the oracle evaluation for simplicity.

Considering the problem of the search of the best-matching template, we represent the index of each template in the database as a computational basis state $|i\rangle$ and prepare the input register in an equal superposition over all indices $|s\rangle$. Suppose there are N templates, the input register can be expressed as:

$$|s\rangle = \frac{1}{\sqrt{N}} \sum_{0}^{N-1} |i\rangle, \tag{10.20}$$

where $\frac{1}{\sqrt{N}}$ represents the amplitude of each state in the superposition. This corresponds to an equal initial weighting of each template. We start with the simplest situation where there is exactly one desired match, $|w\rangle$. The rest of the basis, i.e., the bad solutions can be marked as $|w_\perp\rangle$, which are all perpendicular to the state $|w\rangle$. We can rewrite the input state $|s\rangle$ using the new expression as

$$|s\rangle = \frac{1}{\sqrt{N}}|w\rangle + \frac{\sqrt{N-1}}{\sqrt{N}}|w_\perp\rangle. \tag{10.21}$$

In order to increase the probability of finding the correct solution $|w\rangle$, we need the enquiry to the oracle to increase the amplitude of the state $|w\rangle$ in the superposition. We can use a real two dimensional vector space to represent the state of the input register, $|s\rangle$, as shown in Fig. 10.7a, where the angle is defined as [161]:

$$\theta = \arcsin\left(\langle w|s\rangle\right) = \arcsin\left(\frac{1}{\sqrt{N}}\right). \tag{10.22}$$

Our goal, in this context, is to rotate the state of the register to make it parallel, or closer to parallel, to state $|w\rangle$. After applying the oracle U_f, the input state $|s\rangle$ becomes

$$U_f|s\rangle = -\frac{1}{\sqrt{N}}|w\rangle + \frac{\sqrt{N-1}}{\sqrt{N}}|w_\perp\rangle, \tag{10.23}$$

which is equivalent to flipping the input state $|s\rangle$ with respect to the horizontal axis $|w_\perp\rangle$, as represented in Fig. 10.7b. This procedure itself however, does not make the desired state $|w\rangle$ more

favourable in the measurement. Therefore, an additional diffusion unitary operator is applied as the third step, which is defined as

$$U_s = 2|s\rangle\langle s| - \hat{\mathrm{I}}, \tag{10.24}$$

where $\hat{\mathrm{I}}$ is the identity operator. The action of this operator would result in the state

$$U_s U_f|s\rangle = \frac{1}{\sqrt{N}}\left(3 - \frac{4}{N}\right)|w\rangle + \left(1 - \frac{4}{N}\right)\sqrt{\frac{N-1}{N}}|w_\perp\rangle, \tag{10.25}$$

where the probability of $|w\rangle$ being the outcome of a measurement has increased from $1/N$ to $(3 - \frac{4}{N})^2/N$. Equation 10.23 can be decomposed into $|s\rangle$ and its orthogonal state, $|s_\perp\rangle$, analogously to Eq. 10.21, and where $|s_\perp\rangle$ is chosen to lie within the same two-dimensional subspace spanned by $|w\rangle$ and $|w_\perp\rangle$. In this way,we can write $U_f|s\rangle = \eta_1|s\rangle + \eta_2|s_\perp\rangle$, which means Eq. 10.25 can also be rewritten as [161]:

$$U_s U_f|s\rangle = \eta_1|s\rangle - \eta_2|s_\perp\rangle. \tag{10.26}$$

This shows the diffusion operator is equivalent to flipping the $U_f|s\rangle$ state with respect to the $|s\rangle$ state, as shown in Fig. 10.7c.

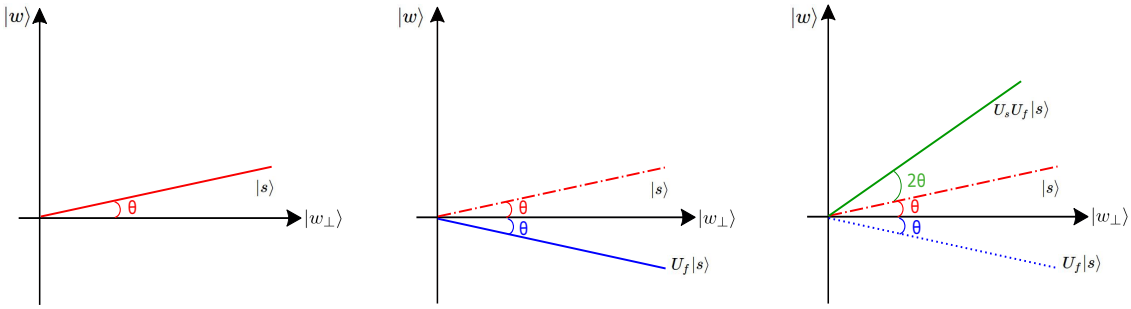

(a) The input state is described by Eq. 10.21, represented by the red line.

(b) The state after the oracle applied is described by Eq. 10.23, represented by the blue line.

(c) The state after the diffusion operator is described by Eq. 10.25, represented by the green line.

Figure 10.7 We show how the input state $|s\rangle$ changes at different stages of Grover's algorithm. The two dimensional space is spanned by the desired match $|w\rangle$ and undesired match $|w_\perp\rangle$. The solid lines represent the current state and the dotted lines represent the previous states.

If we define the Grover operator $\hat{G}$ as

$$\hat{G} = U_s U_f, \tag{10.27}$$

it is clear from the previous discussion, and shown in Fig. 10.7c, that it is equivalent to a rotation operator in the two-dimensional space spanned by $|w\rangle$ and $|w_\perp\rangle$ [161]:

$$\hat{G} = \begin{pmatrix} \cos 2\theta & -\sin 2\theta \\ \sin 2\theta & \cos 2\theta \end{pmatrix}. \tag{10.28}$$

After applying the Grover operator k times, the input state would become

$$\hat{G}^k|s\rangle = \sin\left((2k+1)\theta\right)|w\rangle + \cos\left((2k+1)\theta\right)|w_\perp\rangle \tag{10.29}$$

and in order to maximise the probability of finding the desired match $|w\rangle$, we need to maximise its amplitude $\sin((2k+1)\theta)$. In other words, we need to apply the Grover operator k times such that it satisfies

$$(2k+1)\theta = \frac{\pi}{2}. \tag{10.30}$$

This means that for large N [161],

$$k \approx \frac{\pi}{4}\sqrt{N}. \tag{10.31}$$

If there exist multiple matches, e.g., multiple templates in the bank that return a signal-to-noise ratio greater than the threshold, we can rewrite the input state $|s_t\rangle$ as:

$$|s_t\rangle = \sqrt{\frac{t}{N}}|w_t\rangle + \sqrt{\frac{N-t}{N}}|w_{t\perp}\rangle, \tag{10.32}$$

where t is the number of matching templates, $|w_t\rangle$ refers to all the matching templates, and $|w_{t\perp}\rangle$ are all the non-matching templates. In this case, in the two-dimensional space spanned by $|w_t\rangle$ and $|w_{t\perp}\rangle$, state $|s_t\rangle$ is represented by a vector with an angle θ_t defined as:

$$\theta_t = \arcsin(\langle w_t|s_t\rangle) = \arcsin\left(\sqrt{\frac{t}{N}}\right). \tag{10.33}$$

In this case, in order to maximise the amplitude of the desired templates, we need to apply the Grover's operator k_t times where now $(2k_t+1)\theta_t\pi/2$. Thus, if the number t of matching templates is known, for large values of N/t we find that [161]

$$k_t \approx \frac{\pi}{4}\sqrt{\frac{N}{t}}. \tag{10.34}$$

After k_t applications of Grover's algorithm, because all the matching templates are in superposition, a measurement of the $|s_t\rangle$ register will return only one of them at random. To obtain additional matching templates the algorithm must be repeated.

10.6 Quantum Counting

In most cases we do not know the number of matching templates, t, in advance. Complementing Grover's algorithm with one of the most important subroutines in quantum computing, quantum phase estimation [165] results in a quantum counting algorithm [166], which is able to determine the number of desired templates in the database and therefore the number of applications of the Grover operator needed to find a matching template with high probability.

Recall that we introduced the Grover operator $\hat{G}$ as a rotation in the two-dimensional space spanned by $|w_t\rangle$ and $|w_{t\perp}\rangle$ in Eq. 10.28. The eigenvectors of $\hat{G}$ are

$$|s_+\rangle = \begin{pmatrix} \frac{i}{\sqrt{2}} \\ \frac{1}{\sqrt{2}} \end{pmatrix}, \qquad |s_-\rangle = \begin{pmatrix} \frac{-i}{\sqrt{2}} \\ \frac{1}{\sqrt{2}} \end{pmatrix}, \tag{10.35}$$

with eigenvalues of $e^{2i\theta_t}$ and $e^{-2i\theta_t}$ respectively. The input state $|s\rangle$ (Eq. 10.20) is not an eigenstate

of the Grover's operator. Instead, it is a equal superposition of the two eigenstates, $|s_+\rangle$ and $|s_-\rangle$:

$$|s_t\rangle = \frac{1}{\sqrt{2}}\left(|s_+\rangle + |s_-\rangle\right). \tag{10.36}$$

If we can find θ_t then we can use Eq. 10.33 to find the number of matching templates. Therefore the problem of finding the number of desired templates is transformed into an eigenvalue estimation problem, which can be solved using quantum phase estimation, a well-known primitive in quantum information theory [162].

We thus assume that we know how to apply $\hat{G}$, and outline the phase estimation algorithm which allows us to extract an estimate of θ_t from applications of $\hat{G}$. An example circuit is presented in Fig. 10.8. We first set up a register to store our estimate of θ_t. For an estimate with p bits of precision, we need a p qubit register. We refer to this as the counting register, as it determines how many times the Grover gate is applied. The counting register is initialised in an equal superposition over all possible computational basis states:

$$\hat{H}^{\otimes p}|0\rangle^{\otimes p} = \frac{1}{2^{\frac{p}{2}}}\left(|0\rangle + |1\rangle\right) \otimes \ldots \otimes \left(|0\rangle + |1\rangle\right) = \sum_{a=0}^{2^p-1} |a\rangle. \tag{10.37}$$

A phase is naturally represented in the Fourier basis $\{|\tilde{a}\rangle\}$, defined as follows:

$$\begin{aligned} |\tilde{a}\rangle = \hat{U}_{QFT}|a\rangle &= \sum_{b=0}^{2^p-1} e^{i\frac{2\pi ab}{2^p}}|b\rangle \\ &= \frac{1}{2^{\frac{p}{2}}}(|0\rangle + e^{i\pi a}|1\rangle) \otimes (|0\rangle + e^{i\frac{\pi a}{2}}|1\rangle) \otimes \ldots \otimes (|0\rangle + e^{i\frac{\pi a}{2^{p-1}}}|1\rangle). \end{aligned} \tag{10.38}$$

where $\hat{U}_{QFT}$ is the quantum Fourier transform (QFT) [132]. Each basis element $|\tilde{a}\rangle$ corresponds to a different phase $2\pi a/2^p$ appearing in the superposition, so the inverse Fourier transform gives a way to extract information encoded as a phase.

In quantum counting, the desired phase θ_t is encoded in this way in the counting register by applying Grover's operator to the input state, where the number of applications of the Grover gate is controlled by the counting register:

$$\begin{aligned} &\sum_{a=0}^{2^p-1} C\text{-}\hat{G}^a|a\rangle \otimes |s_t\rangle = \frac{1}{\sqrt{2}}\left(\sum_{a=0}^{2^p-1} e^{i2\theta_t a}|a\rangle \otimes |s_+\rangle + \sum_{a=0}^{2^p-1} e^{-i2\theta_t a}|a\rangle \otimes |s_-\rangle\right) \\ &= \frac{1}{2^{p+\frac{1}{2}}}\Big(\left(|0\rangle + e^{i2\theta_t 2^0}|1\rangle\right) \otimes \ldots \otimes \left(|0\rangle + e^{i2\theta_t 2^{p-1}}|1\rangle\right) \otimes |s_+\rangle \\ &+ \left(|0\rangle + e^{-i2\theta_t 2^0}|1\rangle\right) \otimes \ldots \otimes \left(|0\rangle + e^{-i2\theta_t 2^{p-1}}|1\rangle\right) \otimes |s_-\rangle\Big), \end{aligned} \tag{10.39}$$

where $C\text{-}\hat{G}^a$ represents applying the controlled Grover's operator a times. Comparing Eq. 10.38 and Eq. 10.39, we naturally proceed to apply an inverse QFT to Equation 10.39 to extract the

eigenvalue θ_t contained in the phase information:

$$\begin{aligned}&\hat{U}_{QFT}^{-1}\sum_{a=0}^{2^p-1} C\text{-}\hat{G}^a|a\rangle\otimes|s_t\rangle\\ =&\frac{1}{2^p}\sum_{a=0}^{2^p-1}\sum_{b=0}^{2^p-1}\left(\alpha e^{i2\pi a\left(\frac{\theta_t}{\pi}-\frac{b}{2^p}\right)}|b\rangle\otimes|s_+\rangle+\beta e^{i2\pi a\left(\frac{\pi-\theta_t}{\pi}-\frac{b}{2^p}\right)}|b\rangle\otimes|s_-\rangle\right).\end{aligned}\tag{10.40}$$

A measurement of the counting register in the computational basis returns an integer value b

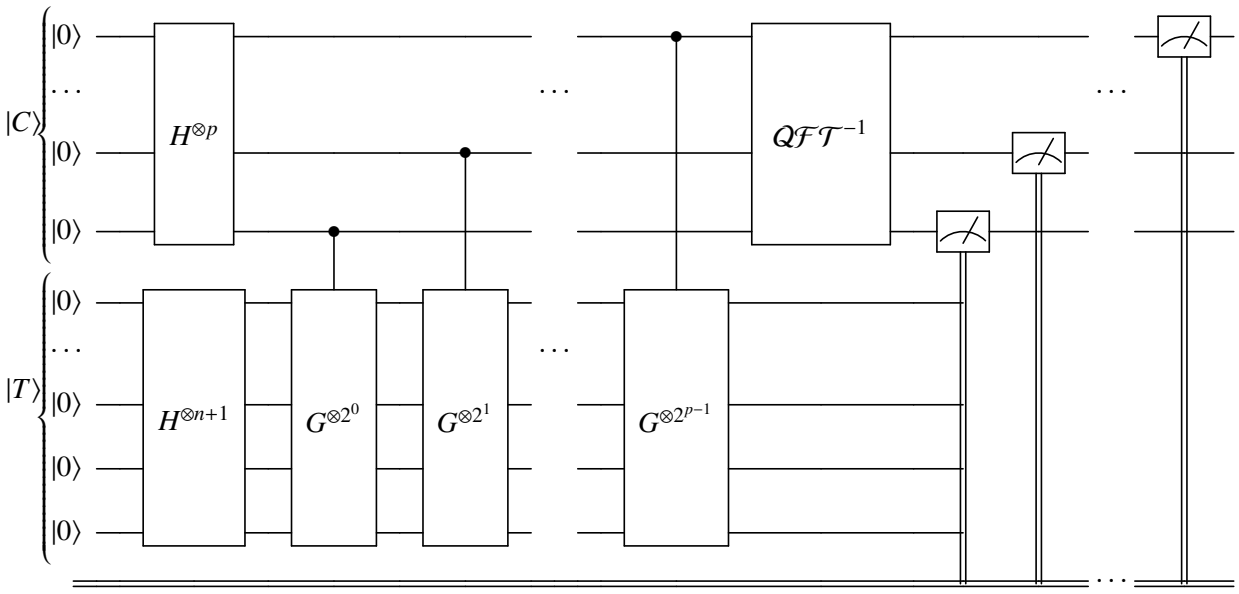

Figure 10.8 A circuit diagram of the quantum counting algorithm. $|C\rangle$ and $|T\rangle$ represents the counting register with p qubits and the input register with $n+1$ qubits respectively. The $+1$ in the input register is the ancilla qubit used in Grover's algorithm.

between 0 and 2^p-1, from which we can now extract the desired estimate of the phase. Intuitively, constructive interference occurs for those elements $|b\rangle$ for which

$$\frac{\theta_t}{\pi}-\frac{b}{2^p}\simeq 0,\qquad \text{or}\qquad \frac{\pi-\theta_t}{\pi}-\frac{b}{2^p}\simeq 0.\tag{10.41}$$

In the rest of this section, subscript '$_{th}$' refers to the theoretical value; '$_{obs}$' refers to the observed value and θ_t refers to theoretical eigenvalue. We will only be interested in cases in which $t_{\text{th}} \ll N$, and thus $\theta_t \ll 1$. Therefore, the measured value b_{obs} gives an unambiguous estimate of θ_t as follows:

$$\theta_{\text{obs}}=\begin{cases}\frac{b_{\text{obs}}\pi}{2^p}, & \frac{b_{\text{obs}}}{2^p}\le\frac{1}{2}\\ \pi-\frac{b_{\text{obs}}\pi}{2^p}, & \frac{b_{\text{obs}}}{2^p}>\frac{1}{2}.\end{cases}\tag{10.42}$$

In reality, values of b_{obs} which differ slightly from the constructive interference condition are possible; an example of the probability distribution over b is shown in Fig. 10.9. However, it may be shown that the measured value b_{obs} gives an estimate of θ_t to m bits of accuracy with a probability of success at least $1-\epsilon$ if p is chosen such that $p = m+\log(2+1/2\epsilon)$ [132]. In quantum counting, we require an estimate of accuracy at least $O(N^{-1/2})$, as θ_t itself is of this magnitude.

Thus m and p are each of size $1/2 \log N$. The maximum number of applications of G is given by 2^p, which is therefore $O(\sqrt{N})$. From the estimate of θ_t we can estimate t_{th} and k_{th}, the number of applications of G needed to subsequently retrieve a marked entry with high probability. In Chapter 11 we will discuss the choice of p in more detail for the application to quantum matched filtering.

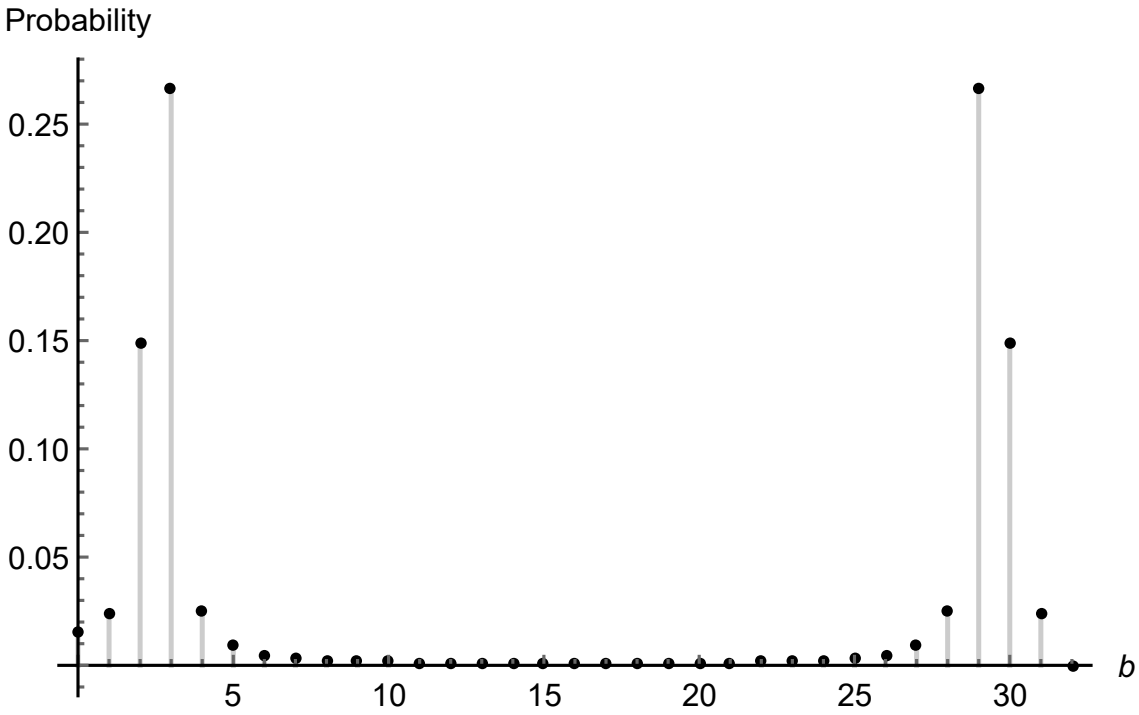

Figure 10.9 The probability distribution for each state in a 5-qubit counting register, with two matching entries in a 64-entry database. The two peaks corresponds to the two eigenstates defined in Eq. 10.35. Constructive interference only happens at states close to $2^p\theta_t/\pi$ or $2^p(\pi - \theta_t)/\pi$ and destructive interference elsewhere, resulting in this probability distribution.

If we are only interested in retrieving a matched template, rather than the number of matched template, there are altered protocols. One example involves choosing a random number between 0 and 2^m as the number of applications of the Grover's algorithm on the template register. After the measurement, the output template is checked to inquire if it is a matching template. If not, m, the limiting factor is incremented and the whole process is repeated until 2^m exceeds N. This protocol scraps the necessity of the counting register and requires less run time (number of Grover's algorithm application) if there is a match in the template bank [162]. Another example involving updating threshold to find the minimum [167, 168] to avoid the problem of no matches. Although these algorithms might require less space and less complexity, in the majority of gravitational wave matched filtering problems, we are interested in if there is a match against a predetermined threshold at all. Therefore, the original quantum counting algorithm is still the most optimal option in this case.

Chapter 11

Quantum matched filtering

11.1 Quantum matched filtering algorithm

In the previous chapter we introduced matched filtering, Grover's algorithm and its extension to quantum counting, and outlined the computational speed-up promised by quantum algorithms for the process of search in an unstructured database. In this section we argue that matched filtering for gravitational wave detection provides a natural application of quantum counting. We detail the pseudo-code of a possible implementation and prove that we can effectively construct the required oracle. We will also compare the computational cost of the quantum approach with the classical cost, taking account of the cost of the oracle evaluation, to evaluate overall complexity in each case and the relative speed-up. In this chapter, Sec. 11.1.1 to Sec. 11.2 are conducted by the author while Sec. 11.3 is done by our collaborators in the Institute for Gravitational Research (IGR) group in University of Glasgow. The work presented in this chpater is included in our recent publication [2].

As discussed in the previous section, matched filtering involves comparing data (originally) in the form of a time series against templates drawn from a template bank, searching for one or more matches above a pre-determined threshold. The templates for gravitational wave data analysis are well modelled by general relativity, and rather than performing comparisons against a previously populated database, these are calculated as part of the matched filtering procedure. Indeed the number of templates can be so large that pre-calculating and storing these in a database may have prohibitive memory requirements even in the classical case. Thus a pre-loaded database is not necessary for a quantum implementation, avoiding the need for a large amount of data to be loaded into **qRAM**. Further, the steps needed in order to construct an oracle which determines whether or not a given template is a match are already part of the classical data analysis, and including these explicitly does not diminish the speed-up of the quantum approach, which we outline below.

We note that the cost of an oracle call (i.e., a single **SNR** calculation) is not negligible; this scales with the observing time period and the frequency bandwidth over which the data is analysed, and must be taken into account in a full complexity analysis. Grover's algorithm does not speed up this step, and one might wonder whether a more sophisticated approach could give a speed up here also. We return to this in the discussion, and compare our quantum counting based approach to related tasks from the literature. What quantum counting *can* do is improve the dependence of the overall computational cost on the number of templates, making previously intractable searches

possible. In particular, as it is the spacing of templates, and therefore the overall number of templates required, that determines the sensitivity of the search, a quantum implementation of matched filtering based on quantum counting promises to enable the detection of signals too weak to detect by classical data processing techniques.

11.1.1 Oracle construction

We propose two applications of quantum counting to gravitational wave matched-filtering: one to determine whether there is a match at all, which is often the problem of interest in gravitational wave matched filtering; and the other to retrieve a matching template in the case in which there is at least one match. In order to apply quantum counting in each case, we first require an oracle to perform matched filtering with a predefined threshold. Thus we begin by detailing in Algorithm 1 the pseudo code to construct the Grover's gate.

We begin with some preliminaries: recall that the number of templates is denoted by N, and the number of data points in the time-series by M. We choose a digital encoding, i.e. to represent the data and templates as classical bits encoded in the computational basis. Standard techniques exist to convert any, in general, irreversible classical logic circuit to a reversible one, which may readily be implemented on a quantum computer by replacing classical reversible gates by their quantum equivalents [163, 169]. In general some scratch space is needed to aid in performing all calculations reversibly. We outline a specific implementation, making use of four registers: one *data register* which must be of size (number of qubits) linear in M, and one *index register*, which requires $\log N$ qubits. For intermediate calculations we specify also one register to hold the computed template, which must be of size linear in M, and one to hold the computed **SNR** value, which does not scale with N or M and is $O(1)$. We discuss the space requirements further in Section 11.4.

The basic element of Grover's algorithm is a search over an index into a database, and an oracle construction must calculate the template from the index i, proceed to calculate the **SNR**, and finally perform the check against the threshold value. We denote the number of gates needed to compute a template waveform from its parameters by k_1[1]. As each template consists of M data points, this takes time linear in M. The number of gates needed to calculate the **SNR** between a template and the data is denoted k_2. From the introduction in Sec. 10.2, this requires time $O(M \log M)$. Finally, checking whether the result is above a given threshold ρ_{thr}, as defined in Sec. 10.2 takes $O(1)$ gates, and is denoted k_3. In this way, to compute the match against all templates we need $N \cdot (k_1 + k_2 + k_3)$ steps, which is the total classical cost. Consequently, the total computational complexity of the classical algorithm is $O(NM \log M)$.

To construct a quantum algorithm we require all the same steps, but in addition we need to erase the intermediate calculations, in order to disentangle the index register from everything else to complete the oracle application. The pseudo code for Grover's gate is given in Algorithm 1.

Discussion: The following is the explanation for each step and the related computational cost for Algorithm 1.

Oracle construction:

[1]We also need to specify the mapping from index to template parameters. For reasons of clarity we have not included this step explicitly here, but note that efficient algorithms exist (see [170]), which add a modest complexity $O(\text{polylog}N)$. We discuss template placing in the example in Section 11.3.1.

Algorithm 1 Grover's Gate
Complexity: $O(M \log M + \log N)$

1: **function** GROVER'S SEARCH ALGORITHM(N, $|D\rangle$, ρ_{thr})
2: **procedure** ORACLE CONSTRUCTION
3: *Creating templates*:
4: **for all** $i < N$ **do**
5: $|i\rangle|0\rangle \leftarrow |i\rangle|T_i\rangle$
6: *Comparison with the data*:
7: $|i\rangle|D\rangle|T_i\rangle|0\rangle \leftarrow |i\rangle|D\rangle|T_i\rangle|\rho(i)\rangle$
8: **if** $\rho(i) < \rho_{\text{thr}}$ **then**
9: $f(i) = 0$
10: **else**
11: $f(i) = 1$
$|i\rangle|D\rangle|T_i\rangle|\rho(i)\rangle \leftarrow (-1)^{f(i)}|i\rangle|D\rangle|T_i\rangle|\rho(i)\rangle$
12: *Dis-entangling registers*:
13: $(-1)^{f(i)}|i\rangle|D\rangle|T_i\rangle|\rho(i)\rangle \leftarrow (-1)^{f(i)}|i\rangle|D\rangle|T_i\rangle|0\rangle$
14: $(-1)^{f(i)}|i\rangle|D\rangle|T_i\rangle|0\rangle \leftarrow (-1)^{f(i)}|i\rangle|D\rangle|0\rangle|0\rangle$
15: **procedure** DIFFUSION OPERATOR
16: $\sum(-1)^{f(i)}|i\rangle \leftarrow \sum(2|i\rangle\langle i| - \hat{1})(-1)^{f(i)}|i\rangle$

- Step 0: Initialisation
  [Cost: $O(M + \log N)$]
  The initial state is comprised of four registers:

$$|\psi_0\rangle = \frac{1}{\sqrt{N}} \sum_i^N |i\rangle_I |0\rangle_T |D\rangle_D |0\rangle_\rho, \tag{11.1}$$

  where the subscripts I, T, D and ρ represent the indices, templates, data, and the **SNR** register respectively. Becasue this step can be done in paralle for each index, loading the data takes time linear and initialising the index register to an equal superposition would each add a complexity of $O(1)$ [132].

- Step 1 (line 3-5): Creating templates
  [Cost: $O(M)$]
  Calculating the templates from the index is performed in superposition over all index values, at a cost of $k_1 \sim O(M)$ gates. The state after this step would be:

$$|\psi_1\rangle = \frac{1}{\sqrt{N}} \sum_i^N |i\rangle_I |T_i\rangle_T |D\rangle_D |0\rangle_\rho. \tag{11.2}$$

- Step 2 (line 6-11): Comparison with the data
  [Cost: $O(M \log M)$]
  The cost of calculating **SNR** between the template and the data is $k_2 \sim O(M \log M)$. Finally we compare this result to a predetermined threshold to determine the value of $f(i)$; the function that determines whether a given template is a match or not at a cost of $k_3 \sim O(1)$.

After this step the state becomes:

$$|\psi_2\rangle = \frac{1}{\sqrt{N}} \sum_i^N (-1)^{f(i)} |i\rangle_I |T_i\rangle_T |D\rangle_D |\rho(i)\rangle_\rho. \tag{11.3}$$

- Step 3 (line 12-14): Disentangling registers
  [Cost: $O(M \log M)$]
  The diffusion operator part of Grover's gate must act on the index register alone. If the index register is entangled with any other register, it will not have the desired effect. Therefore, we need to erase the computation of $\rho(i)$ and T_i to remove any correlation between these registers and the index register. The erasure process is the reverse of the generation process. Accordingly, another $k_1 + k_2$ cost is generated. The state after this step is

$$|\psi_3\rangle = \frac{1}{\sqrt{N}} \sum_i^N (-1)^{f_i} |i\rangle_I |0\rangle_T |D\rangle_D |0\rangle_\rho. \tag{11.4}$$

- Step 4 (line 15-16): Applying the Diffusion Operator
  [Cost: $O(\log N)$]
  This step is unique to the quantum algorithm and requires $O(\log N)$ quantum gates [171].

Total Cost: The total cost for a single oracle call is therefore

$$O\left(M \log M + \log N\right). \tag{11.5}$$

11.1.2 Signal detection

Now that we have constructed the required oracle for quantum matched filtering, we can readily apply quantum counting to problems of relevance to gravitational wave data analysis. Our application will firstly focus on whether there is a signal existing in the data, a common example in matched filtering. Once it has been identified that a signal is present a full Bayesian parameter analysis to determine the properties of the source must be performed separately [172, 173]. Quantum counting returns r_{obs}, an estimate of the number of matches, and so is ideally suited to this task.

In order to identify if there is a signal, we are interested in four conditional probabilities: a *true negative*, the probability of correctly returning that there is no template with an SNR above the predetermined threshold when there is no such template existing in the template bank, $P(r_* = 0|r = 0)$; a *false negative*, the probability of identifying that there is no match when indeed there is no template in the template bank with an SNR above the predetermined threshold, $P(r_{obs} = 0|r > 0)$; a *true positive*, the probability of identifying that there are templates with a SNR above the predetermined threshold when there exists such templates in the template bank, $P(r_{obs} > 0|r > 0)$; and a *false alarm*, the probability of identifying that there are templates with a SNR above the predetermined threshold when there no such template exists it template bank, $P(r_{obs} > 0|r = 0)$.

Recall that quantum counting returns an integer b, between 0 and $2^p - 1$, from which we can estimate θ and therefore r. If there are no matches, perfect constructive interference occurs for $b = 0$ in Eq. 10.40 and $b = 0$ is returned with certainty. Thus identifying whether or not there

is a signal present simply requires us to check whether $b = 0$ or $b \neq 0$. There will be some probability of returning $b = 0$ in cases where there are in fact one or more matches, resulting in a false negative output of the algorithm. This may be made exponentially small through a constant number of repetitions. The resulting pseudocode is detailed in Algorithm 2. As discussed earlier 2^p is required to be $O(\sqrt{N})$ to give a sufficient accuracy to distinguish θ from zero. At the end of this subsection we discuss further the impact of the choice of p on the probability of a false negative.

Algorithm 2 Signal Detection
Complexity: $O\left((M \log M + \log N) \cdot \sqrt{N}\right)$

1: $p \leftarrow$ number of *precision digits*
2: $N \leftarrow$ number of *templates*
3: $i \leftarrow$index of *templates*
4: $\rho_{\text{thr}} \leftarrow$ *threshold*
5: $|0\rangle \leftarrow$ *Data* $|D\rangle$
6: **procedure** QUANTUM COUNTING(p, N, $|D\rangle$, ρ_{thr})
7: *Creating the counting register* :
8: $|i\rangle \leftarrow |0\rangle^p |i\rangle$
9: $|0\rangle^p |i\rangle \leftarrow \frac{1}{2^{p/2}}(|0\rangle + |1\rangle)^p \otimes |i\rangle$
10: *Controlled Grover' gate*:
11: **for all** $j < 2^p$ **do**
12: $a \leftarrow j$
13: **repeat**
14: Algorithm 1 GROVER'S GATE(N, $|D\rangle$, ρ_{thr}), $a - -$
15: **until** $a == 0$
16: $\frac{1}{2^{p/2}}(|0\rangle + |1\rangle)^n \otimes |i\rangle \leftarrow \frac{1}{2^{(p+1)/2}} \sum (e^{2i\theta j}|j\rangle \otimes |s_+\rangle + e^{-2i\theta j}|j\rangle \otimes |s_-\rangle)$
17: *Inverse Quantum Fourier Transform*:
18: $\frac{1}{2^{(p+1)/2}} \sum (e^{2i\theta j}|j\rangle \otimes |s_+\rangle + e^{-2i\theta j}|j\rangle \otimes |s_-\rangle) \leftarrow \frac{1}{2^{p+1/2}} \sum \sum (e^{i2\pi j(\frac{\theta}{\pi} - \frac{l}{2^p})}|l\rangle \otimes |s_+\rangle + e^{i2\pi j(\frac{\pi-\theta}{\pi} - \frac{l}{2^p})}|l\rangle \otimes |s_-\rangle)$
19: *Measurement (b)*:
20: **if** $b = 0$ **then**
21: **return** 'There is no match.'
22: **else** $r_{obs} \leftarrow$ **Round** $\left[N \sin\left(\frac{b}{2^p}\pi\right)^2\right]$
23: **if** $r_{obs} = 0$ **then**
24: $r_{obs} \leftarrow 1$

Discussion: The following is the explanation for each step and the related computational cost for Algorithm 2.

Signal detection:

- Step 0: Initialisation
  [Cost: $O(M + \log N)$]
  This is the same as the step 0 in Algorithm 1.

Quantum counting:

- Step 1 (line 7-9): Creating counting register
  [Cost: $O(\frac{1}{2} \log N)$]

This step involves applying a Hadamard gate to each qubit. Because this can be done in parallel for each indices, it would only incur a cost of 1. The state after this step would be

$$|\psi_4\rangle = \frac{1}{2^{p/2}} (|0\rangle_C + |1\rangle_C)^p \otimes \sum_i^N |i\rangle_I, \tag{11.6}$$

where the subscript C represents the counting register.

- Step 2 (line 10-16): Controlled Grover's Gate
  [Cost: $O((M \log M + \log N)\sqrt{N})$]
  In this step, we apply the Grover's gate a times to state $|a\rangle$. The cost is given by the largest number of iterations needed, 2^{p-1}. The state after this step is

$$|\psi_5\rangle = \frac{1}{\sqrt{2}} \sum_{a=0}^{2^p-1} e^{i2\theta_t a}|a\rangle_C \otimes |s_+\rangle_I + \frac{1}{\sqrt{2}} \sum_{a=0}^{2^p-1} e^{-i2\theta_t a}|a\rangle_C \otimes |s_-\rangle_I. \tag{11.7}$$

  Here we rewrite the index register as the two eigenstates $|s_+\rangle$ and $|s_-\rangle$ introduced in Eq. (10.36).

- Step 3 (line 17-18): Inverse quantum Fourier transform
  [Cost: $\frac{1}{4}(\log N)^2$ [161]]
  The inverse quantum Fourier transform is applied to the counting register to extract the eigenstates encoded in the phases, resulting in the state

$$\begin{aligned} |\psi_6\rangle = \frac{1}{2^{p+\frac{1}{2}}} \sum_{a=0}^{2^p-1} \sum_{b=0}^{2^p-1} \Big\{ & e^{i2\pi a\left(\frac{\theta_t}{\pi} - \frac{b}{2^p}\right)}|b\rangle_C \otimes |s_+\rangle_I \\ & + e^{i2\pi a\left(\frac{\pi-\theta_t}{\pi} - \frac{b}{2^p}\right)}|b\rangle_C \otimes |s_-\rangle_I \Big\}. \end{aligned} \tag{11.8}$$

- Step 4 (line 19-24): Measurement
  [Cost: $O(\frac{1}{2}\log N)$]
  The cost of measurement is 1 for each counting qubit. For the actual measurement we obtain a value b. According to Eq. 10.42, we can calculate an estimate of the number of matching templates r_{obs} based on Eq. 10.33. When there is no matching template, the probability of b being measured as 0 is 1. Therefore, any other observed value of b resulting in zero matching templates can be disregarded and thus corresponds to an estimate of at least one matching template.

Total Cost:

$$O\left((M \log M + \log N) \cdot \sqrt{N}\right), \tag{11.9}$$

We conclude by discussing the effect of the choice of p on the probability of a false negative, denoted δ_n. According to the discussion in Sec. 10.6, p can be written as

$$2^p = c\sqrt{N}, \tag{11.10}$$

and the following discussion is on the choice of the constant c and its effect on the probability of a false negative. We will use well-known bounds from the literature to motivate a particular choice

of c, and therefore p. This is not a unique choice, but rather is a convenient one for which we can readily bound δ_n.

In order to avoid triggering a false negative, the outcome of measurement of the counting register b should not be 0. According to [166], if $\tilde{b}$ is defined as either $\theta 2^p/\pi$ or $(2^p - \theta 2^p/\pi)$ (note that this is not in general an integer value), then the measured value b differs from $\tilde{b}$ by $|b - \tilde{b}| \leq 1$ with a probability at least $8/\pi^2$. Therefore, choosing p such that $\tilde{b} - 1 > 0$ ensures that the probability of a false negative is at most $1 - 8/\pi^2$. With this choice, Eq. 10.33 and 10.41 thus gives the following restriction on p:

$$2^p > \pi \sqrt{\frac{N}{r}}. \tag{11.11}$$

This restriction is most stringent when $r = 1$. Therefore, we obtain a lower bound for the choice of number of counting qubits:

$$2^p > \pi \sqrt{N}. \tag{11.12}$$

With this choice of p we can obtain a slightly tighter bound on the false negative probability as follows. To consider the amplitude for the measured state $|b\rangle$ for eigenstate $|s_+\rangle$, we can sum up all its amplitude across a:

$$\begin{aligned} P(b) &= \frac{1}{2^p} \sum_{a=0}^{2^p-1} e^{i2\pi a(\frac{\theta}{\pi} - \frac{b}{2^p})} |b\rangle && (11.13) \\ &= \frac{1}{2^p} \frac{e^{i2\pi 2^p(\frac{\theta}{\pi} - \frac{b}{2^p})} - 1}{e^{i2\pi(\frac{\theta}{\pi} - \frac{b}{2^p})} - 1} |b\rangle \\ &= \frac{1}{2^p} \frac{\sin\left(\pi 2^p(\frac{\theta}{\pi} - \frac{b}{2^p})\right)}{\sin\left(\pi(\frac{\theta}{\pi} - \frac{b}{2^p})\right)} e^{i\pi(2^p-1)(\frac{\theta}{\pi} - \frac{b}{2^p})} |b\rangle. && (11.14) \end{aligned}$$

The probability of state $|b\rangle$ would be:

$$P(b) = \frac{1}{2^{2p}} \left(\frac{\sin(2^p\theta)}{\sin(\theta - \frac{b\pi}{2^p})} \right)^2. \tag{11.15}$$

From the discussion previously, the only state situation will trigger a no signal result is when $|b\rangle = 0$. According to Eq. 11.15, the probability of false negative is:

$$\begin{aligned} P(r_{obs} = 0 | r > 0) &= P(b = 0) \\ &= \frac{1}{2^{2p}} \left(\frac{\sin(2^p\theta)}{\sin(\theta)} \right)^2. \end{aligned} \tag{11.16}$$

Using angle addition theorem we can simplify this probability into:

$$\begin{aligned} &P(r_{obs} = 0 | r > 0) \\ &= \frac{1}{2^{2p}} \left(\frac{\sin((2^p - 1)\theta)\cos(\theta) + \cos((2^p - 1)\theta)\sin(\theta)}{\sin(\theta)} \right)^2. \end{aligned} \tag{11.17}$$

Using the relation between N and p according to Eq. 11.10 and the relation between N and θ

according to Eq. 10.33, this probability can be further simplified into:

$$\begin{aligned}
&P(r_{obs} = 0|r > 0) \\
&= \frac{1}{c^2 N}\Big(\frac{\sin\left((c\sqrt{N}-1)\theta\right)\cos(\theta)}{\sin(\theta)} + \cos\left((c\sqrt{N}-1)\theta\right)\Big)^2 \\
&= \frac{1}{c^2 N}\Big(\frac{\sin\left((c\sqrt{N}-1)\theta\right)\sqrt{1-\frac{r}{N}}}{\sqrt{\frac{r}{N}}} + \cos\left((c\sqrt{N}-1)\theta\right)\Big)^2 \\
&\leq \frac{1}{c^2 N}\Big(\sqrt{\frac{N}{r}-1}+1\Big)^2.
\end{aligned} \tag{11.18}$$

Because we only consider cases in which $r \ll N$, the probability of false negative can be simplified into:

$$P(r_{obs} = 0|r > 0) = \frac{1}{c^2 r}. \tag{11.19}$$

Therefore, the probability of a false negative when there exists one or more templates can be expressed as:

$$\delta_{\mathrm{n}} = P(b = 0|r > 0) = \frac{1}{2^{2p}}\frac{N\sin^2(2^p\theta)}{r} \leq \frac{1}{2^{2p}}\frac{N}{r}. \tag{11.20}$$

With the choice in Eq. 11.12, this probability is inversely proportional to r, and for all r is bounded by:

$$\delta_{\mathrm{n}} < \frac{1}{\pi^2}. \tag{11.21}$$

We conclude that the signal detection algorithm based on quantum counting has a false alarm probability of 0 under all conditions, and a false negative probability of $1/\pi^2$, given the condition in Eq. 11.12 is met.

If the false negative rate is δ_{n} for each run, by repeating the whole procedure ℓ times, the probability of obtaining $b = 0$ every time is $\delta_{\mathrm{n}}^{\ell}$. Therefore, the total tolerance of our procedure would be $\delta_{\mathrm{n}}^{\ell} < \pi^{-2\ell}$. With a repetition logarithmic to its tolerance, the total complexity of the procedure is $O(\ell\pi\sqrt{N})$.

In gravitational wave research, practical applications normally involve between 10^4 to 10^{12} templates [174, 164]. With the lower bound of the number of templates, 10^4, p can be chosen to be 9 according to Eq. 11.12. In the classical case, the computational cost is approximately 10^4 oracle evaluations, while in the quantum case, 512 evaluations suffice for a single run of the signal detection algorithm. There is therefore an order of magnitude difference in cost even for cases with the lowest number of templates. The upper most extreme case that has been analysed has 10^{12} templates, in which p would be chosen as 22, resulting in a computational cost of around 10^7 oracle evaluations. As a specific example, for a false negative probability of $\pi^{-12} \simeq 10^{-6}$ (one in a million) a total of $6 \times 2^{22} \simeq 3 \times 10^7$ evaluations are required. To reduce this to a one in a billion chance of a false negative, 9 repetitions of the algorithm are needed, or a total of around 4.5×10^7 oracle evaluations. This is orders of magnitude smaller than the classical cost of 10^{12}.

11.1.3 Retrieving matched templates

In the case of a successful signal detection (the identification of 1 or more matching templates), we might wish to further examine its corresponding parameters using (one of) the matching templates. In this section, we will provide a pseudo algorithm to retrieve one or all matching templates.

The procedure to retrieve matching templates is based on Grover's algorithm in Algorithm. 1 and the result r_* of Algorithm 2. This is not the only way to retrieve a matching template given an unknown number of matches [175], but we anticipate that for most applications the signal detection algorithm would run first in order to determine whether there is any match above threshold. In any potential subsequent attempt to retrieve a matching template it is then natural to use the estimate r_* already obtained.

Algorithm 3 Template retrieval
Complexity: $O\left((M\log M+\log N)\cdot\sqrt{N}\right)$

1: $N \leftarrow$ number of *templates*
2: $i \leftarrow$ index of *templates*
3: $\rho_{\text{thr}} \leftarrow$ *threshold*
4: $|0\rangle \leftarrow$ *Data* $|D\rangle$
5: $r_{obs} \leftarrow$ number of *matched templates*
6: *Calculating the number of repetitions*:
7: $k_* \leftarrow$ **Round** $\left[\frac{\pi}{4}\sqrt{\frac{N}{r_{obs}}}-\frac{1}{2}\right]$
8: **procedure** RETRIEVE ONE TEMPLATE
9: **repeat**
10: Algorithm 1 GROVER'S GATE(N, $|D\rangle$, ρ_{thr}), $k_* --$
11: **until** $k_* == 0$
12: *Output*:
13: i_{correct}

Discussion: The following is the explanation for each step and the related computational cost for Algorithm 3. *Templates retrieval:*

- Step 0 (line 6-7): Calculating the number of repetitions
  [Cost: $O(1)$]
  The output r_{obs} from Algorithm 2 is imported into Algorithm 3, and we then calculate the number of required repetitions of Algorithm 1 from Eq. 10.34.

- Procedure 1 (line 8-13): Retrieve one template
  [Cost: $O\left(\sqrt{N/r_{obs}}\,(M\log M+\log N)\right)$]
  Grover's algorithm, Algorithm 1, will be repeated k_* times to achieve the desired template index. The value of k_* according to our previous discussion will be $O(\sqrt{N/r_{obs}})$.

  The total cost of Algorithm 2 and retrieving one template combined is:

$$O\left((M\log M+\log N)\cdot\sqrt{N}\right). \tag{11.22}$$

- Procedure 2 : Retrieve all matched templates
  In the case where all the matched templates are required to be found, it is not as trivial as

repeating Procedure 1 r (assuming $r_{obs} \approx r$) times because it samples with replacement. It is, instead, a coupon collector problem [176], which requires $\Theta(r \log r)$ repetitions of Procedure 1. As long as the number of matching templates is small comparing with the total number of templates in the bank, the complexity is the same for both procedures.

We conclude this section by discussing the overall probability of failing to return a matched template following this procedure. Note that if this probability is less than 0.5, then with a constant number of repetitions, it can be made negligibly small to ensure successful retrieval of a matched template[2].

Without loss of generality we consider in the following analysis only one eigenvalue in Eq. 10.40, corresponding to $|s_+\rangle$. Recall the state of the register after inverse Fourier transform $|\psi_6\rangle$ in Eq. (10.40). Without losing generality, only one eigenstate is considered for the analysis. According to Eq. (10.40), the probability of a certain $|b\rangle$ is measured in the whole state would simply be twice of the probability of that in one eigenstate. The corresponding probability distribution for different measured values b is given in Eq. 11.15. In any given run of the procedure, the probability of returning a matched template according to Eq. 10.29 is therefore given by:

$$P(\text{Match}) = |\sin((2k_* + 1)\theta)|^2, \tag{11.23}$$

where k_* is the number of Grover's applications calculated through Eq. 10.34 from the outcome b of Algorithm 2 and corresponding estimates θ_*, r_*. Using Eq. 11.15, the overall probability of failing to retrieve a matched template is given by:

$$\begin{aligned} P(\text{Fail}) &= \sum_{l=0}^{2^p} P(\text{Fail}|b = l)P(b = l) \\ &= \frac{1}{2^{2p}} \sum_{l=0}^{2^p} \left(\frac{\sin\left(2^p\theta\right)}{\sin(\theta - \frac{\pi l}{2^p})} \right)^2 |\cos((2k_l + 1)\theta)|^2, \end{aligned} \tag{11.24}$$

where k_l is the number of repetitions of Grover's algorithm when $b = l$.

Let b' be the closest integer larger than $2^p\theta/\pi$, i.e. $b' = \lceil 2^p\theta/\pi \rceil = 2^p\theta/\pi + \epsilon$ where $0 \leq \epsilon \leq 1$; and b'' the closest integer smaller than $2^p\theta/\pi$ such that $b'' = 2^p\theta/\pi - (1 - \epsilon)$. b' and b'' are also the most probable values; recall that the probability that the measured b value falls into the interval of $|b - \tilde{b}| \leq 1$ is larger than $8/\pi^2$ [166]. This is illustrated in Fig. 11.1 based on Eq. 11.15 where the central peak contains the two most probable b states.

Now an upper bound for $P(\text{Fail})$ is given by only considering the probability of successfully retrieving a template for these two most probable outcomes:

$$\begin{aligned} P(\text{Fail}) < P(b')P(\text{Fail}|b') + P(b'')P(\text{Fail}|b'') \\ + (1 - P(b') - P(b'')). \end{aligned} \tag{11.25}$$

[2]There is nothing special about 0.5 here, as long as the probability of failure is bounded away from 1 this is enough; 0.5 is a convenient choice.

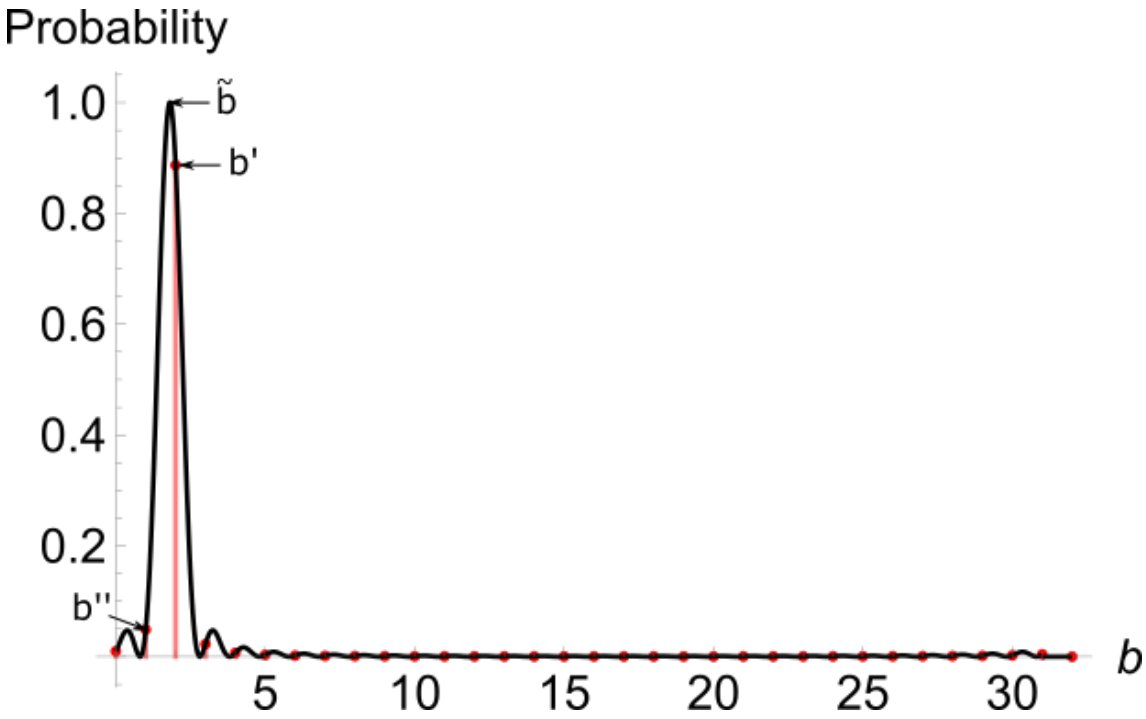

Figure 11.1 The red dotted line corresponds to the probability distribution for each state in a 5-qubit counting register, with two templates matching in a 64-template bank corresponding to one eigenvalue defined in Eq. 10.35. The black line is plotted according to Eq. 11.15 as a continuous function. Each peak contains one b state with a width of 1, except for the central peak which has the two most probable b states and a width of 2. The upper integer b state to $\tilde{b}$ is referred to as b' while the lower as b''. The curve peaks at either $2^p\theta/\pi$ or $2^p(\pi-\theta)/\pi$, depends on which eigenvalue the curve corresponds to, and it is labelled as $\tilde{b}$.

Now, to estimate $P(\text{Fail}|b')$, note using Eq. 10.34 that:

$$\begin{aligned} k_{b'} &= \left[\frac{\pi}{4\theta_*} - \frac{1}{2}\right] \\ &= \frac{\pi}{4\theta_*} - \frac{1}{2} \pm \epsilon_k, \\ &= \frac{2^{p-2}}{b'} - \frac{1}{2} \pm \epsilon_k, \end{aligned} \tag{11.26}$$

where in the second line $0 \leq \epsilon_k \leq 0.5$, and in the third line we have used Eq. 10.42. In the context of gravitational wave searches, i.e. $N \gg r$, the small angle approximation can be applied and consequently, $\theta \approx \sqrt{r/N}$. Thus

$$\begin{aligned} (2k_{b'}+1)\theta &= \frac{2^{p-1}}{b'}\theta \pm 2\epsilon_k\theta \\ &= \frac{\tilde{b}}{b'}\frac{\pi}{2} + O\left(\sqrt{\frac{r}{N}}\right), \end{aligned} \tag{11.27}$$

from which we obtain using Eq. 11.23

$$\begin{aligned} P(\text{Fail}|b') &= 1 - |\sin((2k_{b'}+1)\theta)|^2 \\ &= \left|\cos\left(\frac{\tilde{b}}{b'}\frac{\pi}{2}\right)\right|^2 + O\left(\sqrt{\frac{r}{N}}\right) \\ &= \left|\cos\left(\frac{b'-\epsilon}{b'}\frac{\pi}{2}\right)\right|^2 + O\left(\sqrt{\frac{r}{N}}\right) \\ &= \left|\sin\left(\frac{\epsilon}{b'}\frac{\pi}{2}\right)\right|^2 + O\left(\sqrt{\frac{r}{N}}\right). \end{aligned} \tag{11.28}$$

We can also rewrite $P(b')$ as follows:

$$\begin{aligned} P(b') &= \frac{1}{2^{2p}}\left(\frac{\sin\left(2^p\theta\right)}{\sin(\theta - \frac{\pi b'}{2^p})}\right)^2 \\ &= \frac{1}{2^{2p}}\left(\frac{\sin\left(\tilde{b}\pi\right)}{\sin\left(\frac{\pi}{2^p}\epsilon\right)}\right)^2 \\ &\simeq \left(\frac{\sin\left(\epsilon\pi\right)}{\pi\epsilon}\right)^2 \end{aligned} \tag{11.29}$$

where in the last line we have used the small angle approximation for $\pi\epsilon/2^p$, and $\tilde{b} = b' - \epsilon$. With similar arguments for b'', the bound becomes:

$$\begin{aligned} P(\text{Fail}) < 1 &- \left(\frac{\sin\left(\pi\epsilon\right)}{\pi\epsilon}\right)^2 \left(\cos\left(\frac{\epsilon}{b'}\frac{\pi}{2}\right)\right)^2 \\ &- \left(\frac{\sin\left(\pi(1-\epsilon)\right)}{\pi(1-\epsilon)}\right)^2 \left(\cos\left(\frac{1-\epsilon}{b''}\frac{\pi}{2}\right)\right)^2 + O\left(\sqrt{\frac{r}{N}}\right) \end{aligned} \tag{11.30}$$

Recall from Eq. 11.12, we choose $p = \lceil \log_2(\pi\sqrt{N})\rceil$. It is convenient to express this as $p = \log_2(\pi\sqrt{N}) + \epsilon_p$, where $0 < \epsilon_p < 1$. Therefore $\tilde{b}$ may be written:

$$\begin{aligned} \tilde{b} &= \frac{2^p\theta}{\pi} \\ &= \frac{\pi\sqrt{N}2^{\epsilon_p}}{\pi}\sqrt{\frac{r}{N}} \\ &= 2^{\epsilon_p}\sqrt{r}. \end{aligned} \tag{11.31}$$

Recall that $b' = \lceil\tilde{b}\rceil$, and so b', ϵ become:

$$b' = \lceil 2^{\epsilon_p}\sqrt{r}\rceil; \quad \epsilon = \lceil 2^{\epsilon_p}\sqrt{r}\rceil - 2^{\epsilon_p}\sqrt{r}. \tag{11.32}$$

Thus for each r we can write Eq. 11.30 in terms of a single parameter, ϵ_p, between 0 and 1 (neglecting the $O(\sqrt{r/N})$ term). We optimise this numerically and plot the bound for various values of r in Fig. 11.2. In all cases this is less than 0.453, the value found numerically for $r = 1$,

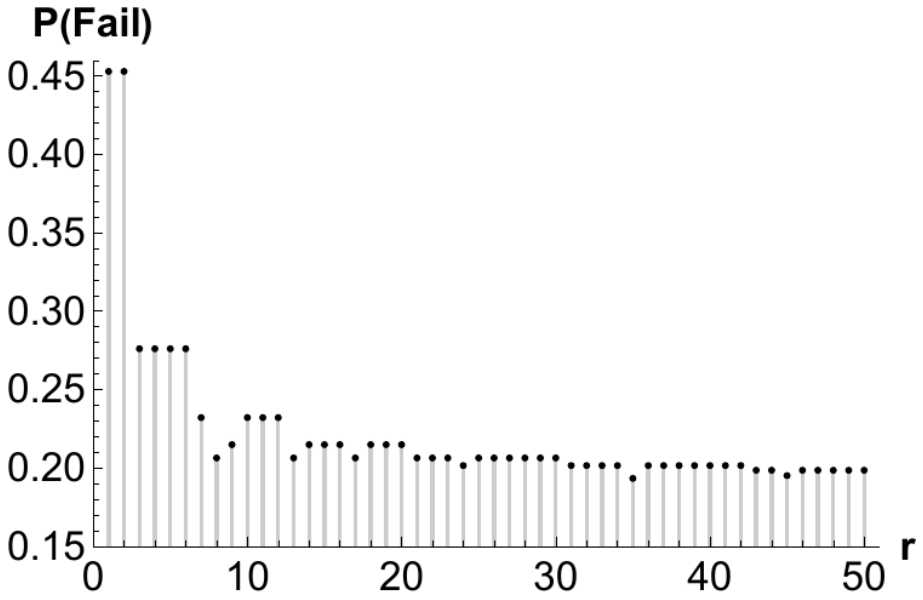

Figure 11.2 This shows for large N, the joint probability of obtaining outcome b and subsequently failing to retrieve a matched template is bounded by 0.45 for different number of matching templates r, according to Eq. 11.30.

ensuring the probability of successfully retrieving a template is no smaller than:

$$P(\text{Success}) \geq 0.547. \tag{11.33}$$

Note that for large r (but still requiring $r << N$),

$$P(\text{Fail}|b') \simeq P(\text{Fail}|b'') \simeq \sin^2\left(\frac{1}{\sqrt{r}}\frac{\pi}{2}\right) \simeq O\left(\frac{1}{r}\right)$$

and thus we can expect the bound on the probability of failure to decrease with r to a limit given by:

$$\begin{aligned} P(\text{Fail}) &< 1 - P(b') - P(b'') + O\left(\frac{1}{r}\right) \\ &= 1 - \frac{8}{\pi^2} + O\left(\frac{1}{r}\right). \end{aligned} \tag{11.34}$$

We here provide a specific example of the total probability of failing to retrieve a matching template corresponding to Eq. 11.24 in Fig. 11.3. This example has a template bank of 2^{17} templates, with $r = 9$, a real gravitational wave signal GW150914 that will be discussed in Sec. 11.3. The total failing probability $P(\text{Fail}) \approx 0.34 < 0.5$. Therefore, with a constant number of repetitions of Alg. 2 and Alg. 3, we are guaranteed with a matched template returned at a complexity of $O\left((M \log M + \log N) \cdot \sqrt{N}\right)$. This is less than the classical cost of $O(NM \log M)$. Therefore, we conclude that our quantum algorithm offers a $\sqrt{N}$ speed up with a practical oracle when the number of matching templates is small compared with the total number of templates in the bank.

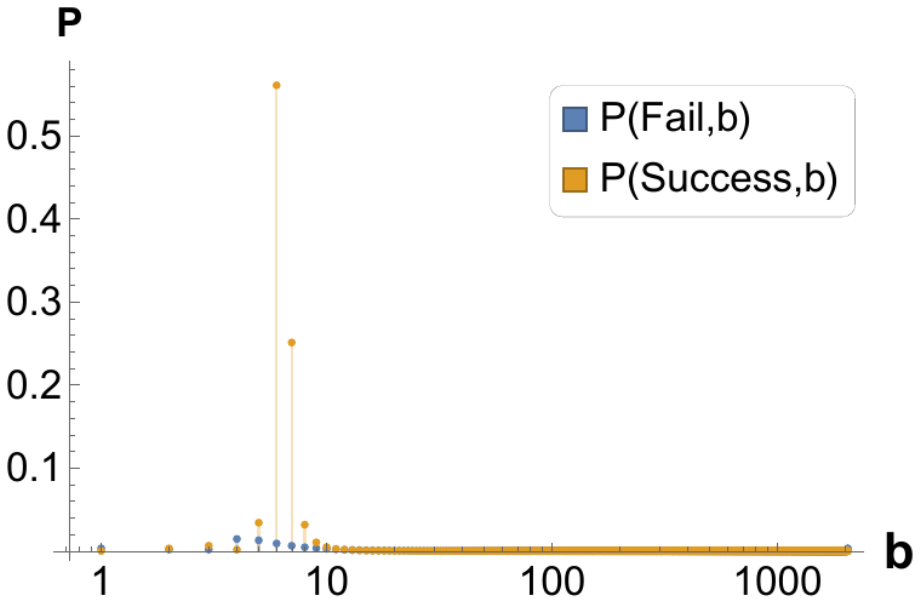

Figure 11.3 For the case of a template bank with 2^{17} templates, and $r = 9$, the joint probability of obtaining outcome b and subsequently failing to or succeeding at retrieving a matched template are plotted in blue and yellow respectively. The total probability of $P(\text{Fail}) \approx 0.34 < 0.5$.

11.2 Example using Qiskit

In this section, we will present our proof of principle model of template matching on a quantum computer using IBM's Qiskit library [177] and their quantum computer simulator *ibmq_qasm_simulator*[3].

Matching to real gravitational wave data requires a much larger quantum processor than is currently available; in Section 11.3 we will present a classical simulation of matching to actual detector data using python. Later we also discuss the space requirements of the matched filtering algorithm. Here, in order to demonstrate the basic features of a realisation on a quantum processor, we implement a simplified algorithm in which we imagine the data is an n-bit string and the templates are all possible n-bit strings. This means that the templates themselves are identical to the index, and there is no need to explicitly perform the template generation steps (Algorithm 1 Step 1). We consider that a template is a match to the data if the bit strings are identical, however to simulate the possibility of non-exact matches, we disregard the q lowest order bits and require only the $n - q$ highest order bits to match. The choice of q is analogous to the choice of threshold SNR value ρ_{thr} in the main algorithm. The proof of principle demonstration presented here is thus an example of string matching, a problem considered in [178, 179, 180].

The data consists of an n-qubit string stored in binary form in the data register $|D\rangle$, where the first q qubits are ignored allowing for 2^q matching templates among 2^n total templates. Hadamard gates are used to initialise the template register $|T\rangle$ to store a superposition of all possible n-bit templates. The output qubit $|d\rangle$ in Eq. 10.18 is stored in the ancilla register $|A\rangle$. An extra counting register with p qubits is added for the quantum counting procedure.

In our template matching oracle, which is presented in Fig. 11.4, we match the template reg-

[3]The QasmSimulator backend is designed to mimic an actual device. It executes a Qiskit QuantumCircuit and returns a count dictionary containing the final values of any classical registers in the circuit.

ister and the data register qubit-by-qubit using CNOT gates. In the case of an exact match, all the qubits in the template register would be turned into state $|0\rangle$. Therefore, after bit flipping, we can use a multiple-control-NOT gate to realise phase kickback on the ancillary qubit initialised into the $|-\rangle$ state. The diffusion operator is constructed by a combination of Hadamard gates, NOT gates and a C^n-Z gate, and is illustrated in Fig. 11.4.

In gravitational wave searches, the true signal parameters will lie somewhere within the template bank parameter space and no template will be identical to the signal. Therefore, a predetermined ρ_{thr} is chosen as the threshold in Algorithm. 1. The number of templates possessing ρ over this threshold, if there are any, is unknown. Since the optimal number of applications of Grover's search algorithm is dependent on the number of templates with ρ over the threshold, we need to apply the quantum counting algorithm first.

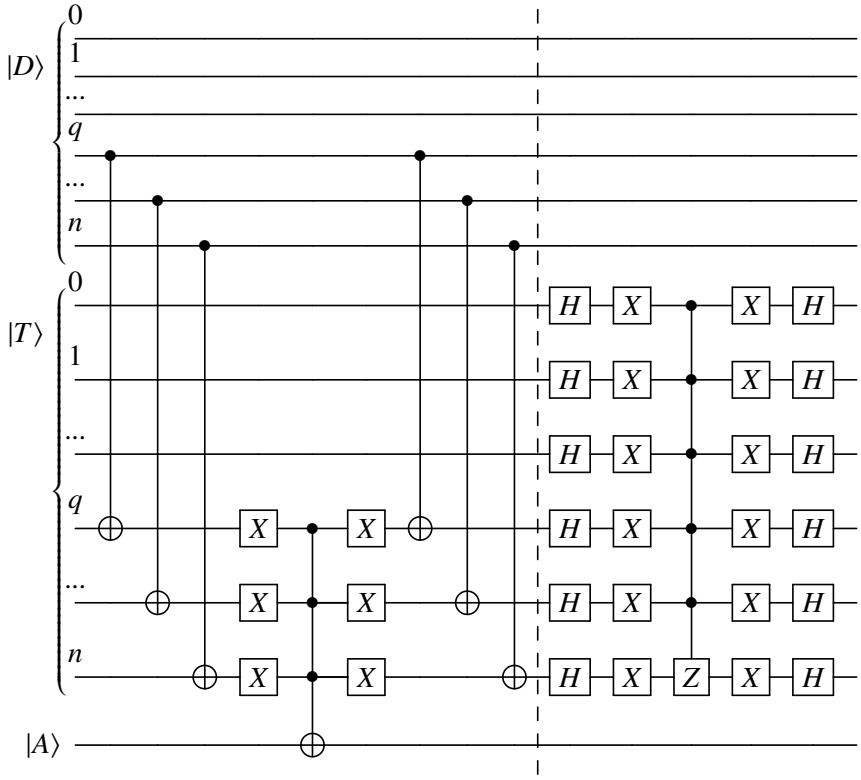

Figure 11.4 Quantum circuit diagram for our multiple-template matching oracle and the diffusion operator, which are separated by the vertical dashed line. The $|D\rangle$ and $|T\rangle$ variables represent the data and template registers respectively and $|A\rangle$ is the ancilla qubit. The numbers label the i^{th} qubit in the respective register. To simulate multiple matches, the oracle does not act on the first q qubits. When there is only one matching template q would be 0.

To demonstrate a proof of principle of our algorithm, we implement this simplified version with a range of qubits for data and omission, allowing for multiple templates matching. For each pair n, q, we run the quantum counting algorithm first, in order to estimate the number of matches r, and then Grover's algorithm to find a match. From the output of the quantum counting algorithm, we take the most probable value of b to calculate an estimated r_* and k_* for the template retrieval phase. For each algorithm the experiment is trialed 2048 times and the output of the simulator gives a set of probabilities calculated from the number of occurrences of each possible measured value. The results are presented in Table. 11.1. The number of counting qubits, p, is based on

Eq. 11.12. When the number of qubits for the data, n, is small, p is close to n. However, as n increases, the difference between n and p increases as well, allowing us to maintain the speedup of $\sqrt{N}$ discussed in Sec. 11.1. The parameters k_* and k are the estimated and true number of applications of Grover's gate needed, given by the quantum counting process by Eq. 10.42 and Eq. 10.34 with $r = 2^q$ respectively. The probability of the search process returning us with one of the matched templates given the most probable value of b is over 78% in all cases, and the estimated number of templates, r_{obs} differs from the actual number of matched templates, 2^q, by no more than 2.

ignored qubits q	data length n	counting qubits p	measured count b	Grover's iter. est. k_*	est. No. templates r_{obs}	Grover's iter. theo. k	P(Succ.)
0	5	5	30	4	1	4	0.9995
	6	5	1	6	1	6	0.9961
	7	5	1	8	1	8	0.9956
	8	6	1	12	1	12	1
	9	7	2	17	1	17	0.9990
1	5	5	3	2	3	3	0.9092
	6	5	30	4	2	4	0.9985
	7	6	61	5	3	6	0.9619
	8	6	2	8	2	8	0.9961
	9	7	125	10	3	12	0.9365
	10	7	126	17	2	17	0.9995
2	5	5	4	1	5	2	0.7885
	6	5	29	2	5	3	0.9072
	7	6	60	3	5	4	0.8926
	8	6	61	5	6	6	0.9688
	9	7	124	7	5	8	0.9429
	10	7	125	10	6	12	0.9395

Table 11.1 Trial runs of our algorithm with 2048 iterations on *ibmq_qasm_simulator*. We compare the number of iterations Grover's algorithm should apply and the number of matched templates based on the measured result, to their theoretical counterparts across a range of data with different number of qubits with various number of omitted qubits in the matching process. We also state the P(Success) as the probability of our algorithm returning us with a matched template in the final search in each case. The number of counting qubits is the minimum allowed by Eq. 11.12 to minimise the false negative rate, δ_n.

A specific instance is illustrated in Fig. 11.5 and 11.6. This case corresponds to $n = 6$, $q = 1$, and the data is fixed to be 000110. $q = 1$ means that we look to find templates that match at least the last 5 qubits, i.e., 000110 and 000111. This is the same scenario as the analytical example we presented in Fig. 10.9, and described in Sec. 10.6. The result of the quantum counting process is shown in Fig. 11.5 where we can see that the measured values corresponding to the two eigenvalues from Eq. 10.35 are the most probable to be obtained. Converting the state indices from binary to decimal, our result is a bimodal distribution with 2 modes: 2 and 30 are the locations of the mode peaks with a standard deviation less than 2. Both cases correspond to an estimate of 4 for k_*, the same as the true value of k calculated from the real number of templates. Although this result does

not exactly equal that given in Fig. 10.9, the fact that this algorithm is performed on a quantum simulator with limited number of runs needs to be taken into consideration.

In Fig. 11.6, we show the result of the Grover's search process based on the result from Fig. 11.5, in which the two matching templates are recovered with high probability in relation to other templates. Since they form an equal superposition, the two matched templates are assigned approximately equal probability. After performing 2048 trials of simulation in our results, the two matched templates constitute altogether a success probability > 99%.

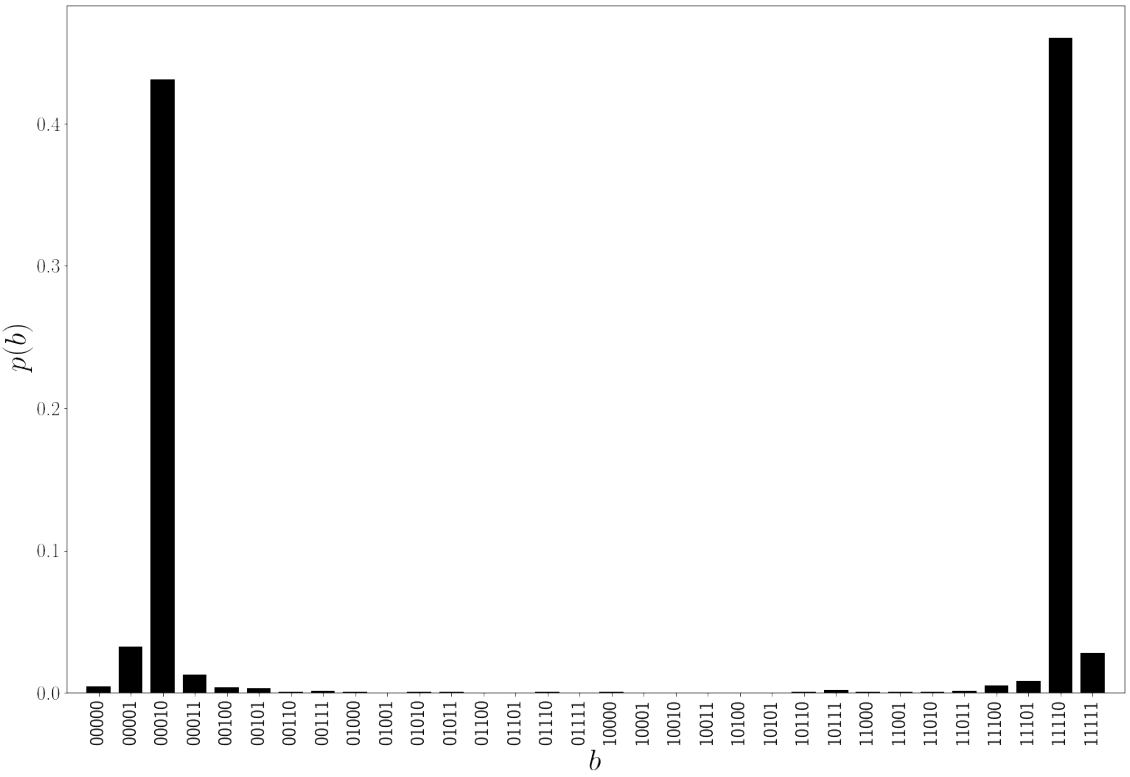

Figure 11.5 The measurement of the quantum counting process for 6-qubit data matching with a 5-qubit counting register. The first qubit is ignored to allow for two templates matching. The theoretically most frequent outcome b in this case, according to Eq. 10.41, should be either 2 or 30. The most probable measurement result is 11110, which in decimal is 30.

11.3 Example Search for GW150914

Our collaborator in the Institute for Gravitational Research in University of Glasgow applied this method to gravitational wave detection. The specific case chosen is the detection of the first gravitational wave event GW150914 [18]. The template bank size is not possible to be analysed on Qiskit platform, because it has at most 32 qubits at the time of this project being conducted. We compute the amplitudes of quantum states that correspond to the template and counting register at various stages of the algorithm described in Sec. 11.1 using python code. The gravitational wave strain time-series data that we choose to analyse is from the LIGO Hanford detector and is centered around the GW150914 event time (GPS time 1126259462.4). It is 28 s in duration and sampled at a rate of 4096 Hz. The data is initially whitened and passed through a high-pass filter with a 20 Hz

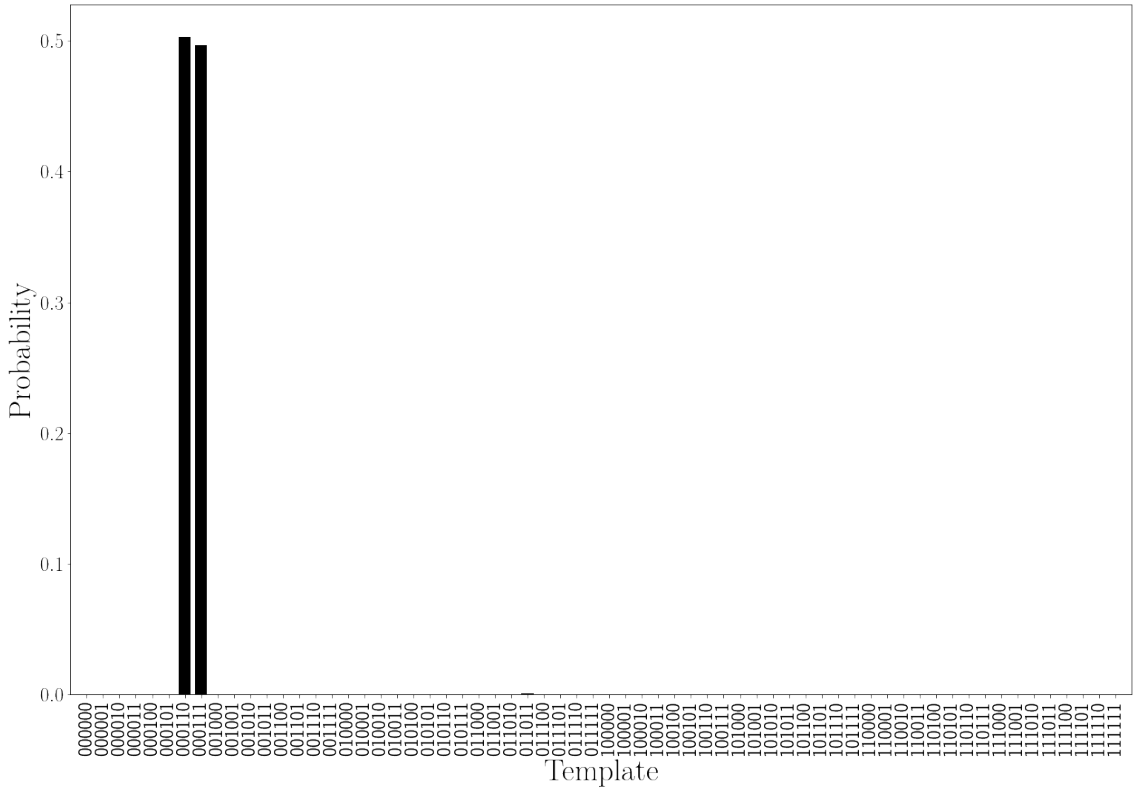

Figure 11.6 The measurement of the Grover's search process for 6-qubit data matching. The data is set as 000110 and the lowest qubit is ignored to allow for two templates matching. With 4 iterations suggested by the quantum counting process as a numerical output, the two templates that meet the matching criteria are returned with a probability higher than 99% altogether after 2048 trials on *ibmq_qasm_simulator*.

lower cut-off frequency. The resulting time-series is shown in Fig. 11.7 in black. An approximate matching template is plotted overlaying the data in orange. We perform our analysis on a bank of 2^{17} templates covering the 4-dimensional search space defined by the component masses $m_{1,2}$ and the aligned spin magnitudes $s_{1,2}$ of the binary system. We search these templates to find instances that correspond to matching templates with a SNR higher than a predefined threshold.

11.3.1 Signal Detection

After FFT the strain data into frequency domain, it is stored in $|D\rangle$, the data register, in computation basis. The indices for each of the N template are represented by $|i\rangle$ in superposition. The same is done to the 2^p states in the counting register as described in Alg. 2 lines 7-9. The controlled Grover's operator is applied to $|\psi_0\rangle$ as described by Alg. 2 lines 10-16 to compare the templates to the data using Alg. 1 as a subroutine. The templates are created from $|i\rangle$ to produce $|T_i\rangle$ as described in lines 3-5 of Alg. 1. Like the current measures in most classical examples, in this project, this step is done by using a look-up table that is computed prior to the analysis [182] that accepts a given index as a key and returns the set of parameters $\{m_1, m_2, s_1, s_2\}$ corresponding to the template. The parameters are then given to the phenomenological waveform model IMRPhenomD to produce the template [183, 184, 185]. For a quantum computer this step cannot be done using such a look-up table as this would rely on using qRAM. Instead an algorithm is required that maps

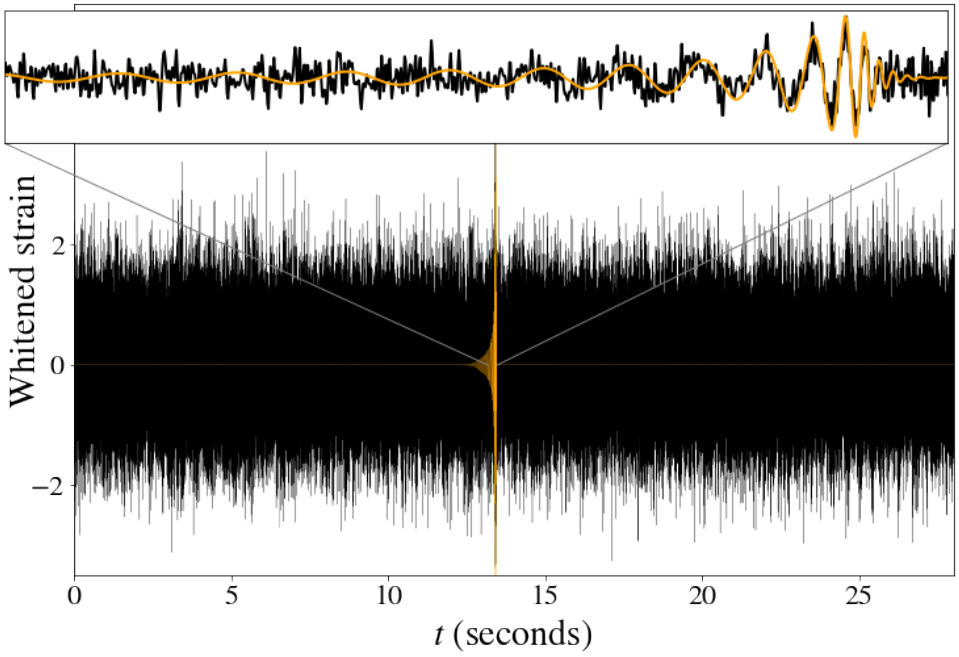

Figure 11.7 Whitened time-series data (black) of the gravitational wave event GW150914 sampled at 4096 Hz after a 20 Hz highpass filter overlaid by a signal template (orange) with component masses $m_1 = 35.6\,M_\odot$ and $m_2 = 30.6\,M_\odot$ and with zero aligned spin, taken from [181]. The signal can be more clearly seen in the 0.25 s plot in the upper panel.

the N template indices to their respective locations in the parameter space as long as this algorithm is executable on a classical computer. This is based on the fact that any classical algorithm can be performed on a quantum computer and made reversible with at most polynomial overhead [163]. This kind of algorithm can be based on existing classical algorithms, such as those used for lattice-based template placement [186, 187, 188, 189, 190].

For each template in the bank, the oracle calculates ρ for each time step using Eq. 10.11 which produces $\{\rho_i(t_1), \ldots, \rho_i(t_M)\}$ where $M = 28 \times 4096$ is the number of time steps. A classical search algorithm is also written into the oracle to find $\rho_i^{\max} = \max(\{\rho_i(t_1), \ldots, \rho_i(t_M)\})$. In actual quantum computing, it would be possible to conduct these two steps in parallel for each mass templates. The analysis is repeated with $\rho_{\text{thr}} = 8, 12, 16, 18$ for $p = 11$, which is the fewest number of qubits in the counting register to meet the condition set in Eq. 11.11.

An estimate of the number of matching templates can be made from quantum counting as described in lines 17-18 of Alg. 2 by applying the inverse QFT across the counting register states $\{|j\rangle\}$ to obtain $\{|l\rangle\}$. Fig. 11.8 displays the probabilities of each outcome b after a measurement is performed on the counting register for different ρ_{thr} with $p = 11$. The probability of different outcomes after measuring the counting register for the four different cases are compared to the non-integer value $\tilde{b}$, defined by the exact solutions of Eq. 10.41, and plotted with a dotted line in Fig. 11.8. The most probable outcome corresponds to b' or b'' for each case, where the form of the distributions are governed by Eq. 11.15. The outcome of measuring the counting register can equally be represented in terms of a prediction of the number of matching templates according to

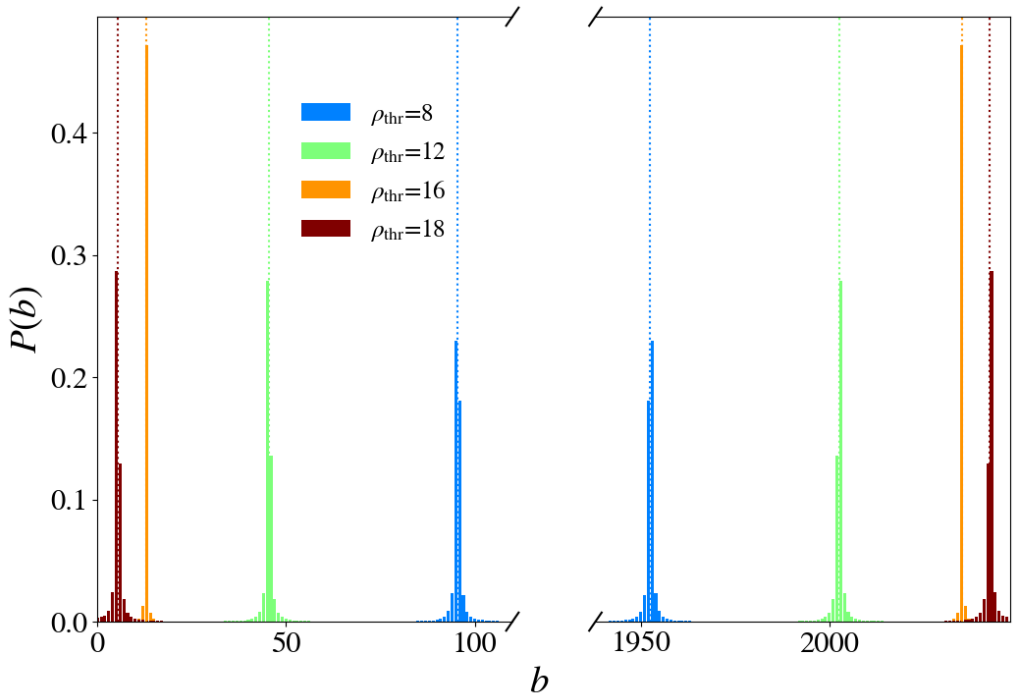

Figure 11.8 The probability of different outcomes b of measuring the counting register after the inverse quantum Fourier transform is applied. This process is described by lines 17-18 for the different cases of ρ_{thr} given $p = 11$. The distributions are compared to the corresponding value of $\tilde{b}$ (dotted). The probability distributions corresponding to the two eigenvalues of Grover's operator are closer to 2^{p-1} for cases with more matched templates (lower ρ_{thr}). Cases with fewer matched templates are closer to the extremities of the range of b and have an increased probability of not identifying any matched templates, corresponding to $P(b = 0)$. This probability can be reduced by repeating the algorithm.

Eq. 10.33 and Eq. 10.41 as shown in Fig. 11.9 for the example cases. For each ρ_{thr} considered, the distributions peak near the actual number of matching templates. Notably, the probability of obtaining an outcome that corresponds to a non-zero number of matching templates is much greater than the probability of an outcome corresponding to zero matching templates for all cases. This is equivalent to the probability of obtaining an outcome other than $b = 0$ in Fig. 11.8. Obtaining an outcome of $b = 0$ given the case where there are matching templates is a false negative, the probability of which is governed by Eq. 11.21. Therefore the rate of false negatives (made in addition to that produced from the classical matched filtering approach) can be reduced by repeating the Signal Detection procedure. This should be compared to the case where there are no matching templates to identify. In this case the measurement of the counting register always results in $b = 0$ corresponding to no matching templates. This negates the possibility of the analysis producing additional false alarms to the classical matched filtering approach as $P(r_{obs} > 0|r = 0) = 0$. If we only wish to determine if a signal is present in the data or not then the analysis can stop at this stage after the counting register is measured. The cost of determining this outcome requires $2^p - 1$ enquiries of the oracle, in comparison to the $\sim O(N)$ calculations of $\{\rho(t_1), \ldots, \rho(t_M)\}$ from Eq. 10.11 in the classical case.

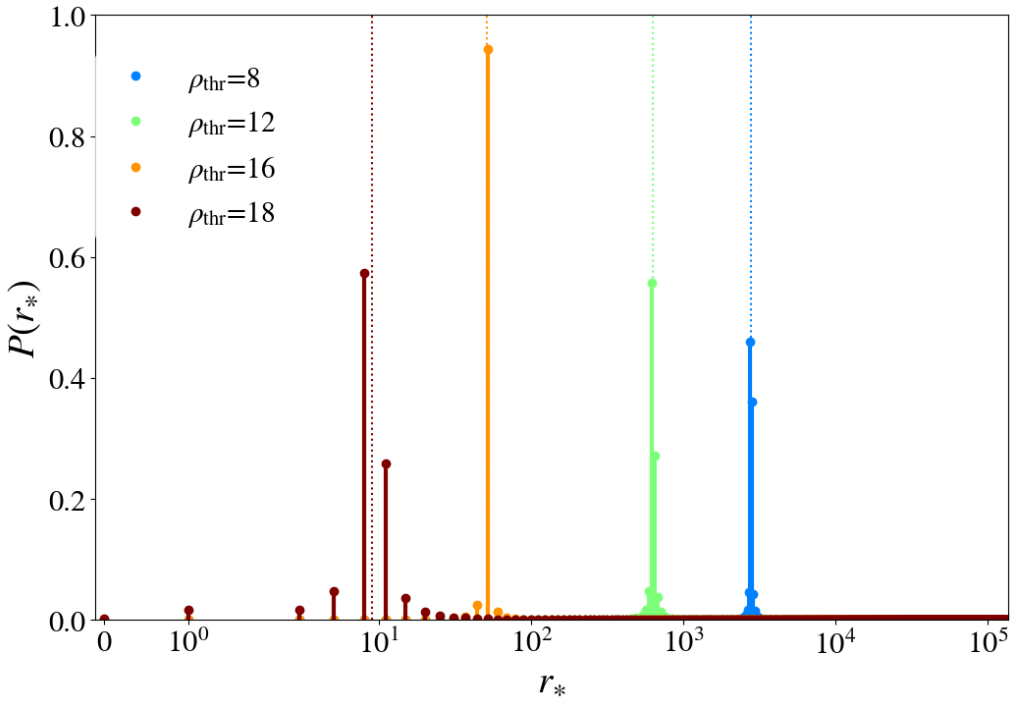

Figure 11.9 The probability distributions of outcomes from measuring the counting register from Fig. 11.8 transformed to estimates on the number of matching templates r_{obs} for each of the different cases of ρ_{thr}. The distributions are compared to the true number of matching templates r (dotted).

11.3.2 Retrieving Matching Templates

The optimal number of Grover's operations is estimated using Eq. 10.34 based on the output of r_{obs} from the prvious procedure in Sec. 11.3.1. Fig. 11.10 shows the probability of obtaining different values of k_* from the measurement for different **SNR** of $\rho_{\text{thr}} = 8, 12, 16, 18$. The distributions peak around k which is indicated by the dotted line. Fig. 11.10 is truncated at $(2^{p-1} - 1)/2$, so as to exclude the outcome corresponding to zero matching templates and only consider outcomes of $b > 0$.

The Template Retrieval procedure in Alg. 3 can be applied to obtain a matching template based on the resulting k_*. Similar to the previous procedure Signal Detection, this also requires initializing $|\psi_0\rangle$ from Eq. 11.1 and then applying Grover's Gate in Alg. 1 to this state iteratively k_* times. In this way, the probability of an index corresponding to a matching template will be maximized. As demonstrated from Eq. 10.40, being degenerate states, each state corresponding to a match will be amplified equally so that the probability of obtaining any given matching template is the same. For a given k_*, the probability of obtaining a matching template is governed by Eq. 11.23.

Fig. 11.11 shows how the template states respond to the the Template Retrieval procedure in their corresponding positions in the parameter space for each of the different ρ_{thr} cases from Sec. 11.3.1. The parameter space is comprised of three parameters: the component masses m_1 and m_2 of each binary system and the system's effective spin $\chi_{\text{eff}} = (s_1/m_1 + s_2/m_2)/(m_1 + m_2)$, a reparameterization of the component spins that adequately expresses their effect on the template waveforms as a single parameter. Fig. 11.11 contains three projections, each one demonstrating

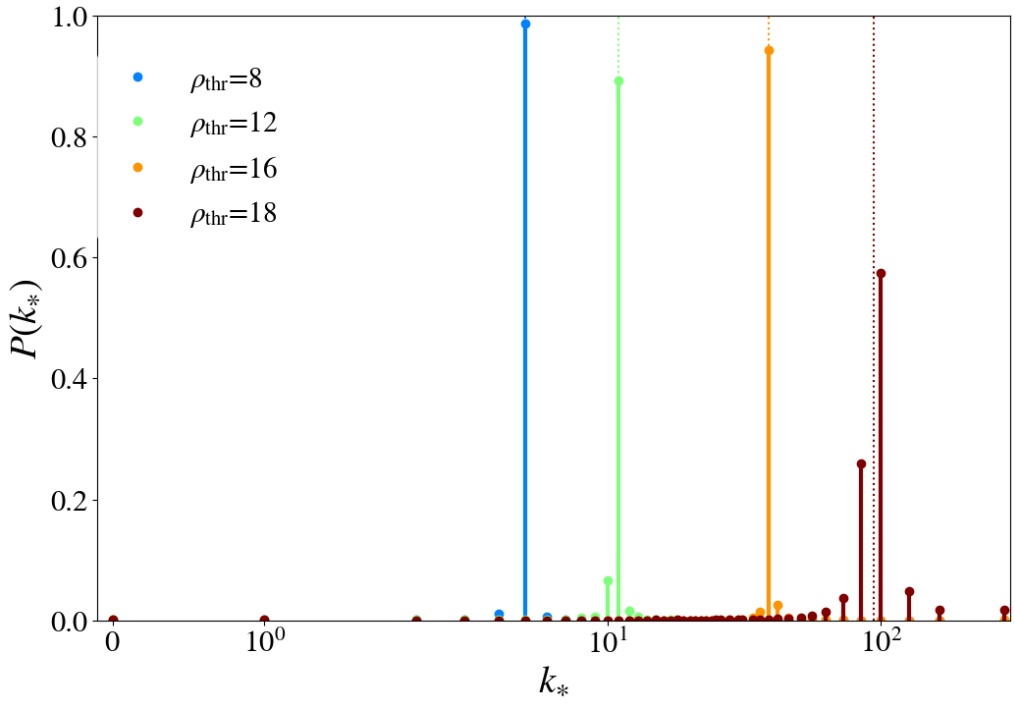

Figure 11.10 The probability distributions of outcomes from measuring the counting register from Fig. 11.8 transformed to estimates on the optimal number of Grover's applications k_* for each of the different cases of ρ_{thr}. The probabilities are compared to the true k (dotted) for each case.

how one parameter is compared with another one. The templates meeting the matching criteria are marked by the colour corresponding to the maximum ρ_{thr}. Therefore templates with a high ρ_{thr} are a subset of lower ρ_{thr} values. The size of the template labels is scaled to the log probability of obtaining the index of that template from the measurement after k_* application of Grover's operations. The highest ρ in this template bank is 19.05 from classical calculation. This template is highlighted in the figure which coincides with one of the templates corresponding to a match with $\rho_{\text{thr}} = 18$.

As we have discussed previously in Sec. 11.1.3, if the Template Retrieval procedure fails to return a matching template then we can choose to repeat our algorithm until a matching template is found. In Fig. 11.12, given the $\rho_{\text{thr}} = 18$ case with $p = 11$, we compare two scenarios with the classical case in order to demonstrate there does exist a $\sqrt{N}$ speed up. The first scenario, as shown in the red histogram, 10,000 simulations of measuring the counting register are made after the Signal Detection procedure to obtain k_*, before repeating Template Retrieval for each k_* until a matched template is found. The second scenario, as demonstrated in the blue histogram, is to only repeat the Signal Detection procedure after repeated failures to retrieve a matching template to obtain another k_* to use. In Fig. 11.12 we adopted the most extreme case, that the Signal Detection procedure is repeated after each Template Retrieval procedure that failed to retrieve a matching template. The number of times of accessing the oracle U_f (phase kickback in Eq. 10.19, which is comparable to the cost of **SNR** calculation) for each simulation is shown in the corresponding histogram of Fig. 11.12 with its mean indicated by the same coloured dashed line. These can be compared to the number of times **SNR** is evaluated in the classical search case

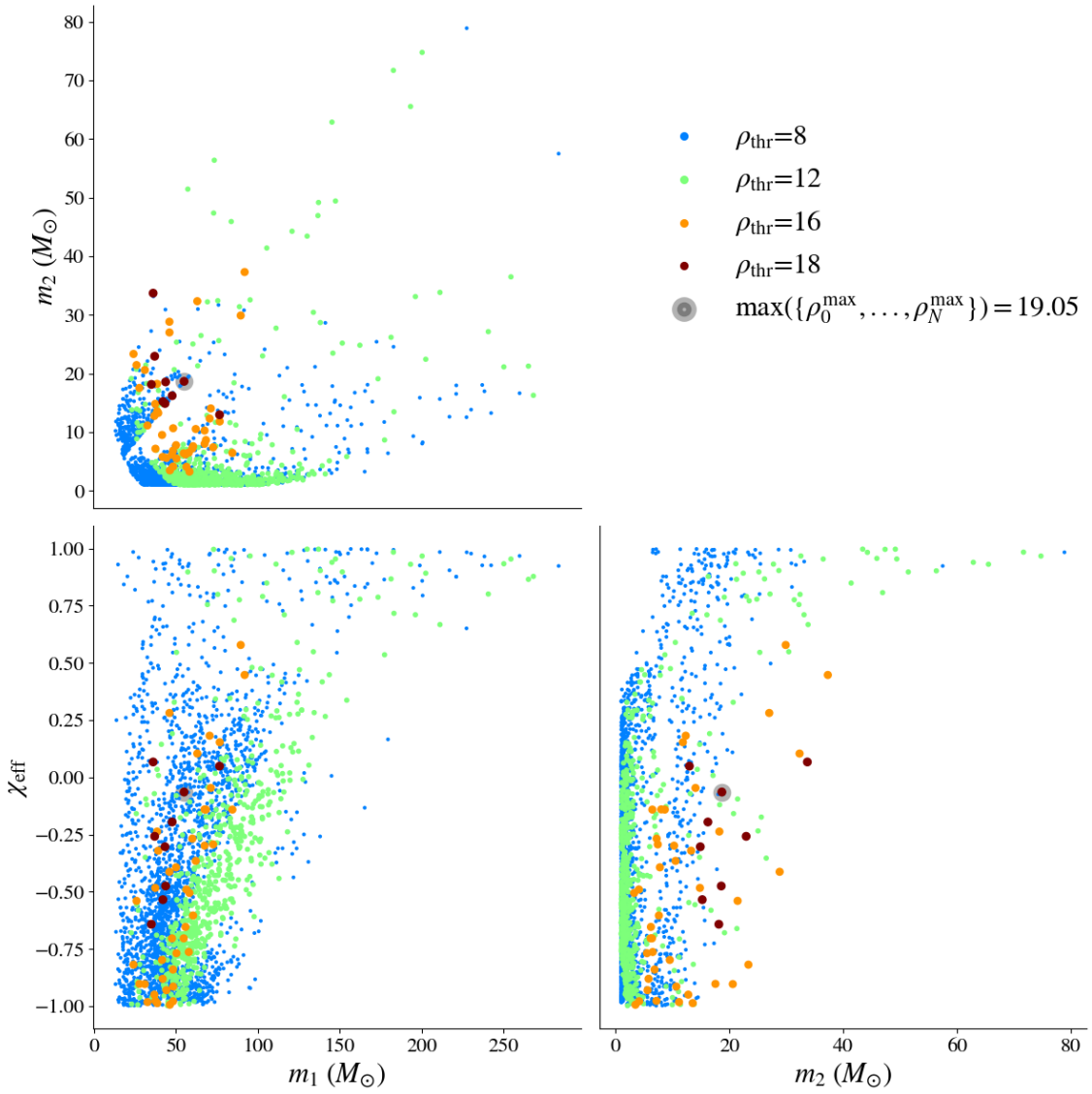

Figure 11.11 The positions of templates in the bank that have their corresponding states amplified after applying Grover's operator k_* times to an initially equal superposition of template states for ρ_{thr}. Here k_* is assumed to be the most probable k_* from the outcome probabilities shown in Fig. 11.10. The templates are scattered across the binary system's component masses m_1 and m_2 as well as the effective spin χ_{eff}. The template marker size is proportional to the log probability of obtaining that template state from a measurement of the template register. With increasing ρ_{thr} the matching templates cluster more tightly together and around the template found to have the maximum ρ out of all the template (found from a classical search).

where it is calculated for every template, indicated by the black dotted line. From Fig. 11.12, it demonstrates the $\sqrt{N}$ speed up of our procedures comparing with the classical cost.

For the case when all matching templates are desired, then the step described previously must be repeated as described in Step 6 of Sec. 11.1, which leads to matching templates being sampled with replacement. This step would be costly when the number of matching template r is not small comparing with N. This can happen for a loud signal and a low ρ_{thr} used for detection. Therefore, because the cost of retreiving a template is inversely related to the ratio of r/N as stated in Sec. 11.1.3, a procedure can be made using these algorithms as subroutines to obtain matches

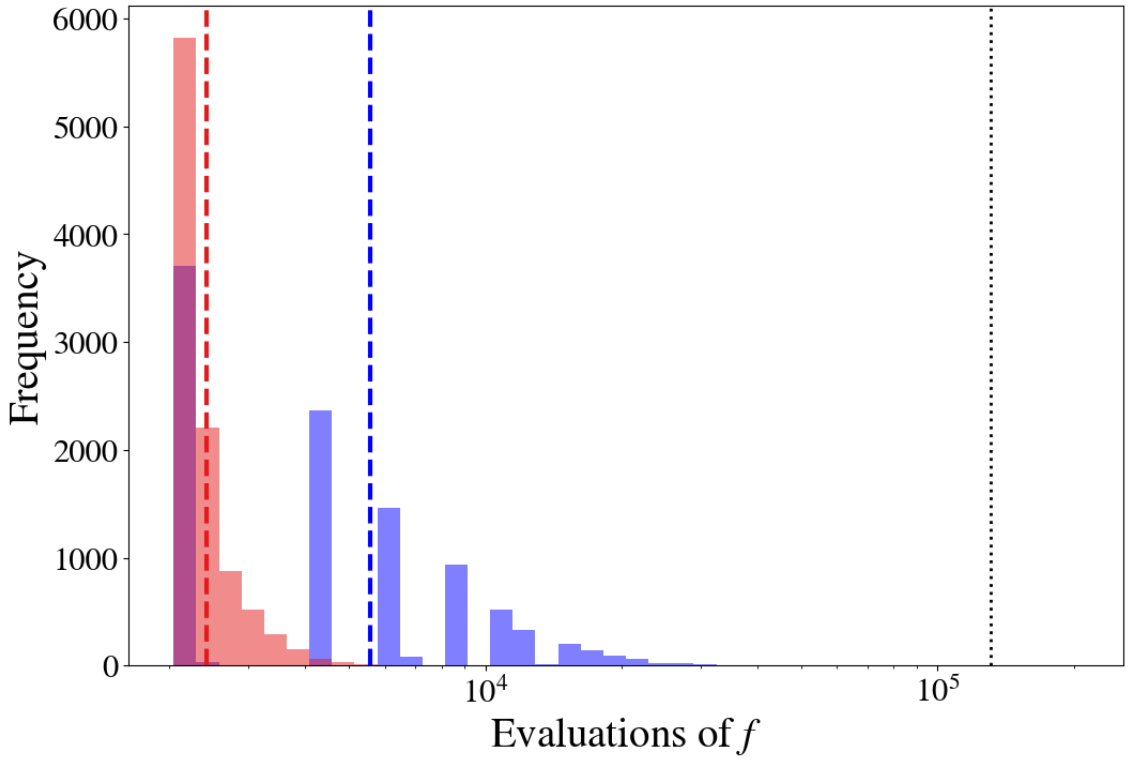

Figure 11.12 The number of evaluations of f required to retrieve a matching template for 10,000 simulations given the GW150914 example with $\rho_{\text{thr}} = 18$ and $p = 11$. The red histogram and blue histograms correspond to two extreme situations of applying the Signal Detection and the Template Retrieval procedures. The red histograms represent simulations where the Signal Detection procedure is only applied once and the value of k_* obtained is assumed for Template Retrieval. The latter procedure is repeated until a matching template is found. The blue histogram depicts simulations where the quantum counting algorithm, the Signal Detection procedure, is repeated to obtain a new k_* for each application of the Template Retrieval algorithm. The mean for both extreme methods of $\sim 2,418$ and $\sim 5,575$ (red, blue dashed lines respectively) are compared to the classical case where all 2^{17} templates are evaluated (dotted line).

with a high ρ while searching using a low ρ_{thr}; a low ρ_{thr} can initially be assumed for the search specified in Sec. 11.3.1, and given a measurement corresponding to $P(r_{obs} > 0)$, the value of r_{obs} obtained can be assessed. If $r_{obs} \gg 1$, and the signal is presumed to be loud, then the steps in Sec. 11.3.1 can be repeated with the ρ_{thr} being updated as the ρ of the retrieved template.

11.4 Conclusion

We have presented a quantum analogue of the classical matched filtering algorithm with a square-root speed-up. Our algorithm is based on Grover's algorithm, using SNR to implement a feasible oracle to search through an unstructured large template bank. The algorithm is separated into two parts: the Signal Detection and the Template Retrieving algorithms. The former is more crucial to gravitational wave detection whereas the latter is more optional when needed. We have discussed the effect of the number of counting qubits p on the accuracy of the algorithms through formulating the additional false alarm rate and false negative rate caused by the algorithms. Through this

discussion, we are able to prove that the total probability of successfully retrieving a template using our algorithm once is no less than 0.547.

We have also demonstrated a toy model of our algorithm on the IBM Qiskit platform, and a classical simulation on the GW150914 event of gravitational wave detection. In both cases, the results are successful at returning a matched template. For the simulation on the GW150914 event of gravitational wave detection, our collaborator has analysed two different failure tolerances: one where Signal Detection is applied for every application of Template Retrieval until a matching template is found; and the other one where Signal Detection is applied once and then Template Retrieval is repeated until a matching template is retrieved. We have demonstrated the computational cost and probability of the best and worst case outcomes of the whole process and compare them to the classical computational cost. In both scenarios, the average computational cost of quantum matched filtering is shown to be an order of magnitude cheaper than that of the classical counterpart.

Chapter 12

Summary and outlook of Part 2

In Part. II, we have proposed a quantum algorithm analogous to the classical matched filtering algorithm for gravitational wave data analysis. Our algorithm is based on the Grover's algorithm and offers a square-root speed up in computational cost for unstructured data base search. We propose that the number of counting qubit should be no less than $(\log \pi + 0.5 \log N)$ based on analyses on the additional false alarm rate and false negative rate caused by the algorithm. We are able to prove the total probability of successfully retrieving a template using our algorithm once is no less than 0.547. We also have demonstrated our algorithm on the IBM Qiskit platform with a toy model as well as a classical simulation on the GW150914 event of gravitational wave detection. In both cases, we have demonstrated our algorithm is successful at returning a matched template.

In past studies, quantum template matching have focused more on the size of the data, especially when the dimension spanned by the data is large, and demands more than one copy of the data and templates in quantum states [191, 192, 193]. In the case of interest here, for astrophysical researches the current limitation in computation is the number of templates. Furthermore, both the data and the templates are originally in classical form. An alternative from the basis encoding method adopted in our algorithm is amplitude encoding. In amplitude encoding a normalized classical N-dimensional datapoint x is represented by the amplitudes of a n-qubit quantum state. This would require repeatedly loading them into the quantum register. Therefore, this could offset any computation advantage the current quantum template matching algorithms offer. Although this could be solved by adopting qRAM, it would induce prohibitive time and space requirements [194, 195]. Our method bypasses the problem of loading data and templates into the quantum registers repetitively by calculating the templates from their associate indices using a classical algorithm. For the novel oracle we provided, the complexity associated with loading data and templates is not comparable to the square-root speed-up, although we require erasing and producing the templates for each application of Grover's algorithm. This is caveated that such classical algorithms used to produce templates do exist. Therefore, the quantum advantage persists and our algorithm remains a practical application for error corrected quantum computers once they become available.

However, it is worth pointing out the space requirement of our algorithm and how it compares with existing quantum processors. Let us consider a case with N templates and M bits of signal data. In our algorithm, we require a data register of size M: large enough to hold the data in

computational basis. We need two registers of such size: one to store the signal, and one for templates. Because the templates are stored in superposition, entangled with their indices, only one is needed for all the templates. If each time sample is stored using 64 bits and we analyse data as in the example of the GW150914 event included in Section. 11.3 (28 seconds of data at 4096Hz) then 28×4096 number of time samples are needed. If each time sample is stored using 64 bits (8 bytes), our algorithm becomes feasible with an error-corrected device with a few Megabytes of memory. With N templates, we require a counting register in the order of $\frac{1}{2}\log_2 N$ and an index register of size $\log_2 N$. In gravitational wave research, the template bank typically hold up to $N = 10^{12}$ templates [182, 181]. Overall, the size of data is more of a limiting factor for our algorithm. In addition, to produce the templates and perform the matched filtering calculation reversibly, we may need a scratch space polynomial in the size of the signal. IBM has announced a new quantum processor 'Eagle' with 127 qubits in December 2021 [196] and according its road map released earlier this year, a quantum processor 'Osprey' with 433 qubits will be available in 2022 and pushing this limit to over 1000 qubit in 2023 [197]. Although these are by no means fault tolerant quantum computers and the number of qubits is not the sole measure of computation ability, this does shine some optimism that the day for us to use quantum computing in gravitational wave research is not that far away.

We note that here we did not discuss the physical gate complexity: the cost of constructing, executing and error-correcting the gates. Rather, we just compare the number of executions with the classical algorithm. Quadratic speed-ups, such as provided by our algorithm, do not seem to be promising for runtime advantages for modest fault-tolerant devices [198]. Taking this into account, combined with the quite demanding space requirements outlined above, we do not claim this as a near term application. However, in the medium to long term with improvements in quantum hardware and in error correction, quantum algorithms have the potential to offer significantly improved sensitivity in gravitational wave searches.

Our algorithm of course is not only limited to speed up the current gravitational wave research, but rather applicable for any template matching problem in which the number of templates is much bigger than the size of any one template or the data, and in which the templates can be calculated efficiently through classical algorithms. Some examples where our algorithm may help the intractable search using classical algorithm tractable include the continuous wave detection in gravitational wave research and even dark matter detection [199].

Gravitational wave research has always been on the frontier of adopting novel computing methods such as classical machine learning techniques [200, 201, 202], and we expect that more sophisticated quantum machine learning techniques may contribute further quantum advantages to it. In the future, there are three possible opportunities for further improvement of our algorithm. The first opportunity is to explore the possibility of involving prior knowledge into the template bank setup to favour certain templates, as was done classically in [203, 204]. Although this method would still remain a quadratic algorithm, the overall efficiency could be improved. The second one is by incorporating amplitude encoding. As we have discussed before, the advantage of this method is that it will reduce space requirement. But for our algorithm, it is more difficult to perform the matching steps using amplitude encoding, and would likely add extra complexity. The last opportunity is to apply machine learning techniques as it is considered a possible

application of NISQ devices[205]. As we fully enter the era of gravitational wave astronomy and quantum computing, joining those two areas would produce better performing and more efficient data processing techniques to fully exploit these new windows on the Universe and computation.

Bibliography

[1] Sijia Gao, Fiona C Speirits, Francesco Castellucci, Sonja Franke-Arnold, Stephen M Barnett, and Jörg B Götte. Paraxial skyrmionic beams. *Physical Review A*, 102(5):053513, 2020.

[2] Sijia Gao, Fergus Hayes, Sarah Croke, Chris Messenger, and John Veitch. A quantum algorithm for gravitational wave matched filtering. *arXiv preprint arXiv:2109.01535*, 2021.

[3] Halina Rubinsztein-Dunlop, Andrew Forbes, Michael V Berry, Mark R Dennis, David L Andrews, Masud Mansuripur, Cornelia Denz, Christina Alpmann, Peter Banzer, Thomas Bauer, et al. Roadmap on structured light. *Journal of Optics*, 19(1):013001, 2016.

[4] N Radwell, G Walker, and S Franke-Arnold. Cold-atom densities of more than 10 12 cm-3 in a holographically shaped dark spontaneous-force optical trap. *Physical Review A*, 88(4):043409, 2013.

[5] A Turpin, J Polo, Yu V Loiko, Johannes Küber, F Schmaltz, Todor Kirilov Kalkandjiev, Verònica Ahufinger, Gerhard Birkl, and J Mompart. Blue-detuned optical ring trap for bose-einstein condensates based on conical refraction. *Optics express*, 23(2):1638–1650, 2015.

[6] A Ramanathan, KC Wright, SR Muniz, M Zelan, WT Hill III, CJ Lobb, Kristian Helmerson, WD Phillips, and GK Campbell. Superflow in a toroidal bose-einstein condensate: an atom circuit with a tunable weak link. *Physical review letters*, 106(13):130401, 2011.

[7] Aidan S Arnold. Extending dark optical trapping geometries. *Optics letters*, 37(13):2505–2507, 2012.

[8] KC Wright, LS Leslie, and NP Bigelow. Optical control of the internal and external angular momentum of a bose-einstein condensate. *Physical Review A*, 77(4):041601, 2008.

[9] David L Andrews. *Structured light and its applications: An introduction to phase-structured beams and nanoscale optical forces*. Academic press, 2011.

[10] S Tsesses, E Ostrovsky, K Cohen, B Gjonaj, NH Lindner, and G Bartal. Optical skyrmion lattice in evanescent electromagnetic fields. *Science*, 361(6406):993–996, 2018.

[11] Luping Du, Aiping Yang, Anatoly V Zayats, and Xiaocong Yuan. Deep-subwavelength features of photonic skyrmions in a confined electromagnetic field with orbital angular momentum. *Nature Physics*, 15(7):650–654, 2019.

[12] Yanan Dai, Zhikang Zhou, Atreyie Ghosh, Roger SK Mong, Atsushi Kubo, Chen-Bin Huang, and Hrvoje Petek. Plasmonic topological quasiparticle on the nanometre and femtosecond scales. *Nature*, 588(7839):616–619, 2020.

[13] Aviv Karnieli, Shai Tsesses, Guy Bartal, and Ady Arie. Emulating spin transport with nonlinear optics, from high-order skyrmions to the topological hall effect. *Nature communications*, 12(1):1–9, 2021.

[14] Lov K Grover. A fast quantum mechanical algorithm for database search. In *Proceedings of the twenty-eighth annual ACM symposium on Theory of computing*, pages 212–219, 1996.

[15] Peter W. Shor. Polynomial-Time Algorithms for Prime Factorization and Discrete Logarithms on a Quantum Computer. *arXiv e-prints*, pages quant–ph/9508027, August 1995.

[16] Frank Arute, Kunal Arya, Ryan Babbush, Dave Bacon, Joseph C Bardin, Rami Barends, Rupak Biswas, Sergio Boixo, Fernando GSL Brandao, David A Buell, et al. Quantum supremacy using a programmable superconducting processor. *Nature*, 574(7779):505–510, 2019.

[17] Han-Sen Zhong, Hui Wang, Yu-Hao Deng, Ming-Cheng Chen, Li-Chao Peng, Yi-Han Luo, Jian Qin, Dian Wu, Xing Ding, Yi Hu, et al. Quantum computational advantage using photons. *Science*, 370(6523):1460–1463, 2020.

[18] B. P. Abbott et al. Observation of Gravitational Waves from a Binary Black Hole Merger. , 116(6):061102, February 2016.

[19] Harry Edwin Burton. The optics of euclid1. *JOSA*, 35(5):357–372, 1945.

[20] Jian Wang, Jeng-Yuan Yang, Irfan M Fazal, Nisar Ahmed, Yan Yan, Hao Huang, Yongxiong Ren, Yang Yue, Samuel Dolinar, Moshe Tur, et al. Terabit free-space data transmission employing orbital angular momentum multiplexing. *Nature photonics*, 6(7):488–496, 2012.

[21] Alan E Willner, Hao Huang, Yan Yan, Yongxiong Ren, Nisar Ahmed, Goudong Xie, Changjing Bao, L Li, Y Cao, Z Zhao, et al. Optical communications using orbital angular momentum beams. *Advances in Optics and Photonics*, 7(1):66–106, 2015.

[22] Nenad Bozinovic, Yang Yue, Yongxiong Ren, Moshe Tur, Poul Kristensen, Hao Huang, Alan E Willner, and Siddharth Ramachandran. Terabit-scale orbital angular momentum mode division multiplexing in fibers. *science*, 340(6140):1545–1548, 2013.

[23] Mario Krenn, Johannes Handsteiner, Matthias Fink, Robert Fickler, Rupert Ursin, Mehul Malik, and Anton Zeilinger. Twisted light transmission over 143 km. *Proceedings of the National Academy of Sciences*, 113(48):13648–13653, 2016.

[24] Mario Krenn, Marcus Huber, Robert Fickler, Radek Lapkiewicz, Sven Ramelow, and Anton Zeilinger. Generation and confirmation of a (100× 100)-dimensional entangled quantum system. *Proceedings of the National Academy of Sciences*, 111(17):6243–6247, 2014.

[25] Mario Krenn, Johannes Handsteiner, Matthias Fink, Robert Fickler, and Anton Zeilinger. Twisted photon entanglement through turbulent air across vienna. *Proceedings of the National Academy of Sciences*, 112(46):14197–14201, 2015.

[26] Mohammad Mirhosseini, Omar S Magaña-Loaiza, Malcolm N O'Sullivan, Brandon Rodenburg, Mehul Malik, Martin PJ Lavery, Miles J Padgett, Daniel J Gauthier, and Robert W Boyd. High-dimensional quantum cryptography with twisted light. *New Journal of Physics*, 17(3):033033, 2015.

[27] Hans Wolter. Zur frage des lichtweges bei totalreflexion. *Zeitschrift für Naturforschung A*, 5(5):276–283, 1950.

[28] W Braunbek and G Laukien. Features of refraction by a semi-plane. *Optik*, 9:174–179, 1952.

[29] Joseph O Hirschfelder, Albert C Christoph, and William E Palke. Quantum mechanical streamlines. i. square potential barrier. *The Journal of Chemical Physics*, 61(12):5435–5455, 1974.

[30] Joseph O Hirschfelder, Charles J Goebel, and Ludwig W Bruch. Quantized vortices around wavefunction nodes. ii. *The Journal of Chemical Physics*, 61(12):5456–5459, 1974.

[31] Les Allen, Marco W Beijersbergen, RJC Spreeuw, and JP Woerdman. Orbital angular momentum of light and the transformation of laguerre-gaussian laser modes. *Physical review A*, 45(11):8185, 1992.

[32] J D Jackson. *Classical electrodynamics, 3rd ed*. John Wiley Sons, New York, 1999.

[33] G. B. Arfken and H. J. Weber. *Mathematical methods for physicists*. Elsevier, Boston, MA, 2005.

[34] J B Götte. *Integral and Fractional Orbital Angular Momentum of Light*. PhD thesis, University of Strathclyde, 2006.

[35] Max Born and Emil Wolf. *Principles of optics: electromagnetic theory of propagation, interference and diffraction of light*. Elsevier, 2013.

[36] Stephen M Barnett and L Allen. Orbital angular momentum and nonparaxial light beams. *Optics communications*, 110(5-6):670–678, 1994.

[37] Bahaa EA Saleh and Malvin Carl Teich. *Fundamentals of photonics*. john Wiley & sons, 2019.

[38] H. A. Haus. *Waves and Fields in Optoelectronics*. Prentice-Hall, New Jersey, 1984.

[39] Melvin Lax, William H Louisell, and William B McKnight. From maxwell to paraxial wave optics. *Physical Review A*, 11(4):1365, 1975.

[40] Anthony E. Siegman. *Lasers*. University Science Books, 1986.

[41] Wilhelm Magnus, Fritz Oberhettinger, and Raj Pal Soni. *Formulas and theorems for the special functions of mathematical physics*, volume 52. Springer Science & Business Media, 2013.

[42] Michael V Berry. Paraxial beams of spinning light. In *International conference on singular optics*, volume 3487, pages 6–12. International Society for Optics and Photonics, 1998.

[43] Konstantin Y Bliokh and Franco Nori. Transverse and longitudinal angular momenta of light. *Physics Reports*, 592:1–38, 2015.

[44] JF Nye and MV Berry. Dislocations in wave trains. *Proc. R. Soc. Lond. A*, 336(1605):165–190, 1974.

[45] John Frederick Nye. *Natural focusing and fine structure of light: caustics and wave dislocations*. CRC Press, 1999.

[46] Johan Verbeeck, He Tian, and Peter Schattschneider. Production and application of electron vortex beams. *Nature*, 467(7313):301–304, 2010.

[47] Masaya Uchida and Akira Tonomura. Generation of electron beams carrying orbital angular momentum. *nature*, 464(7289):737–739, 2010.

[48] Benjamin J McMorran, Amit Agrawal, Ian M Anderson, Andrew A Herzing, Henri J Lezec, Jabez J McClelland, and John Unguris. Electron vortex beams with high quanta of orbital angular momentum. *science*, 331(6014):192–195, 2011.

[49] Roy Shiloh, Yuval Tsur, Roei Remez, Yossi Lereah, Boris A Malomed, Vladlen Shvedov, Cyril Hnatovsky, Wieslaw Krolikowski, and Ady Arie. Unveiling the orbital angular momentum and acceleration of electron beams. *Physical review letters*, 114(9):096102, 2015.

[50] Iwo Bialynicki-Birula and Zofia Bialynicka-Birula. Relativistic electron wave packets carrying angular momentum. *Physical review letters*, 118(11):114801, 2017.

[51] Stephen M Barnett. Relativistic electron vortices. *Physical review letters*, 118(11):114802, 2017.

[52] Stephen M Barnett. Barnett replies. *Physical review letters*, 119(2):029502, 2017.

[53] R Clark Jones. A new calculus for the treatment of optical systemsiii. the sohncke theory of optical activity. *Josa*, 31(7):500–503, 1941.

[54] R Clark Jones. A new calculus for the treatment of optical systems. iv. *Josa*, 32(8):486–493, 1942.

[55] Dennis G Hall. Vector-beam solutions of maxwell's wave equation. *Optics letters*, 21(1):9–11, 1996.

[56] Qiwen Zhan. Cylindrical vector beams: from mathematical concepts to applications. *Advances in Optics and Photonics*, 1(1):1–57, 2009.

[57] THR Skyrme and A Non. linear field theory. *Proc. Roy. Soc*, 260:l27, 1961.

[58] Tony Hilton Royle Skyrme. A unified field theory of mesons and baryons. *Nuclear Physics*, 31:556–569, 1962.

[59] Sang-Wook Cheong and Maxim Mostovoy. Multiferroics: a magnetic twist for ferroelectricity. *Nature materials*, 6(1):13–20, 2007.

[60] Shivaji Lal Sondhi, A Karlhede, SA Kivelson, and EH Rezayi. Skyrmions and the crossover from the integer to fractional quantum hall effect at small zeeman energies. *Physical Review B*, 47(24):16419, 1993.

[61] I Raičević, Dragana Popović, C Panagopoulos, L Benfatto, MB Silva Neto, ES Choi, and T Sasagawa. Skyrmions in a doped antiferromagnet. *Physical review letters*, 106(22):227206, 2011.

[62] Marco Finazzi, Matteo Savoini, AR Khorsand, A Tsukamoto, A Itoh, Lamberto Duo, Andrei Kirilyuk, Th Rasing, and M Ezawa. Laser-induced magnetic nanostructures with tunable topological properties. *Physical review letters*, 110(17):177205, 2013.

[63] Wataru Koshibae, Yoshio Kaneko, Junichi Iwasaki, Masashi Kawasaki, Yoshinori Tokura, and Naoto Nagaosa. Memory functions of magnetic skyrmions. *Japanese Journal of Applied Physics*, 54(5):053001, 2015.

[64] Dieter Vollhardt and Peter Wölfle. *The superfluid phases of helium 3*. Courier Corporation, 2013.

[65] Anthony James Leggett et al. *Quantum liquids: Bose condensation and Cooper pairing in condensed-matter systems*. Oxford university press, 2006.

[66] David R Tilley and John Tilley. *Superfluidity and superconductivity*. Routledge, 2019.

[67] John Scott Russell. *Report on Waves: Made to the Meetings of the British Association in 1842-43*. 1845.

[68] Hubert Chanson. Current knowledge in hydraulic jumps and related phenomena. a survey of experimental results. *European Journal of Mechanics-B/Fluids*, 28(2):191–210, 2009.

[69] Søren SL Andersen, Andrew D Jackson, and Thomas Heimburg. Towards a thermodynamic theory of nerve pulse propagation. *Progress in neurobiology*, 88(2):104–113, 2009.

[70] James Roy Taylor. *Optical Solitons*. 1992.

[71] William L Kath. Making waves: solitons and their optical applications. *Siam News*, 1998.

[72] Nicholas Manton and Paul Sutcliffe. *Topological solitons*. Cambridge University Press, 2004.

[73] Horst Schubert. *Topology*. Allyn and Bacon, 1968.

[74] James S Tanton. *Encyclopedia of mathematics*. Infobase Publishing, 2005.

[75] Christopher H Marrows. An inside view of magnetic skyrmions. *Physics*, 8:40, 2015.

[76] Bernard MAG Piette, Bernd J Schroers, and WJ Zakrzewski. Multisolitons in a two-dimensional skyrme model. *Zeitschrift für Physik C Particles and Fields*, 65(1):165–174, 1995.

[77] S. Sachdev. *Quantum Phase Transitions*. Cambridge University Press, 2011.

[78] S. Seki and M. Mochizuki. *Skyrmions in Magnetic Materials*. Springer International Publishing, 2015.

[79] Mark R Dennis. Fermionic out-of-plane structure of polarization singularities. *Optics Letters*, 36(19):3765–3767, October 2011.

[80] Todd Van Mechelen and Zubin Jacob. Photonic dirac monopoles and skyrmions: spin-1 quantization. *Opt. Mater. Express*, 9(1):95–111, Jan 2019.

[81] F. Wilczek. *Fractional Statistics and Anyon Superconductivity*. World Scientific, 1990.

[82] Stefano Donati, Lorenzo Dominici, Galbadrakh Dagvadorj, Dario Ballarini, Milena De Giorgi, Alberto Bramati, Giuseppe Gigli, Yuri G Rubo, Marzena Hanna Szymańska, and Daniele Sanvitto. Twist of generalized skyrmions and spin vortices in a polariton superfluid. *Proceedings of the National Academy of Sciences*, 113(52):14926–14931, 2016.

[83] Yusuke Ishihara, Takeshi Mizushima, Atsushi Tsuruta, and Satoshi Fujimoto. Torsional chiral magnetic effect due to skyrmion textures in a weyl superfluid he 3- a. *Physical Review B*, 99(2):024513, 2019.

[84] G.E. Volovik and Oxford University Press. *The Universe in a Helium Droplet*. Clarendon Press, 2003.

[85] Jie Zhu, Sheng Liu, and Yong-Sheng Zhang. Synthesis and observation of optical skyrmionic structure in free space. *arXiv preprint arXiv:2103.11293*, 2021.

[86] Yijie Shen, Yaonan Hou, Nikitas Papasimakis, and Nikolay I Zheludev. Supertoroidal light pulses: Propagating electromagnetic skyrmions in free space. *arXiv preprint arXiv:2103.08431*, 2021.

[87] THR Skyrme. The effective nuclear potential. *Nuclear Physics*, 9(4):615–634, 1958.

[88] AN Bogdanov and UK Rößler. Chiral symmetry breaking in magnetic thin films and multilayers. *Physical review letters*, 87(3):037203, 2001.

[89] UK Rößler, AN Bogdanov, and C Pfleiderer. Spontaneous skyrmion ground states in magnetic metals. *Nature*, 442(7104):797, 2006.

[90] Bertrand Dupé, Markus Hoffmann, Charles Paillard, and Stefan Heinze. Tailoring magnetic skyrmions in ultra-thin transition metal films. *Nature communications*, 5(1):1–6, 2014.

[91] Niklas Romming, Christian Hanneken, Matthias Menzel, Jessica E Bickel, Boris Wolter, Kirsten von Bergmann, André Kubetzka, and Roland Wiesendanger. Writing and deleting single magnetic skyrmions. *Science*, 341(6146):636–639, 2013.

[92] Sebastian Mühlbauer, Benedikt Binz, F Jonietz, Christian Pfleiderer, Achim Rosch, Anja Neubauer, Robert Georgii, and Peter Böni. Skyrmion lattice in a chiral magnet. *Science*, 323(5916):915–919, 2009.

[93] Pin-Jui Hsu, André Kubetzka, Aurore Finco, Niklas Romming, Kirsten von Bergmann, and Roland Wiesendanger. Electric-field-driven switching of individual magnetic skyrmions. *Nature nanotechnology*, 12(2):123–126, 2017.

[94] S Seki, M Garst, J Waizner, R Takagi, ND Khanh, Y Okamura, K Kondou, F Kagawa, Y Otani, and Y Tokura. Propagation dynamics of spin excitations along skyrmion strings. *Nature communications*, 11(1):1–7, 2020.

[95] MT Birch, D Cortés-Ortuño, LA Turnbull, MN Wilson, F Groß, N Träger, A Laurenson, N Bukin, SH Moody, M Weigand, et al. Real-space imaging of confined magnetic skyrmion tubes. *Nature communications*, 11(1):1–8, 2020.

[96] AA Belavin and AM Polyakov. Metastable states of two-dimensional isotropic ferromagnets. *JETP lett*, 22(10):245–248, 1975.

[97] Alexei N Bogdanov and DA Yablonskii. Thermodynamically stable "vortices" in magnetically ordered crystals. the mixed state of magnets. *Zh. Eksp. Teor. Fiz*, 95(1):178, 1989.

[98] A Bogdanov and A Hubert. Thermodynamically stable magnetic vortex states in magnetic crystals. *Journal of magnetism and magnetic materials*, 138(3):255–269, 1994.

[99] Ulrich K Roessler, AN Bogdanov, and C Pfleiderer. Spontaneous skyrmion ground states in magnetic metals. *Nature*, 442(7104):797–801, 2006.

[100] Albert S Schwarz. *Topology for physicists*, volume 308. Springer Science & Business Media, 2013.

[101] Kayla Fallon. A lorentz microscopy study of chiral magnetic textures stabilised in thin films by an interfacial dzyaloshinskii-moriya interaction. 2019.

[102] Albert Fert, Vincent Cros, and Joao Sampaio. Skyrmions on the track. *Nature nanotechnology*, 8(3):152–156, 2013.

[103] Junichi Iwasaki, Masahito Mochizuki, and Naoto Nagaosa. Current-induced skyrmion dynamics in constricted geometries. *Nature nanotechnology*, 8(10):742–747, 2013.

[104] Bertrand Dupé, Gustav Bihlmayer, Marie Böttcher, Stefan Blügel, and Stefan Heinze. Engineering skyrmions in transition-metal multilayers for spintronics. *Nature communications*, 7(1):1–6, 2016.

[105] Xichao Zhang, Motohiko Ezawa, and Yan Zhou. Magnetic skyrmion logic gates: conversion, duplication and merging of skyrmions. *Scientific reports*, 5:9400, 2015.

[106] Diana Prychynenko, Matthias Sitte, Kai Litzius, Benjamin Krüger, George Bourianoff, Mathias Kläui, Jairo Sinova, and Karin Everschor-Sitte. Magnetic skyrmion as a nonlinear resistive element: A potential building block for reservoir computing. *Physical Review Applied*, 9(1):014034, 2018.

[107] PHILIP W Anderson and Pierre Morel. Generalized bardeen-cooper-schrieffer states and the proposed low-temperature phase of liquid he 3. *Physical Review*, 123(6):1911, 1961.

[108] R Balian and NR Werthamer. Superconductivity with pairs in a relative p wave. *Physical review*, 131(4):1553, 1963.

[109] MM Salomaa and GE Volovik. Quantized vortices in superfluid he 3. *Reviews of modern physics*, 59(3):533, 1987.

[110] ND Mermin and Tin-Lun Ho. Circulation and angular momentum in the a phase of superfluid helium-3. *Physical Review Letters*, 36(11):594, 1976.

[111] Ü Parts, JM Karimäki, JH Koivuniemi, M Krusius, VMH Ruutu, EV Thuneberg, and GE Volovik. Phase diagram of vortices in superfluid 3 h e- a. *Physical review letters*, 75(18):3320, 1995.

[112] Giandomenico Palumbo and Mauro Cirio. Skyrmion superfluidity in two-dimensional interacting fermionic systems. *Scientific reports*, 5(1):1–8, 2015.

[113] Paul Adrien Maurice Dirac. Quantised singularities in the electromagnetic field. *Proceedings of the Royal Society of London. Series A, Containing Papers of a Mathematical and Physical Character*, 133(821):60–72, 1931.

[114] John Frederick Nye and JV Hajnal. The wave structure of monochromatic electromagnetic radiation. *Proceedings of the Royal Society of London. A. Mathematical and Physical Sciences*, 409(1836):21–36, 1987.

[115] Miguel A Alonso. Geometric descriptions for the polarization for nonparaxial optical fields: a tutorial. *arXiv preprint arXiv:2008.02720*, 2020.

[116] Rodrigo Gutiérrez-Cuevas and Emilio Pisanty. Optical polarization skyrmionic fields in free space. *Journal of Optics*, 23(2):024004, 2021.

[117] Maria J Esteban. A direct variational approach to skyrme's model for meson fields. *Communications in mathematical physics*, 105(4):571–591, 1986.

[118] Stephen M Barnett, Les Allen, Robert P Cameron, Claire R Gilson, Miles John Padgett, Fiona C Speirits, and Alison M Yao. On the natures of the spin and orbital parts of optical angular momentum. *Journal of Optics*, 18(6):064004–12, April 2016.

[119] Mark J Ablowitz, Athanassios S Fokas, and Athanassios S Fokas. *Complex variables: introduction and applications*. Cambridge University Press, 2003.

[120] Tin-Lun Ho. Coreless vortices in superfluid he 3-a: Topological structure, nucleation, and the screening effect. *Physical Review B*, 18(3):1144, 1978.

[121] HE Hall and JR Hook. The hydrodynamics of superfluid3he. In *Progress in low temperature physics*, volume 9, pages 143–264. Elsevier, 1986.

[122] Amber M Beckley, Thomas G Brown, and Miguel A Alonso. Full poincaré beams. *Optics express*, 18(10):10777–10785, 2010.

[123] Carmelo Rosales-Guzmán, Bienvenu Ndagano, and Andrew Forbes. A review of complex vector light fields and their applications. *Journal of Optics*, 20(12):123001, 2018.

[124] Jian Chen, Chenhao Wan, and Qiwen Zhan. Vectorial optical fields: recent advances and future prospects. *Science Bulletin*, 63(1):54–74, 2018.

[125] Stefano Donati, Lorenzo Dominici, Galbadrakh Dagvadorj, Dario Ballarini, Milena De Giorgi, Alberto Bramati, Giuseppe Gigli, Yuri G. Rubo, Marzena Hanna Szymańska, and Daniele Sanvitto. Twist of generalized skyrmions and spin vortices in a polariton superfluid. *Proceedings of the National Academy of Sciences*, 113(52):14926–14931, 2016.

[126] Bryon R Brown and Adolf W Lohmann. Complex spatial filtering with binary masks. *Applied optics*, 5(6):967–969, 1966.

[127] Wai-Hon Lee. Binary computer-generated holograms. *Applied Optics*, 18(21):3661–3669, 1979.

[128] Kevin J Mitchell, Sergey Turtaev, Miles J Padgett, Tomáš Čižmár, and David B Phillips. High-speed spatial control of the intensity, phase and polarisation of vector beams using a digital micro-mirror device. *Optics express*, 24(25):29269–29282, 2016.

[129] Stephen M Barnett. On the quantum core of an optical vortex. *Journal of Modern Optics*, 55(14):2279–2292, 2008.

[130] Francesco Castellucci, Thomas W. Clark, Adam Selyem, Jinwen Wang, and Sonja Franke-Arnold. Atomic compass: Detecting 3d magnetic field alignment with vector vortex light. *Phys. Rev. Lett.*, 127:233202, Nov 2021.

[131] Richard P Feynman. Simulating physics with computers. *Int. J. Theor. Phys*, 21(6/7), 1982.

[132] Michael A Nielsen and Isaac L Chuang. Quantum computation and quantum information: 10th anniversary edition (10th ed.), 2011.

[133] Maria Schuld, Ilya Sinayskiy, and Francesco Petruccione. An introduction to quantum machine learning. *Contemporary Physics*, 56(2):172–185, 2015.

[134] Peter Wittek. *Quantum machine learning: what quantum computing means to data mining*. Academic Press, 2014.

[135] Srinivasan Arunachalam and Ronald de Wolf. Guest column: A survey of quantum learning theory. *ACM SIGACT News*, 48(2):41–67, 2017.

[136] Aram W Harrow, Avinatan Hassidim, and Seth Lloyd. Quantum algorithm for linear systems of equations. *Physical review letters*, 103(15):150502, 2009.

[137] Seth Lloyd, Masoud Mohseni, and Patrick Rebentrost. Quantum principal component analysis. *Nature Physics*, 10(9):631–633, 2014.

[138] Nathan Wiebe, Daniel Braun, and Seth Lloyd. Quantum algorithm for dagoogta fitting. *Physical review letters*, 109(5):050505, 2012.

[139] Jacob Biamonte, Peter Wittek, Nicola Pancotti, Patrick Rebentrost, Nathan Wiebe, and Seth Lloyd. Quantum machine learning. *Nature*, 549(7671):195–202, 2017.

[140] Vittorio Giovannetti, Seth Lloyd, and Lorenzo Maccone. Quantum random access memory. *Physical review letters*, 100(16):160501, 2008.

[141] Carlo Ciliberto, Mark Herbster, Alessandro Davide Ialongo, Massimiliano Pontil, Andrea Rocchetto, Simone Severini, and Leonard Wossnig. Quantum machine learning: a classical perspective. *Proceedings of the Royal Society A: Mathematical, Physical and Engineering Sciences*, 474(2209):20170551, 2018.

[142] Bangalore Suryanarayana Sathyaprakash and Bernard F Schutz. Physics, astrophysics and cosmology with gravitational waves. *Living reviews in relativity*, 12(1):1–141, 2009.

[143] R Abbott, TD Abbott, S Abraham, F Acernese, K Ackley, A Adams, C Adams, RX Adhikari, VB Adya, C Affeldt, et al. Gwtc-2: Compact binary coalescences observed by ligo and virgo during the first half of the third observing run. *arXiv preprint arXiv:2010.14527*, 2020.

[144] B. P. Abbott et al. GW170817: Measurements of Neutron Star Radii and Equation of State. , 121(16):161101, October 2018.

[145] B. P. Abbott et al. Gravitational Waves and Gamma-Rays from a Binary Neutron Star Merger: GW170817 and GRB 170817A. , 848(2):L13, October 2017.

[146] R. Abbott et al. Tests of General Relativity with Binary Black Holes from the second LIGO-Virgo Gravitational-Wave Transient Catalog. *arXiv e-prints*, page arXiv:2010.14529, October 2020.

[147] B.P. Abbott et al. Prospects for Observing and Localizing Gravitational-Wave Transients with Advanced LIGO, Advanced Virgo and KAGRA. *Living Rev. Rel.*, 21(1):3, 2018.

[148] J. Aasi et al. Advanced LIGO. *Class. Quant. Grav.*, 32:074001, 2015.

[149] F. Acernese et al. Advanced Virgo: a second-generation interferometric gravitational wave detector. *Class. Quant. Grav.*, 32(2):024001, 2015.

[150] Ligo-india, proposal of the consortium for indian initiative in gravitational-wave observations (indigo). https://dcc.ligo.org/LIGO-M1100296/public. Accessed: 2020-11-19.

[151] T Akutsu, M Ando, K Arai, Y Arai, S Araki, A Araya, N Aritomi, Y Aso, S-W Bae, Y-B Bae, et al. Overview of kagra: Detector design and construction history. *arXiv preprint arXiv:2005.05574*, 2020.

[152] R. Balasubramanian, B. S. Sathyaprakash, and S. V. Dhurandhar. Gravitational waves from coalescing binaries: Detection strategies and Monte Carlo estimation of parameters. , 53(6):3033–3055, March 1996.

[153] Benjamin J. Owen and B. S. Sathyaprakash. Matched filtering of gravitational waves from inspiraling compact binaries: Computational cost and template placement. , 60(2):022002, July 1999.

[154] Patrick R. Brady, Teviet Creighton, Curt Cutler, and Bernard F. Schutz. Searching for periodic sources with LIGO. , 57(4):2101–2116, February 1998.

[155] Benjamin J. Owen. Search templates for gravitational waves from inspiraling binaries: Choice of template spacing. , 53(12):6749–6761, June 1996.

[156] Bruce Allen, Warren G. Anderson, Patrick R. Brady, Duncan A. Brown, and Jolien D.E. Creighton. FINDCHIRP: An Algorithm for detection of gravitational waves from inspiraling compact binaries. *Phys. Rev. D*, 85:122006, 2012.

[157] Sanjeev V Dhurandhar and Alberto Vecchio. Searching for continuous gravitational wave sources in binary systems. *Physical Review D*, 63(12):122001, 2001.

[158] Chris Messenger. Semicoherent search strategy for known continuous wave sources in binary systems. *Physical Review D*, 84(8):083003, 2011.

[159] Paola Leaci and Reinhard Prix. Directed searches for continuous gravitational waves from binary systems: Parameter-space metrics and optimal scorpius x-1 sensitivity. *Physical Review D*, 91(10):102003, 2015.

[160] Carl W Helstrom. *Statistical theory of signal detection: international series of monographs in electronics and instrumentation*, volume 9. Elsevier, 2013.

[161] Stephen Barnett. *Quantum information*, volume 16. Oxford University Press, 2009.

[162] Phillip Kaye, Raymond Laflamme, Michele Mosca, et al. *An introduction to quantum computing*. Oxford university press, 2007.

[163] Charles H Bennett, Ethan Bernstein, Gilles Brassard, and Umesh Vazirani. Strengths and weaknesses of quantum computing. *SIAM journal on Computing*, 26(5):1510–1523, 1997.

[164] B. P. Abbott et al. Searches for Continuous Gravitational Waves from 15 Supernova Remnants and Fomalhaut b with Advanced LIGO. , 875(2):122, April 2019.

[165] A Yu Kitaev. Quantum measurements and the abelian stabilizer problem, coll. *Comput. Complex*, 3:3, 1996.

[166] Gilles Brassard, Peter Høyer, and Alain Tapp. Quantum counting. In *International Colloquium on Automata, Languages, and Programming*, pages 820–831. Springer, 1998.

[167] Christoph Durr and Peter Hoyer. A quantum algorithm for finding the minimum. *arXiv preprint quant-ph/9607014*, 1996.

[168] Michel Boyer, Gilles Brassard, Peter Høyer, and Alain Tapp. Tight bounds on quantum searching. *Fortschritte der Physik: Progress of Physics*, 46(4-5):493–505, 1998.

[169] Eleanor Rieffel and Wolfgang Polak. *Quantum Computing: A gentle introduction*. MIT Press, 2011.

[170] Reinhard Prix. Template-based searches for gravitational waves: efficient lattice covering of flat parameter spaces. *Classical and Quantum Gravity*, 24(19):S481–S490, October 2007.

[171] Adriano Barenco, Charles H Bennett, Richard Cleve, David P DiVincenzo, Norman Margolus, Peter Shor, Tycho Sleator, John A Smolin, and Harald Weinfurter. Elementary gates for quantum computation. *Physical review A*, 52(5):3457, 1995.

[172] J. Veitch, V. Raymond, B. Farr, W. Farr, P. Graff, S. Vitale, B. Aylott, K. Blackburn, N. Christensen, M. Coughlin, W. Del Pozzo, F. Feroz, J. Gair, C. J. Haster, V. Kalogera, T. Littenberg, I. Mandel, R. O'Shaughnessy, M. Pitkin, C. Rodriguez, C. Röver, T. Sidery, R. Smith, M. Van Der Sluys, A. Vecchio, W. Vousden, and L. Wade. Parameter estimation for compact binaries with ground-based gravitational-wave observations using the LALInference software library. , 91(4):042003, February 2015.

[173] Gregory Ashton et al. BILBY: A user-friendly Bayesian inference library for gravitational-wave astronomy. *Astrophys. J. Suppl.*, 241(2):27, 2019.

[174] Tito Dal Canton and Ian W. Harry. Designing a template bank to observe compact binary coalescences in Advanced LIGO's second observing run. 5 2017.

[175] Michele Mosca. Counting by quantum eigenvalue estimation. *Theoretical Computer Science*, 264(1):139–153, 2001.

[176] Philippe Flajolet, Daniele Gardy, and Loÿs Thimonier. Birthday paradox, coupon collectors, caching algorithms and self-organizing search. *Discrete Applied Mathematics*, 39(3):207–229, 1992.

[177] Héctor Abraham, AduOffei, Rochisha Agarwal, et al. Qiskit: An open-source framework for quantum computing, 2019.

[178] Hariharan Ramesh and V Vinay. String matching in o (n+ m) quantum time. *Journal of Discrete Algorithms*, 1(1):103–110, 2003.

[179] Ashley Montanaro. Quantum pattern matching fast on average. *Algorithmica*, 77(1):16–39, 2017.

[180] Pradeep Niroula and Yunseong Nam. A quantum algorithm for string matching. *npj Quantum Information*, 7(1):1–5, 2021.

[181] BP Abbott, Richard Abbott, TD Abbott, S Abraham, F Acernese, K Ackley, C Adams, RX Adhikari, VB Adya, C Affeldt, et al. Gwtc-1: a gravitational-wave transient catalog of compact binary mergers observed by ligo and virgo during the first and second observing runs. *Physical Review X*, 9(3):031040, 2019.

[182] Tito Dal Canton and Ian W Harry. Designing a template bank to observe compact binary coalescences in advanced ligo's second observing run. *arXiv preprint arXiv:1705.01845*, 2017.

[183] Sascha Husa, Sebastian Khan, Mark Hannam, Michael Pürrer, Frank Ohme, Xisco Jiménez Forteza, and Alejandro Bohé. Frequency-domain gravitational waves from nonprecessing black-hole binaries. i. new numerical waveforms and anatomy of the signal. *Physical Review D*, 93(4):044006, 2016.

[184] Sebastian Khan, Sascha Husa, Mark Hannam, Frank Ohme, Michael Pürrer, Xisco Jiménez Forteza, and Alejandro Bohé. Frequency-domain gravitational waves from nonprecessing black-hole binaries. ii. a phenomenological model for the advanced detector era. *Physical Review D*, 93(4):044007, 2016.

[185] Sebastian Khan, Katerina Chatziioannou, Mark Hannam, and Frank Ohme. Phenomenological model for the gravitational-wave signal from precessing binary black holes with two-spin effects. *Physical Review D*, 100(2):024059, 2019.

[186] Reinhard Prix. Template-based searches for gravitational waves: efficient lattice covering of flat parameter spaces. *Classical and Quantum Gravity*, 24(19):S481, 2007.

[187] Thomas Cokelaer. Gravitational waves from inspiralling compact binaries: hexagonal template placement and its efficiency in detecting physical signals. *Physical Review D*, 76(10):102004, 2007.

[188] Christopher Messenger, Reinhard Prix, and Maria Alessandra Papa. Random template banks and relaxed lattice coverings. *Physical Review D*, 79(10):104017, 2009.

[189] Duncan A Brown, Ian Harry, Andrew Lundgren, and Alexander H Nitz. Detecting binary neutron star systems with spin in advanced gravitational-wave detectors. *Physical Review D*, 86(8):084017, 2012.

[190] Ian W Harry, Alexander H Nitz, Duncan A Brown, Andrew P Lundgren, Evan Ochsner, and Drew Keppel. Investigating the effect of precession on searches for neutron-star–black-hole binaries with advanced ligo. *Physical Review D*, 89(2):024010, 2014.

[191] Masahide Sasaki and Alberto Carlini. Quantum learning and universal quantum matching machine. , 66(2):022303, August 2002.

[192] Masahide Sasaki, Alberto Carlini, and Richard Jozsa. Quantum template matching. , 64(2):022317, August 2001.

[193] Harry Buhrman, Richard Cleve, John Watrous, and Ronald de Wolf. Quantum Fingerprinting. , 87(16):167902, October 2001.

[194] Scott Aaronson. Read the fine print. *Nature Physics*, 11(4):291–293, April 2015.

[195] John Preskill. Quantum Computing in the NISQ era and beyond. *Quantum*, 2:79, August 2018.

[196] Ibm quantum breaks the 100-qubit processor barrier.

[197] Ismael Faro Karl Wehden and Jay Gambetta. Ibm's roadmap for building an open quantum software ecosystem. https://www.ibm.com/blogs/research/2021/02/quantum-development-roadmap/, February 2021.

[198] Ryan Babbush, Jarrod R. McClean, Michael Newman, Craig Gidney, Sergio Boixo, and Hartmut Neven. Focus beyond quadratic speedups for error-corrected quantum advantage. *PRX Quantum*, 2:010103, Mar 2021.

[199] The windchime project.

[200] Hunter Gabbard, Michael Williams, Fergus Hayes, and Chris Messenger. Matching matched filtering with deep networks for gravitational-wave astronomy. *Physical review letters*, 120(14):141103, 2018.

[201] Hunter Gabbard, Chris Messenger, Ik Siong Heng, Francesco Tonolini, and Roderick Murray-Smith. Bayesian parameter estimation using conditional variational autoencoders for gravitational-wave astronomy. *arXiv e-prints*, page arXiv:1909.06296, September 2019.

[202] Elena Cuoco, Jade Powell, Marco Cavaglià, Kendall Ackley, Michal Bejger, Chayan Chatterjee, Michael Coughlin, Scott Coughlin, Paul Easter, Reed Essick, et al. Enhancing gravitational-wave science with machine learning. *arXiv preprint arXiv:2005.03745*, 2020.

[203] Christian Röver. Random template placement and prior information. In *Journal of Physics Conference Series*, volume 228 of *Journal of Physics Conference Series*, page 012008, May 2010.

[204] T. Dent and J. Veitch. Optimizing gravitational-wave searches for a population of coalescing binaries: Intrinsic parameters. *Phys. Rev. D*, 89(6):062002, 2014.

[205] John Preskill. Quantum Computing in the NISQ era and beyond. *Quantum*, 2:79, Aug 2018.